Crystallographic and Modelling Studies of Industrially Relevant Metal Complexes

Fraser J. White

Doctor of Philosophy

University of Edinburgh

2008

Abstract

Increasing the efficacy of ligands is crucial to many industrial processes and products. The design of new organic reagents which might find applications in automotive lubrication and extractive metallurgy are reported.

Force-field based molecular modelling has been used in chapters 2 and 3 to investigate the structure of complexes of malonic acids and benzohydroxamic acids formed on binding to iron(III) oxide surfaces for which both have shown high affinity. Models were constructed in which the ligands were docked to planes in the lepidocrocite crystal structure to simulate their interaction with steel engine surfaces. The Cambridge Structural Database has been used to elucidate the structures of polynuclear complexes of carboxylic acids to define appropriate geometries for malonate complex models. The most plausible modes of surface binding involving malonic acid were modelled to establish which would show the most favourable ligand-surface and ligand-ligand secondary bonding. Modelling of hydroxamate surface binding was guided by structural motifs observed in a mononuclear trishydroxamato iron(III) complexes in a dinuclear complex $[Fe_2L_2(\mu_2L)_2Br_2]$ where LH = benzohydroxamic acid. The resulting model predicted the surface activity of a range of hydroxamic acid derivatives which have been confirmed by measurements of adsorption isotherms carried out on high surface area goethite.

The structures of square planar copper(II) complexes of 3-substituted salicylaldoxime ligands which are closely related to systems used in industrial hydrometallurgical processes have been investigated (chapter 4) to ascertain whether there are correlations between the solid state structures and the relative strengths of the ligands as copper extractants. It was expected that electronegative groups would enhance hydrogen bonding between ligands, pulling them towards one another with a consequent decrease in the binding cavity presented by the donor atoms. In practice the structures were found to be influenced by interactions present in the solid state. In particular, axial interactions were found to influence the inner coordination sphere

geometry and these were also investigated (chapter 5) using high pressure X-ray crystal structures. Contrary to expectation, application of pressure was found to increase axial bond lengths in order to improve molecular packing efficiency so that the cell volume could decrease.

Declaration

I hereby declare that, except where specific reference is made to the work of others, all of the written and experimental work contained within these pages was conducted by the author.

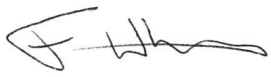

Fraser White, 2008

Acknowledgements

I would like thank my supervisors Prof. Peter Tasker, Prof. Simon Parsons and Dr Steve Harris. Peter, I have never met a busier man, I don't know how you manage to fit everything in to a day and still have time to be patient with a wayward student like me. You have an extraordinary ability to shake me out of a slump with your enthusiasm. Without your perspective this thesis might not have materialised. Simon, you have been a great boss and a better friend, there were several times you gave me a pep talk I badly needed and I don't think I told you at those times that I really appreciated it. I also want to thank you for introducing me to crystallography and teaching me so well. Steve, your visits spurred me on more than you probably know. There is nothing like a healthy fear of attending a meeting with nothing to report to focus the mind. It all began with your thesis too, so I guess I owe you one.

That brings me to the Tasker group. There are so many of you that it would be impossible to thank everyone by name, but you have all in some small or large way helped me greatly. The steady stream of crystals kept me busy and taught me a lot. Iria, Robert and Ross, these pages would be very thin on material without you. To all of you, your experimental work and friendship are greatly appreciated.

I feel privileged to have shared an office with the Parsons group. Steve, what can I say, you've become one of my best friends and offered sage council over the years, I think I owe you more than just that beer. You are a top bloke and I'm glad I met you and Fiona. Pete, you are one of the cleverest people I know. It's a shame you had to move so far away, makes going to the cinema a tad more difficult. Thank you for being a sounding board and a good friend. Russell, Iain, Laura, Alex, Patty, Francesca, James, and Anna, I consider you all good friends and each of you deserve more space than I have left to write in.

Finally, to my family, what can I say? Mum and Dad, this thesis is as much your achievement as it is mine. Dad, I will be eternally grateful for your generosity in the last year, you shouldn't have to support me anymore but you did it without question, so thank you. Mum, the emotional support you gave me kept me sane. Fiona and Jason thanks for your support and for entertaining me with bad jokes.

Lecture Courses and Meetings

Oct-04	Radiation Protection	Edinburgh University	
Nov-04	Unix I and II	Edinburgh University	
Nov-04	Laser Safety	Edinburgh University	
Nov-04	BCA CCG Autumn Meeting	Aston University	
Apr-05	Intensive Crystallography School	Durham University	
Apr-05	BCA Spring Meeting	Loughborough University	*poster*
Jul-05	Coord. Chem. Discussion Group	Cardiff University	*poster*
Aug-05	IUCr Congress	Florence	*poster*
Nov-05	Eastchem Len Lindoy Symposium	Edinburgh/St. Andrews	
Nov-05	BCA CCG Autumn Meeting	Daresbury Laboratory	
May-06	Eastchem paper writing course	St Andrews University	
Jul-06	Eastchem Bruno Chaudret Symposium	Edinburgh University	*talk*
Jul-06	Eastchem Harry Gray Symposium	Edinburgh University	
Sep-06	Advanced Refinement Course	Southampton University	
Nov-06	BCA CCG Autumn Meeting	Glasgow University	
Apr-07	BCA Spring Meeting	University of Kent	*poster*
Nov-07	BCA CCG Autumn Meeting	Diamond Light Source	

Publications

Chartres, Jy D.; Dahir, Ahmed; Tasker, Peter A.; **White, Fraser J**.. **Zirconium complexes of amino(polyphenolic) ligands and their hydrolytic stability.** *Inorganic Chemistry Communications* (2007), 10(10), p1154-1158

Forgan, Ross S.; Parsons, Simon; Tasker, Peter A.; **White, Fraser J**.. **3-(5-tert-Butyl-2-hydroxybenzoyl)propanoic acid.** *Acta Crystallographica, Section E: Structure Reports Online* (2007), E63(7), p3249

Hunter Tina M; McNae Iain W; Simpson Daniel P; Smith Alison M; Moggach Stephen; **White Fraser**; Walkinshaw Malcolm D; Parsons Simon; Sadler Peter J **Configurations of nickel-cyclam antiviral complexes and protein recognition**. *Chemistry (Weinheim an der Bergstrasse, Germany)* (2007), 13(1), p40-50

Maganas, Dimitrios; Staniland, Sarah S.; Grigoropoulos, Alexios; **White, Fraser**; Parsons, Simon; Robertson, Neil; Kyritsis, Panayotis; Pneumatikakis, Georgios. **Structural, spectroscopic and magnetic properties of $M[R_2P(E)NP(E)R'_2]_2$ complexes, M = Co, Mn, E = S, Se and R, R' = Ph or ^{i}Pr. Covalency of M-S bonds from experimental data and theoretical calculations.** *Dalton Trans.,* (2006), (19), p2301-2315

Milios, Constantinos J.; Manoli, Maria; Rajaraman, Gopalan; Mishra, Abhudaya; Budd, Laura E.; **White, Fraser**; Parsons, Simon; Wernsdorfer, Wolfgang; Christou, George; Brechin, Euan K. **A Family of [Mn6] Complexes Featuring Tripodal Ligands.** *Inorganic Chemistry* (2006), 45(17), p6782-6793

Gass, Ian A.; Milios, Constantinos J.; Collins, Anna; **White, Fraser J.**; Budd, Laura; Parsons, Simon; Murrie, Mark; Perlepes, Spyros P.; Brechin, Euan K. **Polymetallic clusters of iron(III) with derivatised salicylaldoximes.** *Dalton Trans.*, (2008), 2043–2053

Gordon, Ross J.; Campbell, John; Henderson, David K.; Henry, Dorothy C. R.; Swart, Ronald M.; Tasker, Peter A.; **White, Fraser J**.; Wood, Jenny L.; Yellowlees, Lesley J. **Polyacidic multiloading metal extractants.** *Chem. Comm.,* (2008), 39, 4801-4803

Rio-Echevarria, Iria M.; White, Fraser J.; Brechin, Euan K.; Tasker, Peter A.; Harris, Steven G. **Surface binding vs. sequestration; the uptake of benzohydroxamic acid at iron(iii) oxide surfaces.** *Chem. Comm*., (2008), 38, 4570-4572.

Forgan, Ross S.; Davidson, James E.; Galbraith, Stuart G.; Henderson, David K.; Parsons, Simon; Tasker, Peter A.; White, Fraser J. **Transport of metal salts by zwitterionic ligands; simple but highly efficient salicylaldoxime extractants.** *Chem. Comm.,* (2008), 34, 4049-4051.

Forgan, R. S.; Henderson, D. K.; Mcallister, F. E.; Tasker, P. A.; White, F. J.; Campbell, J.; Swart, R. M. **Copper extractant strength: the effect of substituents in the 3-position on hydroxyoxime performance.** *Canadian Metallurgical Quarterly* (2008), 47(3), 293-300

Abbreviations

1-D	One dimensional
2-D	Two dimensional
3-D	Three dimensional
AFM	Atomic force microscopy
bhaH	benzohydroxamic acid
ChEq	Charge equilibration
CI	Corrosion inhibitor
CSD	Cambridge structural database
DAC	Diamond anvil cell
DFT	Density functional theory
e.s.d.	Estimated standard deviation
en	Ethylene diamine
FF	Force-field
FM	Friction modifier
HF	Hartree-Fock theory
HFRR	High frequency reciprocating rig
INS	Inelastic neutron scattering
LEED	Low energy electron diffraction
MM	Molecular mechanics
MoDTC	Molybdenum dialkyldithiocarbamate
MP2	Møller-Plessett perturbation theory (2^{nd} order)
OBD	Overbased detergent
pipCH_2	N-methylpiperidine
pmaH	Phenylmalonic acid
saloxH	Salicylaldoxime
SEM	Scanning electron microscopy
SNOM	Scanning near-field optical microscopy
SQUID	Spin quantum interference device
STM	Scanning tunnelling microscopy
UFF	Universal force-field
XPS	X-ray induced photoelectron spectroscopy
ZDDP	Zinc dialkyldithiophosphate

Contents

Chapter 3 – The Interaction of Benzohydroxamic Acid with Iron Oxide Surfaces

Chapter 4 – Crystallographic Studies of Phenolic Oxime Solvent Extraction Agents

Chapter 1

Introduction

Contents

1. Introduction

This thesis is concerned with the enhancement of knowledge of ligand design in surface engineering and solvent extraction. Designing more efficient reagents for these industrial applications is very challenging because it is usually difficult to determine the structures of complexes under the conditions of use. The structural studies and modelling presented herein provide methods to understand and predict surface activity and the strength and selectivity of metal ion transport processes.

The research was part funded by Infineum UK Ltd, suppliers of lubricant additives, and consequently one of the areas of application of ligand design undertaken was related to the development of friction modifiers, discussed further in this chapter. The other area of application is concerned with development of more efficient solvent extraction agents for the recovery of copper by extractive metallurgy and is introduced in chapter 4.

1.1. The environment and the automobile

Climate change is a subject of much controversy and its origins and causes in recent times are largely believed to be the result of human industrial activity.[1] The consequences of climate change are becoming more and more apparent with glacial ice disappearing and the shrinking of the polar ice caps. In 1958 Charles Keeling began monitoring atmospheric CO_2 levels, work which continues to this day, and the result of his work is known as the Keeling curve.[2] It is an upward curve showing atmospheric CO_2 levels increasing year on year and as CO_2 is a greenhouse gas, it is commonly attributed with bringing the issue of global warming to the fore.

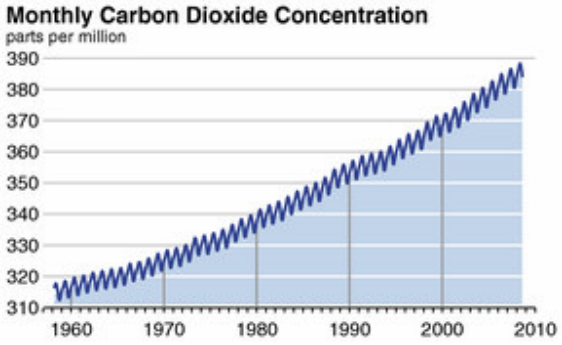

Figure 1-1: The Keeling curve which is measured at Mauna Loa in Hawaii and is currently maintained by the Scripps Institute of Oceanography.[3]

The high profile of environmental issues in recent times has led to growing public concern which has put pressure on governments to introduce tougher legislation regarding the emission of greenhouse gases. A major culprit, the automobile, has become ubiquitous in today's society. The combustion of hydrocarbon fuels obtained from crude oil in an engine can produce many pollutants such as NO_x, SO_x, particulates, CO_2 and water vapour. Whilst legislation is succeeding in reducing these harmful emissions, the number of cars on the roads continues to rise. Statistics issued by the Department for Transport[4] showed that 511 billion kilometres were covered by vehicles in the UK in 2006 compared with 277 billion in 1980 and increases are expected to continue. Taking just CO_2 emissions for the same year, 2006, the average CO_2 emission for a new car was 167.2 g/km. This translates to approximately 85 million tons of CO_2 a year, although actual levels would be higher, given most vehicles on the road were older and had higher emissions.

Clearly reducing the emission levels of cars is desirable not only to combat global warming, but also to improve air quality in cities. The simplest way to reduce emissions from cars is to improve fuel economy.

1.2. The motor engine

Internal combustion engines use the chemical energy stored in hydrocarbons such as petroleum or diesel to power many types of device, most notably cars and other forms of vehicular transport. The first functional four-stroke engine was developed in 1876 by Nicolaus Otto,[5] in collaboration with Gottlieb Daimler and Wilhelm Maybach and is often referred to as the Otto engine. In such engines, which are usually made with steel, the combustion is carried out in a steel cylinder which is sealed by a number of valves at the top and a piston connected to a cam on the crankshaft at the bottom. The valves at the top of the cylinder are controlled by a camshaft which opens and closes them at the correct times so that the intake of fuel and air and expulsion of exhaust gases is possible. The four stroke engine, as implied by the name, has four specific phases or strokes during its operation.[6]

- *Intake stroke*. The intake valve(s) open and petroleum and air are taken into the combustion chamber by the action of the piston drawing back in the cylinder. In more modern engines fuel may be introduced using injectors which ensure dispersal and more precisely control the fuel to air ratio.
- *Compression stroke.* During this phase all valves are closed and the piston moves forward reducing the cylinder volume and compressing the combustion mixture.
- *Power stroke.* This phase is initiated by an electrical spark supplied by a spark plug at the head of the cylinder which ignites the gas mixture causing an explosion which forces the piston back turning the crank shaft and generating power.
- *Exhaust stroke.* The exhaust valve(s) open and the combustion products are pushed out of the cylinder by the forward stroke of the piston.

Since the engine is comprised of many moving parts, friction and its associated effect on the engine are an issue. The effects of friction are a notable part of everyday life, sometimes being beneficial e.g. the grip provide by shoes on the ground, and sometimes it is a hindrance, e.g. power generation and transmission.

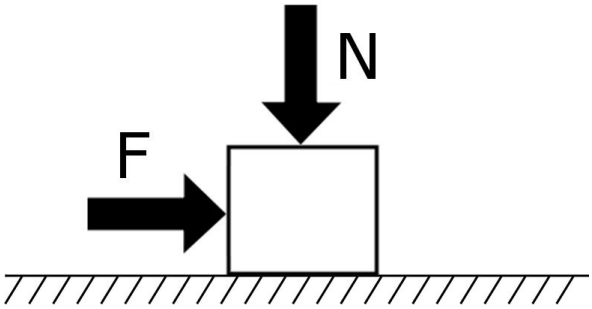

Figure 1-2: The force applied to move an object along a surface, *F*, is related to the normal force, *N* by the friction co-efficient, μ, by the relationship $F=\mu N$

In macroscopic terms friction can be summarised by the diagram shown in Figure 1-2. It can be described as the difficulty experienced in moving one surface over another as a consequence of the force applied pushing one into the other. It is a consequence of surface roughness which is apparent right up to the macroscopic scale e.g. chunky tyre grips, and also applies to the microscopic scale due to imperfect flatness on the atomic scale see Figure 1-3.[7] Friction manifests itself in liquids as viscosity and is a consequence of interaction between molecules.[8] This phenomenon is not completely understood, but secondary interactions can occur between molecules which contribute to viscosity. In order to move molecules away from one another these secondary interactions must be broken, which requires the input of energy. This can be likened to walking through a muddy field where shoes stick to the ground and are difficult to lift away making progress difficult. Alternatively viscosity can be as a result of molecular entanglements where long chain molecules are involved.[8] Conformational changes must occur to separate molecules which requires the input of energy.

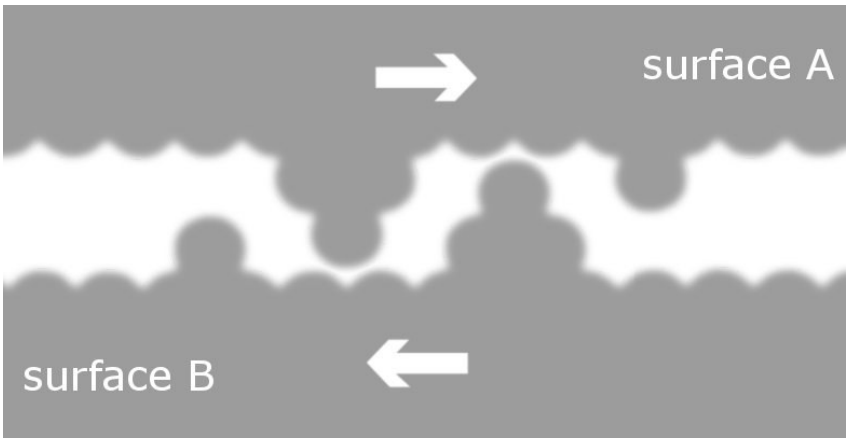

Figure 1-3: Surface roughness on the atomic scale means physical barriers exist which impede the movement of surfaces A and B as they slide over one another.

Historically, friction has been managed using oil which reduces friction by coating the internal surfaces of the engine.[9, 10] This coating provides a low shear interface between the surfaces but it has several drawbacks. In the course of operation combustion processes produce variable temperatures along with acidic chemicals and the consequences of this are manyfold.[11] The temperature of the engine can have an effect on the viscosity of the oil which can impact upon its performance. Also, over time the oil degrades through combustion and attack from combustion products. Acidic combustion products also attack the steel surfaces in the engine leading to pitting which contributes to friction and ultimately reduced life for the engine. Further combustion products, like soot, can form clogs which impact on the efficiency of the engine.

The overall efficiency of the engine can be improved by adding compounds to the oil which are intended to counteract these effects. Collectively these are referred to as an additive package. Commercially additive packages contain several different components each with a specific function aimed at enhancing a particular aspect of engine operation, including viscosity-modifying polymers, antiwear agents, corrosion inhibitors, overbased detergents, dispersants, antioxidants and friction modifiers.[12]

1.3. Engine oil and additive packages.

The composition of an additive package is usually determined by trial and error as the competitive effects of the components and factors affecting its stability are not well understood.[12] Each of the ingredients of a lubrication solution must perform its function with the minimum interference from the other components so selectivity is a consideration. The major components of a modern crankcase lubricant are:

- *Base mineral oil.* This is usually a mineral oil comprised of a mixture of different length hydrocarbons. The oil performs two functions; it provides base lubrication and acts as a heat sink, which prevents localised heat build-up.[12]
- *Viscosity modifying polymers.* The temperature in an engine varies during operation with the work being done, and as the viscosity of the oil is dependant on temperature, it is desirable to add to it viscosity modifying polymers. These coil up at low temperature and unravel at high temperatures allowing the oil to maintain a more consistent viscosity over the entire treated region and over the large temperature ranges experienced meaning more consistent performance and efficiency.[12]
- *Antiwear agents*. These are molecules such as zinc dialkyldithiophosphates (ZDDP)[13], which form a sacrificial layer on the steel surfaces to protect them when rubbing directly on one another.
- *Corrosion inhibitors.* Corrosion inhibitors are surfactants which are designed to attach themselves to the steel surfaces in the engine providing high surface coverage with a hydrophobic layer which prevents corrosive materials such as oxygen, acids and water from accessing surfaces and chemically damaging them.[14]
- *Overbased detergents.* These are colloidal particles containing a core of calcium carbonate surrounded by a layer of surfactants to provide solubility. These are

present to neutralise acidic compustion products, e.g. H_2SO_4, and HNO_3, produced in the combustion chamber.[11]

- *Dispersants*. Soot formed during combustion can aggregate and form large particles which can clog various operationally important parts of the engine. Dispersants are usually surfactants which attach to soot particles and make them soluble in oil, thus preventing aggregation, build up and clogging.[12]
- *Antioxidants*. Engines are not airtight systems since they require oxygen for combustion and there are many other points of entry. Combustion can also produce oxidising agents which represent reduced oil performance over time. Antioxidants are molecules such as hindered phenols and are used to increase the lifetime of the oil by suppressing degradation by oxidising agents.[15]
- *Friction modifiers.* Friction, as discussed in the previous section, is treated by friction modifiers which provide a low shear interface between surfaces reducing wear and friction. These are discussed further in the following section.

1.3.1. Treating friction

The first defence against friction is the base oil which provides friction reduction over all regions of the engine. However, within an engine there are components which are continually changing direction and with varying speed. These result in different forces of contact in different regions and at different times. In the crankcase of a working engine it is not possible to treat these areas uniquely. Consequently effective treatment requires a solution which can address several different requirements simultaneously.

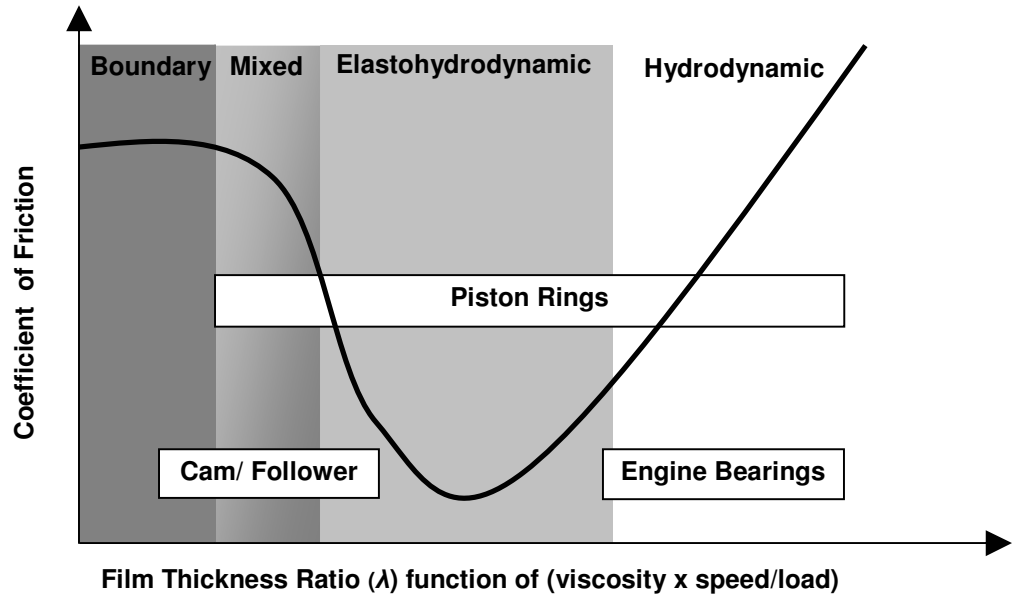

Figure 1-4: The Stribeck Curve

The types of surface contacts which can be found in an engine can be separated into distinct regions (Figure 1-4). The Stribeck curve[16] relates the friction co-efficients to a parameter λ, the film thickness ratio. It shows how the friction coefficient changes with varying contact load in the presence of oil. In the boundary and mixed regions, contact is heavily loaded and occurs in areas such as on the camshaft attached to the pistons which bear the full force generated by the explosions in the cylinders. In this region thick oil is most suitable which, unlike thinner oils, will coat the surfaces well and form a barrier between hard metal-on-metal contacts.

The elastohydrodynamic region is where the surfaces are in contact but are not pressed together with significant force, e.g. close to the piston rings which generally experience forces parallel to the surface plane which they contact. This region generally has the lowest friction coefficient regardless of the type of oil used.

The hydrodynamic region is where there is very little or no direct contact between surfaces and the forces of friction experienced here are caused by the viscosity of the oil itself. This means that the more viscous the oil is, the higher the friction co-efficient will be. It is obvious that the boundary region and the hydrodynamic region have conflicting requirements in terms of lubrication and therefore for improved engine performance, oil alone cannot address both.

1.3.2. Friction modification

The problem highlighted by the Stribeck curve can be tackled by replacing thick oil with thin oil and using an additional component to treat the loaded contact regions. This allows for the reduction of friction in both the boundary region and also in the hydrodynamic region. This additional component is the friction modifier.

Friction modification has previously been achieved by using inorganic materials which contain heavy metals and sulfur. More specifically a family of friction modifiers which has commonly been used are molybdenum dialkyldithiocarbamates (MoDTC) often in conjunction with zinc dialkyldithiophosphates (ZDDP) which also provide antiwear properties (see section 1.3).[17-19] The method by which these compounds are thought to reduce friction is the *in-situ* formation of molybdenum disulfide. Molybdenum disulfide is a well-known lamellar solid phase lubricant[20] whose plates can then be sheared from the bulk MoS_2 quite easily reducing friction. This method of tackling friction is extremely efficient. However, increasing environmental concern has lead to legislation controlling the emissions which are acceptable from modern motor cars which has made use of such compounds undesirable.

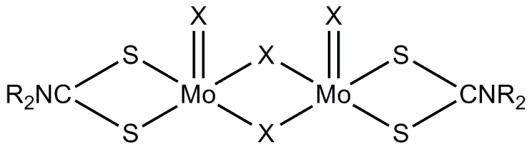

Figure 1-5: Molydenum dithiocarbamate, where R groups are alkyl chains and X are non-carbon atoms such as oxygen.

As mentioned in section 1.1, the process of combustion of petroleum or diesel produces many harmful compounds such as SO_x, NO_x, polyaromatic hydrocarbons, and particulates amongst others. The quantity of each released into the atmosphere is largely dependent upon the composition of the fuel and lubricant used. Use of molybdenum dialkylthiocarbamate as a friction modifier has become undesirable as it provides a source of sulfur allowing the production of SO_x compounds, which can either lead to the formation of H_2SO_4 which is harmful to engine components, or be released in exhaust gases.

For these reasons more efficient organic friction modifiers are being sought. A current trend is to introduce benign organic materials into the oil which are surfactant molecules, having a hydrophilic head group and a hydrophobic tail group.[21] Since car engines are primarily made from steel there is a layer of iron oxide on the surfaces. The head group polarity makes it possible for the molecule to attach itself to the polar metal oxide surface. The tail group in general will incorporate extended alkyl chains which not only solubilise the molecule in the base oil so that it may be delivered to the surfaces but also provide the necessary friction-reducing functionality. A commonly used friction modifier of this type is stearic acid[22] which is the carboxylic acid carrying a linear aliphatic $C_{18}H_{37}$ chain.

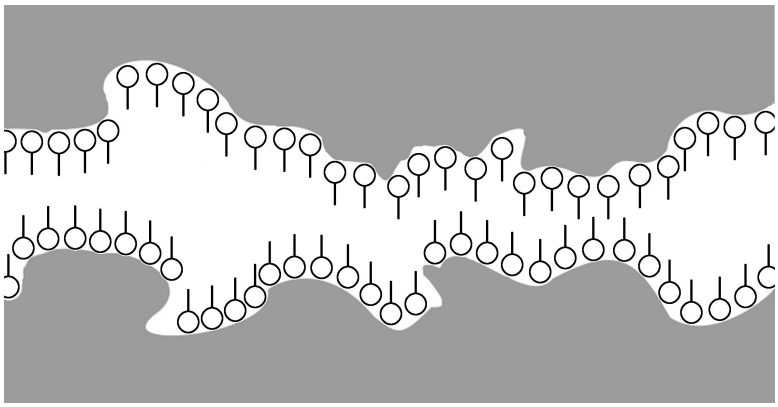

Figure 1-6: A representation of surfaces treated with friction modifying surfactants. The tail groups are long alkyl chains which are greasy and can easily slide over one another.

1.4. Designing friction modifying molecules

The collaborative work in this PhD project to develop potential friction modifiers involved the steps which are outlined in Figure 1-7.

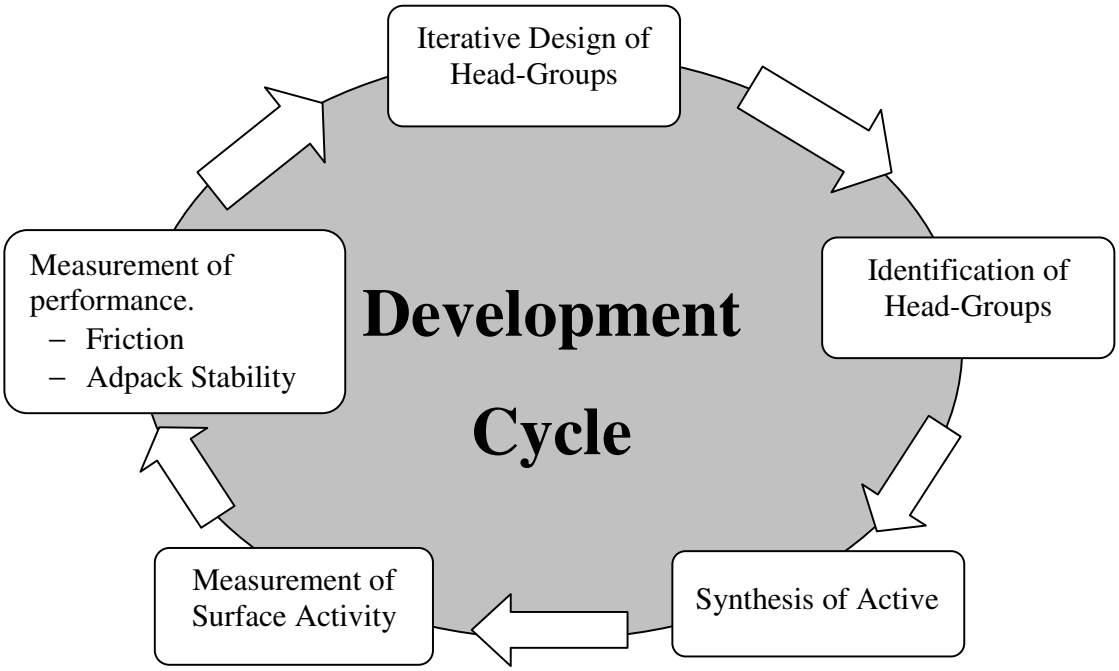

Figure 1-7: The development cycle employed for this project. Identification, syntheses and measurement of isotherms were conducted at Edinburgh University by Drs Iria Rio and Robert Renz. Measurement of performance was undertaken by Dr Steve Harris of Infineum UK Ltd. The iterative design steps were the responsibility of the author.

1.4.1. Multi-site attachment

Attachment of ligands to surfaces requires different chemistry from that of ligands for discrete metal ions in solution. The chelate effect is an important feature in designing ligands which bind strongly to single metal ions.[23] Complexes in which multidentate ligands bind to a metal ion will have a higher thermodynamically stability than those in which equivalent individual ligands which have the same donor atoms bind to the same metal ion. The high stability was initially attributed to an entropic argument. If we take the case of ethylenediamine vs. ammonia as ligands for copper, Figure 1-8, the former case, ethylenediamine, involves a more favourable increase in entropy upon formation of the complex in comparison to the latter case.

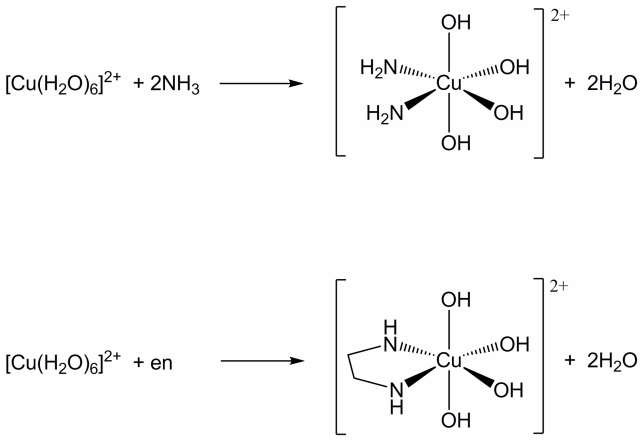

Figure 1-8: Two reactions demonstrating the chelate effect.

In the reaction of a complex with ammonia the 3 moles of reactant give 3 moles of product. In the case of ethylenediamine, 2 moles of reactants give 3 moles of product representing an increase in entropy. This is reflected in the measured ΔS values of -8.4 and +23 J K^{-1} mol^{-1} for ammonia and ethylenediamine respectively.[23] Enthalpic energy terms also contribute to complex stability when the chelate effect is in operation. As an example, replacing multidentate ligands with discrete ligands would require desolvation of several ligands plus the complex and then the solvation of the multidentate ligand and resolvation of the complex. The enthalpy of desolvation of several ligands is likely to be higher than for one multidentate ligand so the overall process requires an input of energy.[23] Consequently the stability of complexes of multidentate ligands is higher.

Ligands which have multiple chelating units can occupy all of the coordination sites of a single metal ion. This is known as sequestration. Such behaviour in a ligand is undesirable if we wish it to bind to a surface as the stability of the mono-nuclear complex is so high that it is thermodynamically favourable to remove ions from the surface (see top in Figure 1-9). However, if we use a *poly*nucleating ligand which is rigid and does not generate strain-free five or six-membered chelate rings as illustrated

in Figure 1-9 surface binding is likely to be favoured over sequestration. The surface complexes will also be thermodynamically favoured over those formed by *di*nucleating ligands (see bottom of Figure 1-9). Attachment of dinucleating ligands (bottom right of Figure 1-9) will not result in a major change in entropy as one water molecule is released for each attached ligand. If, however, a ligand binds to multiple sites (bottom left of Figure 1-9), one ligand now displaces several water molecules resulting in a favourable increase in entropy. Consequently, in terms of optimising the free energy of surface complex formation, ligands should be multi-dentate but care should be taken to ensure that sequestration of metal ions from the surface does not occur (ligands should be polynucleating).

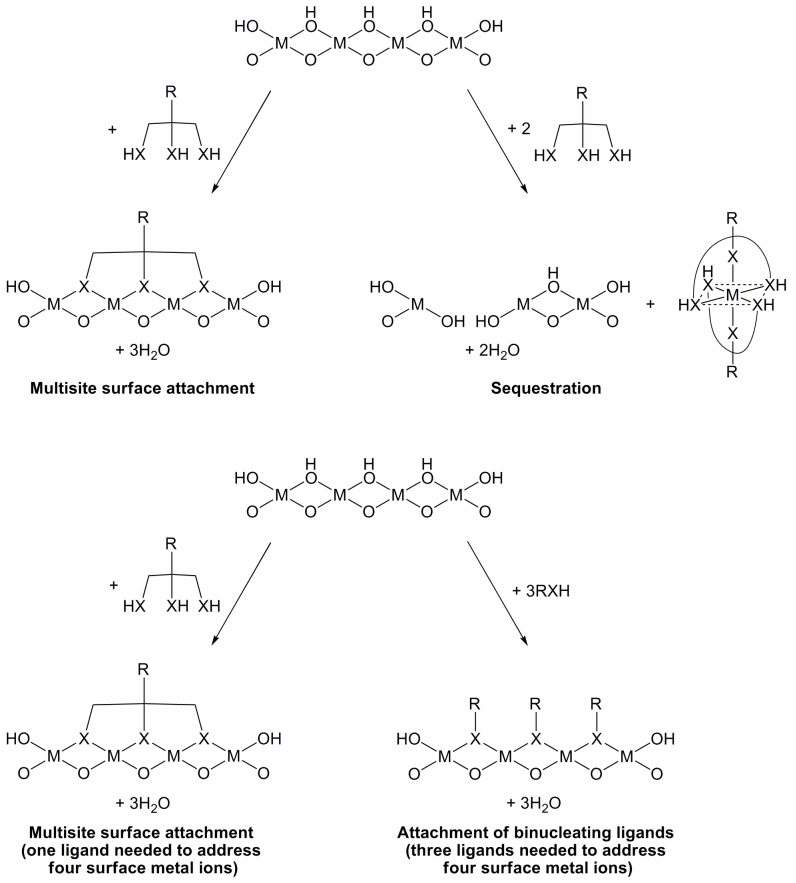

Figure 1-9: Schematic representation of the requirements for stable surface complex formation. Ligands should favour "multisite attachment" over sequestration (top) and should favour formation of *poly*nuclear complexes (bottom).

1.4.2. Characterising surface attachment

Understanding how molecules interact with a surface is essential for designing all types of surfactants. In this thesis it is essential to define whether desirable multi-site attachment modes are in operation and if not, why not. This requires the use of techniques which will give information about the structure of complexes found *on the surface*.

Studying reactions at metal oxide surfaces is important in many fields including heterogeneous catalysis,[24] corrosion science,[25] environmental chemistry,[26] metallurgy,[27] soil science[28] and tribology. A commonly used method of determining adsorption properties is to measure adsorption isotherms. Whilst a very useful technique, employed in this thesis and related work,[29-31] it does not yield structural information about surface complexes. Adsorption isotherms are discussed in section 1.5.1.

1.4.2.1. Techniques for studying the structure of surface complexes.

There are many techniques which can yield information about surface complex structure and stability. Most of the available techniques such as X-ray induced photoelectron spectroscopy (XPS), low energy electron diffraction (LEED), and inelastic neutron scattering (INS) can give information about bond types and energies which exist in the topmost layers of a surface. Atomic force microscopy (AFM),[32] scanning tunnelling microscopy, (STM),[33] scanning near field optical microscopy (SNOM)[34] and scanning electron microscopy (SEM)[35] are useful techniques for obtaining information from a surface. None of these techniques can provide high resolution three-dimensional structural information regarding surfactant binding. Determining the three-dimensional structure of materials is extremely useful in understanding structure/activity relationships which can lead to development of more effective materials. A recent

example[36] of the success of this approach is the study of single molecule magnets by single crystal X-ray crystallography both at ambient and high pressure and correlating structural parameters to magnetic properties measured using a spin quantum interference device (SQUID). Computational methods can be used to produce three dimensional atomic models of surface complexes which can provide more detailed, albeit theoretical, structural information and has successfully been used in surface complex characterisation previously in the study of 4-keto acids as corrosion inhibitors in crankcase lubrication packages.[14, 30]

1.4.2.2. Computational methods

There are two main approaches in computational methods derived from the branches of physics, classical and quantum mechanical. Quantum mechanical methods encompass both *ab initio* and semi empirical methods and require a solution to the Schrödinger equation.[37] In order to calculate a solution, two components must be known. All of the kinetic and potential energy terms describing the system must be defined which are described by a Hamiltonian, H in Equation 1-1. Secondly, the wavefunction, Ψ, describing the atomic orbitals of all atoms in the system needs to be determined. This is non-trivial as a result of the many-body problem.[37]

$$E\Psi = H\Psi$$

Equation 1-1: The Schrödinger equation

The many-body problem arises due to the correlation of electrons. The electrostatic field of one electron has an effect on the positions of all other electrons and its position is in turn affected by their fields. This makes the system so complex that directly solving the Schrödinger equation is impossible. To deal with this problem an approximation must be used which allows positions to be calculated. Some prominent

examples of such approximations are Hartree-Fock theory (HF),[38] Møller-Plesset perturbation theory (MP2),[39] and density functional theory (DFT).[40, 41] The wavefunction must also be determined in order to solve the Schrödinger equation which is done by combining Gaussian waveforms from what is known as a basis set. The basis set contains different Gaussian peak shapes which can be mixed to describe the atomic orbitals in the system. The basis set can be changed in order to use more or fewer Gaussian peaks to describe the system more or less accurately. Examples of basis sets are 3-21G*, 6-31G* and 6-311G*.[42-47] Extensions can be made to model polarisation. *Ab initio* calculations are very computationally demanding and only in the last few decades has computational power increased to the extent that they have become a viable means of determining structure and chemistry of small systems.

Molecular mechanics (MM) is a classical physics approach to the problem. Individual electrons are ignored and atoms and bonds are treated as balls and springs. This means that interatomic potentials can be described using simple equations which can be solved easily, e.g. Hooke's Law shown in Figure 1-10, and so are computationally undemanding.[48]

$$\nu(x) = \frac{k}{2}(x - x_0)^2$$

k = force constant

x = bond length

x_0 = reference bond length

Figure 1-10: Hooke's law describing harmonic bond stretching.

The equations require force constants and reference bond lengths in order that the energy may be calculated and these are contained in a parameter list known as a force field (FF).[48] Many force fields are available and modern force fields contain parameters to describe bond stretching, bond bending, torsion angles and non-bonding terms although

the terms included differ between forcefields.[49] As atoms of the same element can behave in different ways depending on their bonding environment, different atom types are often defined within the force field. The atom type is assigned prior to calculation so that e.g. an aromatic carbon atom is correctly modelled as trigonal with 120° angles as opposed to tetrahedral. The variation in behaviour of atoms of a given element, coupled with the number of elements in the periodic table, means that an immense number of combinations of atomic interactions are possible. Consequently force fields are generally aimed at a small subset of the periodic table. In this thesis, the force field used is the universal force field (UFF) by Rappe *et al.*[50] The UFF attempts to provide parameters for all atoms. The general form of the energy expression for UFF is shown in Figure 1-11.

$$E_{tot} = \sum E_R + \sum E_\theta + \sum E_\phi + \sum E_\omega + \sum E_{vdw} + \sum E_{el}$$

E_R = bond stretching energy

E_θ = angle bending energy

E_ϕ = torsion twisting energy

E_ω = inversion energy

E_{vdw} = van der Waals energy

E_{el} = electrostatic energy

Figure 1-11: The form of the Universal Force Field energy terms.

Force fields do not normally contain parameters to describe electrostatic interactions as these require charges to be known for each atom. Calculation of the electrostatic energy terms is therefore only done if partial atomic charges are present and can be important in order to correctly model interactions such as hydrogen bonds which are primarily charge based interactions. Some force fields, such as the Dreiding force field,[51] contain atom types for hydrogen atoms likely to hydrogen bond, i.e. those bonded to heteroatoms, which have non-bonded interaction terms describing hydrogen bonding.

Various methods exist to calculate partial atomic charges so that coulombic interactions may be calculated. The method used in this thesis is the charge equilibration derived by Rappe and Goddard.[52]

1.5. Testing of candidates

Two methods for testing the performance of actives are used in this thesis. The first and more important is the use of adsorption isotherms to evaluate relative "strengths" of surface attachment.

1.5.1. Adsorption isotherms

The efficiency of uptake of potential surface actives from aqueous media onto powdered iron oxide minerals can be evaluated by determining an adsorption isotherm.[14, 29-31] These are measured by preparing a series of solutions of various concentrations of ligand and contacting them with a known quantity of a high surface area form of an iron oxy/hydroxide (powdered goethite was used in the work at the University of Edinburgh). The concentration of ligand remaining in solution is measured and this allows the quantity adsorbed onto the surface of the goethite to be calculated. Plotting the initial concentration of the ligand in solution against the quantity adsorbed gives a graph of the isotherm. The shape of the isotherm and the equation which best fits the plot depend on the nature of adsorption.[53] Isotherms take several forms. Figure 1-12 contains three examples of isotherm shapes.

Figure 1-12: Isotherms showing monolayering (left), bilayering (middle) and multilayering (right).[53]

The leftmost isotherm in Figure 1-12 represents mono-layering and is of the form expected for surfactants such as those studied in chapters 4 and 5. Datasets of this type form are classed as Langmuir isotherms and are fitted with the equation shown in Figure 1-13. The parameters determined during the fitting process *a* and *b* give the surface binding equilibrium constant, *K*, and the surface coverage.

$$y = a\left(\frac{bx}{1+bx}\right)$$

Figure 1-13: Equation used to fit Langmuir adsorption isotherm data. *y* is the quantity of adsorbed material and *x* is the concentration of adsorbate in solution.

The isotherm data contained in this thesis were provided by Dr Robert Renz[31] for the malonates presented in chapter 2 and by Dr Iria Rio[29] for hydroxamates which are presented in chapter 3.

1.5.2. High frequency reciprocating rig

In some cases where a high binding strength to iron oxide had been proven for a novel head group it was appropriate to investigate whether a "greasy" derivative showed useful friction reduction. The testing of friction reduction was undertaken by Dr Steve Harris of Infineum using a high frequency reciprocating rig (HFRR), see Figure 1-14.

This machine allows measurement of friction and wear by pressing a steel ball onto a steel plate and moving it back and forth at high frequency.[54, 55] Weights can be added to control the force with which the ball is pushed into the plate. The steel plate is submerged in the lubricant which is being tested and measurements of resistive forces taken at different temperatures. The force required to drag the steel ball across the surface is measured and if the normal force is known, the dynamic friction co-efficient can be calculated using the equation $F = \mu N$.

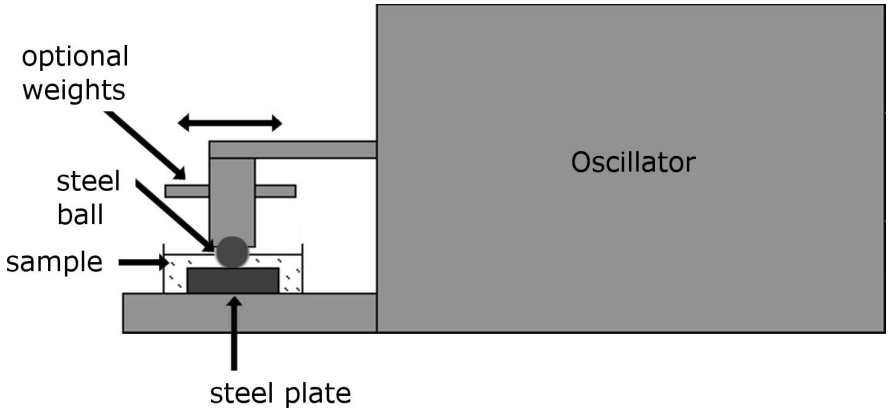

Figure 1-14: A diagram of a high frequency reciprocating rig (HFRR) showing the various important components.

1.6. Thesis outline

Chapter 2 investigates the structure of surface complexes formed when malonates bind to iron oxide surfaces with the aim of determining plausible surface geometries and guiding the design of new surface actives. The work was undertaken because malonates had been shown[31] to form significantly more stable surface complexes than "single" carboxylic acids. Carboxylate coordination geometry is explored using data from the Cambridge structural database. These data are used to guide the modelling of the

structures of malonates on iron oxide surface complexes using force-field methods. These models reveal structural key features important to strong binding.

Chapter 3 uses the crystal structure of an iron hydroxamate complex as the foundation for modelling surface complexes formed with iron oxides. Various models were constructed and subjected to an elimination process which produced one model. Hydroxamic acid derivatives were synthesised and used successfully to test the validity of the model.[29] Friction performance of a "greasy" derivative is also reported.

Chapter 4 introduces hydrometallurgical solvent extraction as a means of recovering copper from its ores. X-ray crystallography is used to establish correlations between the performance of salicylaldoxime derivatives as solvent extraction agents and structures of the ligands, including a new class of reagents which form copper *salt* complexes in the organic phase.

Chapter 5 uses high pressure as a probe to investigate the effect of axial interactions on the structure of a Jahn-Teller distorted copper *salt* complex determined by X-ray crystallography. Counterintuitive results were obtained and their cause was explored by looking at crystal structure packing.

1.7. References

1. P. Falkowski, R. J. Scholes, E. Boyle, J. Canadell, D. Canfield, J. Elser, N. Gruber, K. Hibbard, P. Hogberg, S. Linder, F. T. Mackenzie, B. Moore III, T. Pedersen, Y. Rosenthal, S. Seitzinger, V. Smetacek and W. Steffen, *Science*, 2000, **290**, 291-296.
2. C. D. Keeling, *Annual Review of Energy and the Environment*, 1998, **23**, 25-82.
3. http://scrippsco2.ucsd.edu, Accessed 22/11/2008.
4. *Department for Transport - Transport Trends*, http://www.dft.gov.uk/pgr/statistics/datatablespublications/trends/, Accessed 08/10/2008.
5. Otto N., *U.S. Pat.*, 194047, 1877.
6. F. W. Sterling, *Internal Combustion Engine Manual*, Read Books, 2007.
7. B. U. Division of Engineering, *Introduction to Statics: Friction*, http://www.engin.brown.edu/courses/en3/Notes/Statics/friction/friction.htm, Accessed 26/11/08.
8. W. Horobin, *How it Works*, Marshall Cavendish, 2003.
9. M. D. Hersey, *Theory and Research in Lubrication*, John Wiley & Sons Inc, New York, 1966.
10. B. Bhushan, *Modern Tribology Handbook*, CRC Press, London, 2001.
11. B. Besergil, A. Akin and S. Celik, *Industrial & Engineering Chemistry Research*, 2007, **46**, 1867-1873.
12. R. W. Glyde, *Chemistry in Britain*, 1997, **33**, 39-41.
13. J. Hongbing, M. A. Nicholls, P. R. Norton, M. Kasrai, W. T. Capehart, T. A. Perry and Y.-T. Cheng, *Wear*, 2005, **258**, 789-799.
14. M. Frey, S. G. Harris, J. M. Holmes, D. A. Nation, S. Parsons, P. A. Tasker and R. E. Winpenny, *Chemistry - A European Journal*, 2000, **6**, 1407-1415.
15. P. Mousavi, D. Wang, C. S. Grant, W. Oxenham and P. J. Hauser, *Industrial & Engineering Chemistry Research*, 2006, **45**, 15-22.
16. C. Bovington, S. Korcek and J. Sorab, *Tribology Series*, 1999, **36**, 205-214.
17. Y. Yamamoto and S. Gondo, *Tribology Transactions*, 1989, **32**, 251-257.
18. F. A. Davis and T. S. Eyre, *Tribology International*, 1990, **23**, 163-171.
19. J. Graham, H. Spikes and S. Korcek, *2001*, 2001, **44**, 626-647.
20. J. M. Martin, C. Donnet and T. Le Mogne, *Physics Reviews*, 1993, **B48**, 10583-10586.
21. M. Beltzer, *Journal of Tribology*, 1992, **114**, 675-682.
22. J. Galligan, A. A. Torrance and G. Liraut, *Wear*, 1999, **236**, 199-209.
23. Shriver and Atkins, *Inorganic Chemistry*, 3rd edn., Oxford University Press, 1999.
24. V. Ponec and G. C. Bond, *Catalysis by Metals and Alloys*, Elsevier Science, Amsterdam, 1995.

25. S. Lyon, *Materials World*, 2007, **15**, 19-21.
26. A. Dabrowski, *Adsorption and its Applications in Industry and Environmental Protection*, Elsevier Science, Amsterdam, 1998.
27. D. Briggs, *Surface Science*, 1987, **189-190**, 801-822.
28. J. J. Fripiat, *Ingenieursblad*, 1967, **36**, 110-113.
29. I. M. Río-Echevarría, *PhD Thesis*, University of Edinburgh, 2007.
30. S. G. Harris, *PhD Thesis*, University of Edinburgh, 1999.
31. R. P. Renz, *PhD Thesis*, University of Edinburgh, 2007.
32. M. Fuji, *Surfactant Science Series*, 2003, **112**, 749-787.
33. X.-L. Yin, L.-J. Wan, Z.-Y. Yang and J.-Y. Yu, *Applied Surface Science*, 2005, **240**, 13-18.
34. R. Zenobi and V. Deckert, *Angew. Chem. Int. Ed.*, 2000, **39**, 1747-1756.
35. K. Hoyberg, *Scanning*, 1997, **19**, 109-113.
36. A. Prescimone, C. J. Milios, S. A. Moggach, J. E. Warren, A. R. Lennie, J. Sanchez-Benitez, K. V. Kamenev, R. Bircher, M. Murrie, S. Parsons and E. K. Brechin, *Angew. Chem. Int. Ed.*, 2008, **47**, 2828-2831.
37. P. W. Atkins, *Physical Chemistry*, 6th edn., Oxford University Press, Oxford, 1998.
38. C. C. J. Roothaan, *Rev. Mod. Phys*, 1951, **23**, 69.
39. C. Møller and M. S. Plesset, *Physical Review*, 1934, **46**, 618.
40. P. Hohenberg and W. Kohn, *Physical Review*, 1964, **136**, B864.
41. W. Kohn and L. J. Sham, *Physical Review*, 1965, **140**, A1133.
42. J. S. Binkley, J. A. Pople and W. J. Hehre, *J. Am. Chem. Soc*, 1980, **102**, 939.
43. M. S. Gordon, J. S. Binkley, J. A. Pople, W. J. Pietro and W. J. Hehre, *J. Am. Chem. Soc.*, 1984, **104**, 2797.
44. W. J. Hehre, R. Ditchfield and J. A. Pople, *Journal of Chemical Physics*, 1972, 2257.
45. M. S. Gordon, *Chemical Physics Letters*, 1980, **76**, 163.
46. A. D. McLean and G. S. Chandler, *Journal of Chemical Physics*, 1980, **72**, 5639.
47. R. Krishnan, J. S. Binkley, R. Seeger and J. A. Pople, *Journal of Chemical Physics*, 1980, **72**, 650.
48. J.-R. Hill, C. M. Freeman and L. Subramanian, *Reviews in Computational Chemistry* 2000, **16**, 141-216.
49. M. Jalaie and K. B. Lipkowitz, *Reviews in Computational Chemistry*, 2000, **14**, 441-486.
50. A. K. Rappe, C. J. Casewit, K. S. Colwell, W. A. Goddard-III and W. M. Skiff, *J. Am. Chem. Soc*, 1992, **114**, 10024-10035.
51. S. L. Mayo, B. D. Olafson and W. A. Goddard-III, *Journal of Physical Chemistry*, 1990, **94**, 8897-8909.
52. A. K. Rappe and W. A. Goddard-III, *Journal of Physical Chemistry*, 1991, **95**, 3358-3363.
53. C. H. Giles, T. H. MacEwan, S. N. Nakhwa and D. Smith, *Journal of the Chemical Society*, 1960, 3973-3993.

54. I. T. S. W. 6, *Diesel fuel - Assessment of lubricity using the high-frequency reciprocating rig (HFRR) - Part 1: Test method*, American National Standards Institute, 2007.
55. J. E. Davidson, *PhD Thesis*, University of Edinburgh, 2005.

Chapter 2

Surface Binding of Carboxylates and Modelling the Uptake of Malonates on Iron Oxides

Contents

2 Introduction

2.1 Background

This chapter is concerned with the surface coordination chemistry of carboxylic acids and seeks to identify the possible modes of attachment of malonates to iron(III) oxides, following the discovery that 2-(4-chlorophenyl)malonic acid binds strongly to goethite.[1] Other carboxylic acid derivatives have previously been shown to have an affinity for iron oxide surfaces by determining isotherms for uptake from solution onto high surface area oxides and molecular modelling simulations have been used to propose modes of binding.[2]

The modification of base oil lubrication properties by adding small quantities of organic molecules to them was first reported in 1918 by Wells and Southcombe.[3] Most organic friction modifiers are molecules which have both a long alkyl chain and an "attachment group" which is a polar group such as a carboxylate group. An example is stearic acid, $CH_3(CH_2)_{16}COOH$.[4]

Carboxylic acids commonly form salts or complexes with metals as can be seen by survey of the Cambridge Structural Database (CSD)[5] where over 31,000 such structures can be found. The nature of the interactions between the anionic oxygen donors and the metal cations in such materials is likely to vary considerably with the nature of the metal cation, particularly its hardness or softness.[6]

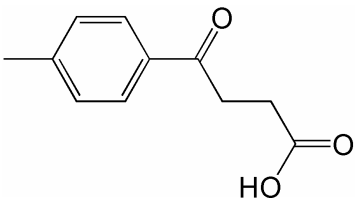

Figure 2-1: 3-(4-Methylbenzoyl)-propionic acid, Irgacor 419®

The possible modes of attachment of 3-(4-methylbenzoyl)-propionic acid, a commercial corrosion inhibitor for mild steel, Irgacor 419®, (Figure 2-1) to iron(III) oxides suggested by Frey *et al*,[2] incorporate the concept of 'multi-site attachment.' This proposes that surface stability is enhanced by increasing the number of ligand-surface interactions. In the specific case of 3-(4-methylbenzoyl)-propionic acid two coordinate bonds can be formed by the carboxylate along with a hydrogen bond by the carbonyl group, accounting for the enhancement in surface stability over other simpler carboxylic acid derivatives.

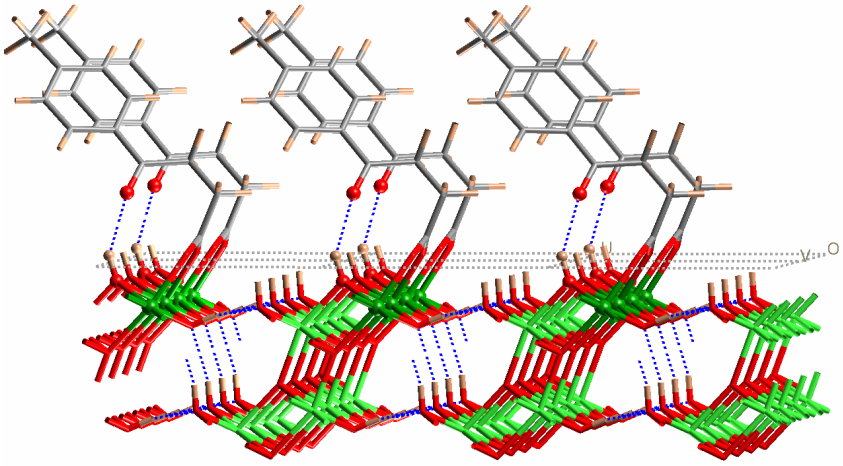

Figure 2-2: 3-(4-Methylbenzoyl)-propionic acid on the 0 2 $\bar{1}$ face of lepidocrocite showing the two bonds formed by the carboxylate to Fe(III) atoms and the hydrogen bond formed by the additional carbonyl group.

In order to design useful new friction modifiers the mode of attachment of carboxylates to metal oxide surfaces and the consequences this has on the orientation and packing of the pendant groups needs to be understood. Database mining of the Cambridge Structural Database was undertaken to define possible modes of attachment.

2.2 Analysis of structures in the Cambridge Structural Database (CSD)

The Cambridge Structural Database[5] was searched for crystal structures of compounds which contain carboxylates attached to one or more iron atoms in a manner which would be possible at an iron oxide surface. Work previously carried out by Steve Harris[7] has established a method for this and a basis for nomenclature and classification of results returned from such searches.

2.2.1 Classification of carboxylate structures and nomenclature

The 'Harris notation' is used to indicate the metal nuclearity of the entire fragment and, for each donor atom, the number of metal atoms bonded.[7] In the case of interaction of carboxylates and metals this is represented as N.AB in Figure 2-3 where N is the number of metal atoms bound to the entire fragment, A is the number bonded to oxygen A, O_A, and B is the number bonded to oxygen B, O_B. Extensions can be made easily to this system to cover different types of polynucleating (multiple attachment) motifs. It is necessary to provide a diagram to identify potential binding sites and their sequence in the Harris label.

Figure 2-3 : Harris notation[7] for formation of metal complexes with a deprotonated carboxylic acid; N.AB defines the total nuclearity (N) and the numbers of metal atoms bonded to O_A and O_B, thus the system shown on the right has a 2.21 structure

As part of the work for which this nomenclature was devised,[7] results were obtained for metal atoms of any type bound to carboxylate derivatives. This approach was used in this thesis to determine whether any significant changes in types had occurred in the intervening 8 years and also to extract those structures containing carboxylates bound to iron(III). There is potential for a large number of binding modes but only those which return hits are outlined in Figure 2-4 using the aforementioned Harris notation.

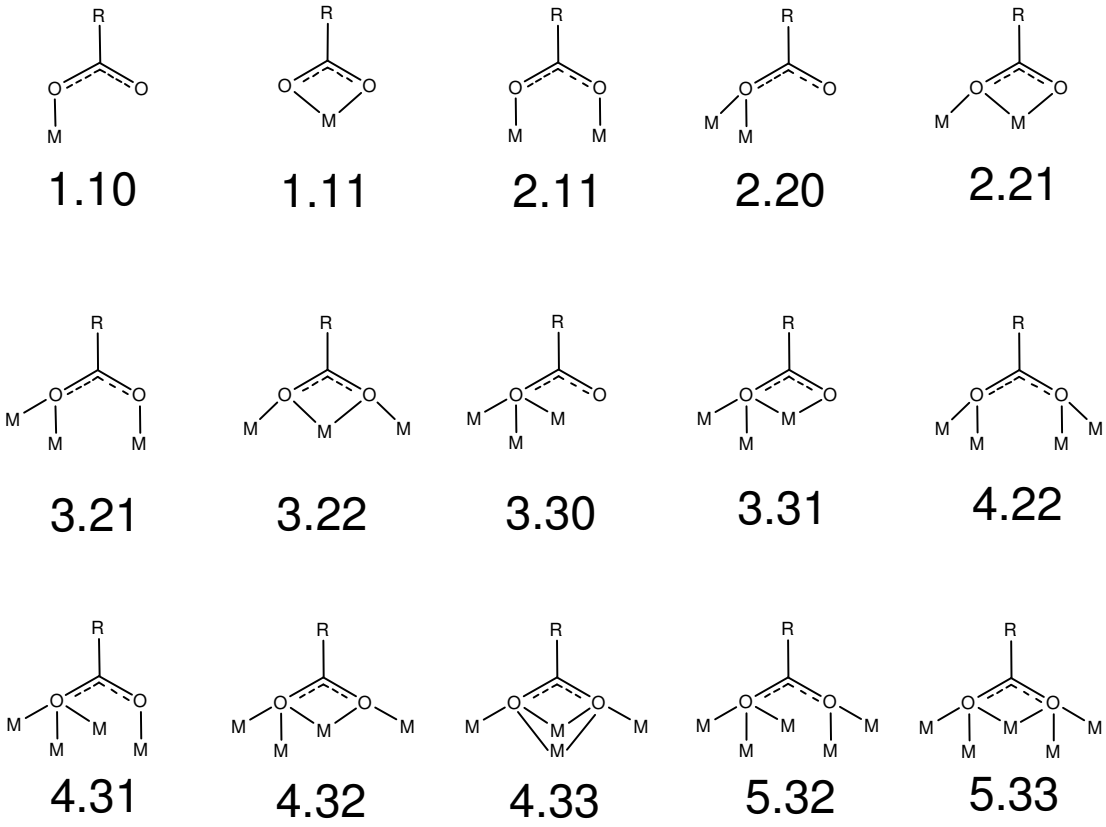

Figure 2-4: Possible modes of carboxylate-to-metal binding present in the CSD for any metal

2.2.2 Structural types recorded in the CSD

The data from database mining for carboxylate complexes of all metals in the CSD is shown in Figure 2-5. For each of the 15 modes listed, the frequency of occurrence is also presented. This gives some insight into which modes provide stable entities. During analysis one must not lose sight of the fact any observed trends are the product of both chemical stability AND how commonly studied the various types of metal elements and their complexes are.

The simple monodentate binding mode (1.10) is the most common mode over all metals with 14759 hits returned over all metals. The next most common is the dinucleating mode (2.11) which has 10289 hits. In distinguishing between the 1.10 and 1.11 modes and in many other cases a judgement often needs to be made as to whether the second oxygen atom is within bonding distance of the metal cation. This point has previously been addressed using structural information from the CSD and involves observing the similarity of C-O bond lengths in the carboxylate.[8] Put simply, the bond lengths will tend towards being equal if the oxygen atoms' bonding environments are the same and will be different if only one oxygen atom is bonded.

Binding Mode	Previous work[7] (all metals)	All Metals	Transition Metals	Iron	Group 2 Metals
1.10	4196	14759	12115	581	242
1.11	621	3402	2097	112	47
2.11	2904	10289	8317	874	99
2.20	134	756	472	13	16
2.21	231	1040	388	8	43
3.21	215	730	467	21	23
3.22	7	65	14	0	11
3.30	4	10	5	0	0
3.31	4	7	0	0	1
4.22	35	55	36	2	6
4.31	3	17	6	0	0
4.32	1	9	1	0	1
4.33	0	2	0	0	0
5.32	1	2	0	0	1
5.33	1	2	0	0	1

Figure 2-5: Occurrence in the CSD of carboxylate complexes with the binding modes shown in Figure 2-4

The Conquest software[9] employed in this thesis to search entries in the CSD uses a predetermined definition of bond existence and order. Upon submitting a structure to the CCDC, the user may provide a definition of bonds. If this information is provided it is checked by an editor before addition to the CSD. Should a structure be provided without a connectivity scheme, bond existence is determined by calculation using the formula show in Equation 2-1, where for two atoms A and B, the values R_A and R_B are radii determined through empirical observation of the database, T is a tolerance factor which is usually 0.4 Å and D_{AB} is the distance between atoms. The connectivity

generated by calculation is also checked by an editor. As bonding may be defined by human input in some cases, this is subject to human error or evolving opinion. Similarly bond order is always determined by inspection and is subjective. So too are the results obtained from a chemical drawing. In this thesis the CSD definition of metal-oxygen bond lengths have been used without corrections.

$$R_A + R_B - T \leq D_{AB} \leq R_A + R_B + T$$

Equation 2-1 used in the CSD to define whether a bond exists between atoms A and B.[10]

In contrast to most other metals, for iron the dinucleating (2.11) mode is favoured, having 874 hits, and is approximately 50% more common than the monodentate (1.10) mode which has 581 hits. Also it is worthy of note that the motifs involving higher nuclearities (decreasing with multiple metal atoms bound to each oxygen) have a low occurrence. Such low numbers are expected since the steric hindrance involved in crowding metal atoms around the oxygen atoms of the carboxylate will increase with each additional metal introduced.

2.2.3 Geometric analysis of the dinucleating 2.11 binding mode

Given that the 2.11 mode is the most commonly observed for iron, it can be inferred that it is stable and is thus a favourable potential model for the binding of carboxylate groups to iron oxide surfaces.

Further analysis of the iron 2.11 structure revealed that it can be subcategorised. The first of these subcategories contains species where the iron atoms have no additional single atom bridge between them (see Figure 2-6i). This includes structures where there is no bridge other than a carboxylate or, if there is a bridging ligand which is flexible

and does not place external strain on the carboxylate geometries and, as such, these are loosely referred to as "unbridged". The second subcategory contains structures in which the two iron atoms are bridged by a single atom. In the vast majority of these structures, 297 in total, the bridging atom is an oxygen atom (see Figure 2-6ii). However, phosphorus, sulfur, chloride, and the second most common with 11 structures, fluoride, are also possible. Of the subcategory ii in Figure 2-6, only hits with oxygen bridges have been used in further analysis because they relate more closely to oxide surface structures.

With 341 hits, the next most common structural subcategory involves a trinuclear Fe_3O core with neighbouring iron atoms bridged by carboxylate ligands (see Figure 2-6iii). Clusters such as these are quite commonly found either as linked units or as discrete units and have been studied for their magnetic properties and their potential use as single molecule magnets.[11-13] They are also used as catalyst precursors for single walled carbon nanotube growth[14] and are also commonly found for other metals such as chromium, manganese and ruthenium.[15-17]

The final subcategory (see Figure 2-6iv) of structure has 147 hits and contains two oxo bridges between the two iron atoms. This unit is also a common motif in iron(III) minerals and thus means that such structures are very relevant to attachment of carboxylates to surface oxides and the modelling approaches used later in this chapter.

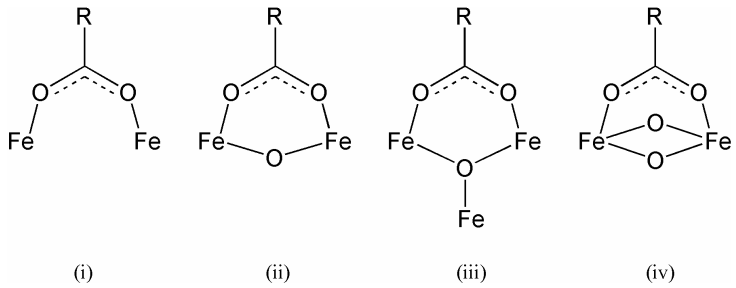

Figure 2-6: The (i) "Unbridged," (ii) singly bridged, (iii) iron trimer and (iv) doubly bridged species.

For the modelling of carboxylate surface complexes, an understanding of variations of bond angles and distances in 2.11 type fragments is essential (Figure 2-7). Of immediate interest is a comparison of the Fe…Fe and O…O contact distances denoted a, and b respectively, in Figure 2-7.

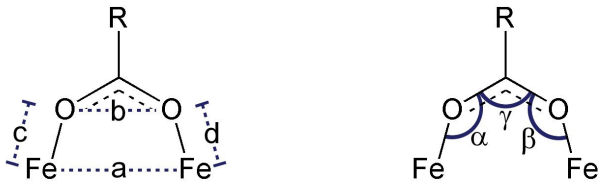

Figure 2-7: Distances and angles in the 2.11 Fe(III) carboxylate

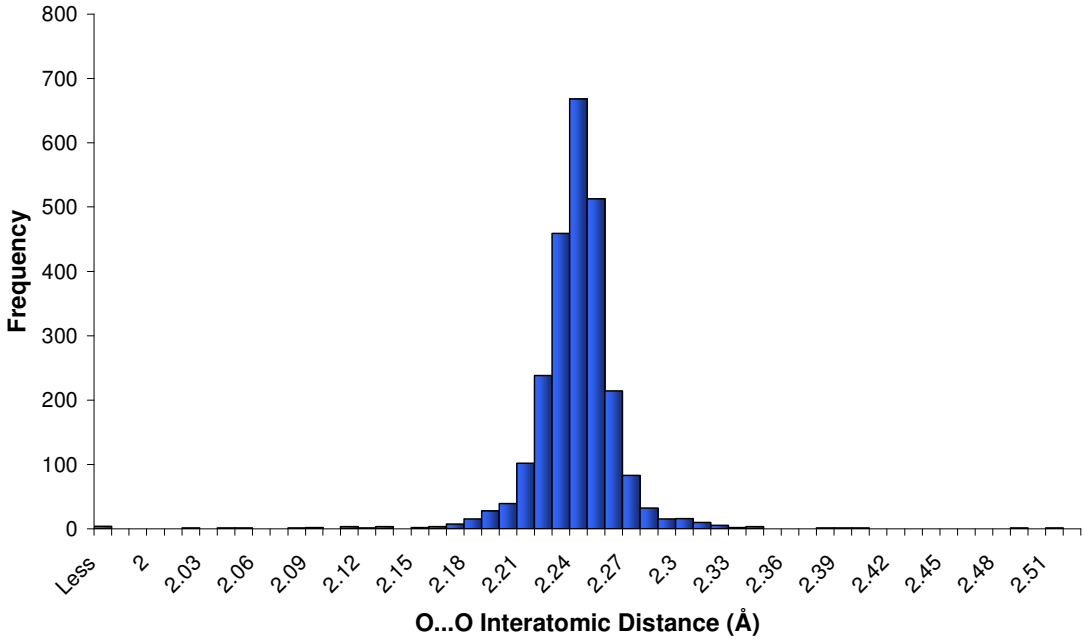

Figure 2-8: The statistical distribution of carboxylate interatomic oxygen - oxygen distances found in 2.11 systems extracted from the CSD. Distances < ~2.15 Å and > 2.35 Å in compounds with CSD codes HEQSUR, JUJMEG, QEQQAE, REZXIE, REZXIE01, REZXOK, WAGRUS, YAPRUD, YAPSAK, YESTIZ, ZOTTEH are erroneously reported in the database (see text).

The interatomic distance between the two oxygen atoms on the carboxylate ligand shown as distance b in Figure 2-7 has been represented in Figure 2-8 as a histogram. As would be expected for such a rigid ligand, the distribution is tightly clustered and varies by only about ±0.15 Å from a mean value of 2.24 Å with only a very small number outwith this range. Some hits exist below 2.15 Å and above 2.35 Å; these are unexpected values for this distance and closer inspection of the structures in which they were reported reveals the claimed distances to be erroneous, occurring in either structures with large R-factors or with other anomalous characteristics, such as distorted benzene rings, non planar carboxylate entities or disorder. Such errors can and do occur within the CSD and are unavoidable but fortunately are quite rare.[18]

If we consider the interatomic separation of the two iron atoms being addressed by the ligand (distance a in Figure 2-7), a large range of values is observed. One main peak can be seen in the histogram, at 3.30 – 3.40 Å and there are shoulders at shorter and longer distances. There are also some structures at much higher and much lower separation than the others; these do not represent erroneous structures but have not been included for reasons given later. The rigidity of the carboxylate O...O distance and the wide range of Fe…Fe distances, implies that the Fe-O-C angles (labelled α & β in Figure 2-7) may vary considerably allowing the carboxylate unit to accommodate significant variation in surface geometry. This is examined in more detail below in Figures 2-14 and 2-15.

The iron…iron distances shown in Figure 2-9 can be ascribed to the subcategories proposed earlier (shown in Figure 2-6). The data are presented in Figure 2-10.

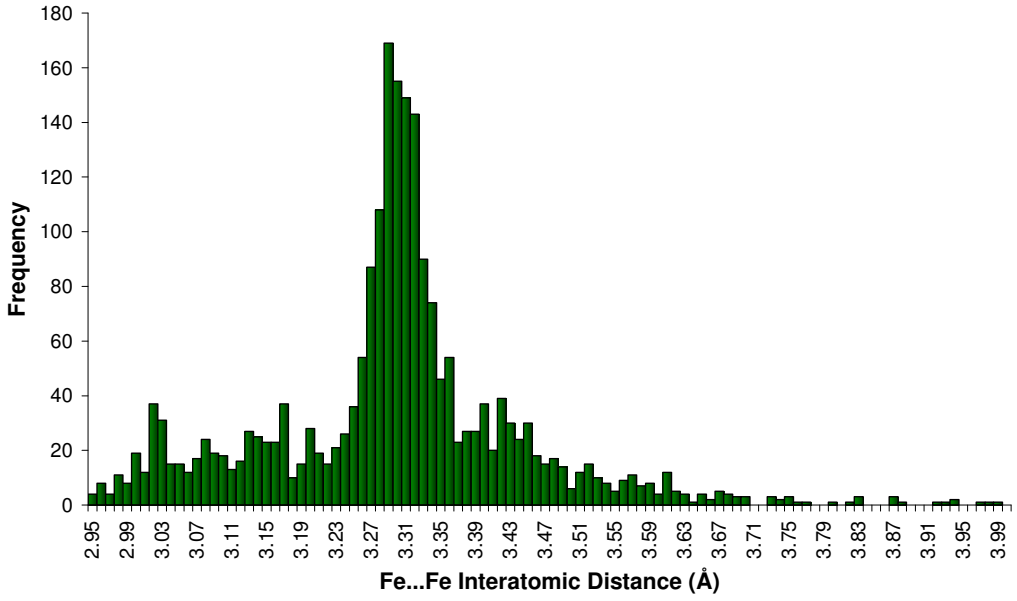

Figure 2-9: The statistical distribution of the interatomic iron…iron separation found in 2.11 type structures extracted from the CSD. The histogram has been truncated below 2.95 Å and above 4.00 Å. The reason for this is given below.

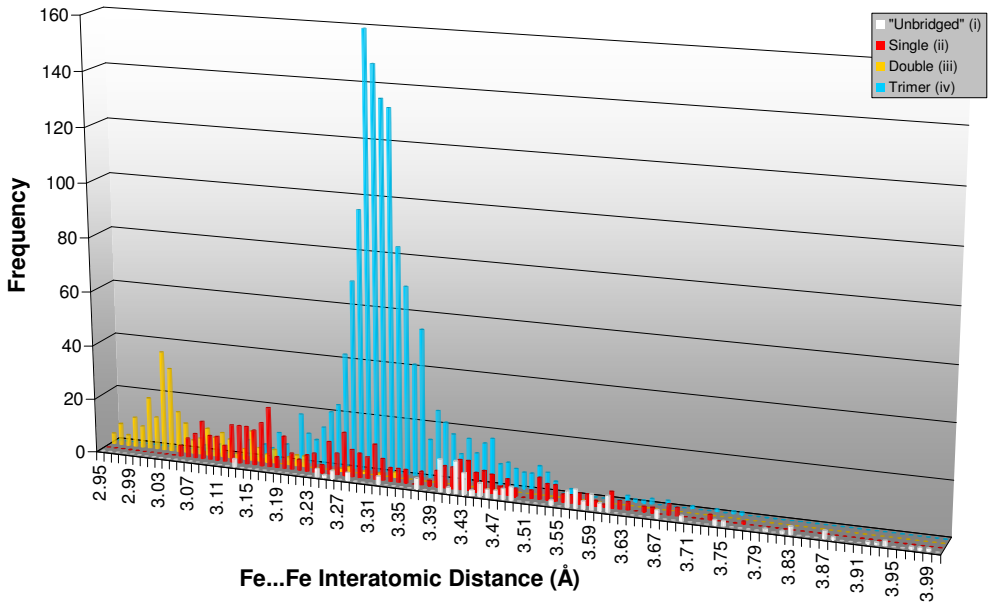

Figure 2-10: Iron-iron distances separated according to the subcategories presented in Figure 2-6, truncated below 2.95 Å and above 4.00 Å as in Figure 2-9

"Unbridged" structural types (see Figure 2-6(i)) were included to examine trends in relatively unstrained systems and are shown in white in Figure 2-10. Little information can be gained from this however, as the relatively low number of hits produce broad low 'peaks' which correspond to wide ranges within the three conformations shown if Figure 2-11 typically at around 2.5 to 3.5 Å, 4.5 to 5.5 Å and 5.5 to 6.0 Å. The histogram has been truncated below 2.95 Å and above 4.00 Å and focuses on the more interesting differences in Fe...Fe distances observed between bridged species.

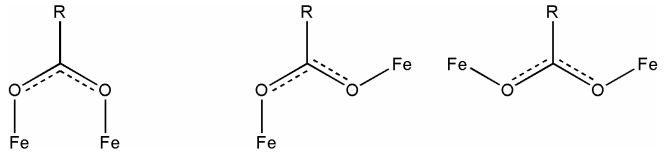

Figure 2-11: Conformations possible in the unconstrained forms of the 2.11 binding mode which is shown in Figure 2-6(i).

The single bridged species (defined as ii in Figure 2-6) has Fe…Fe distances shown in red in Figure 2-10 which exhibit no significant statistical trends with iron…iron separations evenly distributed over the range 2.6 – 3.7 Å. The bridge in these structures merely serves to impose limits on the range possible but beyond this has little apparent effect.

The majority of hits are observed for Fe_3O species (structure iii in Figure 2-6) and are associated with the peak shown in blue clustered at 3.30 – 3.40 Å. In these compounds iron atoms show deviations from octahedral geometry with angles formed between two metals at the μ_3-oxygen atom being close to 120° and iron to μ_3-oxygen distances in the range 1.85-2.0 Å. The iron-iron distance as a result is in the range 3.30 – 3.40 Å.

The doubly oxo bridged species (structure iv in Figure 2-6) accounts for the clustering of iron-iron distances shown in yellow in Figure 2-10 around 3.05 – 3.10 Å . For these structures the iron-iron separation is smaller than for the other bridged species, because the two oxo bridges between the iron atoms constrain the atoms to be closer together. Figure 2-10 clearly shows the differences between this and the other species presented in Figure 2-6. This substructure is closely related to a model used in previous work[7] for the surface complexation of 3-(4-methylbenzoyl)-propionic acid and other 4-ketoacids with the (0 2 -1) face of lepidocrocite shown previously in Figure 2-2.

In terms of potential usefulness in modelling surface-binding, the Fe_3O carboxylate system (Figure 2-6(iii)) is unlikely to have much relevance since its structure is 3 dimensional and unique to hexacarboxylate systems and the Fe_3O motif was not found in any relevant mineral structures. The singly bridged species (Figure 2-6(ii)) is theoretically possible for surface attachment but is not very realistic as it is expected that stable surfaces will have more than one oxo or hydroxy bridge between iron atoms. Also it is not very practical for modelling because it does not define a preferred iron-iron distance. The doubly bridged species (Figure 2-6(iv)) as has been stated, is closely related to the binding mode used previously[7] for the modelling work carried out for 4-ketoacids. Consequently it is analysed in more detail in this thesis.

Only small variations of the O…O separation in a carboxylate group are expected because the unit has a rigidity resulting from its delocalised electronic structure which in turn places severe restrictions on the positions of atoms to ensure effective overlap of π-type orbitals. Some evidence for this has already been seen in the narrow distribution in Figure 2-8. From the standpoint of modelling the surface-binding of carboxylate derivatives (section 2.3.4), it is important to define how much strain energy is required to generate the complexed form from the non-complexed carboxylate anion or the conjugate acid.

The O-C-O angles in non-complexed carboxylate anions are compared with values in complexed carboxylates in Figure 2-12. The non-complexed anion was defined as a deprotonated carboxylate in CSD searches. C-O bonds were defined as resonant bonds with nothing else bonded to the oxygen atoms. This was done as they are expected to be more similar to each other and more representative of complexed forms than carboxylic acids or esters. This is a consequence of delocalisation providing two 1.5 order C-O bonds in the anion as opposed to one single and one double bond in the acids and esters.

The two histograms were normalised to the same maximum to make comparison easier. Both are distributed about 126°. They are very similar, but the complexed carboxylates have a slightly sharper distribution and a more positive skew. This is expected since binding of the carboxylate will introduce geometrical constraints on the carboxylate unit. However, the similarities suggest that deviations from the ideal angle will be associated with high energy in 2.11 binding assemblies.

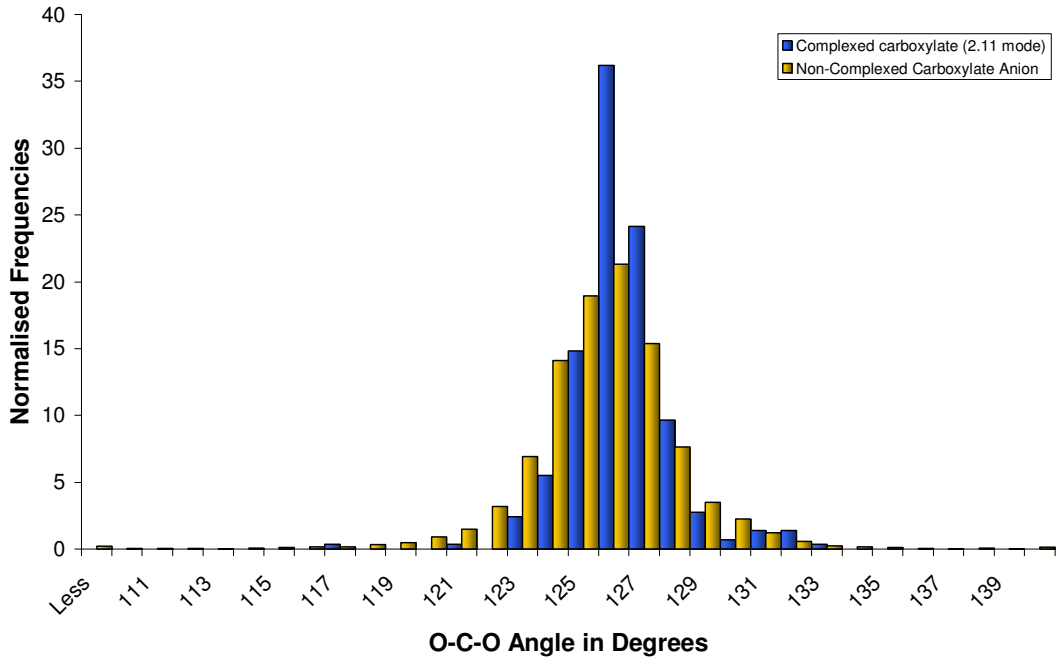

Figure 2-12: A comparison of the O-C-O angles /° (shown as γ in Figure 2-7) found in carboxylates complexed with iron in the 2.11 arrangement and non-complexed carboxylate anions.

The symmetry of the 2.11 binding mode was considered. Preferences for symmetrical binding may place constraints on favourable sites or tail group configurations relative to a surface. It is important that the Fe-O distances, c and d in Figure 2-7, are modelled correctly (section 2.3.4), and so these were extracted from the CSD data and filtered according to which was shorter and which longer. The data are presented in a histogram, Figure 2-13, and show a fairly narrow spread. The shorter bond length is clustered at 2.03 Å and the longer at 2.08 Å. As a percentage of the bond length, this difference is within a value of 2.5%. Both have a smaller secondary peak about 0.07 Å higher than their main peak. In general these hits represent structures with bulky R groups which appear to become asymmetric in order to relieve steric clashes.

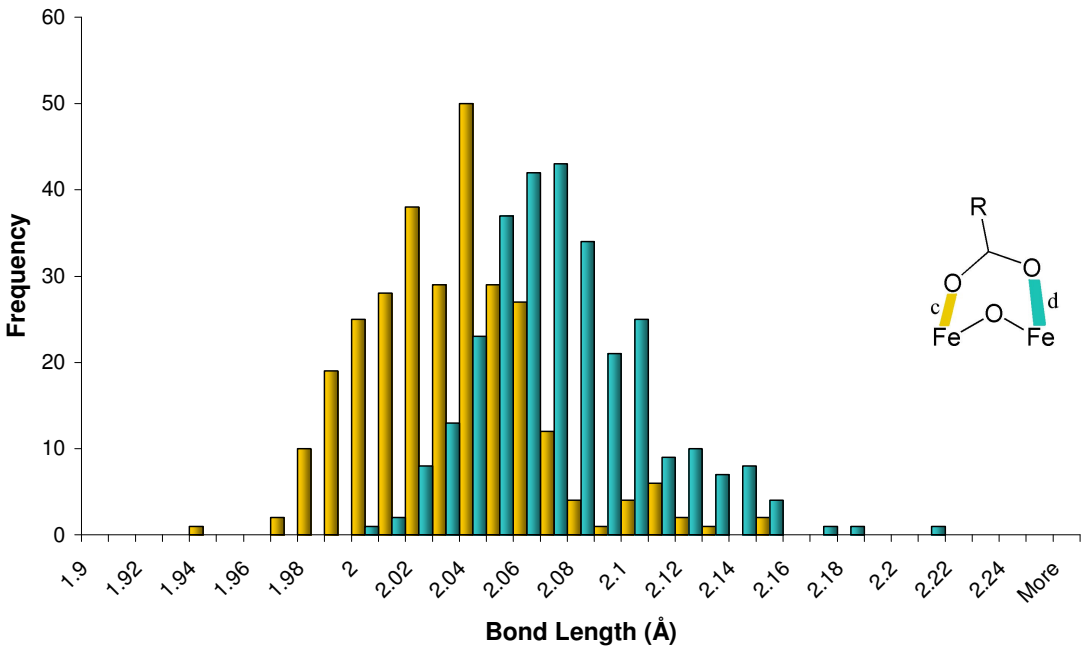

Figure 2-13: Symmetry in the 2.11 binding mode and distribution of iron-oxygen bond lengths /Å (c and d in Figure 2-7, also shown inset).

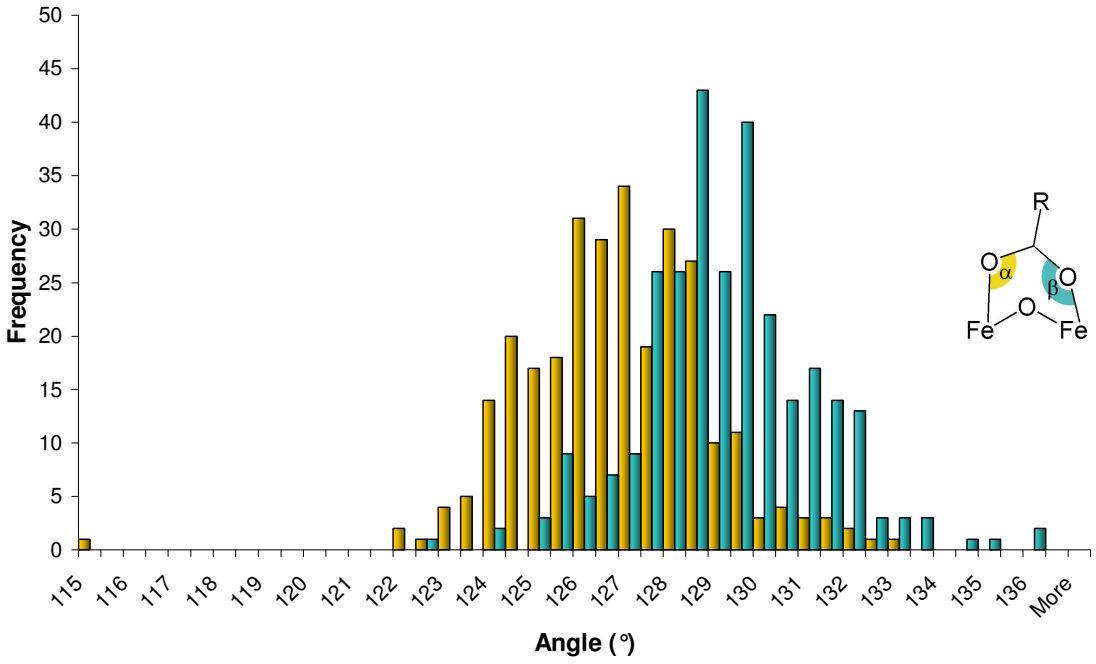

Figure 2-14: Distribution of Fe-O-C angles /° in the 2.11 binding mode (α and β in Figure 2-7, also shown inset).

A similar method was applied to the angles α and β defined in Figure 2-7. These were also extracted from the CSD and filtered according to their size. The larger and smaller angles are presented in Figure 2-14. The mean value for the smaller angle was 126.5° and for the larger, 128.9°. The ocurrences of differences between the two angles, in increments of 0.25°, are plotted in Figure 2-15. The mean difference between the two angles, 2.35°, is relatively small. This indicates a preference for symmetrical binding with 99% having a difference less than 10° and 86% with a difference less than 5°. The maximum value recorded for the difference was 15.5°.

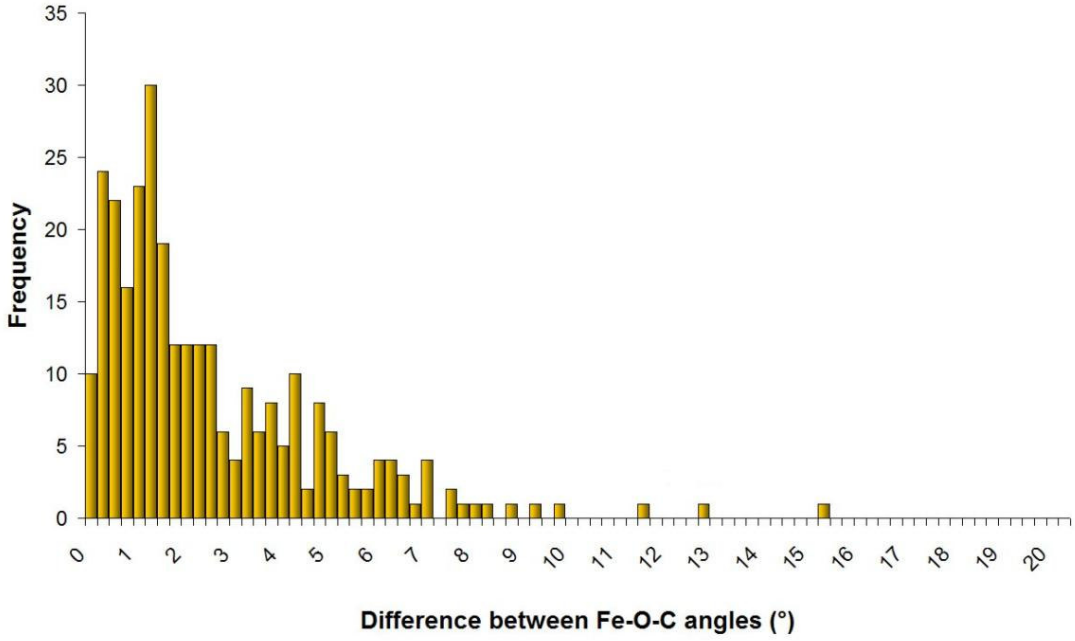

Figure 2-15: Statistical distribution of the difference between Fe-O-C angles (α and β in Figure 2-7) in increments of 0.25°.

Finally, for the doubly oxygen-bridged motif (structure iv in Figure 2-6) the angle made between the carboxylate plane and the Fe_2O_2 plane was plotted as a histogram (Figure 2-16). This information is relevant to the modelling of surface-binding see for example Figure 2-2 as it defines the orientation of the ligand relative to the surface plane. The data displayed in Figure 2-16 indicate that the carboxylate prefers to be perpendicular to a surface, but there are a number of structures with considerable deviations from this geometry and inclinations of up to 30° from the normal can be accommodated.

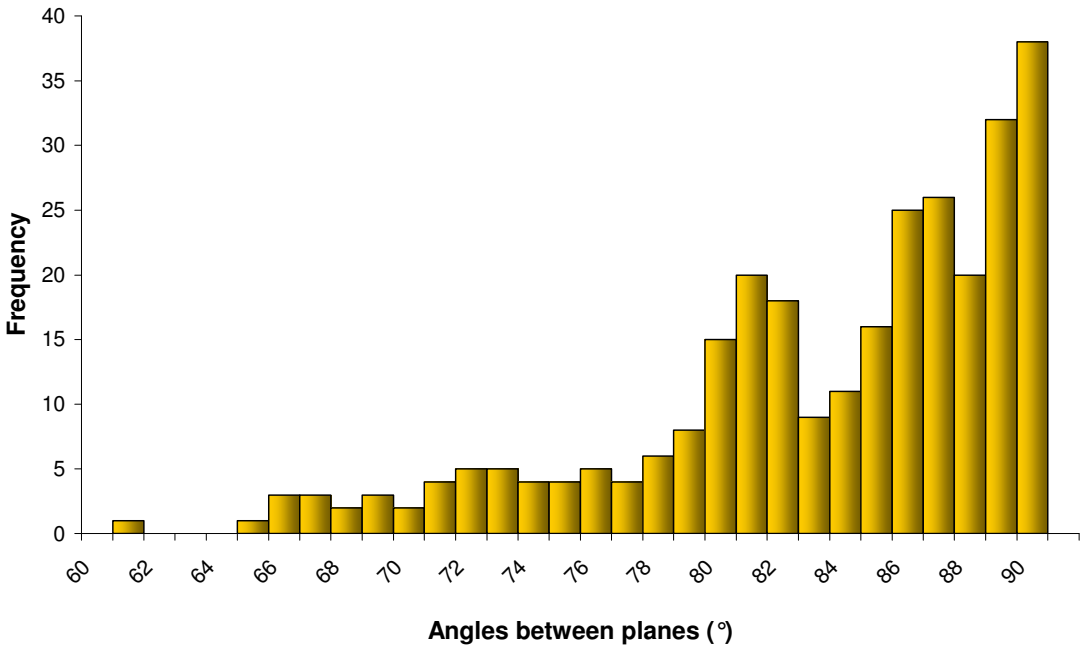

Figure 2-16: Distribution of the angle between the carboxylate plane and the Fe-O_2-Fe plane in structures containing the 2.11 binding mode, shown as iv in Figure 2-6.

2.2.4 Outcomes of carboxylate database mining

The frequent observation of the 2.11 binding mode of carboxylates implies that this generates stable Fe(III) complexes and provides a good basis for a model for surface binding. The carboxylate appears to prefer to bind symmetrically with respect to the bond lengths and angles formed but, despite the carboxylate unit itself being quite rigid, distortions associated with flexibility of the Fe-O-C angles can be readily accomodated. On the basis of the database mining it should be possible for a carboxylate unit to address a surface with iron atoms separated by 2.8 to 3.3 Å using the 2.11 binding mode. This is helpful in the context of using carboxylates for surface engineering because iron oxide minerals found in the ICSD generally have iron-iron atom separations of about 3 Å.

2.3 Malonic Acid

It has been shown that an additional keto group in a carboxylic acid can improve the strength of binding to a metal oxide surface.[7] More recent studies at the University of Edinburgh[1] carried out in parallel with the work in this thesis have involved the synthesis of derivatised carboxylic acids of various types and have confirmed that the presence of additional keto functionalities is useful for improving surface activity. A range of ligands with functional groups such as amides (Figure 2-17c) which could facilitate the formation of ligand:ligand and ligand:surface hydrogen bonds in surface layers were also considered in earlier work[7] at Edinburgh. Malonic acids, succinic acids and glutaric acids, (shown in Figure 2-17b, where n = 1, 2 and 3 respectively) all show stronger binding to goethite than unfunctionalised alkyl and aryl monocarboxylic acids.[1] An additional acid keto function is potentially useful for secondary interactions with both the surface and with other ligands. This stronger binding supports the potential importance of multi-site attachment and inter-ligand interactions in the design of new actives and therefore it is important to consider how such concepts manifest themselves in surface binding models. In the case of the dicarboxylic acids decreasing the length of the linking chain between the acid groups (see Figure 2-17b) improved binding characteristics[1] and using modelling to define the origins of this observation was deemed important to the design of new surface active materials.

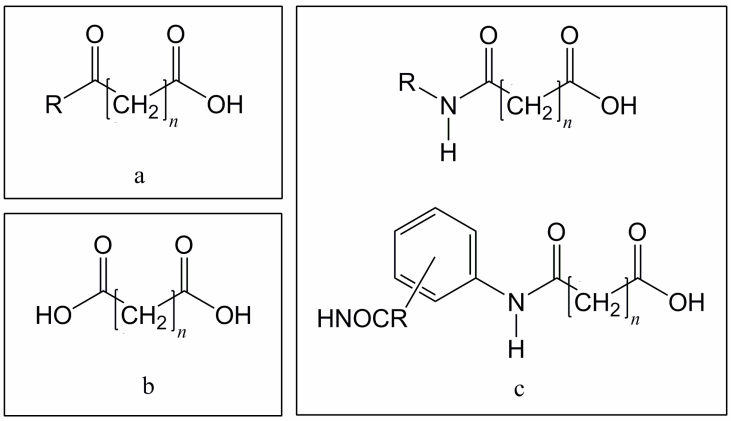

Figure 2-17: Scheme showing a) keto acids, b) dicarboxylic acids and c) amido carboxylic acids.

In the particular case of malonic acid derivatives, 2-(4-chlorophenyl)malonic acid, shown in Figure 2-18, was used in binding studies because the aryl chromophore facilitated analysis of residual ligand in solution in isotherm determinations. It was shown in studies undertaken by Robert Renz in his PhD programme,[1] Figure 2-19, that this malonic acid derivative bound slightly more strongly to goethite, and with a higher surface coverage than the commercial anticorrosive 3-(4-methylbenzoyl)propionic acid (Figure 2-1) whose adsorption isotherm was used as a positive control in Renz's studies[1] in screening for new anticorrosives for iron.

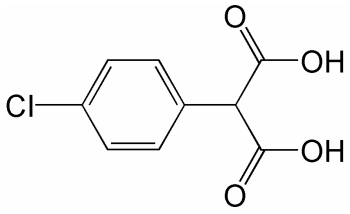

Figure 2-18: 2-(4-chlorophenyl)-malonic acid

The isotherm for 2-(4-chlorophenyl)malonic was obtained by measuring the uptake onto high surface area (22.5 m^2g^{-1}) goethite from 95% MeOH/H_2O solutions with initial concentrations of the malonic acid in the range 0 to 4 x 10^{-3} mol dm^{-3}. Curve fitting procedures were used[1] to generate the isotherm data shown in Table 2-1.

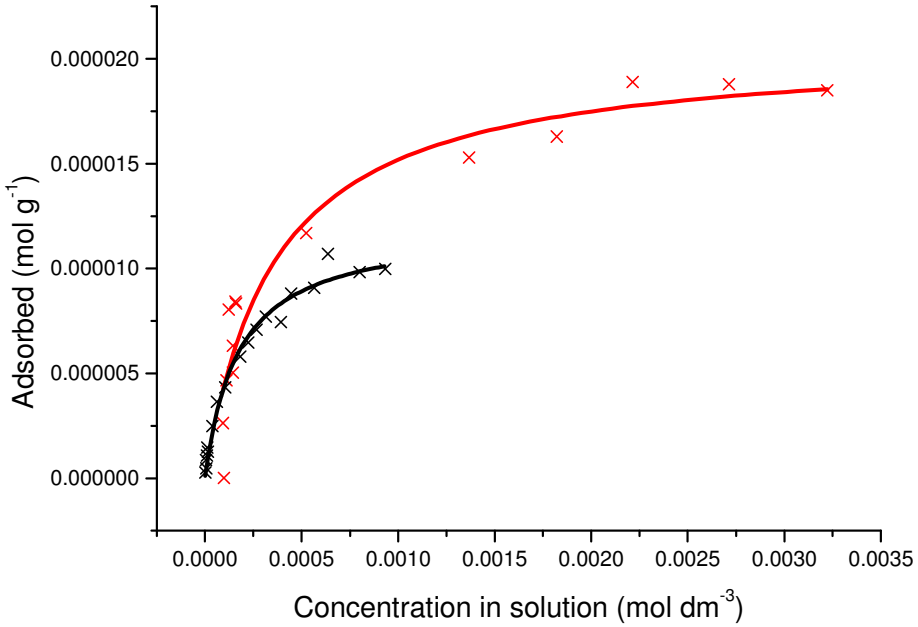

Figure 2-19: Adsorption isotherms for the uptake of 2-(4-chlorophenyl)malonic acid (red) and 3-(4-methylbenzoyl)propionic acid (black) onto high surface area goethite from 95% MeOH/H_2O.

	3-(4-methylbenzoyl)propionic acid	2-(4-chlorophenyl)malonic acid
Equilibrium binding constant (10^{-3}) / K	1.5(2)	2.8(6)
Surface coverage /10^5 mol g^{-1}	1.6(1)	2.1(1)
Required surface area per molecule /Å^2	238(15)	185(9)

Table 2-1: Adsorption isotherm data for the uptake of 3-(4-methylbenzoyl)propionic acid and 2-(4-chlorophenyl)malonic acid onto high surface area goethite from 95% MeOH/H_2O[1]

2.3.1 Modelling of malonic acid on an iron(III) oxide surface.

The Cerius2 software package[19] was used for modelling the binding of malonic acid to a surface generated from the lepidocrocite crystal structure[20] which is an orthorhombic

structure in the space group $Cmc2_1$ with a = 3.0600(6), b = 12.5100(25), and c = 3.8700(8) Å.

$$\begin{pmatrix} 4 & 0 & 0 \\ 0 & 1 & 2 \\ 0 & -1 & 4 \end{pmatrix}$$

Figure 2-20: Matrix used to convert the lepidocrocite $Cmc2_1$ cell into the cell used for docking models.

This cell was transformed using the matrix shown in Figure 2-20 to give more convenient axes. The surface for modelling the binding of malonic acids was then generated by removing atoms above a plane which is represented by the (0 2 $\bar{1}$) plane in the $Cmc2_1$ structure, now the (1 1 0) plane. This procedure produced atoms with unconventional coordination numbers and generated a charged surface which was made neutral by adding hydroxyl ions or protons. The result was a layer of iron oxide approximately 10 Å thick in a cell with axes a = 12.2400, b = 14.7023, and c = 19.8967 Å, α = 97.1549, β = 90, and γ = 90° with $P1$ symmetry. An image of this surface is shown in Figure 2-21. This surface provides for carboxylate binding by displacement of the three different types of hydroxyl groups, mono-, di-, and tri-nucleating, shown in Figure 2-21.

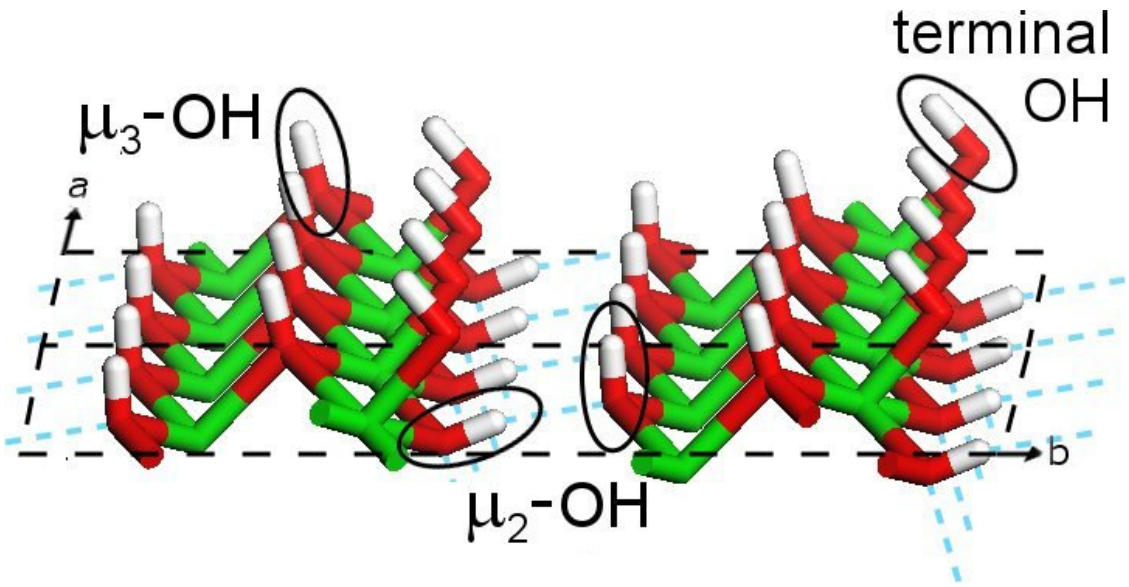

Figure 2-21: The surface, related to the of the (0 2 $\bar{1}$) plane of the *Cmc*2_1 lepidocrocite structure,[20] showing the uppermost atoms on the surface and the three types of hydroxyl group which could be replaced by a docking ligand.

Whilst the software package[19] provides two-dimensional periodicity to facilitate surface modelling, unfortunately using this prevents the application of charge equilibration[21] to derive partial atomic charges. This has implications regarding appropriate choice of force field. The inability to use partial atomic charges means that the force field must provide additional information to model some non-bonded interactions. Many force fields are aimed at specific types of molecular geometry which allows them to generate more accurate structures since the parameters needed cover a smaller subset of the periodic table. This generally means that the force fields will be optimised for a specific application, one example being CFF93 for modelling polycarbonates.[22] The studies in this section of the thesis require modelling of iron geometry as well as organic ligand structures and the interaction between the two. Consequently a general purpose force field which can cater for both should be used. The universal force field developed by Rappe and Casewit[23] contains parameters which cover the all atoms in the periodic table. The field does not explicitly provide atom types for modelling of all non-bonded interactions, having terms only for van der Waals interactions. In order to account for

other types of non-bonded interactions, an electrostatic interaction term is also included. However, this requires the assignment of partial atomic charges to atoms. Due to limitations in the charge equilibration method provided in the Cerius2 software package,[19] assignment of partial atomic charges is not possible for 2D periodic surface models and so the models used in this chapter, by necessity, have three-dimensional periodicity. Due to the nature of the potentials used, see chapter 1, interactions between atoms are usually truncated at a particular distance. In the case of the UFF the default value is 11 Å. Whilst interactions between periodic images in the two dimensions of the surface are legitimate interactions, those above and below the surface are not. This was addressed by placing a 40 Å layer of vacuum above the surface by increasing the length of the *c* axis placing periodic images beyond the default 11 Å cut-off specified for non-bonded interactions within the force field.

2.3.2 Structures of malonates complexes in the CSD

As malonates offer additional possibilities for addressing a surface to those for simple monocarboxylic acids, there is a need to define a nomenclature system to identify the different binding modes unambiguously. The Harris notation[7] used previously was extended to define the ways in which the four oxygen atoms, A-D in Figure 2-22, can interact with one or more metal cations.

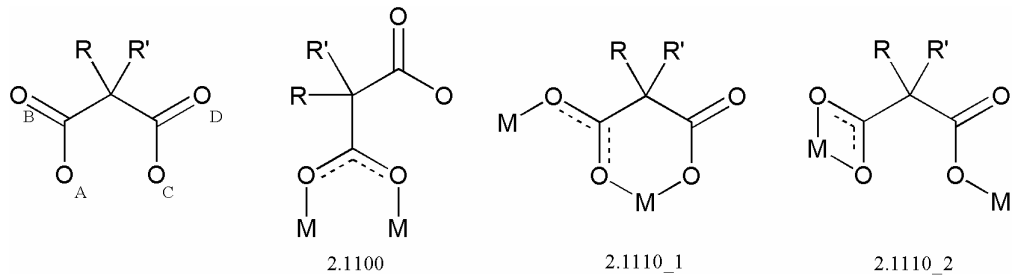

Figure 2-22: Harris notation for binding of malonates to one or more metal cations. The examples show a motif (2.1100) analogous to the most common for monocarboxylates (2.11 in Figure 2-4) and a case (2.1110) where there is an ambiguity in the structure (see text)

As before with carboxylates (shown in Figures 2-3 and 2-4), each potential donor atom is assigned a number which represents the number of metal atoms to which it is bonded. When one of the carboxylate groups is not bonded to metal atoms e.g. 2.1100 in Figure 2-22 the motifs are analogous to those shown by monocarboxylates. Situations arise where the Harris notation fails to distinguish between two different motifs when the first and second carboxylic acid become non-equivalent upon binding, which effectively imposes chirality on the ligand if R and R' are different. There may also be two binding modes which are named identically but have slightly different connectivity, e.g. 2.1110_1 and 2.1110_2 shown in Figure 2-22. In these cases an arbitrary number has been assigned to distinguish between these 'sub'-modes and is suffixed to the Harris label following an underscore.

The additional functionality and the possibilities it allows make it neccessary to consider any structures in the CSD which may contain additional modes beyond those observed for monocarboxylates (Figure 2-4). These additional modes are discussed below.

2.3.3 Malonate binding motifs

Working under the same assumption that chemisorption is involved, as in the previous study,[7] a large number of new binding modes are possible. In order to ensure that all modes present in the CSD were identified, an initial search was conducted for a fragment containing a malonate bound to at least one metal. This produced 575 hits. Binding motifs which were expected to exist were then searched for and recorded. This accounted for 525 hits. The remaining structures were then manually classified. A total of 40 different binding motifs were identified. These are shown in Figure 2-23 and the number of structures returned for each is given in Table 2-2.

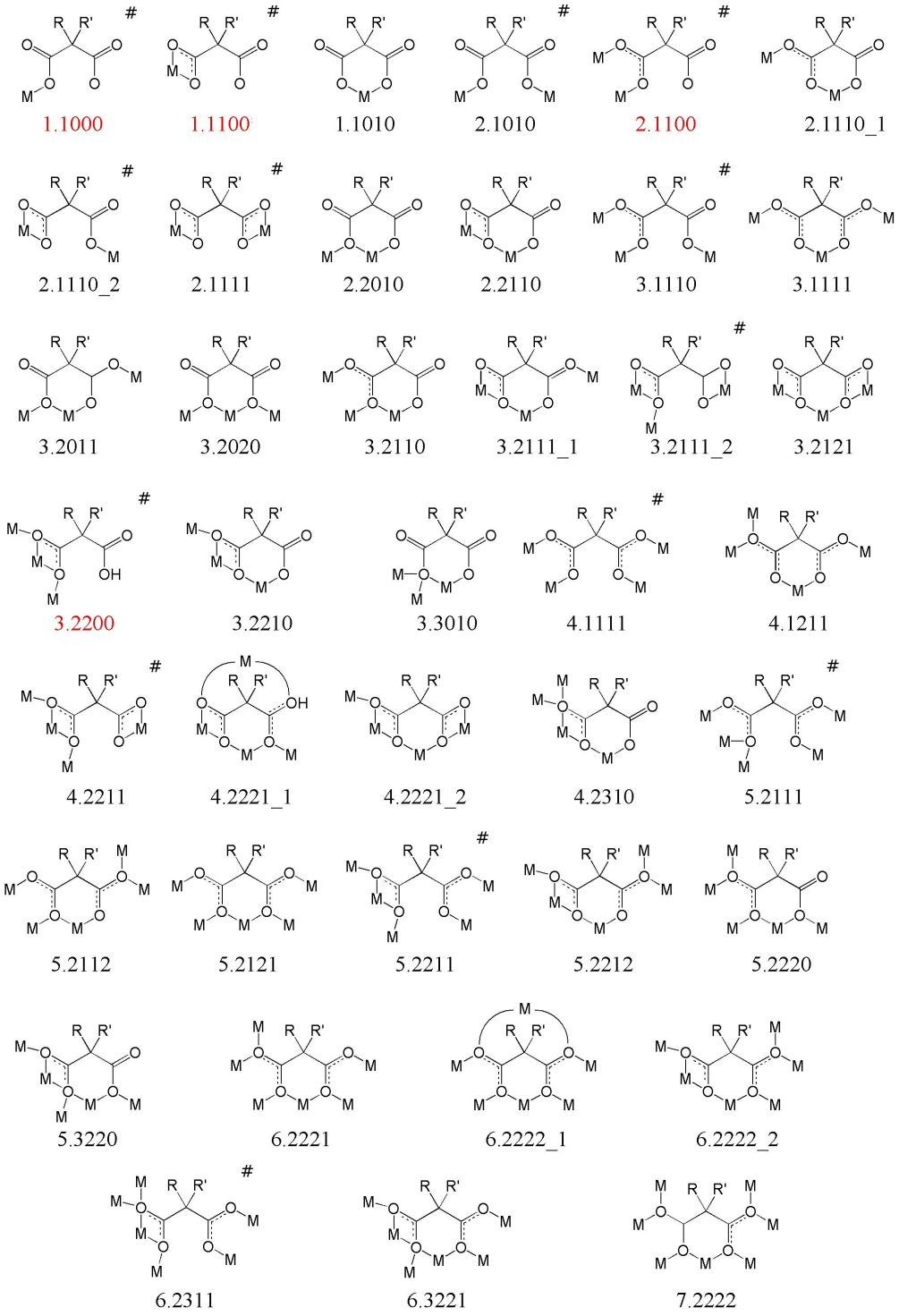

Figure 2-23: Modes of binding for malonates to all types of metals found in the CSD. Modes marked in red are analogous to those shown by monocarboxylate ligands (see Figure 2-4).

Binding Mode	Number of Hits (M = any metal)	Binding Mode	Number of Hits (M = any metal)
1.1000	31	3.3010	1
1.1010	289	4.1111	12
1.1100	3	4.1211	3
2.1010	20	4.2211	2
2.1100	10	4.2221_1	1
2.1110_1	75	4.2221_2	1
2.1110_2	4	4.2310	1
2.1111	9	5.2111	2
2.2010	7	5.2112	1
2.2110	5	5.2121	2
3.1110	1	5.2211	1
3.1111	75	5.2212	1
3.2011	1	5.2220	1
3.2020	1	5.3220	1
3.2110	7	6.2221	7
3.2111_1	8	6.2222_1	1
3.2111_2	1	6.2222_2	1
3.2121	14	6.2311	1
3.2200	4	6.3221	1
3.2210	1	7.2222	2

Table 2-2: Occurrences of the malonate binding modes described in Figure 2-23 in the CSD for all metals

The majority of hits are for structures containing the 1.1010 binding mode. These are prevalent because the malonate ligand can easily form 6 membered chelate ring structures with metals cations. Amongst these structures, four are iron(III) tris-malonate chelates, [Fe(mal_3)]. Only two other structures exist in the CSD where iron(III) is coordinated to the malonate. Both involve the simplest monodentate 1.1000 arrangement.

For all types of metals the 2.1110_1 and 3.1111 binding modes are the next most common. These are extended forms of the 1.1010 mode differing only by the addition

of one or two metals to oxygen atoms not involved in the chelate. This suggests that the chelate ring formed in the 1.1010 mode is a particularly stable entity. In fact of the 40 modes shown in Figure 2-23, only 14, marked with a # in Figure 2-23 and representing 101 structures, do not contain the chelate ring.

2.3.4 Relevance of binding motifs in the CSD to surface attachment of malonates.

Due to the large number of binding modes observed in metal complexes and salts in the CSD (shown in Figure 2-23), it is necessary to reduce the number of motifs down from 40 to a more managable subset which includes only those which are relevant to the surface binding. The following sections endeavour to achieve this through use of chemical knowledge, surface geometry and, where necessary, some simple modelling.

2.3.4.1 The 1.1000, 1.1100 and derived binding modes

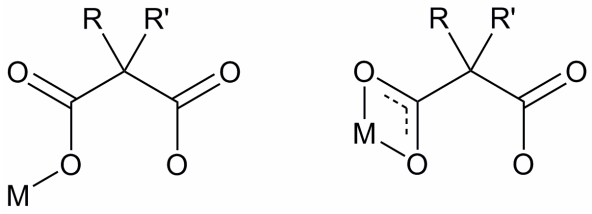

Figure 2-24: The 1.1000 and 1.1100 binding modes

The monodentate 1.1000 mode is the simplest binding mode possible for a malonate addressing a metal oxide surface. It is analogous to the 1.10 binding mode for monocarboxylate metal complex formation (Figure 2-4). On the basis of the study into monocarboxylates in previous sections, which favoured the 2.11 mode over the 1.10 mode, this mode is unlikely to explain any enhancement of binding strength exhibited by

malonates when compared to monocarboxylates, since the additional acid group is not involved in chemisorption.

On a similar basis the 1.1100 mode is also unlikely to lead to strong surface binding. Whilst the formation of this motif is clearly possible, as shown both here and as the 1.11 binding mode in the study of monocarboxylates, it is quite rare, probably due to the distorted Fe(III) coordination geometry required to give the O-Fe-O angle, which is considerably smaller than 90°. Structures in the CSD exhibiting this binding motif, typically have O-M-O angles of 55-65°.

Due to the short linking unit between the two acid groups in malonates, there is no configuration which will allow *both* groups to adopt 1.11-style surface binding since this directs one of the carboxylate groups away from the surface. The second acid group could only address the surface through one of its oxygen atoms if the first shows 1.11 attachment. Consequently, all binding modes where one acid displays 1.11 binding and the second acid interacts via both of its oxygen atoms e.g. the 2.1111 mode or the 5.2211 mode (shown in Figure 2-23), can be eliminated from further consideration on the grounds of not being relevant to surface binding.

In the context of the lepidocrocite surface used in this study, the only mode which is potentially reasonable and related to the 1.1100 mode is the 3.2200. This and the 4.3200 and 5.3300 modes (shown in Figure 2-25 but not observed in the CSD) are unreasonable structures for iron(III) complexes based the bond angles at the donor oxygen atoms and at the chelated iron(III) atom (see also above). These higher nuclearity motifs become less favourable, at least in part, as a consequence of the rigidity imposed by "multisite attachment" to several metal ions. As the latter are part of rigid three dimensional networks it is inevitable that the disposition of the ligand groups relative to other metal ions is severely restricted.

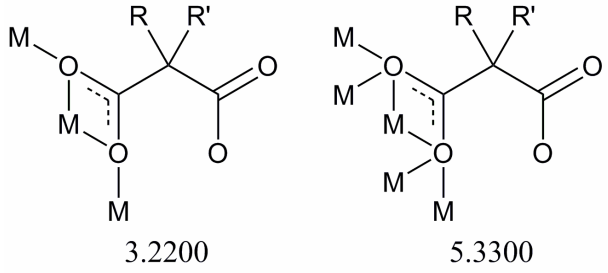

Figure 2-25: The 3.2200 and 5.3300 binding modes

They also fail to stand up to closer scrutiny as surface binding models since they require that the carboxylic acid must "embed" itself into the surface by displacing two of the μ_2 or μ_3 surface hydroxyl groups shown in Figure 2-21. In either case the distance between the two oxygen atoms on the surface is 3.060 Å and as has been shown in Figure 2-8, carboxylic acid O…O distances from the CSD have a maximum of ~2.35 Å. In order for the carboxylate to address the surface in either manner, the surface must undergo a major rearrangement.

2.3.4.2 The 1.1010 and derived modes with a six membered chelate ring

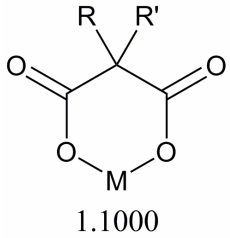

Figure 2-26: The 1.1010 binding mode

The 1.1010 mode (shown again in Figure 2-26) is the most prevalent for malonate complexes and is also found as a component of the other modes listed in Figure 2-23 with higher nuclearity, e.g. the 2.2010 and 3.2020 modes. As stated earlier, it involves the binding of one oxygen atom from each carboxylate to the same metal ion to form an approximately planar 6-membered chelate ring. Structures of metal-free malonic acid or

ester compounds in the CSD have a median of 2.81 Å between oxygen atoms in the carboxylate groups linked by the central carbon (distance a in Figure 2-27). The comparable O…O distances (b in Figure 2-27) in the four [Fe(III)(malonato)$_3$] structures in the CSD is similar, 2.74 ± 0.04 Å.

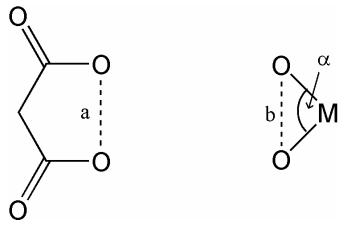

Figure 2-27: Comparison of malonate and metal oxide geometries.

The lone pairs on the oxygen atom are also directed towards the metal binding site due to their sp^2 hybridisation. This, combined with a small amount of flexibility in the O...O distance may explain why the 1.1010 motif and its derivatives are commonly observed structural motifs. Some tris-malonato complexes, [M(mal)$_3$], exist but are quite uncommon with only 8 of the 289 hits for 1.1010 structures being of this form.

In the context of the 2D surface being considered in these studies, formation of 1.1010 mode units is most unlikely. There would need to be discrete iron atoms lying above the plane of the surface with accessible *cis*-coordination sites, probably two hydroxyl groups. Attempts to place a malonate on the surface of the types used in modelling in this work (shown in Figure 2-21) in the *mono*nucleating 1.1010 mode will result in at least one of the oxygen atoms being within bonding distance of another iron atom. This in turn will lead to an increase in the nuclearity. Modes which include the 6-membered chelate ring where neither oxygen atom is bonded to other metal cations (e.g. 1.1010, 2.1110_1, 3.1111, 4.1211) can thus be eliminated from consideration in surface binding.

The nature of the chelate ring and the necessity for at least one of the oxygen atoms to be *poly*nucleating requires that one of these oxygen atoms displaces an oxygen atom

from the surface since there is no other way to ensure that two *cis*- sites on a particular iron atom are addressed in the surface being used (Figure 2-21) for modelling. With this information in mind, the possibilities which contain the 6-membered chelate ring are limited, and are shown in Figure 2-28, two of which, the 3.3020 and 4.3020 modes, were not detected in the CSD. These are discussed in more detail in section 2.3.4.5. For the reasons outlined above all other modes containing the chelate ring which are not shown in Figure 2-28 were eliminated from consideration as surface binding modes.

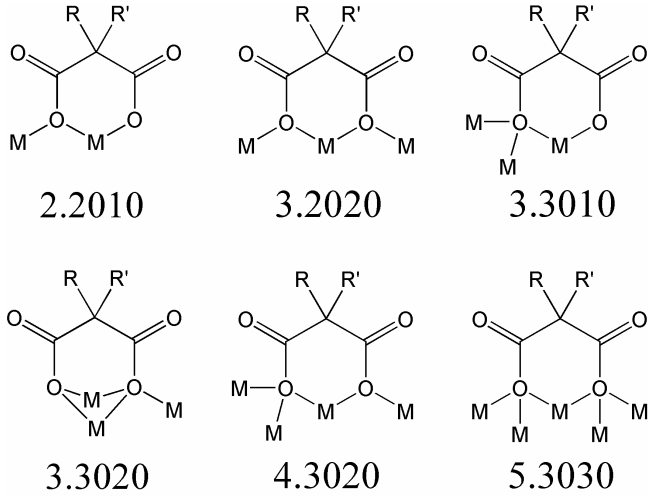

Figure 2-28: Binding modes containing chelate rings which are possible in complex formation with the surface shown in Figure 2-21

In the structures shown Figure 2-28 one or both of the oxygen atoms are embedded in the surface, displacing bridging hydroxyls. This feature makes them very interesting as the multisite attachment may provide an explanation for the higher equilibrium binding constants obtained from the isotherm data shown in Figure 2-19.

2.3.4.3 The 2.1010 and 3.2010 binding modes

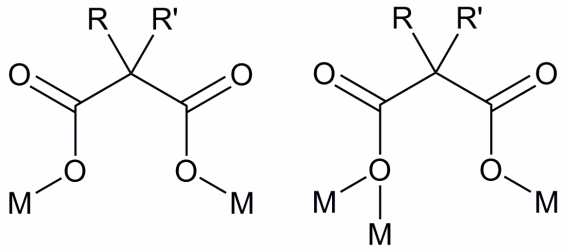

Figure 2-29: The 2.1010 and 3.2010 binding modes

The 2.1010 binding mode involves the binding of each acid group to a different iron atom in the surface. The shortest distance between adjacent iron atoms on the surface (show in Figure 2-21) is 3.060 Å, in the middle of the range (2.2 - 4.9 Å) which is observed for intramolecular O…O distances in malonate esters and acids in the CSD. The conformation adopted by the malonate upon binding to the lepidocrocite (0 2 $\bar{1}$) surface, displacing two *terminal* OH groups (see Figure 2-30) places the carbonyl oxygen atoms within hydrogen bonding distance of the surface hydroxyls adjacent to the binding site. This produces two rather long hydrogen bonds (2.292 and 2.356 Å) to each carbonyl making four hydrogen bonds in total to three μ_3 hydroxyls (see Figure 2-30). This model is a very plausible means by which the malonate could bind to this surface.

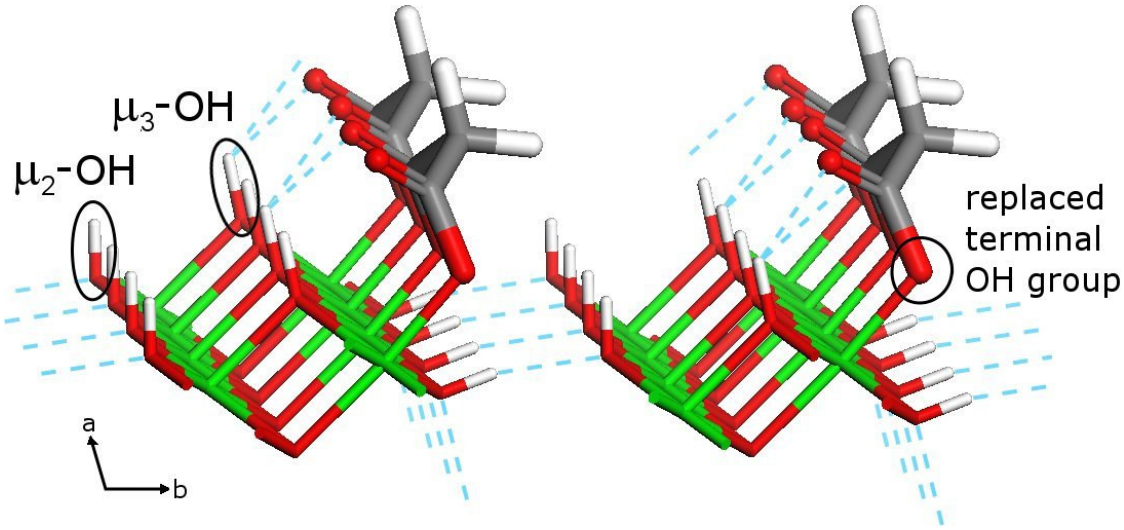

Figure 2-30: The 2.1010 binding mode docked onto the terminal OH sites showing hydrogen bonding between carbonyl oxygen atoms and μ_3 hydroxyl sites on the lepidocrocite (0 2 $\bar{1}$) surface.

The malonate can also potentially adopt the 3.2010 binding mode, shown above in Figure 2-29, which was not found in the CSD. When this mode is applied to surface attachment the most reasonable arrangement is shown in Figure 2-31 with the mononucleating oxygen of the malonate having displaced a terminal hydroxyl and the dinucleating, a μ_2 hydroxyl group. Hydrogen bonding to the carbonyl oxygen atoms is also possible in this model albeit with hydrogen to acceptor distances in the range 2.1 - 2.5 Å which are likely to be mid to weak strength bonds.

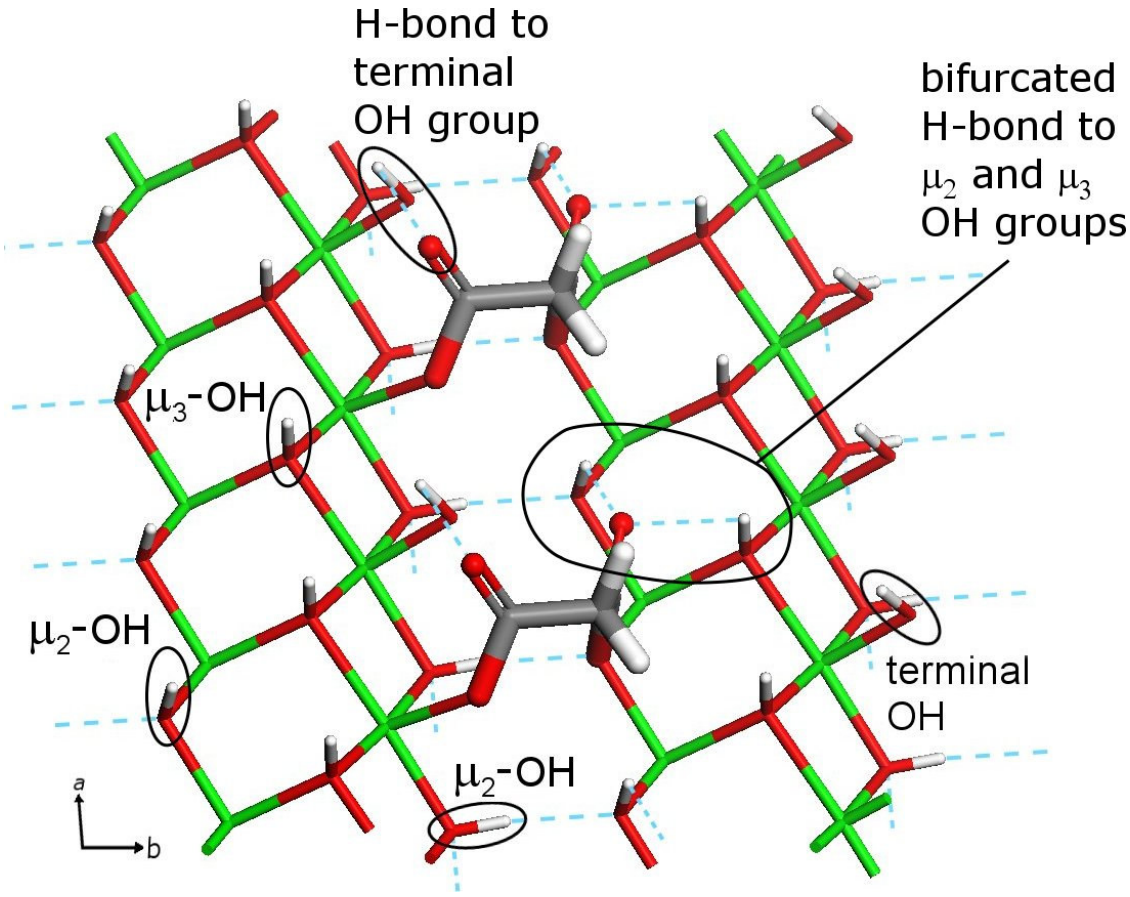

Figure 2-31: The 3.2010 binding model showing formation of a hydrogen bond between a carbonyl oxygen atom and a terminal hydroxyl group (top left) and bifurcated hydrogen bonds from the other carbonyl oxygen to μ_2 and μ_3 hydroxyl sites on the lepidocrocite (0 2 $\bar{1}$) surface.

2.3.4.4 Binding involving coordination of just one of the carboxylates, e.g. the 2.1100 binding mode

If only one acid group is chemisorbed onto the surface, the study of carboxylates in section 2.2.2 suggests that the 2.11 mode would be the most favoured. When extended to malonates, this is the 2.1100 mode shown. The other acid may take on several different roles including secondary bonding interactions with the surface or with malonic acid molecules directly attached to the surface or in a second layer. If there are no

secondary bonds it is likely that the pendant acid groups will be solvated. Some of these possibilities are shown schematically in Figure 2-33 and are discussed below.

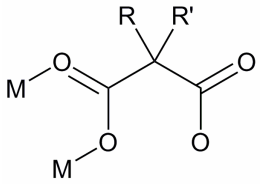

2.1100

Figure 2-32: The 2.1100 binding mode

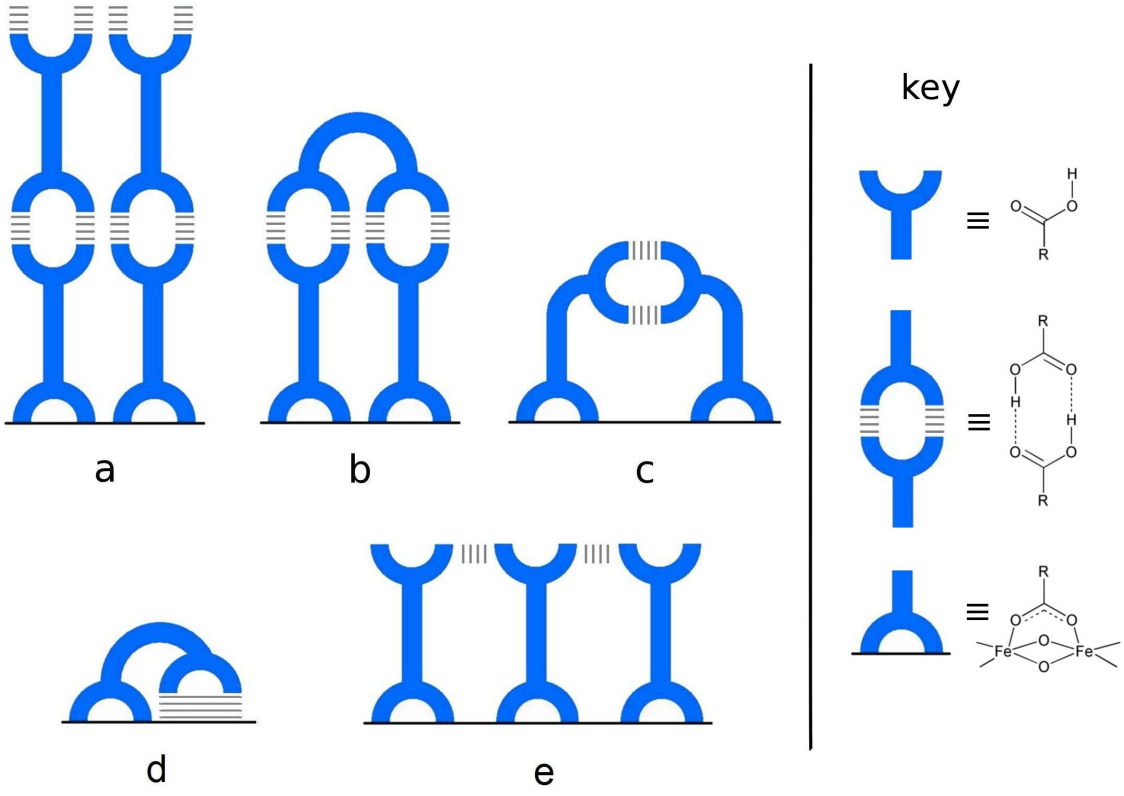

Figure 2-33: Schematic representation of malonate ligand-ligand and ligand-surface interactions in surface complex assemblies. Multilayering is shown in *a*; termination of multi-layering in *b*; dimerisation of ligands attached to the surface in *c*; ligand surface interaction through one or both of the O and OH is shown in *d*; and 1D chain formation in *e*.

The situation where the pendant carboxylic acid forms no secondary interactions either with the surface or with other malonates compares closely with the 2.11 binding of monocarboxylates (section 2.2.3). Whilst this is a favourable mode of attachment, it fails to explain the stronger binding of malonates compared with monocarboxylates. Also we would expect malonates to have a weaker isotherm than the 4-keto acids, which are thought to involve stabilising secondary interactions through the keto group.[2]

If formation of coordinate bonds through only one carboxylate as in the 2.1100 mode is to be used to explain the enhanced surface binding of malonates, the pendant acid group must stabilise the assembly formed at the surface by some form of interaction with ligands on the surface, hydroxyl groups, other malonates or solvent molecules. Carboxylic acids are commonly known to form stable dimers (see Figure 2-34) both in solution[24] and in the solid state. In the CSD 2368 of the 13437 carboxylic acid-containing structures can be found in this arrangement. The most plausible secondary interactions for the pendant acid within the 2.1100 mode can be placed in the five categories represented schematically in Figure 2-33. These are: 'infinite' multi-layering, Figure 2-33a; 'terminated' layering, Figure 2-33b; formation of carboxylic acid dimers between neighbouring surface bound ligands, Figure 2-33c; interaction with the surface, Figure 2-33d; and formation of 1D chains, Figure 2-33e.

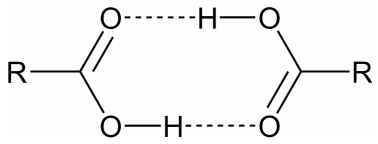

Figure 2-34: Dimeric interaction of two carboxylic acid units

Infinite multi-layering is not likely to be occurring upon surface binding because the appearance of an adsorption isotherm expected for such a system would be quite different from that obtained. The surface coverage would continue to increase with

increasing concentration of ligand in solution instead of levelling off to a plateau as in Figure 2-19.

Termination of multi-layering in the second layer, as shown schematically in Figure 2-33b is unlikely to occur in the *b* direction (see Figure 2-21) since the angled binding sites, coupled with the rigidity of the diacid, point the pendant acid groups in the surface bound malonates in unfavourable directions to allow hydrogen bonds to the 'capping' diacid to form effectively. Adjacent molecules in the *a* direction are too close to be capped in this fashion. Molecules on every other binding site, however, are more favourably spaced to hydrogen bond to a capping diacid. In practice, when modelled, this does not generate strong hydrogen bonds, even when restraints are placed on the hydrogen bond lengths. It also requires a vacant binding site between the two capped molecules. It is possible that some combination of the two multi-layering types shown in Figure 2-33 exists but the isotherm appearance would be expected to be more complex and so this was discounted as being a serious candidate for the mode of surface binding.

Secondary interactions with the surface have been proposed[2] as a mode of attachment for 4-keto acids and so analogous arrangements as shown schematically in Figure 2-33a must be considered here. On the lepidocrocite (0 2 $\bar{1}$) surface there are two potential hydrogen bond donors which could form bonds with the pendant carboxylate. On one side of the binding site there is a μ_2 hydroxyl group and on the other there is a μ_3 hydroxyl group, see Figure 2-35. Interaction with these sites was considered in molecular mechanics models. Hydrogen bonds to the ligand from either of these hydroxyl groups did not form spontaneously during energy minimisation and required restraints to be placed on their distance in order to form. This resulted in higher energy structures due to unfavourable torsion angles and on releasing the restraints the structures relax, breaking the hydrogen bonds. The rigidity of the ligand does not allow the pendant acid groups to get close enough to the surface to accommodate such bonds.

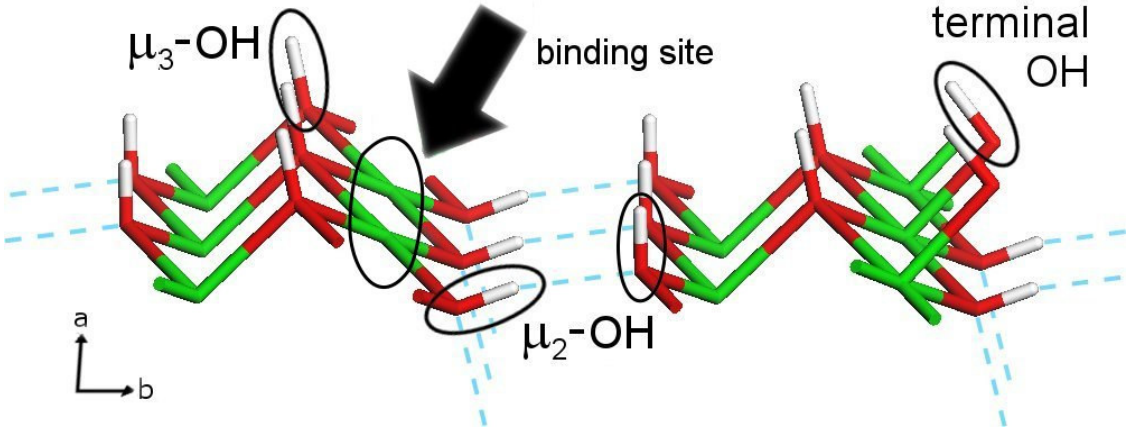

Figure 2-35: A binding site on the lepidocrocite (0 2 $\bar{1}$) surface showing the adjacent μ_2 and μ_3 sites which could act as H-bond donors to pendant carboxylate groups. The terminal OH groups shown on the right are displaced to form the binding sites.

Secondary interaction with other ligands on the surface could take place in two ways, either the formation of classic carboxylic acid dimers, or the formation of 1D chains by providing an acceptor for the neighbouring molecule's donor (structures *c* and *e* in Figure 2-33). The formation of dimers on the surface, as in Figure 2-33c, is not very likely as the angle between the acid groups on each molecule forces suboptimal geometry upon the hydrogen bonds. The angle between the two planes containing the carbon and two oxygen atoms in each acid making up the dimer was 70.9° in the energy minimised system. A survey of CSD structures shows a strong preference for coplanarity of the two units. Only small deviations from an interplanar angle of 0° are observed (Figure 2-36).

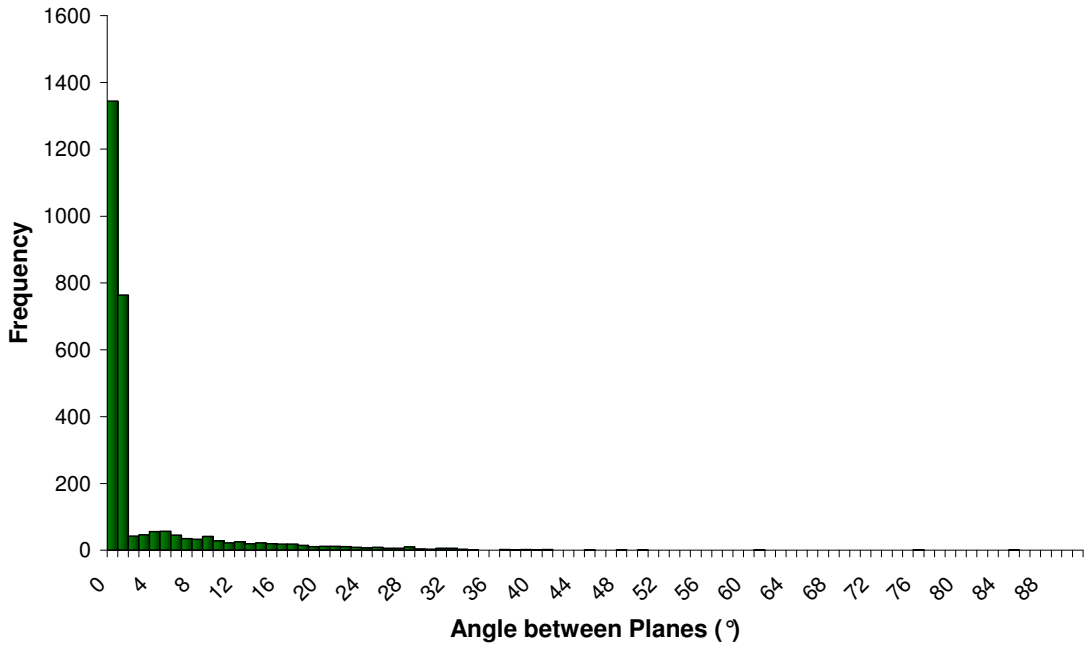

Figure 2-36: Histogram of angles between carboxylic acid planes in carboxylic acid dimers retrieved from the CSD.

Two different directions are possible for the formation of one dimensional chains of the type shown in Figure 2-33e. These two arrangements are shown in Figure 2-37. Forming chains in the *ab* direction is not possible on this surface because the *ab* face diagonal length is 14.702 Å long. For a chain to form this distance must contain those of two hydrogen bonds and two acid groups. The largest intramolecular distance which may be adopted between the acidic proton and the carbonyl oxygen atom of a carboxylic acid is ca. 3.2 Å according to molecular mechanics models. This means that by placing two malonates per surface unit cell in this direction, 6.4 Å of the 14.7 Å can be accounted for by carboxylic acid groups leaving about 8.3 Å to be accounted for by hydrogen bonding. If hydrogen bonding chains were to exist in this direction, there would be two hydrogen bonds per unit cell, thus each H…A distance would be ca. 4.15 Å which is too long to be considered a hydrogen bond. Forming chains in the *a* direction is similarly unlikely. In this case the minimum distance which a hydrogen bond

would be required to cover, from the hydrogen to its acceptor, would be ~3 Å. Again this is too long to be considered a hydrogen bond as COO-H...O=C bonds are typically less than ~2.3 Å according to CSD data. With such extremely weak interaction it is unlikely that hydrogen bonding chains of the type represented in Figure 2-33e will enhance the stability of surface assemblies and the strength of surface binding by malonates.

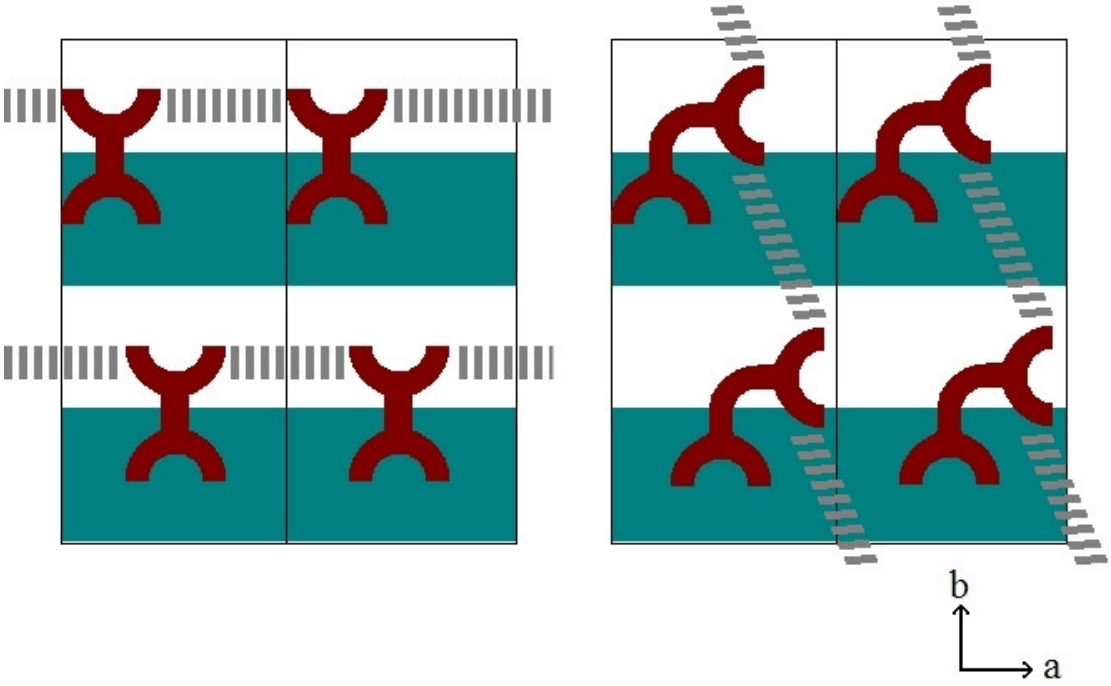

Figure 2-37: Schematic representation of one dimensional hydrogen bond chains in the *a* direction (left) and *ab* direction (right) on the lepidocrocite (0 2 $\bar{1}$) surface.

Surface structures containing the 2.1100-motif which have not yet been discussed are the 3.1110, 4.1111 and 5.2111 modes. These binding modes are shown again in Figure 2-39 below. When one of the acid groups adopts the 2.11 binding mode the nearest potential sites which the oxygen atoms of the other acid group could occupy are the μ_2 and μ_3

oxygen atoms on either side of the binding site in the *b* direction, see Figure 2-35, or the hydroxyls on either side in the *a* direction. On the basis of distance, the only type of oxygen atom which can provide these modes is that adjacent to the binding site in the *a* direction as other oxygen atoms are too far away. These sites are inaccessible to the additional acid group since the angle at the linking carbon atom is too obtuse.

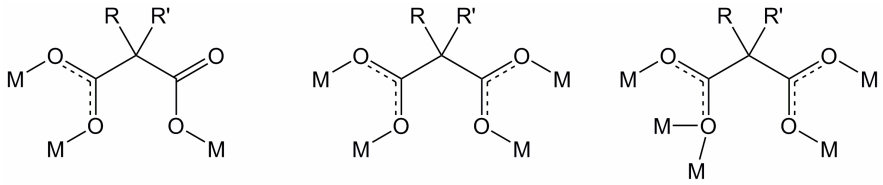

Figure 2-38: The 3.1110, 4.1111 and 5.2111 binding modes

The 2.1100 binding mode and those derived from it are therefore unlikely to account for malonates binding more strongly than 4-keto acids as fewer or equal interactions with the surface are predicted.

2.3.4.5 Modelling the 6-membered chelate ring structures

From the analysis presented above, the most plausible models to account for the favourable surface binding of malonates are those involving 6-membered chelate rings. Which variant of this motif is most favourable is considered in the following four sections.

2.3.4.5.1 The 4.3020 mode and 3.3010 binding modes

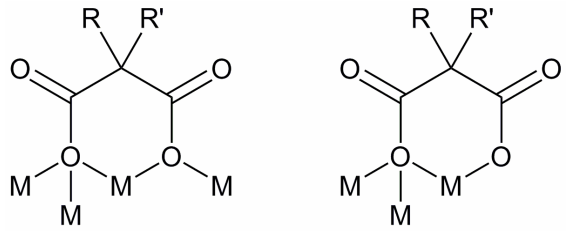

Figure 2-39: The 4.3020 and 3.3010 binding modes

Surface binding involving the 4.3020 and 3.3010 binding modes is similar. Both require use of one of the μ_3 oxo sites (Figure 2-21) and an additional binding site to form a chelate ring. In the case of the 4.3020 mode, the additional site is the μ_2 type and a total of five O-Fe coordinate bonds are formed as shown in Figure 2-40. The energy minimised form of this model also contains three hydrogen bonds (2.208, 2.283 and 2.302 Å) between surface hydroxyl groups and malonate oxygen atoms. These are also shown in Figure 2-40.

The 3.3010 mode uses a terminal OH site in addition to the μ_3 site to form the six membered ring, and as a consequence a total of four O-Fe coordinate bonds to the surface are formed as shown in Figure 2-41. The energy minimised model has two hydrogen bonds (2.305, 2.365 Å) which are also shown in Figure 2-41.

Parameters pertaining to the chelate ring in the energy minimised structures for 3.3010 and 4.3020 type surface binding are presented alongside data extracted from the CSD for related structures. Only one iron(III) malonate complex, DAJWAM, was found in the CSD which was of sufficient quality to use for comparison. It contains the unsubstituted trismalonatoiron(III) trianion.

The parameters for both models fall within ranges observed in the CSD for complexes with other transition metals and are similar to those seen in DAJWAM. This is a good indication that the structures produced upon energy minimisation are plausible models for the binding of malonates to iron oxide surfaces.

Parameter	Malonic acids	Chelate malonate complexes (any metal)	DAJWAM	3.3010 mode	4.3020 mode
O-C-O /°	118.3 - 126.6	115.2 - 127.6	121.2 - 123.0	119.1, 115.7	119.0, 120.3
C-C-O /°	110.3 - 122.2	111.2 - 124.3	117.7 - 120.6	122.6, 126.1	122.3, 126.0
C-C=O /°	116.7 - 126.8	114.2 - 128.1	117.6 - 119.8	118.1, 118.3	114.5, 117.4
C-C-C /°	107.1 - 117.9	104.7 - 128.0	116.0 - 120.3	119.8	113.2
C=O /Å	1.188 - 1.277	1.152 - 1.514	1.230 - 1.241	1.221, 1.268	1.208, 1.214
C-O /Å	1.205 - 1.342	1.217 - 1.402	1.279 - 1.286	1.271, 1.366	1.382, 1.410
C-C /Å	1.482 - 1.533	1.374 - 1.632	1.502 - 1.578	1.498, 1.515	1.481, 1.482
C-C-C=O /°	2.4 - 179.3	103.6 - 179.6	132.8 - 166.4	153.6, 167.2	112.3, 147.1
C-C-C-O /°	0.7 - 177.9	0.1 - 76.0	15.5 - 49.1	16.0, 23.6	33.7, 59.2
M-O-C-C /°	N/A	0.0 - 51.325	2.8 - 28.0	11.0, 17.2	17.7, 21.0

Table 2-3: Parameters from the energy minimised 3.3010 and 4.3020 models alongside data retrieved from the CSD. DAJWAM is $[Fe(malonate)_3]^{3-}$ $[Co(NH_3)_6]^{3+}.5H_2O$

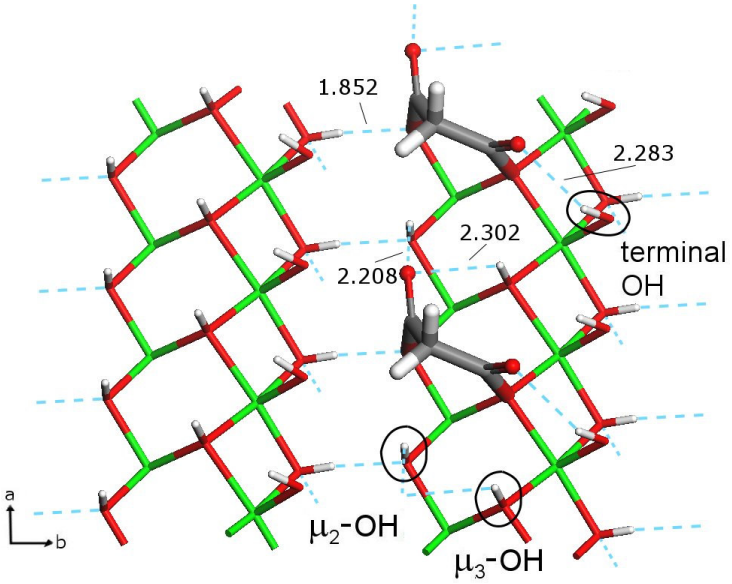

Figure 2-40: The energy minimised structure for 4.3020 binding involving replacement of μ_2 and μ_3 hydroxyl groups and formation of three hydrogen bonds from surface hydroxyl groups to malonate oxygen atoms.

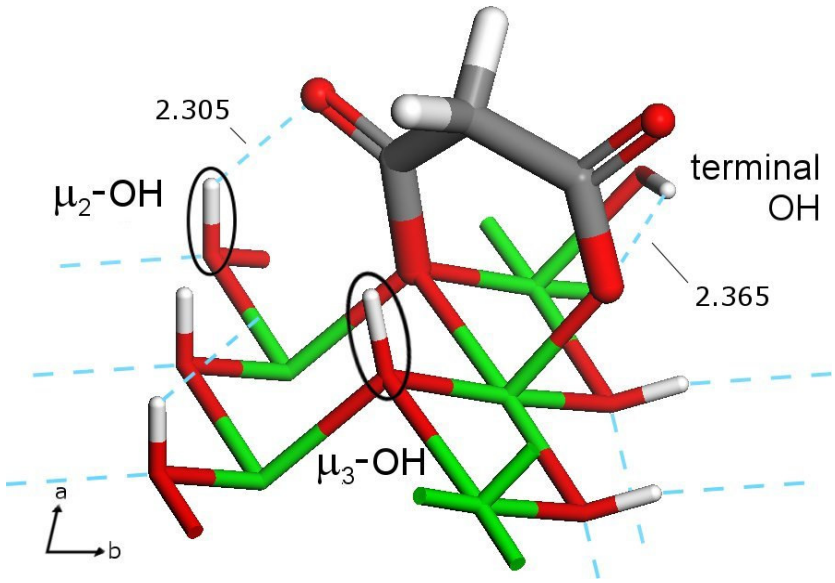

Figure 2-41: The energy minimised structure for 3.3010 binding involving the replacement μ_3 and terminal hydroxyl groups and formation of two hydrogen bonds from surface hydroxyl groups to malonate oxygen atoms.

2.3.4.5.2 The 3.2020 binding mode

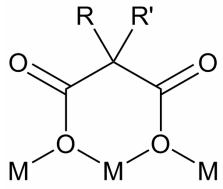

Figure 2-42: The 3.2020 binding mode

The 3.2020 mode for surface binding can occur when the plane of the malonate molecule is parallel to the *a* direction (see Figure 2-44). Displacement of surface μ_2 hydroxyl groups by carboxylate groups will lead to the oxygen atoms taking trigonal pyramidal sp^3 geometry with the lone pair of the oxygen pointing towards a hydrogen

bond donor. One might expect there would be a preference for sp^2 geometry at the oxygen atom but in this case the existence of a hydrogen bond to the lone pair may stabilise the oxo anion. The CSD does not include many structures displaying a 3.2020 motif. Only 1 hit was retrieved although there are several modes, e.g. the 6.2221 mode (shown again in Figure 2-43), which derive from this but cannot apply in surface binding. The reason for this can be seen in Figure 2-44. Once the chelate ring has been formed the carbonyl oxygen atoms of the carboxylate groups are directed upwards, away from the surface and therefore cannot interact with *surface* metal ions to form the 6.2221 motif.

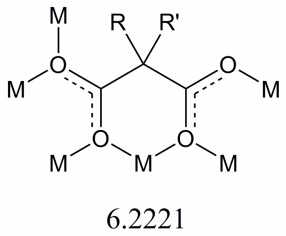

Figure 2-43: The 6.2221 binding motif.

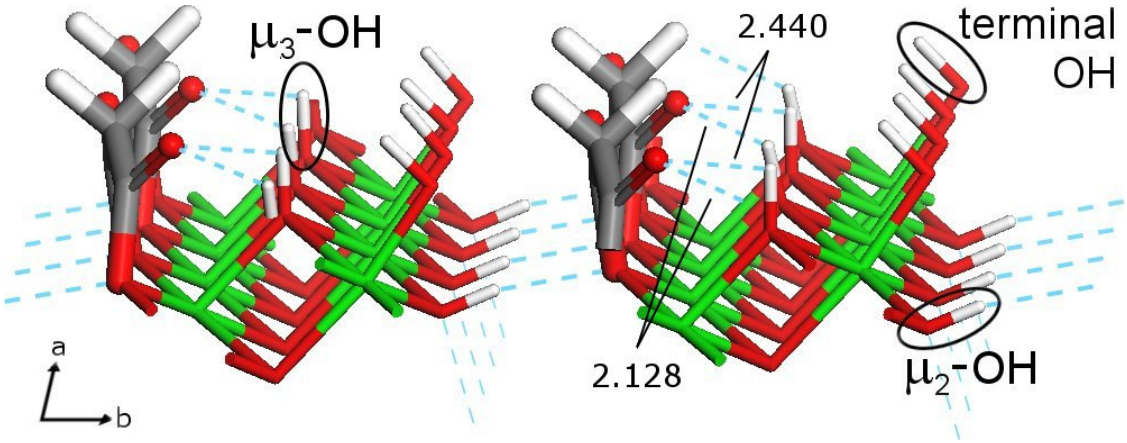

Figure 2-44: The energy minimised structure for binding of malonates in a 3.2020 arrangement on the (0 2 $\bar{1}$) surface of lepidocrocite involving the replacement of μ_2 hydroxyl groups and the formation of 4 hydrogen bonds from surface hydroxyls to malonate oxygen atoms.

2.3.4.5.3 The 3.3020 binding mode

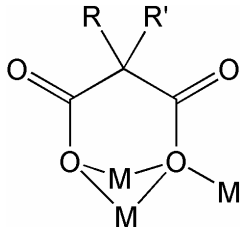

Figure 2-45: The 3.3020 binding mode

The 3.3020 motif (Figure 2-45) is only possible if the plane of the malonate molecule is parallel to the *b* direction (see Figure 2-46). The lepidocrocite (0 2 $\bar{1}$) surface (Figure 2-21) consists of a series of angled 'terraces' in the *b* direction. Each of these terraces contains binding sites and therefore the plane of the binding sites is also angled in the *b* direction. This means that molecules on the surface are directed towards parts of the surface comprising the next 'terrace' along and steric interactions are likely to occur which would make binding in this manner unfavourable. The approach to the binding site is hindered and also if binding were successful it will force unusual geometries upon the ligand.

The model (see Figure 2-46 and Figure 2-47) produced upon energy minimisation shows that binding in a 3.3020 arrangement does indeed cause distortions in the surface oxide structure. This is manifest by the angles at oxygen atoms in the surface layer. One would expect that the ligand carboxylate μ_2 oxygen atom, being bonded to three atoms would have similar geometry to the hydroxyl group which was replaced. This implies trigonal pyramidal geometry giving angles slightly smaller than 109.5°. In the energy minimised structure the angles around the oxygen atom, Fe-O-Fe, Fe_1-O-C, and Fe_2-O-C, are 101.5, 88.9, and 62.1° which average to 84.2°, considerably smaller than the expected 109.5°. Even with this distortion the hydroxyl groups which cause this

distortion are still too close to the malonate and thus interact unfavourably with it. For these reasons the 3.3020 mode is an unreasonable model and so can be discarded.

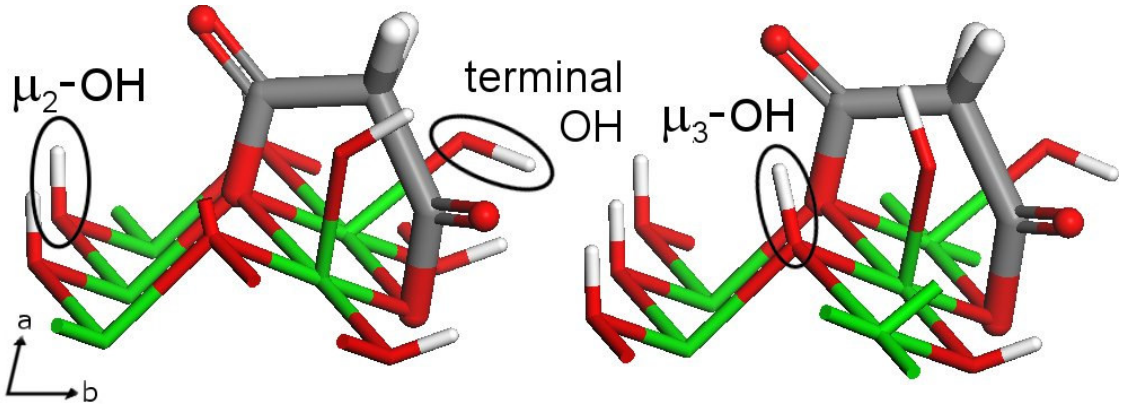

Figure 2-46: The 3.3020 binding model viewed along the *a* direction showing unfavourable steric interaction with the neighbouring terminal OH groups in the *a* direction and neighbouring μ_2-OH groups in the *b* direction

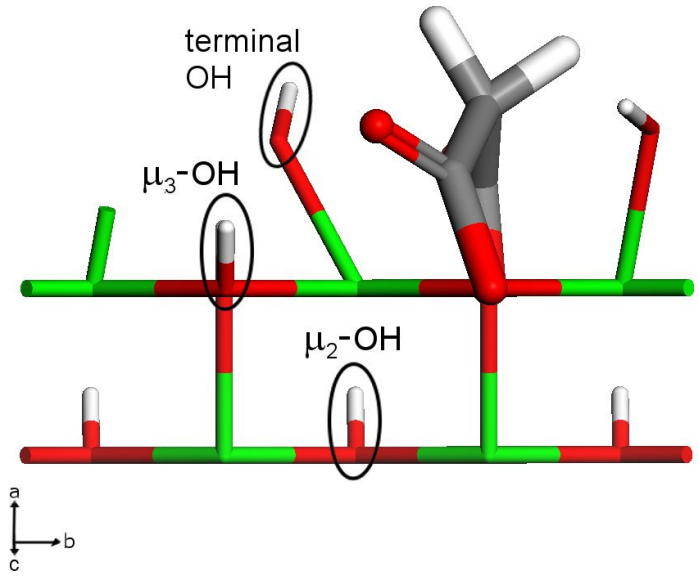

Figure 2-47: A view of the 3.3020 binding model showing the effect of binding on terminal hydroxyl groups adjacent to the binding site in the *a* direction.

2.3.4.5.4 The 5.3030 binding mode

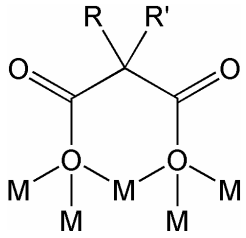

Figure 2-48: The 5.3030 binding mode

The 5.3030 mode (shown in Figure 2-48), also occurs on the surface generated from the lepidocrocite (0 2 $\bar{1}$) face (Figure 2-49) also parallel to the *a* direction. In the 5.3030 model two of the μ_3 hydroxyl groups from the surface are displaced leading to six bonds with the surface to five iron atoms. The carbonyl oxygen atoms from the malonate are pointed towards μ_2 hydroxyl groups from the surface and a bifurcated hydrogen bonding pattern is formed with each. The H…A distances determined for these H-bonds 2.282 and 2.362 Å. Hydrogen bonds involving OH…O in the CSD generally range from ~1.8 – 2.5 Å and so those from this model are probably mid to weak strength. This produces a total of 9 interactions with the surface, 5 bonds and 4 hydrogen bonds, which is a higher number than for any of the other binding modes discussed or for the positive control, Irgacor 419®, used in the adsorption isotherms experiments discussed in section 2.3. The 6-membered ring Fe-O-C-C-C-O is in a chair conformation and selected torsions, angles and distances are tabulated in Table 2-4 which also contains the ranges found for transition metals and for the DAJWAM (an $Fe(mal)_3$ structure) which were previously discussed in the context of the 4.3020 and 3.3010 models in section 2.3.4.5.1.

Parameter	Malonic Acids	Chelate ring Complexes	DAJWAM	5.3030 mode
O-C-O /°	118.3 - 126.6	115.2 - 127.6	121.2 - 123.0	120.370, 119.780
C-C-O /°	110.3 - 122.2	111.2 - 124.3	117.7 - 120.6	121.833, 123.279
C-C=O /°	116.7 - 126.8	114.2 - 128.1	117.6 - 119.8	116.031, 115.779
C-C-C /°	107.1 - 117.9	104.7 - 128.0	116.0 - 120.3	110.889
C=O /Å	1.188 - 1.277	1.152 - 1.514	1.230 - 1.241	1.215, 1.210
C-O /Å	1.205 - 1.342	1.217 - 1.402	1.279 - 1.286	1.392, 1.398
C-C /Å	1.482 - 1.533	1.374 - 1.632	1.502 - 1.578	1.487, 1.505
C-C-C=O /°	2.4 - 179.3	103.6 - 179.6	132.8 - 166.4	101.172, 109.128
C-C-C-O /°	0.7 - 177.9	0.1 - 76.0	15.5 - 49.1	58.491, 63.732
M-O-C-C /°	N/A	0.0 - 51.325	2.8 - 28.0	1.534, 6.992

Table 2-4: Parameters taken from the CSD and the 5.3030 binding model.

The parameters for the 5.3030 motif unsurprisingly do not fall within the ranges observed in the iron malonate structure from the CSD. Using these as a guide for preliminary comparison, the values are quite close for most parameters particularly the angles and distances although the torsions are quite different. Comparison to complexes with other transition metals gives a closer match for torsion values with all now falling within acceptable ranges. Unfortunately the lack of sufficient quality iron malonate structures makes it is difficult to determine whether the chelate ring geometry is acceptable.

The 5.3030 binding has several features which could explain the experimental observation that malonates bind to iron oxide surfaces more strongly than Irgacor 419®.

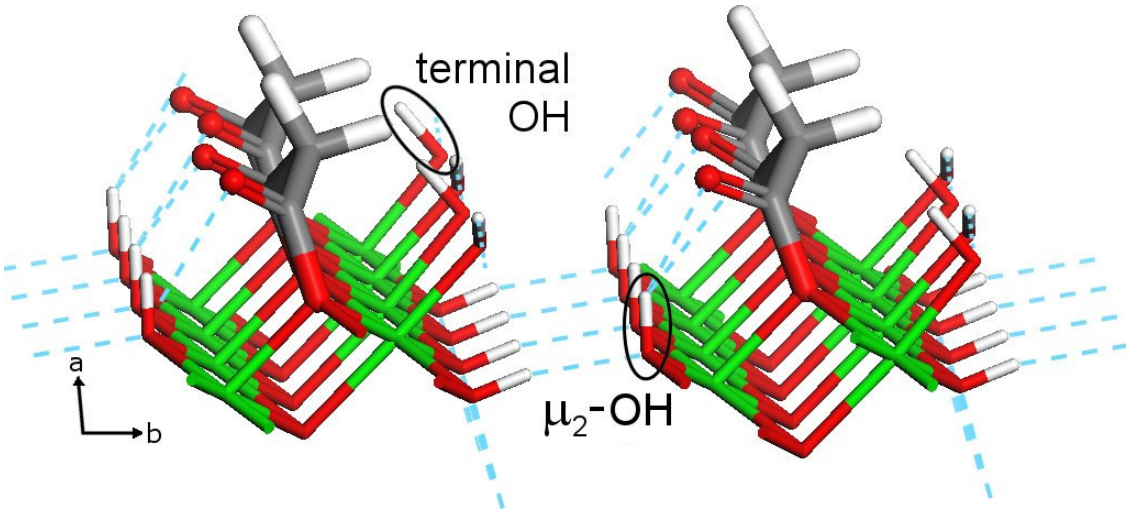

Figure 2-49: The 5.3030 binding model shown along the *a* direction. Zigzag hydrogen bonding chains set up between malonate carbonyl oxygen atoms and μ_2-OH groups on the surface.

2.4 Conclusions

As in a previous project which studied the activity of Irgacor 419®, experimental data provided evidence as to the high surface activity of malonates on iron oxide surfaces, specifically that they bind more strongly to iron oxide surfaces than carboxylates. At the outset of this study the intent was to use the same procedure, which was very successful in the previous situation, to explain this observation and to produce binding models. Consequently, attempts were made to prepare polynuclear iron(III) malonate X-ray crystal structures. These were expected to provide extremely useful starting points for determining plausible surface activity modes through molecular mechanics models. Reliance on the preparation of such structures presented a major problem as none were obtained in the time frame of the project and so an alternative methodology had to be adopted. In the absence of useful polynuclear structures two major database mining studies were conducted using the CSD in order to provide both an understanding of the geometry of closely related iron carboxylates and to uncover any interesting polynuclear transition metal complexes formed with malonates. The survey of malonates produced a very large number of potential binding motifs. These were then subjected to a time

consuming process of elimination using geometry data retrieved in the carboxylate mining exercise and chemical knowledge. This still left a lot of potential models which had to be were validated according using molecular mechanics models, which required significant setup, tweaking and scrutiny. This lengthy process reduced a large number of possibilities down to 4 very plausible models, the 2.1010, 3.3010, 4.3020 and 5.3030 binding modes. Each mode involves a multi-site attachment motif and is polynuclear. In comparison to the Irgacor 419® model, each of these modes has a higher number of interactions with the surface. The fact that multiple models have emerged as plausible is interesting since this may indicate that malonates can bind to different parts of the surface. Such adaptability alone may account for the observed higher surface coverage since real world systems contain a wide range of different environments for the ligand to bind to.

However, the 5.3030 binding mode offers a very plausible model in which the nuclearity of the malonate is high, forming 6 coordinate bonds to the surface and also two secondary interactions with the surface. This is very significant as this means that if we accept the hypothesis that increasing nuclearity is an indication of increasing binding strength, this model explains the experimental observation that malonates bind more strongly to iron oxide surfaces than 4-keto acids.

Molecular modelling in this chapter shows that

- Modelling of surface binding of malonates to iron oxide surfaces is possible and produces plausible models.
- Higher nuclearity modes are possible for malonates than for carboxylates.
- Hydrogen bonding can form between malonates and the surface to assist stability
- Malonates are predicted to be better surface actives than carboxylates.

2.5 References

1. R. P. Renz, PhD Thesis, University of Edinburgh, 2007.
2. M. Frey, S. G. Harris, J. M. Holmes, D. A. Nation, S. Parsons, P. A. Tasker and R. E. Winpenny, *Chemistry - A European Journal*, 2000, **6**, 1407-1415.
3. H. M. Wells, J. E. Southecombe, *GB Pat*, GB130377, 1919.
4. N. J. Fox, B. Tyrer and G. W. Stachowiak, *Tribology Letters*, 2004, **16**, 275-281.
5. F. H. Allen, *Acta Crystallographica, Section B*, 2002, **58**, 380-388.
6. J. J. R. Frausto Da Silva and R. J. P. Williams, *The Biological Chemistry of the Elements: The Inorganic Chemistry of Life*, Oxford University Press, 1991.
7. S. G. Harris, PhD Thesis, University of Edinburgh, 1999.
8. R. K. H. Hocking, T. W, *Dalton Transactions*, 2005, 969-978.
9. I. J. Bruno, J. C. Cole, P. R. Edgington, M. Kessler, C. F. Macrae, P. McCabe, J. Pearson and R. Taylor, *Acta Crystallographica, Section B*, 2002, **58**, 389-397.
10. *Cambridge Structural Database System - Appendices - APPENDIX 10*, http://www.ccdc.cam.ac.uk/support/documentation/quest/volume3/z310.html, Accessed 10/10/2007, 2007.
11. A. A. C. Smith, R. A.; Harrison, A.; Helliwell, M.; Parsons, S.; Winpenny, R. E. P., *Polyhedron*, 2004, **23**, 1557.
12. C. L. Boskovic, G.; Neels, A.; Gudel, H. U., *Dalton Transactions*, 2003, 3671-3672.
13. C. O. B. Canada-Vilalta, T. A.; Brechin, E. K.; Pink, M.; Davidson, E. R.; Christou, G., *Inorganic Chemistry*, 2004, **43**, 5505-5521.
14. D. C. J. Ogrin, Ramon; Maruyama, Benji; Pender Mark J; Smalley, Richard E; Barron, Andrew R, *Dalton Transactions*, 2006, **1**, 229-236.
15. R. A. Coxall, A. Parkin, S. Parsons, A. A. Smith, G. A. Timco and R. E. P. Winpenny, *Journal of Solid State Chemistry*, 2001, **159**, 321.
16. C. Canada-Vilalta, W. E. Streib, J. C. Huffman, T. A. O'Brien, E. R. Davidson and G. Christou, *Inorganic Chemistry*, 2004, **43**, 101.
17. A. Ohto, Y. Sasaki and T. Ito, *Inorganic Chemistry*, 1994, **33**, 1245-1246.
18. A. Parkin, PhD Thesis, University of Edinburgh, 2002.
19. *Cerius*^{2}, Accelrys Inc., Accelrys Inc., San Diego, California, USA, Editon edn., 2000.
20. H. Christensen and A. N. Christensen, *Acta Chemica Scandinavica, Series A*, 1978, **32**, 87-88.
21. A. K. Rappe and W. A. Goddard-III, *Journal of Physical Chemistry*, 1991, **95**, 3358-3363.
22. H. Sun, S. J. Mumby, J. R. Maple and A. T. Hagler, *Journal of the American Chemical Society*, 1994, **116**, 2978.
23. A. K. Rappe, C. J. Casewit, K. S. Colwell, W. A. Goddard-III and W. M. Skiff, *Journal of the American Chemical Society*, 1992, **114**, 10024-10035.

24. J. Chen, C. L. Brooks and H. A. Scheraga, *Journal of Physical Chemistry B*, 2008, **112**, 242-249.

Chapter 3

The Interaction of Benzohydroxamic Acid with Iron Oxide Surfaces

Contents

3. Introduction

This chapter is concerned with the study of benzohydroxamic acid (Figure 3-1) as a surface active compound for iron oxide surfaces. Prior to the work described in this thesis, this compound had been shown to have strong affinity for iron oxide surfaces by determining isotherms for uptake from solution onto high surface area goethite. Crystal structures have been obtained which provide insight into potential surface binding modes. Greasy derivatives have been synthesised and tested for friction reduction performance.

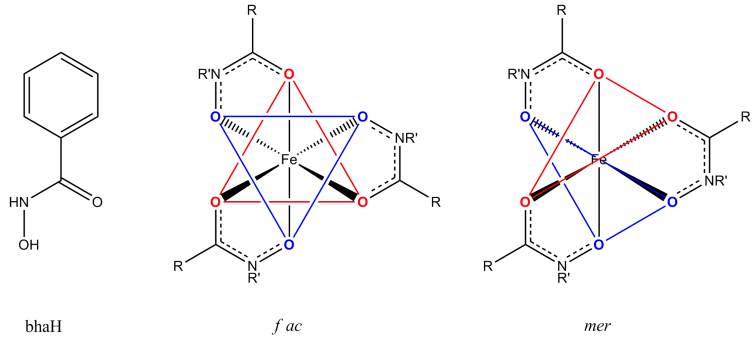

Figure 3-1: Benzohydroxamic acid (bhaH) and its *fac* and *mer* tris chelate complexes [Fe(bha)$_3$] when R = Ph and R' = H.

3.1. Hydroxamic acids as mineral collectors

Hydroxamic acids are weak acids which play important roles in biology such as enzyme inhibition and solubilising iron in transport mechanisms.[1-4] They are so effective at binding to Fe^{3+} ions that micro-organisms such as *E. coli.*, produce siderophores based upon hydroxamates and are able to scavenge sufficient iron, even in an iron-deficient environment, e.g by leaching iron from the lab equipment, to be able to grow and function. This ability to scavenge and solubilise iron in an iron deficient environment

has been attributed to extremely high stability[1, 5] of iron(III) hydroxamato species particularly trishydroxamato complexes.

Given this information, the appearance of hydroxamates on lists[6] of potential flotation agents for ores containing iron(III) oxides is rather surprising because it would be assumed that they would promote the dissolution of iron as in

$$Fe_2O_{3(s)} + 6LH \rightleftharpoons 2FeL_3 + 3H_2O.$$

Flotation agents, or collectors are used in metallurgical froth flotation processes to transfer a desired component of an ore into an oil based froth in order to separate the valuable metal from silicaceous "gangues". Flotation agents are usually surfactant molecules whose head groups attach themselves to surfaces of the desired mineral which is present in the crushed crude ore. As the majority of base and precious metals are obtained from their sulfidic ores these head groups usually contain soft donor atoms such as sulfide groups in thiocarboxylic acids or xanthates. Attachment to the surface of particles of sulfide minerals confers sufficient hydrophobicity to favour incorporation into the oil-based froth which rises in the froth flotation separator Figure 3-2. The hydrophilic silicaceous gangues are wetted by water and fall to the bottom of the separator.

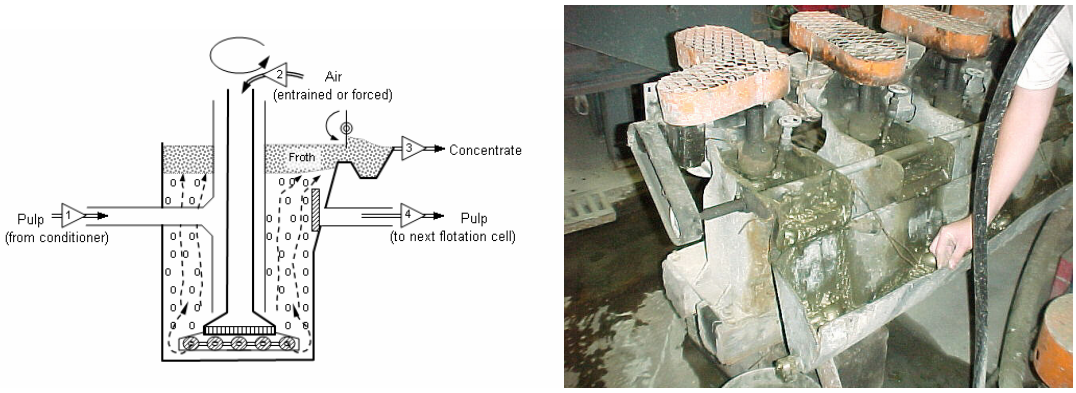

Figure 3-2: A schematic of a froth flotation separator cell (left) and an operating froth flotation system (right)

In a recent PhD thesis[7] "co-collectors" were developed which could be used in conjunction with collectors for sulfides such as chalcopyrite, $CuFeS_2$, to improve the recovery of partially oxidised ores. In these materials the oxidation is associated with the presence of iron(III) oxyhydroxides on the mineral surface. Consequently the incorporation of a small amount of a co-collector with a high affinity for iron(III) oxides, e.g. 3-(4-methylbenzoyl)-propionic acid (Irgacor 419®) to address the oxidised areas was shown to complement sulfur-containing flotation agents such as xanthates in imparting hydrophobicity to ore particles.

3.2. Experimental

3.2.1. X-ray structure determination of benzohydroxamato complexes

3.2.1.1. $[Fe(bha)_3]\cdot 1.5MeOH$

A crystalline sample which was suitable for X-ray diffraction was obtained by evaporation of a 1:1 methanol / ether solution. The crystals produced were orange blocks and one measuring 0.53 x 0.34 x 0.14 mm was selected and diffraction data were collected on a 3 circle Bruker Smart Apex CCD diffractometer with graphite-monochromated Mo-Kα radiation (λ = 0.71073 Å) equipped with an Oxford Cryosystems low temperature device operating at 150 K. The crystal was indexed using the Bruker Smart software and found to be primitive monoclinic with a = 20.2477(8), b = 11.3483(4), c = 22.4035(9) Å and β = 115.874(2)°. From initial indexing a data collection strategy was refined which aimed to collect fully complete data to a resolution of 53° in 2θ in as short a time as possible. In total 62259 reflections were collected and from these the space group was determined to be $P2_1/c$. Absorption correction was performed using a multi-scan method by applying the SADABS[8] program to the data. The data were merged according to the crystal system in SHELX[9] which gave 10126 unique reflections with a merging R-factor of 0.0442. The initial solution was

determined by direct methods with the SHELXS[9] program. All heavy atoms were refined anisotropically and most hydrogen atoms were placed geometrically and allowed to ride on their host atom. Hydrogen atoms on oxygen and nitrogen atoms were found in a Fourier difference map and their positions refined with a restraint on their distance from their host. Full matrix least squares refinement was carried out against F^2 producing a final conventional R-Factor of 0.0371 based on 8192 reflections.

3.2.1.2. $[Fe_2(\mu_2\text{-bha})_2(bha)_2Br_2]$

A crystalline sample which was obtained which was suitable for X-ray diffraction was obtained by evaporation of a 1:1 methanol / acetonitrile solution. The crystals produced were black blocks and one measuring 0.37 x 0.18 x 0.14 mm was selected and diffraction data were collected on a 3 circle Bruker Smart Apex CCD diffractometer with graphite-monochromated Mo-Kα radiation (λ = 0.71073 Å) and equipped with an Oxford Cryosystems low temperature device operating at 150 K. The crystal was indexed using the Bruker Smart software and found to be C-centred monoclinic by examining $|E^2\text{-}1|$ values with indices a = 14.5538(9), b = 16.2543(10), c = 12.9684(8) Å and β = 91.814(4)°. From initial indexing a data collection strategy was refined which aimed to collect fully complete data to a resolution of 53° in 2θ in as short a time as possible. In total 43236 reflections were collected and from these the space group was determined to be *C*2/*c*. Absorption correction was performed using a multi-scan method by applying the SADABS[8] program to the data. The data were merged according to the crystal system in SHELX[9] which gave 4680 unique reflections with a merging R-factor of 0.0422. The initial solution was determined by direct methods with the SHELXS[9] program. All heavy atoms were refined anisotropically and most hydrogen atoms were placed geometrically and allowed to ride on their host atom. Hydrogen atoms on oxygen and nitrogen atoms were found in a Fourier difference map and their positions refined with a restraint on their distance from their host. Some static disorder was encountered

in one of the benzene rings which was refined as two components with the main component assigned a 0.7 site occupancy factor occupancy and the secondary component, 0.3. Full matrix least squares refinement was carried out against F^2 producing a final conventional R-Factor of 0.0338 based on 3511 reflections.

3.2.2. Synthesis and characterisation of N-hydroxy-9(Z)-octadecenamide[10]

Work in this section was carried out by Dr Jy Chartres who also kindly provided the following text.

All solvents and reagents were commercially available from Aldrich or Fisher. ^1H and ^{13}C NMR spectra were obtained on a Bruker ARX 250 spectrometer. The chemical shifts (δ) are reported in parts per million (ppm) relative to the residual solvent signal in $CDCl_3$ (δ_H 7.26 and δ_C 77.0). Fast atom bombardment (FAB) mass spectra were recorded on a Kratos MS50TC instrument in a 3-nitrobenzyl alcohol (NOBA) matrix.

Hydroxylamine hydrochloride (34.8 g, 0.500 mol) was dissolved in water (250 mL) and sodium carbonate (53.0 g, 0.500 mol) was added. To the resulting solution was added ethyl acetate (50 mL) followed by a solution of oleoyl chloride (15.05 g, 0.050 mol) in ethyl acetate (100 mL) and the two phases were vigorously stirred overnight. The organic layer was separated, washed with water (100 mL) and dichloromethane was added. The resultant organic solution was dried over sodium sulfate and allowed to evaporate to give a white precipitate which was recrystallised from acetonitrile (800 mL) to give *N*-hydroxy-9(*Z*)-octadecenamide (9.0 g, 60%) as a white solid. The remaining mother liquor was reduced on a rotary evaporator and the resulting solid recrystallised from acetonitrile (250 mL) to give a second crop of *N*-hydroxy-9(*Z*)-octadecenamide (2.64 g, 18%). ν_{max} (KBr)/cm^{-1} 3285, 3001, 2918, 2849, 1666, 1621, 1464 and 1427; δ_H (250 MHz; $CDCl_3$) 0.88 (3 H, br t, CH_3), 1.2-1.4 (20 H, br m, C(4)H_2, C(5)H_2, C(6)H_2,

$C(7)H_2$, $C(12)H_2$, $C(13)H_2$, $C(14)H_2$, $C(15)H_2$, $C(16)H_2$ and $C(17)H_2$), 1.64 (2 H, m, $COCH_2CH_2$), 2.01 (4 H, m, $CH_2CH{=}CHCH_2$), 2.15 (2 H, br t, $COCH_2$), 5.34 (2H, overlapping m, CH=CH), 8.10 (2 H, br s, OH and NH); δ_C (63 MHz; $CDCl_3$) 14.1, 22.7, 25.4, 27.1, 27.2, 29.1, 29.2, 29.3, 29.5(2), 29.7(2), 29.8, 31.9, 33.0, 129.6, 130.0 and 172.0; *m/z* (FAB) 298 $(M+H)^+$.

3.3. Isotherm data for benzohydroxamic acid

When reviewing the literature to identify ligands to act as such co-collectors, references were found[7] to the ability of hydroxamates to effect flotation of oxides. Consequently, Iria Rio investigated their potential as surface ligands for iron(III) oxides. As part of this study the uptake of benzohydroxamic acid onto powdered, high surface area goethite from 95% $MeOH/H_2O$ solutions was measured by tracking the UV band of the benzene ring for solutions containing residual concentrations in the range 0 - 1.5 x 10^{-3} mol dm^{-3}. Analysis of the supernatant solutions by inductively coupled plasma optical emission spectroscopy (ICP-OES) confirmed that no iron was present. The resulting isotherm is shown in Figure 3-3 and is compared with that of the commercially available surface active compound Irgacor 419® (3-(4-methylbenzoyl)-propionic acid) and of 4-chlorophenyl-2-malonic acid which was the subject of study in the previous chapter. The data extracted from the isotherms in each case are presented in Table 3-1.

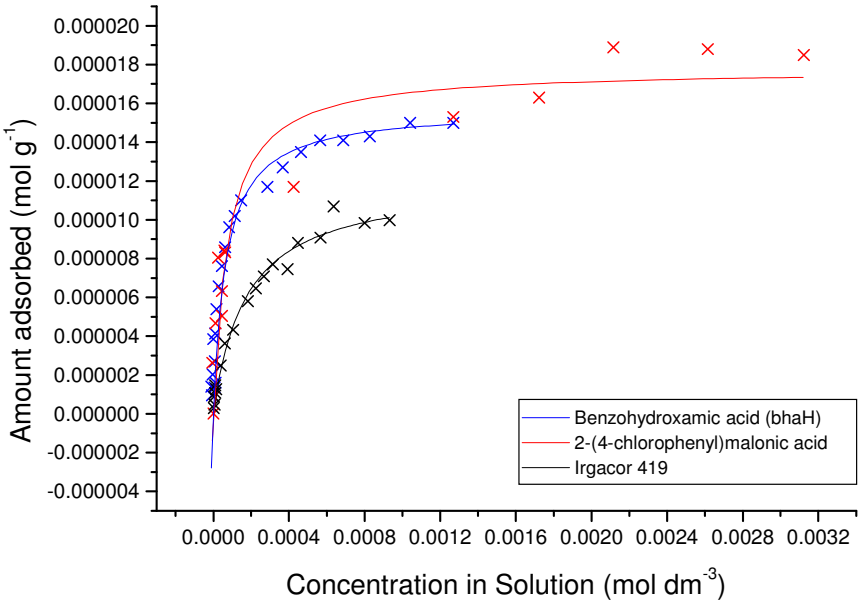

Figure 3-3: Adsorption isotherms for benzohydroxamic acid (blue), 2-(4-chlorophenyl)malonic acid (red) and Irgacor 419, 3-(4-methylbenzoyl)propionic acid (black) onto goethite from methanol/water (95:5) at 25°C

Compound	Equilibrium adsorption constant (K) /10^3	Surface Coverage /10^{-6} mol g^{-1}	Surface area per molecule /$Å^2$ $molecule^{-1}$
Benzohydroxamic acid	15(3)	15.7(9)	238(13)
2-(4-chlorophenyl)malonic acid	13(3)	17.7(10)	210(12)
Irgacor 419®	5.7(8)	11.9(5)	313(13)

Table 3-1: Data extracted from adsorption isotherms for benzohydroxamic acid vs Irgacor 419 and 2-(4-chlorophenyl)malonic acid

The isotherm for benzohydroxamic acid shows stronger surface binding constants than either of the other two compounds and offers greater surface coverage than the commercial surface active compound, Irgacor 419, whilst being comparable to that of the phenylmalonic acid. The adsorption isotherm provides evidence that benzohydroxamic acid is surface active for iron oxides and as such should be capable of forming polynucleating complexes.

3.4. CSD data for hydroxamic acids and their iron(III) complexes

The Cambridge Structural Database was used to determine whether any polynuclear iron hydroxamate complexes had previously been structurally characterised. An initial search for iron complexed to a hydroxamate group produced 48 hits. A recurring structural motif throughout most of these hits is the trishydroxamato arrangement (see Figure 3-1) which was expected to be prevalent as a result of biomimetic studies and the reported stability[1] of such complexes. The 48 structures retrieved included hydroxamate systems in which hydroxamates were linked together, usually involving some form of preorganisation of the hydroxamate groups for ion binding (see Figure 3-4) or including additional functionalities which provide additional sites for metal binding which can lead to more complicated binding arrangements (see Figure 3-5).

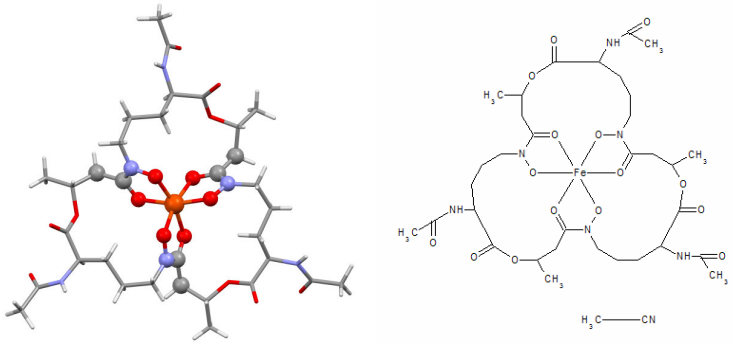

Figure 3-4: The structure of CSD refcode CETWIH showing linked hydroxamate units binding in a tris arrangement with an iron(III) ion.

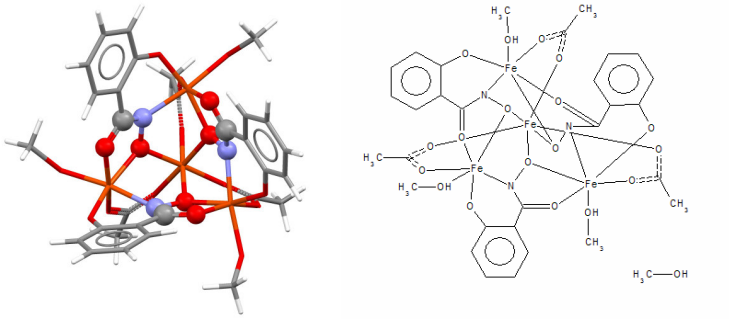

Figure 3-5: The structure of CSD refcode KAXHEW showing the effect of additional functional groups on binding complexity.

In the context of this project the term 'polynucleating' is intended to refer specifically to the minimal hydroxamate unit. We are interested in complexes in which each hydroxamate group interacts with several iron atoms rather than complexes in which several hydroxamate groups each address only one iron atom. Consequently the search was redesigned to exclude hits with preorganised ligands in which there are multiple hydroxamate functionalities on the same ligand backbone, for example the structure shown in Figure 3-4. Also excluded from searches were complexes in which there were additional functionalities in the vicinity of the main hydroxamate group, such as that shown in Figure 3-5, which may have led to more complex binding arrangements.

Considering only simple hydroxamates, according to the rules defined in the previous paragraph, only few remain. The refcodes for these are BURDIB, FEBOAH, FEBOAH01, FEBOAH02, SISSAO, SISSES, SUXREI, VEYFEL, VEYFIP, and WODLEG. The tris-hydroxamato unit is prevalent in these with all but 3 structures, VEYFEL, VEYFIP and WODLEG containing it. WODLEG (see Figure 3-6), involves a single hydroxamate unit per complex which is non-chelating and is the only iron-hydroxamate complex in the CSD to show this behaviour.

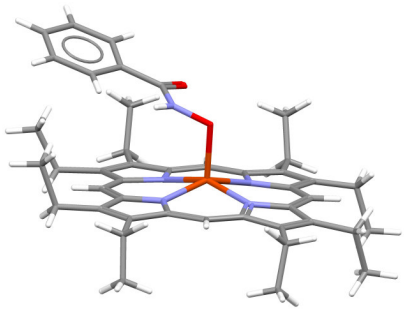

Figure 3-6: The structure of WODLEG, showing a non-chelating bha ligand.

It was also deemed important in modelling attachment to iron(III) atoms in surfaces to consider the structure of bha in other metal complexes. The torsion angle represented in Figure 3-7 reflects the planarity of a delocalised π system. However, there are also competing steric effects to consider which may become important during molecular modelling of these and more complicated systems, such as the N-methyl derivative of bha, discussed later. A search for benzohydroxamic acid with no restriction on the presence of substituents on the phenyl ring produced 25 structures. A similar search was conducted for benzohydroxamic acid and its derivatives chelating a transition metal in mononuclear complexes, in order to observe any differences caused by binding a metal ion. Data for torsion angles in structures containing bha and variants, and equivalent complexes are shown in histogram-form in Figure 3-8.

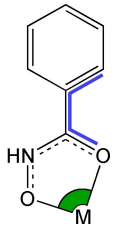

Figure 3-7: A chelating benzohydroxamate, highlighting the torsion angle between the phenyl ring and hydroxamate unit (blue) and the 'bite' angle (green).

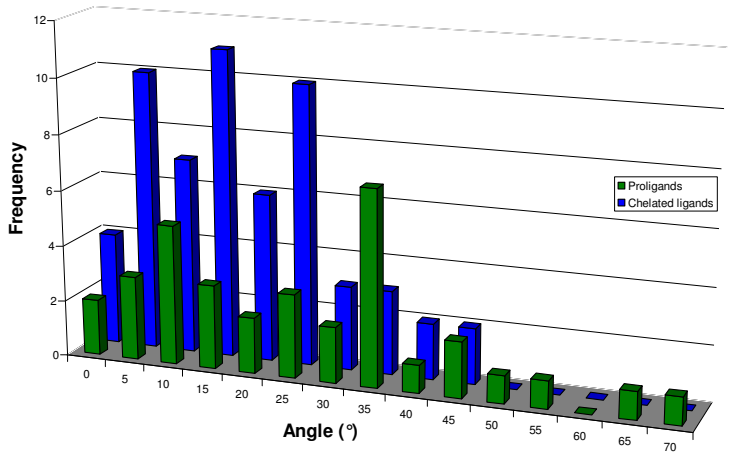

Figure 3-8: Torsion angles in chelating bha ligands, bhaH molecules and derivatives taken from crystal structures in the CSD

It was expected that bha would be planar, however this is not the case. Torsion angles in proligands cover an unexpectedly wide range of values, 0 – 70°, with the majority adopting values between 0 and 45°. Chelated ligands have a smaller range, 0 – 45°, which indicates that there is a significant deviation from planarity for the majority of structures. There appears to be little difference between proligands and chelating ligands given that in both cases the majority of structures have torsion angles of less than 45° although in the case of proligands 4 structures have values greater than this. Also of interest is the "bite" angle found in chelate rings defined as the angle formed at the metal by the bonds it makes with the ligand oxygen atoms and is shown in green in Figure 3-7. The data extracted from 60 structures in the CSD show that angles for hydroxamic acid derivatives complexed with transition metals fall between 72.6° and 86.6°. For iron alone the range is much tighter, falling between 77.7° and 79.6°, and is probably due to the ionic radius of iron. The planarity of the hydroxamate functionality was examined by listing the distances of each constituent atom to the mean plane through them. For each hydroxamate instance the largest deviation from this plane was noted. The mean value was 0.0087 Å which gives an indication of how planar these units are. The

maximum deviation was also relatively small at 0.028 Å. The same method was applied to the chelate ring in each case by including the iron atom which produced a mean of 0.0047 Å and a maximum value of 0.015 Å. The Fe atom however often lies out of the plane of the hydroxamate by up to 0.556 Å, forming a 'hinge' over the two oxygen atoms in the ligand and thus an angle between the plane of the hydroxamate and the FeO_2 plane can be measured. The largest angle observed was 20.94°. Both *mer* and *fac* forms are present in the 7 trishydroxamato iron(III) structures in the CSD with only one isomer present in each structure. The most common is the *fac*-isomer with 6 structures to 1 for the *mer*-isomer.

The CSD yielded no "iron-only" polynuclear hydroxamate complexes which could help to account for the binding of hydroxamates to the surfaces of iron oxides as indicated by the adsorption isotherm data. Consequently, as part of work carried out by Iria Rio attempts were made to prepare polynuclear Fe(III) complexes and to determine their X-ray crystal structures. Obtaining samples of sufficient quality to conduct X-ray diffraction experiments proved quite difficult with only 2 out of 439 proving successful. These are detailed below.

3.5. X-ray crystal structures

3.5.1. The structure of $[Fe(bha)_3]\cdot 1.5MeOH$

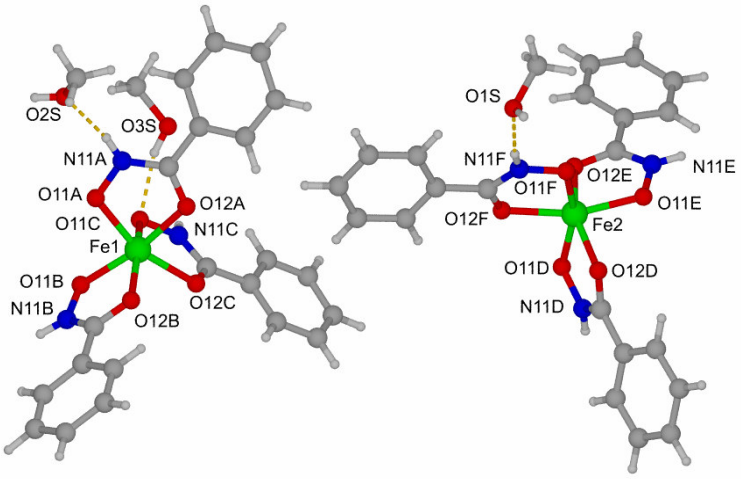

Figure 3-9: Structure of $2Fe(bha)_3.3MeOH$ showing labels for inner coordination sphere atoms and hydrogen bonding interactions with methanol solvate molecules.

The structure of $[Fe(bha)_3]\cdot 1.5MeOH$ contained the expected tris(hydroxamato)iron(III) species with two molecules of $[Fe(bha)_3]$ and three MeOH molecules in the asymmetric unit. The $[Fe(bha)_3]$ unit containing Fe1 (see Figure 3-9) is the *fac*-isomer and that containing Fe2 is the *mer*-isomer. The *mer*-isomer donates and accepts one N-H...O hydrogen bond to a neighbouring *mer*-unit over an inversion centre. Solvate methanol molecules are involved in linking some $[Fe(bha)_3]$ molecules together via hydrogen bonding, although there are some pairs of $[Fe(bha)_3]$ molecules linked directly by N-H...O hydrogen bonds. Hydrogen bond donor acceptor distances are detailed in Table 3-2.

Hydrogen bond	D...A distance /Å	H…A distance /Å	D-H…A angle /°
N11A-H11A...O2S	2.734(2)	1.87(2)	170(2)
O2S-H2S...O11B	2.882(2)	2.10(2)	160(3)
O3S-H3S...O11C	2.728(2)	1.92(2)	164(3)
N11D-H11D...O3S	2.689(2)	1.85(2)	160(2)
O1S-H1S...O11F	2.688(2)	1.88(2)	166(3)
N11F-H11F...O1S	2.756(2)	1.90(2)	164(2)
N11C-H11C...O11A	2.776(2)	1.93(2)	162(2)
N11B-H11B...O11D	2.893(2)	2.07(2)	164(2)
N11E-H11E...O11E	2.732(2)	1.99(2)	146(2)

Table 3-2: Hydrogen bond donor-acceptor distances in the structure of $[Fe(bha)_3]\cdot 1.5MeOH$.

Fac-isomer		*Mer*-isomer	
Parameter	Value	Parameter	Value
Fe1-O11A /Å	1.9965(14)	Fe1-O11D /Å	1.9880(15)
Fe1-O12A /Å	2.0483(16)	Fe1-O12D /Å	2.0235(15)
Fe1-O11B /Å	1.9841(15)	Fe1-O11E /Å	1.9854(15)
Fe1-O12B /Å	2.0118(15)	Fe1-O12E /Å	2.0384(14)
Fe1-O11C /Å	2.0014(16)	Fe1-O11F /Å	1.9987(15)
Fe1-O12C /Å	2.0588(13)	Fe1-O12F /Å	2.0440(14)
O11A-Fe1-O12A /°	78.36(6)	O11D-Fe1-O12D /°	79.32(6)
O11B-Fe1-O12B /°	79.10(6)	O11E-Fe1-O12E /°	78.94(6)
O11C-Fe1-O12C /°	78.45(5)	O11F-Fe1-O12F /°	77.85(6)
Plane A – Plane B /°	77.85(3)	Plane D – Plane E /°	75.44(3)
Plane A – Plane C /°	83.85(4)	Plane D – Plane F /°	71.01(4)
Plane B – Plane C /°	71.81(4)	Plane E – Plane F /°	74.72(4)
C6A-C1A-C10A-O11A /°	21.7(3)	C6D-C1D-C10D-O11D /°	20.4(3)
C6B-C1B-C10B-O11B /°	1.0(3)	C6E-C1E-C10E-O11E /°	17.5(3)
C6C-C1C-C10C-O11C /°	10.2(3)	C6F-C1F-C10F-O11F /°	14.6(3)

Table 3-3: Selected parameters taken from the X-ray crystal structure of 2[Fe(bha)$_3$].3MeOH. The notation "Plane X" where X = A – F refers to the plane of the chelate ring as defined by the appropriate iron atom plus O11, N11, C10, and O12 in ligands A-F respectively (see Figure 3-10)

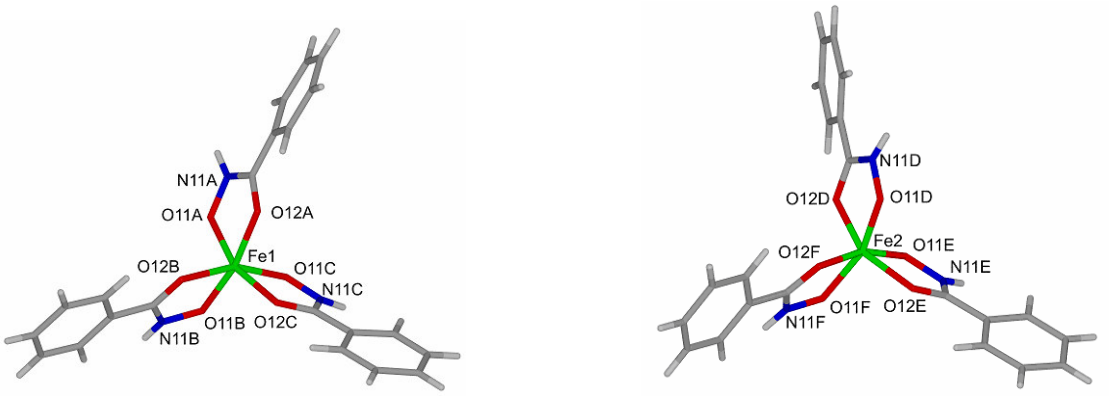

fac *mer*

Figure 3-10: Structures of the *fac*- and *mer*- isomers, showing the atom labelling scheme of the inner coordination sphere

The angle between mean planes through each of the chelate rings would be precisely 90° in an octahedral system. In 2[Fe(bha)$_3$].3MeOH values of 71.01 – 83.85° are observed which indicate that the geometry at the iron atom is distorted octahedral. In the *fac*-isomer the angles are considerably different from one another whereas they are more consistent in the *mer*-isomer. The angles are generally larger in the *fac*-isomer and also the bite angles are slightly larger than in the *mer*-isomer which means the iron geometry is closer to octahedral. Interestingly, the CSD data obtained earlier in section 3.4 indicated that *fac*-complexes were more common for iron which is perhaps related to this observation.

The torsion angles between the carbonyl oxygen, carbon and two carbon atoms from the aromatic ring for each of the ligands are shown in Table 3-3. This angle is of interest because of its potential effect on packing of bha in a surface film. Comparison with the data obtained from the CSD in section 3.4 shows a similar spread of values within this

one crystal structure. This suggests that there is little preference for planarity of this unit over those with minor deviations from planar.

3.5.2. The structure of $[Fe_2(\mu_2\text{-bha})_2(bha)_2Br_2]$

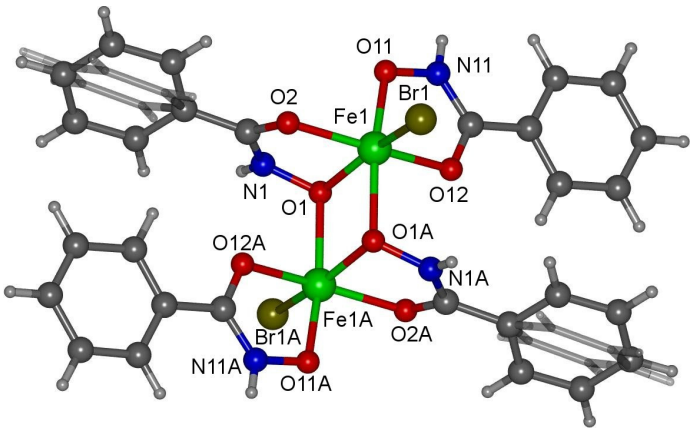

Figure 3-11: Structure of [Fe2(μ2-bha)2(bha)2Br2] as derived by X-ray crystallography. Disordered benzene rings are present and the minor component has been rendered with semi-transparent sticks only.

The structure comprises discrete molecules of $[Fe_2(\mu_2\text{-bha})_2(bha)_2Br_2]$ (shown in Figure 3-11) which lie on inversion centres. Neighbouring molecules form one-dimensional hydrogen bonded chains in the *c* direction with long weak N-H...Br and N-H...O hydrogen bonds which are detailed in Table 3-4.

Hydrogen bond	D...A distance /Å	H…A distance /Å	D-H…A angle /°
N11-H16...Br1	3.3854(17)	2.57(2)	159(2)
N1-H6...O11	2.916(2)	2.41(2)	118(2)
N11-H16...O1	2.981(2)	2.52(2)	114(2)

Table 3-4: Hydrogen bond donor-acceptor distances in the structure of $[Fe_2(\mu_2\text{-bha})_2(bha)_2Br_2]$

The inversion centre is located in the centre of the Fe_2O_2 unit, thus there are two crystallographically independent ligands per molecule. One of these, the dinuclear bridging bha ligand, has a disordered benzene ring which was treated by modelling in two parts, with site occupancy factors of 0.7 and 0.3, each representing one of the possible orientations of the ring. The disorder is indicative of frustration in the position of the benzene ring caused by a steric clash with the benzene ring of the other crystallographically independent hydroxamate ligand. In one component of the disorder, the torsion angle defined by C5-C6-C7-O2 is 20.04° and in the other, C5'-C6-C7-O2, 17.44°. By contrast, in the mononucleating bha ligand the phenyl substituent is nearly co-planar with the chelate ring having a value of 6.94° for the torsion angle C15-C16-C17-O12. Torsion angles close to 0° or 180° (representing planarity) are uncommon for hydroxamates complexes listed in the CSD (Figure 3-8).

The carbonyl oxygen to iron distance formed by the bridging ligand is 2.0150(13) Å whilst the oximic oxygen forms two bonds to each of the iron atoms, one of 2.0872(15) and one of 2.0930(15) Å. It appears that the shared oxygen atom bonds equally strongly to the iron atoms. It is also sp^3 hybridised since it is at the apex of a trigonal pyramid comprised of itself, the two iron atoms, Fe1 and Fe1A and the oximic nitrogen, N1 (Figure 3-11). The angles, Fe1-O1-Fe1A, Fe1-O1-N1 and Fe1A-O1-N1 given in Table 3-5 confirm this. The Fe_2O_2 unit forms a diamond shape with selected parameters given in Table 3-5. The Fe...Fe distance is 3.298 Å and the O...O distance is 2.569 Å. These distances coupled with the Fe-O bond lengths produce angles of 75.83° at the iron atoms, which are slightly more acute than those observed in the CSD for iron(III) complexes, but comfortably within the range seen for all transition metals.

Parameter	Value	Parameter	Value
Fe1-O1 /Å	2.0872(15)	C5-C6-C7-O2 /°	20.0(2)
Fe1-O2 /Å	2.0150(13)	C5'-C6-C7-O2 /°	17.4(2)
Fe1-O11 /Å	1.9554(14)	Fe1-O1-N1 /°	108.58(10)
Fe1-O1A /Å	2.0930(13)	Fe1-O1-Fe1A /°	104.17(6)
Fe1-Br1 /Å	2.4448(4)	Fe1A-O1-N1 /°	114.61(10)
Fe1-O12 /Å	2.0167(13)	Fe1...Fe1A /Å	3.2978(4)
O1-Fe1-O2 /°	76.74(5)	O1...O1A /Å	2.5688(18)
O11-Fe1-O12 /°	79.68(5)	O1-Fe1-O1A /°	75.83(5)
C15-C16-C17-O12 /°	6.9(3)	Fe1-O1-Fe1A /°	104.17(6)

Table 3-5: Distances, angles and torsions found in the crystal structure of $[Fe_2(\mu_2\text{-bha})_2(bha)_2Br_2]$

The mononucleating ligand found in $[Fe_2(\mu_2\text{-bha})_2(bha)_2Br_2]$ has very similar geometry to that found in the structure of $[Fe(bha)_3]\cdot 1.5MeOH$ with a bite angle of 79.68(5)° compared to the range of 77.85 – 79.32°. The dinucleating ligand has a slightly smaller bite angle of 76.74°, which is also below the lowest value observed for structures in the CSD. The Fe-O bond length formed by the bridging ligand, 2.0872(15) Å, is longer than that by the mononucleating ligand, 1.9554(14) Å. The ligands in $[Fe(bha)_3]\cdot 1.5MeOH$ have Fe-O bond lengths of 1.9841 – 2.0014 Å for oximic oxygen atoms. This suggests that binding such oxygen atoms to two Fe atoms weakens the bonding of one in order to accommodate the other.

3.6. Suitability of iron oxide mineral structures for use as a surface in modelling studies

As shown in the previous chapter, the interaction of a ligand with a surface generated from an iron oxide mineral can provide a basis for the rationalisation of the interaction of the ligand with a crude ore in an active froth flotation system, or even steel surfaces, e.g. in car engines, since it is expected that any unprotected metallic surface will become lightly oxidised. This method requires the selection of an appropriate mineral whose crystal structure may then be used as the structural basis for the surface by cleaving the lattice along a desired plane to produce a surface. In chapter 2, choice of the mineral and plane was made based upon the success of previous work[11]. In this chapter the availability of the crystal structure of $[Fe_2(\mu_2\text{-bha})_2(bha)_2Br_2]$ which suggests binding motifs of the type shown in Figure 3-12, which cannot be easily provided by the surface used in chapter 2 (see below).

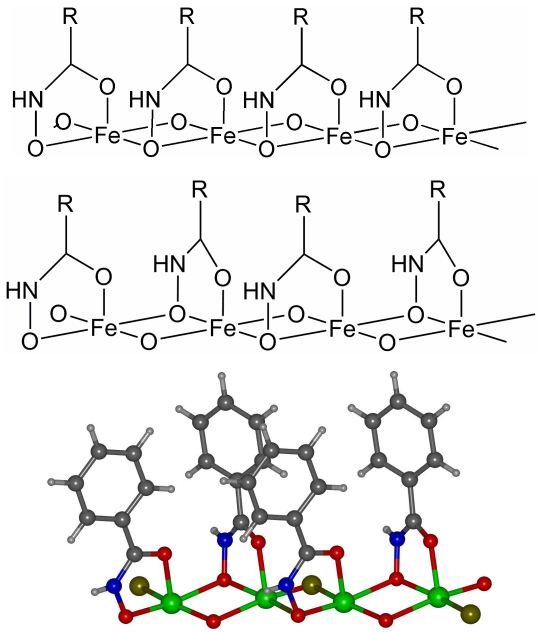

Figure 3-12: Schematic (top and middle) and mock-up (bottom) of potential binding mode for hydroxamates on surfaces derived from crystal structure of $[Fe_2(\mu_2\text{-bha})_2(bha)_2Br_2]$.

The binding motifs shown in Figure 3-12 suggest that the oximic oxygen will displace oxygen from Fe_2O_2 units in the surface resulting in three coordinate bonds with iron(III) atoms in the mineral. Since the structure only provides information for the binding mode of one bridging bha ligand, both of the possibilities given in Figure 3-12 are valid and must be considered. The motif shown in the middle is suggested by the crystal structure since the orientation of the mononucleating bha ligands with respect to the bridging ligands is consistent with this arrangement as shown by the mockup at the bottom of Figure 3-12.

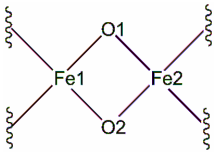

Figure 3-13: Fe_2O_2 labelling for parameters shown in Table 3-1

The Fe_2O_2 units (Figure 3-13) present in $[Fe_2(\mu_2\text{-bha})_2(bha)_2Br_2]$ can also be formed in many iron(III) oxide / iron(III) oxyhydroxide minerals and therefore a comparison of geometries was made. Results are displayed in Table 3-6.

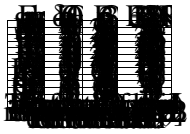

Compound	Goethite[12]	Lepidocrocite[13]	Magnetite[14]
Formula	α-FeO(OH)	γ-FeO(OH)	Fe_3O_4
Space Group	*Pbnm*	$Cmc2_1$	$Fd\bar{3}m$
Fe1...Fe2 /Å	3.0178(1)	3.0600(6)	2.9654(1)
O1...O2 /Å	2.6933(13)	2.7397(5)	2.853(4)
Fe1-O1 /Å	1.9559(6)	1.9763(3)	2.058(3)
Fe1-O2 /Å	2.1062(6)	2.1347(3)	2.058(3)
Fe2-O1 /Å	1.9559(6)	1.9763(3)	2.058(3)
Fe2-O2 /Å	2.1062(6)	2.1347(3)	2.058(3)
Fe1-O1-Fe2 /°	100.97(3)	101.458(3)	92.17(10)
Fe1-O2-Fe2 /°	91.52(3)	91.568(3)	92.17(10)
O1-Fe1-O2 /°	82.97(3)	83.487(3)	87.78(10)
O1-Fe2-O2 /°	82.97(3)	83.487(3)	87.78(10)
r.m.s. /Å	0.148	0.119	0.158

Compound	Ferroxyhyte[15]*	Haematite[16]	$[Fe_2(\mu_2\text{-bha})_2(bha)_2Br_2]$

The Fe_2O_2 unit in lepidocrocite, which was used in the previous chapter, appears to provide the closest geometric match for that in the crystal structure of $[Fe_2(\mu_2\text{-bha})_2(bha)_2Br_2]$. The diamond shape arising from O1-Fe-O2 angles less than 90° appears to be more elongated in the latter than in the mineral structures. This is probably a result of the steric interaction of the benzene rings in the benzohydroxamato complex, evidenced by the presence of disorder. Such an interaction is likely to force the adjacent ligands further apart, distorting the geometry of an ideal Fe_2O_2 unit. In any case, the distance between the iron atoms in lepidocrocite offers the nearest match in this set with a difference of 0.2378 Å. Root mean square fits of the Fe_2O_2 units in the minerals and the crystal structure were performed and the resulting values are given in Table 3-6. These values confirm that lepidocrocite with the lowest value of 0.119 Å is the most appropriate choice of mineral.

Lepidocrocite contains many planes which could be used to provide binding sites for a surface active compound and some criteria must be established in order to make a rational choice for modelling. It is implied through morphology studies that the surfaces of lepidocrocite crystals are dominated by a few key planes,[11] e.g. the (0 2 $\bar{1}$) and the (1 1 0) planes.

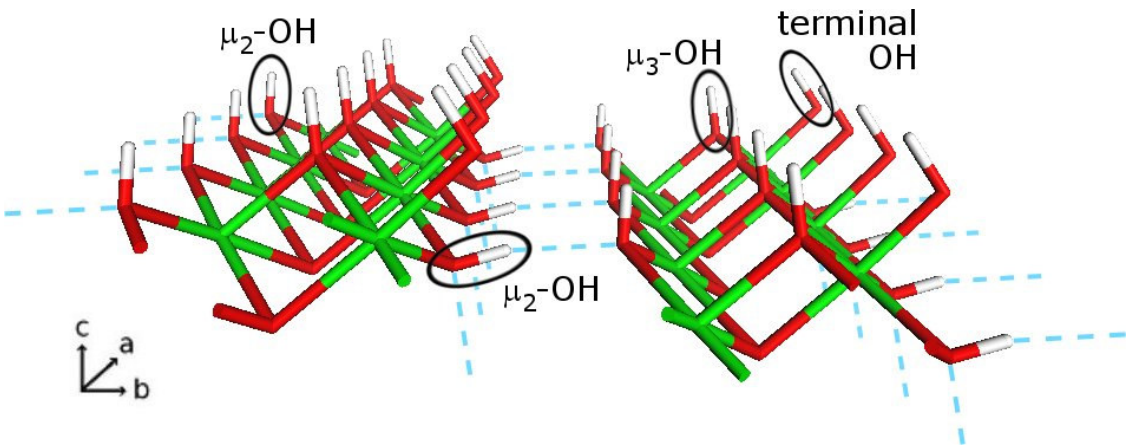

Figure 3-14: The (0 2 1) surface of lepidocrocite with hydroxyl groups relevant to surface binding labelled.

The (0 2 $\bar{1}$) plane (Figure 3-14) was used in the previous chapter to model the activity of malonates on oxidised steel surfaces. For studying hydroxamate binding the crystal structure of $[Fe_2(\mu_2\text{-bha})_2(bha)_2Br_2]$ provides a promising model. The (0 2 $\bar{1}$) plane is not a good choice to study this mode since one of the oxygen atoms in the Fe_2O_2 unit is difficult for the ligand to access and both are indicated to be important. A test calculation was run to confirm the presence of steric issues and a graphic of the model obtained is shown in Figure 3-15. The energy minimisation causes the oximic oxygen to distort from tetrahedral geometry in order to move the NH group away from the surface. The angle made between the O-H vector of surface hydroxyls in similar positions and the plane of the Fe_2O_2 unit is significantly different to that of the O-N vector at 45°. The phenyl ring is also conformationally restricted since it is in very close proximity to the surface also. The bridging ligand in the crystal structure of $[Fe_2(\mu_2\text{-bha})_2(bha)_2Br_2]$ has μ_2 oxygen atoms whilst in the 0 2 $\bar{1}$ surface of lepidocrocite, only μ_3 hydroxyl groups are easily accessible and the more comparable μ_2 hydroxyl groups are hindered.

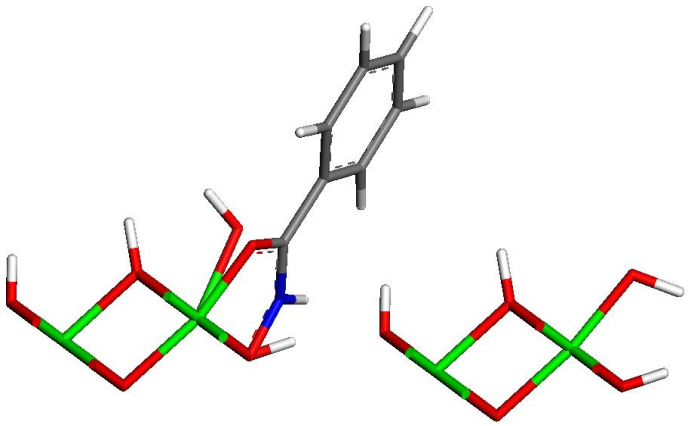

Figure 3-15: Benzohydroxamic acid on the lepidocrocite (0 2 $\bar{1}$) surface after minimisation with UFF.

The (1 1 0) surface of lepidocrocite, shown in Figure 3-16, does not suffer these drawbacks having a Fe_2O_2 unit in which both an iron and two oxygen atoms can be

freely accessed by a ligand and having no issues with steric clash of the ligand with the surface. Modelling studies of benzohydroxamates have therefore used this surface of lepidocrocite in preference to the (0 2 $\bar{1}$) surface.

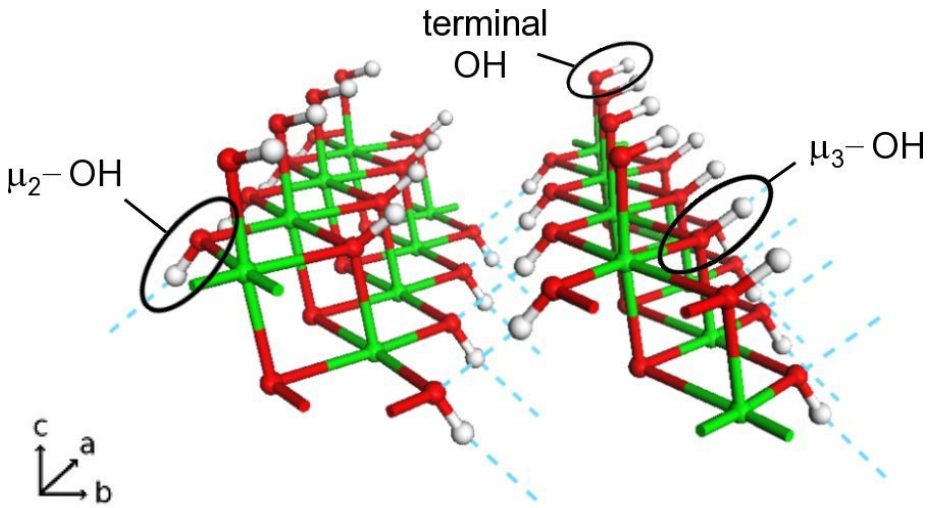

Figure 3-16: Two unit cells in the *a* direction showing the topmost layer of the substrate highlighting the various hydroxyl groups present.

3.7. Discussion of modelling results

The crystal structure of $[Fe_2(\mu_2\text{-bha})_2(bha)_2Br_2]$ provides insight into how an individual hydroxamate might address a surface and also to a lesser extent how multiple hydroxamates might arrange themselves with respect to one another. The lepidocrocite (0 1 0) surface provides the ligand with terminal, μ_2 and μ_3 hydroxyl sites to occupy, shown in Figure 3-16. Which of the hydroxyl sites is preferentially occupied, the packing density and the relative disposition of ligands on the surface were all addressed by constructing models for comparison with one another and the crystal structure of $[Fe_2(\mu_2\text{-bha})_2(bha)_2Br_2]$ described in section 3.2.1.2.

3.7.1. Preliminary modelling

As in the previous chapter, partial atomic charges were required to correctly model non-bonded interactions. A layer approximately 10 Å thick of lepidocrocite was taken from its crystal structure and placed into a 3D periodic box with dimensions a = 6.12, b = 12.5, c = 60 Å, and $\alpha = \beta = \gamma = 90°$. Hydroxyl groups and hydrogen atoms were then added to the surface to neutralise charge. This produced a surface cell of 6.12 x 12.5 Å giving an area of 76.5 Å^2 containing four binding sites. The 3D periodicity allowed for the derivation of partial atomic charges using charge equilibration and the c axis was lengthened to place periodic images in this direction too far apart to interact with each other. Minimisations were done with the UFF[17] on an SGI Octane workstation running Cerius^2.[18]

A preliminary validation of the minimisation method was conducted to ensure geometries obtained were chemically sensible. Firstly a survey of CSD structures was conducted to determine possible and preferred geometries adopted by hydroxamates. Ranges were established containing all observed values for all of the parameters in a benzohydroxamate unit which were broken down into benzohydroxamic acids and esters and benzohydroxamate complexes. These data are presented in Table 3-7. For comparison, a molecule of $[Fe_2(\mu_2\text{-bha})_2(bha)_2Br_2]$ was taken from its crystal structure and minimised in the gas phase using the UFF[17] with partial atomic charges.

Parameter	Hydroxamic Acids and Esters(CSD)	Hydroxamate Complexes (CSD)	Crystal Structure of $[Fe_2(\mu_2\text{-bha})_2(bha)_2Br_2]$	Minimisation of $[Fe_2(\mu_2\text{-bha})_2(bha)_2Br_2]$	
				μ_2-bha	bha
C-Ph Distance /Å	1.472 – 1.516	1.389 – 1.551	1.460(2) - 1.475(3)	1.484	1.484
C=O Distance /Å	1.209 – 1.313	1.191 – 1.320	1.271(2) – 1.273 (2)	1.221	1.218
C-N Distance /Å	1.295 – 1.374	1.248 – 1.381	1.312(3) – 1.317(3)	1.376	1.369
N-O Distance /Å	1.369 – 1.541	1.301 – 1.449	1.364(2) – 1.379 (2)	1.257	1.252
O-N-C Angle /°	116.2 – 134.9	113.5 – 127.3	116.6(2) – 118.5(2)	117.4	118.5
N-C=O Angle /°	120.5 – 133.6	108.3 – 123.1	117.1(2) – 118.4(2)	117.7	118.0
C-C-C-O Torsion /°	1.2 – 70.1	0.6 – 41.6	6.9(3) – 20.0(2)	27.8	32.2
C-C-C-N Torsion /°	1.5 – 72.9	0.8 – 43.5	5.4(3) – 24.3(3)	27.8	33.7
O-N-C-O Torsion /°	0.2 – 14.7	0.0 - 12.9	0.2(3) – 7.0(3)	8.2	0.4

Table 3-7: Ligand parameters extracted from CSD structures presented alongside those from the crystal structure of $[Fe_2(\mu_2\text{-bha})_2(bha)_2Br_2]$ and a preliminary energy minimisation for method validation.

Parameter	$[Fe_2(\mu_2\text{-bha})_2(bha)_2Br_2]$ Crystal Structure	Minimised structure
O_2-Fe /Å	2.015(1)	1.845
O_1-Fe /Å	2.087(1)	1.904
$Fe_1...Fe_2$ /Å	3.298(1)	2.848
$O_1…O_2$ /Å	2.569(2)	2.623
Fe_1-O-Fe_2 /°	104.16(6)	94.73
O_1-Fe-O_1 /°	75.83(6)	85.73

Table 3-8: Selected parameters pertaining to the geometry of iron atoms in the prior to and following geometry optimisation of $[Fe_2(\mu_2\text{-bha})_2(bha)_2Br_2]$.

As can be seen in the table, minimisation produces ligand geometries which fall well within the ranges observed for hydroxamic acid and its esters and complexes in the CSD. This confirms that the method chosen for modelling the system works well for this ligand component. The biggest differences observed between the original and minimised structures are found in the geometry of the iron atoms (see Table 3-8). A large difference of 0.45 Å exists in the distance between the iron atoms. Also oxygen iron bond lengths are reported as shorter than observed and the angles around the binding site are quite different. The parameters given for iron atoms in the UFF are a little too strict in demanding octahedral geometry and so minimisations of the iron oxide substrate used as a surface produce inaccurate models. One solution to this problem could be to customise the force field parameters for this application. However, fine tuning the force field to produce appropriate geometries is non-trivial and not guaranteed to improve the situation for both ligand and substrate. If we assume the iron mineral is a bulk material, it will likely change very little at the surface. The method for modelling to include the surface was upgraded by applying constraints to surface substrate atom positions such that the iron geometry will better reflect that observed experimentally. As a consequence an energy penalty will be incurred, although this will be consistent for all models.

3.7.2. Surface docking procedure

A single molecule of $[Fe_2(\mu_2\text{-bha})_2(bha)_2Br_2]$ was removed from the crystal lattice and placed into a gas-phase environment. A model was then constructed by taking an appropriate fragment of this molecule (shown in Figure 3-17) for overlaying the Fe_2O_2 unit in the surface structure. Docking of the bha molecule was then accomplished by visually orienting the Fe_2O_2 units so that iron atoms in the fragment overlay with those in the surface and the oximato oxygen atom replaces either a μ_2 or μ_3 hydroxyl group (Figure 3-17). The fragment was then trimmed down to leave only the ligand less its

oximic oxygen atom and new bonds were added between the ligand and the surface. Hydroxyl atoms were deprotonated or deleted as necessary to make room for binding and also to preserve charge neutrality. This produces models in which the oximic oxygen atom originally belonged to the surface substrate. This basic method was used to produce all of the models discussed in this section.

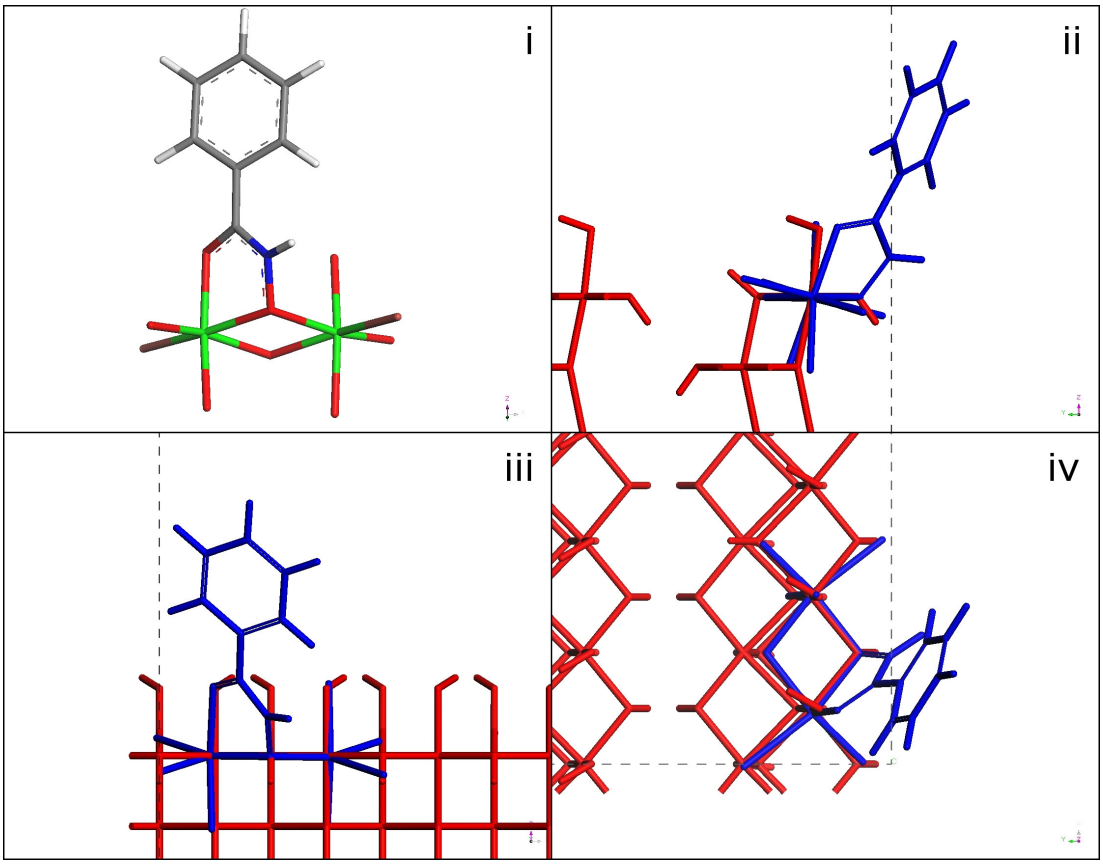

Figure 3-17: (i) The fragment taken from the crystal structure of $[Fe_2(\mu_2\text{-bha})_2(bha)_2Br_2]$ which was used in surface docking procedures. Images illustrating the docking procedure with the fragment in blue and the surface substrate in red looking down the *a*, *b* and *c* directions are shown in ii, iii, and iv.

3.7.3. Hydroxyl site displacement

Addressing which of the hydroxyl sites will be preferentially occupied was done by constructing a simple model of each situation. In these models a 2x1x1 supercell of the unit cell was used to double the length of the *a* dimension so that one ligand per cell allowed the ligand the freedom to optimise its orientation without clashing with other surface bound ligands upon minimisation. The μ_3 and μ_3 substituted models can be seen in Figure 3-18A and B.

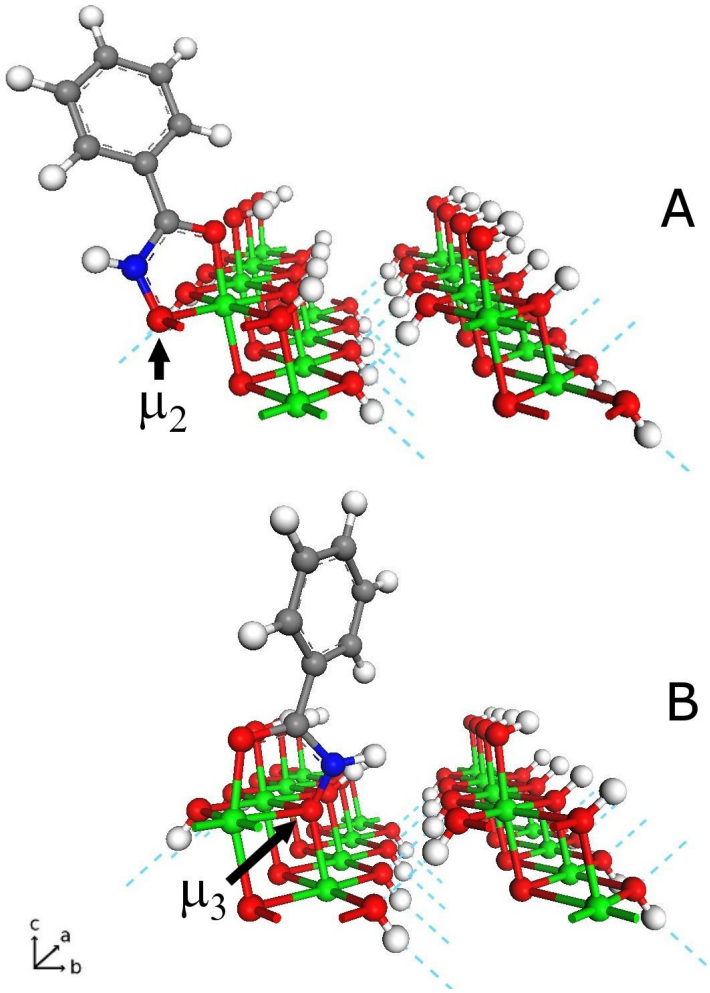

Figure 3-18: The structures produced for μ_2 and μ_3 hydroxyl displacement for one benzohydroxamate ligand on a large surface cell

On first inspection the models (see also Table 3-9) both appear plausible. The geometries of the ligand itself and also the oxygen atoms bound to iron are both reasonable and presumably could occur in real systems. Initial analysis suggested the μ_2 model may be the better of the two since the chelated iron atom geometry is more distorted in the μ_3 case, but for the most part equivalent parameters in both models are very similar. Of the 11 parameters listed, the μ_2 structure matches 7 of those from the crystal structure of $[Fe_2(\mu_2\text{-bha})_2(bha)_2Br_2]$ more closely than the μ_3 structure.

Parameter	$[Fe_2(\mu_2\text{-bha})_2(bha)_2Br_2]$ Crystal Structure	Surface model, μ_2 hydroxyl displacement	Surface model, μ_3 hydroxyl displacement
C-Ph /Å	1.460	1.495	1.480
C-N /Å	1.317	1.367	1.393
$C\text{-}O_1$ /Å	1.271	1.273	1.302
$N\text{-}O_2$ /Å	1.379	1.310	1.288
$O_1\text{-}C\text{-}N$ /°	118.4	117.0	120.6
$C\text{-}N\text{-}O_2$ /°	116.6	117.3	116.5
$N\text{-}O_2\text{-}Fe_1$ /°	108.6	104.8	100.7
$O_1\text{-}Fe_1\text{-}O_2$ /°	76.7	83.9	83.8
$Fe_1\text{-}O_1\text{-}C$ /°	115.1	111.8	109.9
$N\text{-}O_2\text{-}Fe_2$ /°	114.6	112.4	115.5
$Fe_1\text{-}O_2\text{-}Fe_2$ /°	104.2	101.5	91.6

Table 3-9: Comparison of distances and angles found in the crystal structure along with those from energy minimisations of surface models

The biggest difference is seen in the Fe_1-O_2-Fe_2 angle. In the μ_2 structure the value is 101.5° compared to 91.6° in the μ_3 structure which is significantly different from the angle observed in $[Fe_2(\mu_2\text{-bha})_2(bha)_2Br_2]$. It is likely that the bridging oximato oxygen atom would prefer to adopt tetrahedral geometry, i.e. with angles of 109.5°. In the μ_2 case the oxygen atom is bound to three atoms and would be trigonal pyramidal so in an ideal system angles would be expected to be slightly smaller than 109.5° due to the effect of the lone pair repulsion. In the μ_3 case the oxygen atom is bound to four atoms and thus would be expected to be tetrahedral. On inspection the largest deviation from tetrahedral geometry is the 91.6° angle in the μ_3 structure. For the μ_2 structure the average bond angle at the oxygen atom is 106.2° which is closer to the ideal value of 109.5° for a tetrahedron than the μ_3 structure which has an average of 102.6°. However, neither of these deviations from ideal geometry is outwith the range observed in stable structures. The energies associated with the μ_2 and μ_3 structures which have identical unit cell contents are -4816 and -4659 kJ mol^{-1} respectively. This also indicates that the μ_2 structure is the better choice and modelling proceeded with this in mind.

3.7.4. Packing density

The packing density of benzohydroxamates on the surface is a very pertinent question and can help to explain experimental observations. Since benzohydroxamates contain phenyl rings, the possibility of π-π stacking exists. The possibility of hydrogen bonding also exists with the N-H group potentially acting as a donor and the oxygen atoms as acceptors. The surface provides donor and acceptor sites in the form of hydroxyl groups, which are shown in Figure 3-16.

For simplicity the packing density was split into two components, the densities in the *a* and *b* directions. Two models were constructed to test the ability to accommodate molecules in the *a* direction. Firstly, based on the previous conclusions that μ_2 binding

is preferred, ligands were added to all available sites in the *a* direction. This resulted in a model containing two ligands per surface cell which was then geometry optimised by energy minimisation. Results are presented in Figure 3-19.

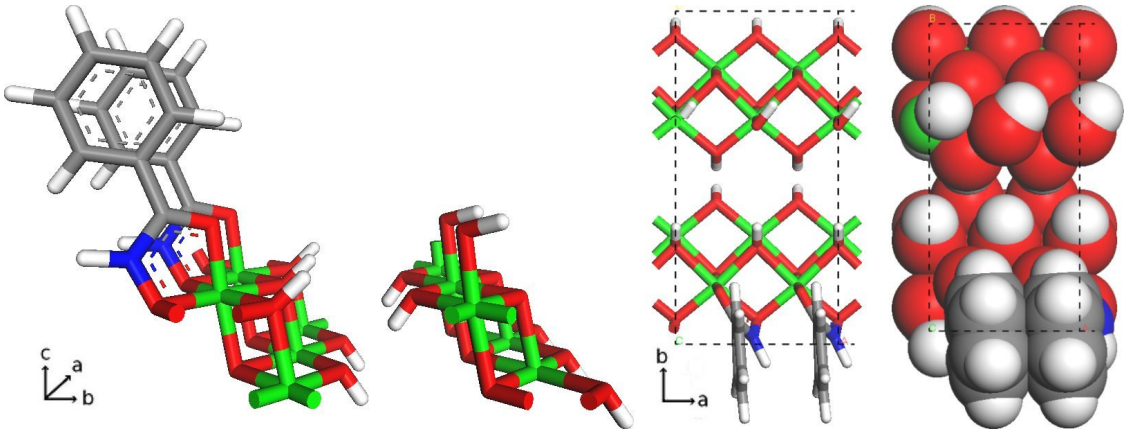

Figure 3-19: The model devised to test density in the *a* direction containing 2 μ_2-mode ligands. Perspective view along *a* (left), the view down *c* (middle) and a space filling plot also down *c*.

The orientation of the phenyl rings in this model is unusual given their close proximity. Normally π-π stacking interactions involve an offset. Offset distances and stacking distances for π-π interactions were taken from the CSD were plotted against each other in Figure 3-20. The red square in the figure shows where the interaction for this model would appear. It is obvious from space filling plots that the rings are too close to one another as no other structures found in the CSD have stacking distances close to this without a significant offset.

Next, the case where two adjacent μ_3-docked molecules in the *a* direction was modelled. The same problem with almost identical stacking features existed as in the μ_2–model and so was discarded. For brevity this model is not shown here but is included in electronic appendices.

The final possibility for maximum stacking in the *a* direction is one μ_2 and one μ_3 molecule. This relates closely to the motif found in the $[Fe_2(\mu_2\text{-bha})_2(bha)_2Br_2]$ crystal structure. Figure 3-21 shows the model produced for this arrangement. Again the arrangement of the phenyl rings gives cause for concern. The relative position of one to the other shows that π-π stacking is not possible, yet very short contacts between the rings exist. Space-filling plots show that the ligands are too close to one another and bend away from one another.

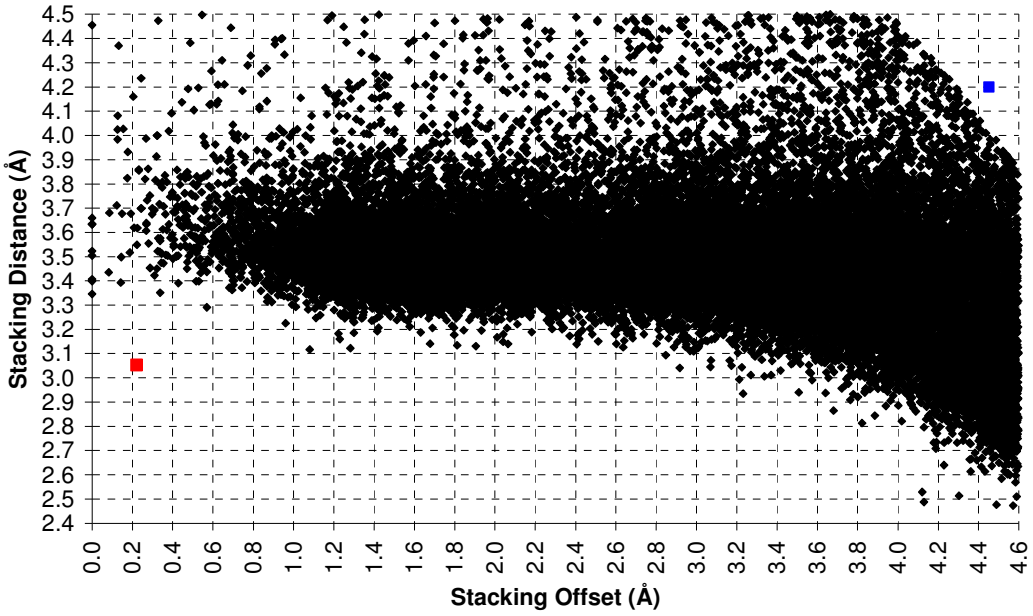

Figure 3-20: π-π stacking distances plotted against their offsets for structures found in the CSD. The red square show the data point for the model shown in Figure 3-19 and the blue square that of the model shown in Figure 3-22.

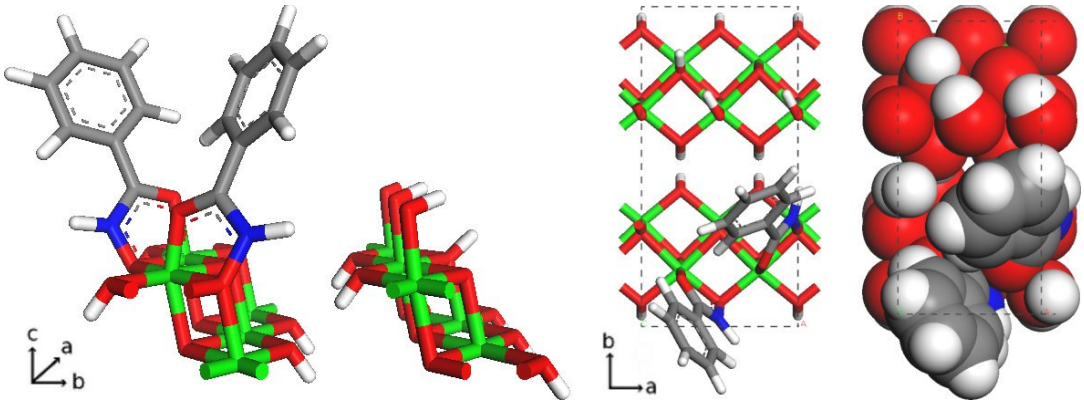

Figure 3-21: The model resulting from minimisation of a model containing one μ_2 and one μ_3 mode ligand in the *a* direction. Perspective view along *a* (left), the view down *c* (middle) and a space-filling plot also down *c*.

The conclusion drawn from these three models is that ligands cannot occupy all available binding sites in the *a* direction. Consequently, packing density in this direction was tested at a level of one ligand per surface cell. Figure 3-22 shows the much more favourable situation for one μ_2 molecule bound to the surface in the *a* direction. There are no indications of excessive strain between adjacent ligands with the π-π stacking distance of 4.199 with an offset of 4.452 Å. These values are rather large to be classed as a π-π interaction; this interaction is marked as a blue square in Figure 3-20. The ligand geometry falls within the expected ranges discussed previously. As the μ_2 mode has been shown to be preferred over the μ_3 mode, the equivalent model for μ_3 binding will not be discussed here but is included in the electronic appendices.

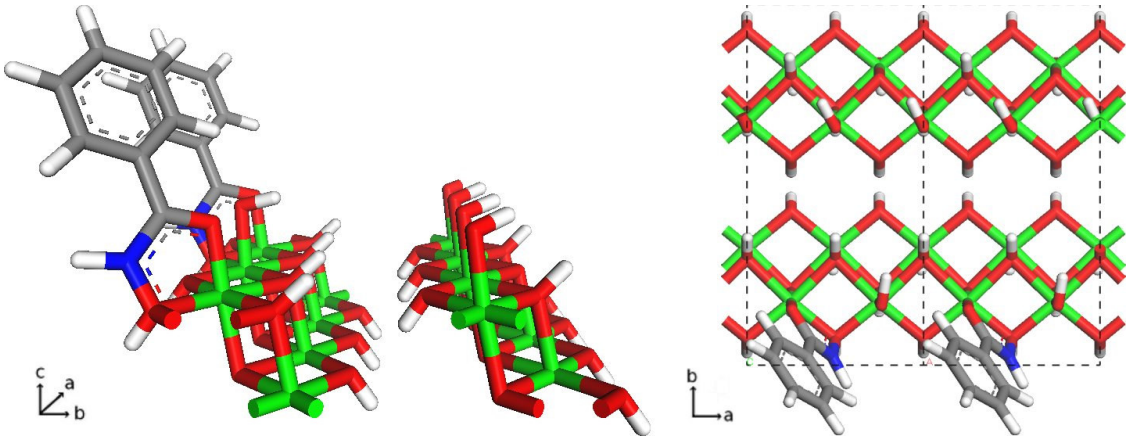

Figure 3-22: Model showing a density level of one μ_2 ligand per unit cell in the *a* direction. Perspective view along the *a* axis is shown on the left and the view down the *c* axis is shown on the right.

Determining the packing density in the *b* direction is less problematic. With the prior knowledge that there can only be one ligand for every two binding sites in the *a* direction and given that all of the binding sites in the surface cell are chemically identical in the *a* direction, the unit cell can only contain either one or two molecules. The model presented in Figure 3-23 shows that two molecules bound to μ_2 sites can be easily accommodated by the surface cell.

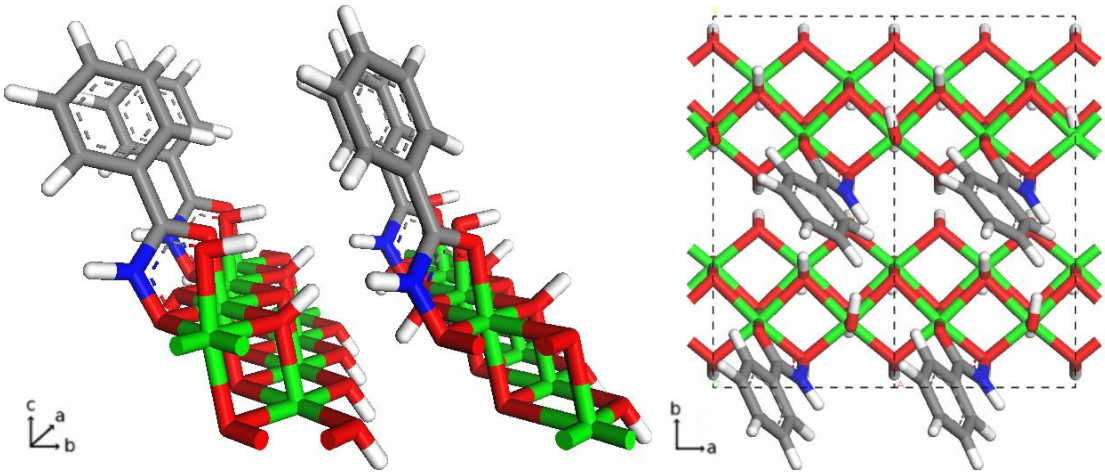

Figure 3-23: A model showing two ligands bound in a μ_2 arrangement. A perpective view along the *a* axis shown on the left, and the view down the *c* axis on the right.

Although further modelling is required to determine the relationship between the two molecules in the surface cell, at this stage it is possible to calculate the surface area per molecule predicted by this model and is 38.25 $Å^2$. The value obtained from experimental results (see section 3.3) was 238(13) $Å^2$. Clearly the predicted value is significantly smaller. Similar differences were found in previous modelling projects[19] and also in the previous chapter. A plausible explanation for these differences is that the models contain infinite, ideal 2D surfaces in which considerably more binding sites are present than in real systems which involve imperfect heterogeneous surfaces. This means that the density of binding sites on the surface is likely to be considerably lower in a real system than for the ideal surface in the model resulting in an overall smaller number of binding sites, and lower observed surface coverage.

3.7.5. Relative orientations of adjacent molecules.

The arrangement of the two molecules in the unit cell with respect to one another was explored. If one molecule is assumed to bind to the preferred μ_2 site, this may have

implications for the binding of the other molecule. The second ligand may chelate either of the two available iron atoms on the next row along in the *b* direction, one of which lies offset from the position of the first bound ligand and one which lies inline. The ligand may bind to a μ_2 or a μ_3 site and it may also bind parallel to the first bound ligand or at an angle. The combination of these two possibilities gives eight arrangements. Energy minimisations were conducted on each of these cases, three of which were considerably lower in energy than the others and these are shown in Figure 3-25. For the three lowest energy models, parameters were extracted for comparison with the CSD data discussed earlier (section 3.7.1) and are presented alongside the energies in Table 3-10.

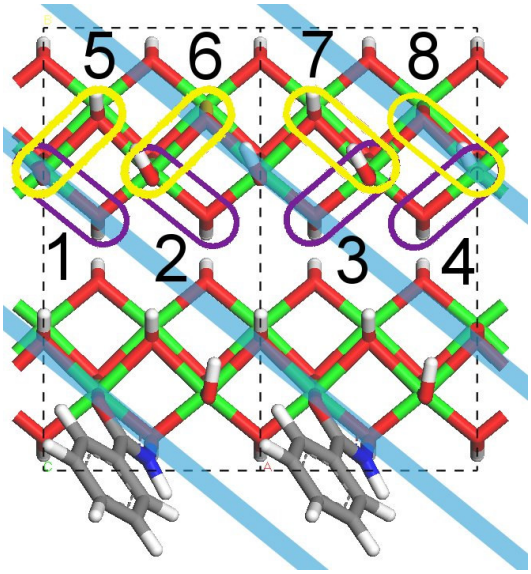

Figure 3-24: Two unit cells containing a benzohydroxamate bound to the lepidocrocite (0 1 0) surface. Numbered are the possibilities for binding locations of a second molecule relative to the first. In purple are μ_2 sites and in yellow, μ_3 sites. Sites in which the iron atom lies on a blue line (1, 4, 5 and 8) are denoted as "inline" sites and those in between (2, 3, 6 and 7) are denoted "offset." Sites parallel or angled with respect to the blue line are labelled "parallel" and "angled" respectively. Lowest energy modes discussed later are denoted 1, 2 and 3.

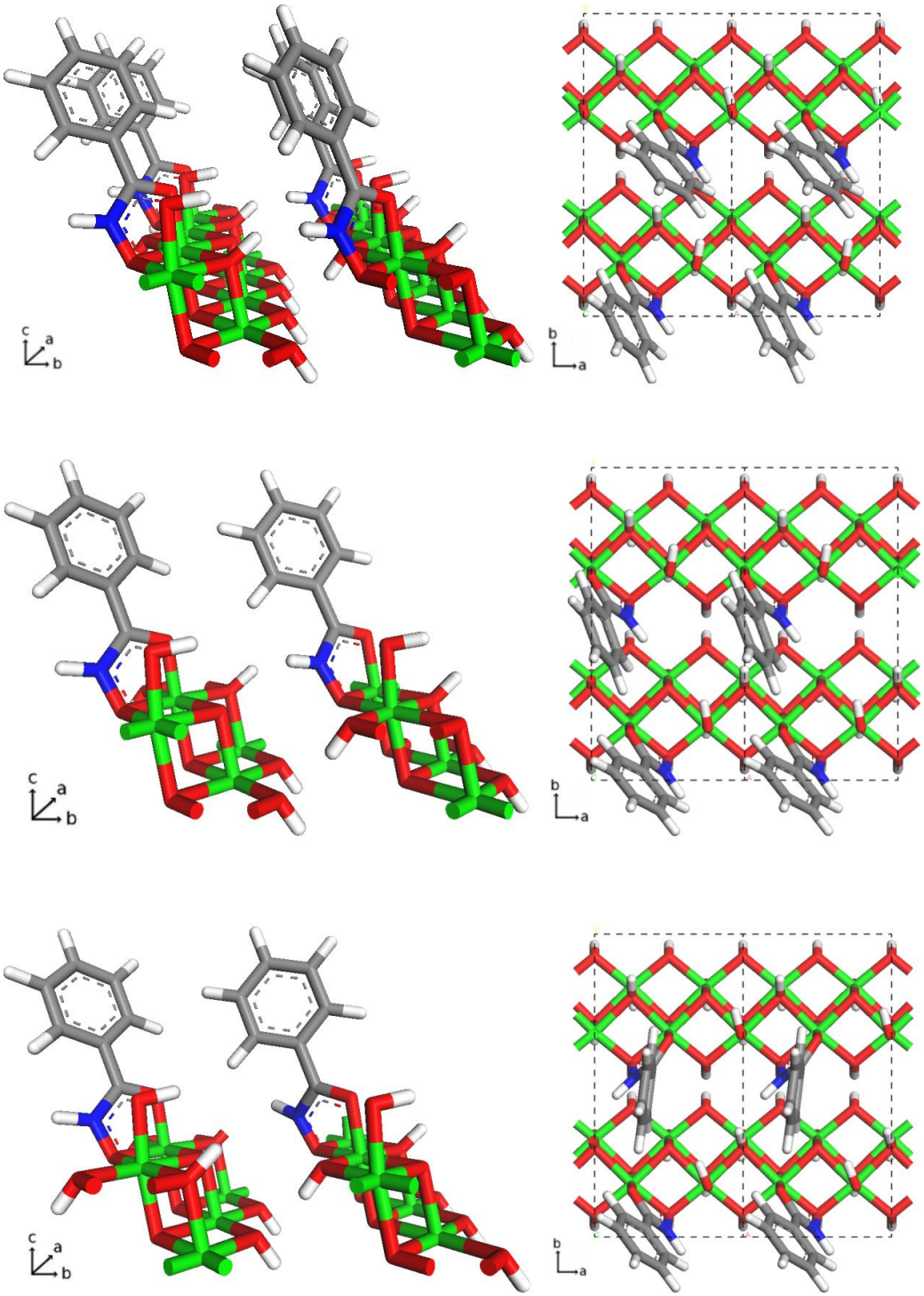

Figure 3-25: The three lowest energy models obtained for hydroxamic acid binding. Top - the 'offset/parallel' model, middle - the 'inline/parallel' model, and bottom - the 'offset/angled' model.

Parameter	CSD	Offset/parallel-$\mu_2\mu_2$		Inline/parallel-$\mu_2\mu_2$		Offset/angled-$\mu_2\mu_2$	
C-Ph Distance /Å	1.389 – 1.551	1.487	1.495	1.494	1.487	1.485	1.490
C=O Distance /Å	1.191 – 1.320	1.264	1.272	1.272	1.265	1.268	1.267
C-N Distance /Å	1.248 – 1.381	1.367	1.365	1.364	1.366	1.354	1.365
N-O Distance /Å	1.301 – 1.541	1.312	1.309	1.307	1.311	1.306	1.310
O-N-C Angle /°	113.530 – 134.874	117.00	117.24	117.23	116.97	118.09	117.05
N-C=O Angle /°	108.347 – 133.640	117.39	117.23	117.29	117.43	117.83	117.40
C-C-C-O Torsion /°	0.628 – 70.117	10.84	1.31	10.04	11.07	36.01	7.46
C-C-C-N Torsion /°	0.847 – 72.9	10.75	4.86	13.78	10.96	34.55	7.39
O-N-C-O Torsion /°	0.020 – 14.739	7.13	4.02	4.83	6.96	8.46	7.68
Energy /kJ mol^{-1}		-1279.8		-1274.5		-1264.4	

Table 3-10: Geometric parameters extracted from the three candidate models (shown in Figure 3-25) alongside the energies calculated for each.

All three of the structures have two μ_2 ligands in them. The next nearest structure was for the $\mu_2\mu_3$ 'offset' structure which had a calculated energy of -893.2 kJ mol^{-1}. This observation serves as further evidence that the hydroxamate prefers to occupy μ_2 sites on the surface. The structures presented in Figure 3-25 and Table 3-10 all produced ligand geometries which fall well within the ranges observed in the CSD and relative to one another, so there are no obvious differences which might enable us to rank them. The energies are also very similar for all three although their ordering reflects that expected based upon crowding i.e. in the lowest energy structure (the offset/parallel $\mu_2\mu_2$ model) each ligand appears to have more room.

The $\mu_2\mu_2$ family, having two ligands per unit cell, is very plausible. It is of considerable interest to ascertain which of the variants in Figure 3-25 provides the best explanation of experimental data. It was concluded that the "offset/parallel" $\mu_2\mu_2$ model (top of Figure 3-25) is the most plausible.

3.7.6. Testing the offset/parallel $\mu_2\mu_2$ model.

The final model chosen on the basis of the analysis in previous sections is presented in Figure 3-26. The binding mode is based upon the crystal structure of [$Fe_2(\mu_2$-bha)$_2$(bha)$_2Br_2$] presented in section 3.5.2. The displacement of a μ_2 hydroxyl was found to produce structures with geometries more similar to [$Fe_2(\mu_2$-bha)$_2$(bha)$_2Br_2$] and also slightly lower in energy. For the unit cell used, it was found that binding two hydroxamates produced the best results. In order to evaluate this model several variants of benzohydroxamic acid were synthesised and tested by Iria Rio, based on the modelling reported in this thesis.

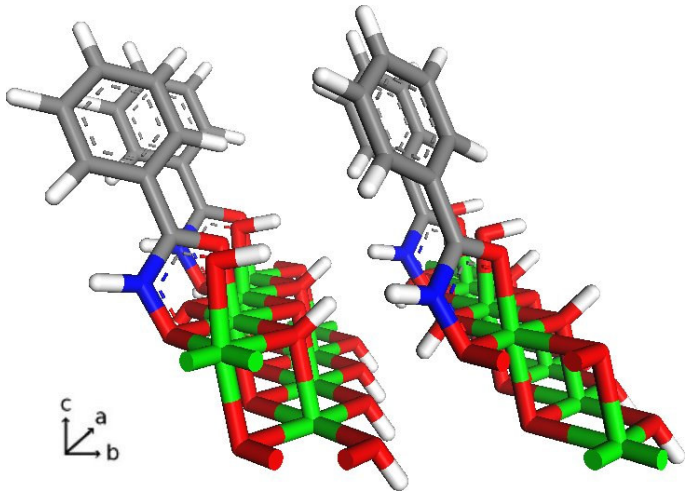

Figure 3-26: The offset/parallel $\mu_2\mu_2$ model looking down the a axis

The role of the oximic oxygen is very important since it embeds itself in the surface by displacing surface hydroxyls. This indicates that it is small enough that it may move into and occupy this position and also that deprotonation of the oxygen atom occurs. Testing these observations can be achieved by increasing the size of the embedding functionality and making it very difficult to produce the anion. Replacement of the O-H with an O-Me group would achieve both of these goals, Figure 3-28 shows the O-Me

ligand in blue and how this replacement makes accommodation of the oximic oxygen difficult. The surface activity of this compound was therefore expected to be significantly lower than benzohydroxamic acid.

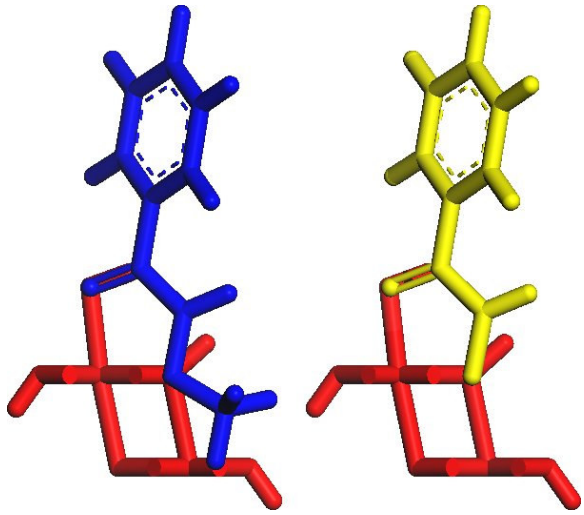

Figure 3-27: A superposition of an O-Me derivative of benzoydroxamic acid (blue) and hydroxamic acid (yellow) onto the surface substrate (red). The OMe group can be seen to interfere with other atoms comprising the surface whereas the benzohydroxamate does not.

Other modifications intended to increase the bulk of the ligand should theoretically decrease its surface coverage. In principle increasing the bulk of substituents on the benzene ring or the nitrogen atom of benzohydroxamic acid should not greatly affect the binding mode of individual hydroxamates, only their interactions with one another. In the benzohydroxamate molecule the N-H group is quite small and steric interactions with the phenyl ring are minimal given planar geometries frequently observed in CSD data. Also the $\mu_2\mu_2$ models do not indicate that the N-H group participates in strong hydrogen bonds to other ligands. Replacement of the N-H group with an N-Me group was expected to increase bulk in two ways. Firstly the steric clash with the phenyl ring will cause a twist making the molecule less planar and thus more bulky and secondly the

Me group occupies space between adjacent ligands increasing the steric clash between them. This substitution also removes hydrogen bonding capacity, but since the model shows these interactions are not important, this should not significantly affect binding strength. Figure 3-28 shows N-Me ligand in green and the expected increases in steric clash. The predicted effect of this substitution is therefore reduced surface coverage but similar binding strength.

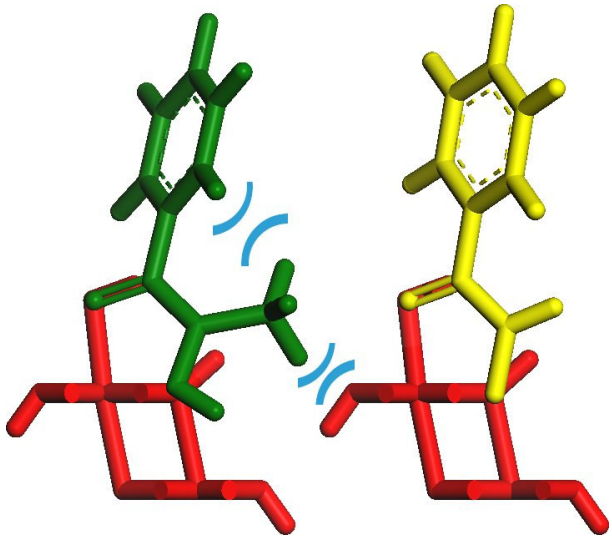

Figure 3-28: A superposition of an N-Me derivative of benzohydroxamic acid (green) and benzohydroxamate (yellow) onto the surface substrate (red). The increased bulk of the N-Me ligand extends towards the next molecule along interfering with the surface. The N-Me group also forces the benzene group to twist away more so than in the benzohydroxamate, increasing the overall bulk of the molecule.

The models developed in sections 3.7.3 to 3.7.5 also indicate that the phenyl ring does not participate in π-π stacking interactions. Experiments to test this hypothesis were devised. The phenyl ring was replaced with a methyl group for testing in adsorption isotherm experiments. This meant that determining the adsorption isotherm by tracking the intensity of the UV band as was done for all other compounds was not possible and so a competitive binding experiment was performed in which benzohydroxamic acid and

methylhydroxamic acid were tested in the presence of a ligand known to bind strongly to iron oxide surfaces, 2-(benzo[d]thiazol-2-ylthio)malonic acid (see Figure 3-29). The presence of the sulfur atoms in the latter makes it easy to determine concentrations in solution using ICP-OES. The molecule which suppresses the isotherm of the positive control to a greater extent can be inferred to be the more surface active ligand. Since the phenyl ring is not expected to have a significant impact on adsorption character, both ligands were expected to produce similar adsorption isotherms.

Synthesis and adsorption isotherm experiments were carried out by Iria Rio[7] and the adsorption isotherms are presented in Figure 3-30 and Figure 3-31. The ligands used to test the binding of O-Me and N-Me derivatives also incorporated sulfur atom substituents to enable analysis by ICP-OES as above.

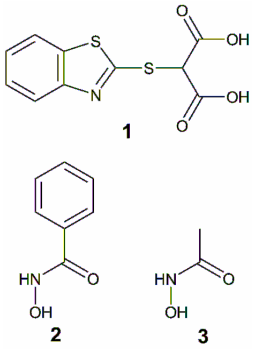

Figure 3-29: Ligands used in competitve binding adsorption isotherm experiments. 2-(benzo[d]thiazol-2-ylthio)malonic acid (1) used as a control in the presence of benzohydroxamic acid (2) and methylhydroxamic acid (3).

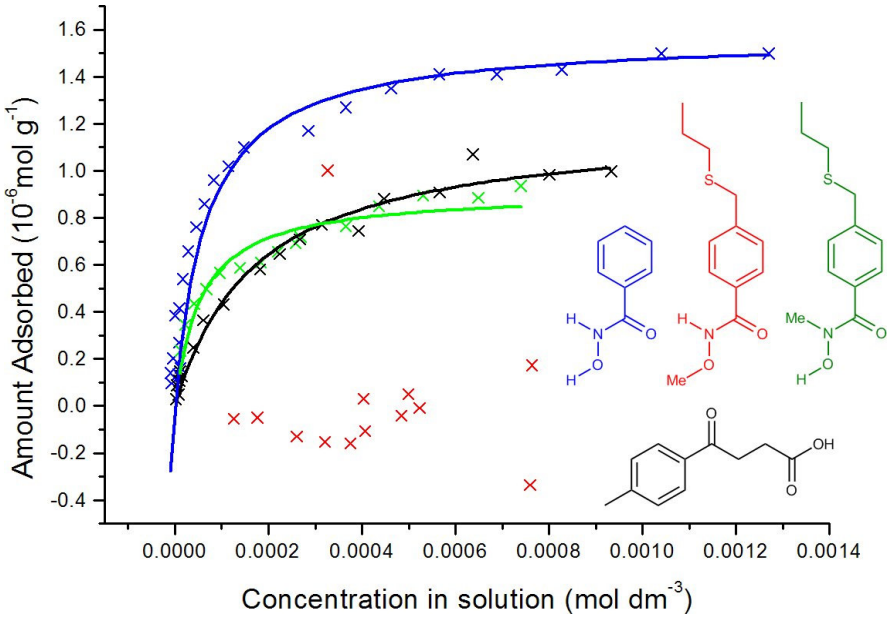

Figure 3-30: Adsorption isotherms of selected ligands from MeOH/H_2O solutions onto powdered goethite determined under identical conditions.[7] Benzohydroxamic acid data is shown in blue and its derivatives O-Me (red) and N-Me (green) derivatives presented against the control, Irgacor 419® (black).

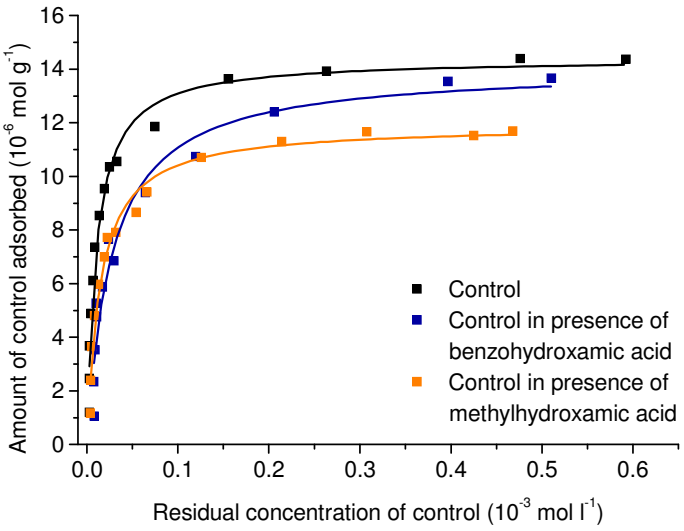

Figure 3-31: Adsorption isotherms of a control, 2-(benzo[d]thiazol-2-ylthio)malonic acid, showing the competitive binding experiment of benzohydroxamic acid and methylhydroxamic acid relative to the control onto goethite in 95% MeOH/H_2O.

As can be seen in the adsorption isotherms, the predictions for the activity of each of these modified benzohydroxamates have been borne out in the experimental work. The O-Me variant does not appear to bind to the surface at all which provides corroborating evidence for the importance and nature of the oximic oxygen shown in the binding model in Figure 3-26. The N-Me variant similarly behaved as predicted in the experimental work, the surface coverage being reduced to around half that observed for the N-H benzohydroxamate.

The competitive binding experiment showed that the phenyl ring only has a small effect on the surface binding of hydroxamates. In the presence of methylhydroxamic acid the surface coverage of the control is lower than in the presence of benzohydramic acid. However, in both cases only a minimal suppression of the control is observed. This result indicated that the phenyl ring is unlikely to participate in π-π stacking as the addition of interactions would be expected to improve the cohesion of the surface film and thus enhance the affinity of the ligand for the surface. The experiment showed that in fact the methyl variant has a higher affinity for the surface and therefore the phenyl ring is detrimental to the performance of hydroxamates as surface actives for iron oxides. This is most probably a consequence of the increased bulk.

3.8. Friction testing of a greasy benzohydroxamate derivative.

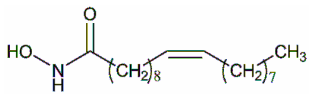

Figure 3-32: N-hydroxy-9(Z)-octadecenamide (oleylhydroxamic acid)

For evaluation as a friction modifier in engine lubricants, it was necessary to modify the solubility and friction-reducing character of benzohydroxamic acid. In order to achieve

this, N-hydroxy-9(Z)-octadecenamide, which is a hydroxamate head group with an oleyl chain attached, was synthesised by Dr Jy Chartres (see section 3.2.2). Friction-reducing performance as a function of temperature was tested on an HFRR (see Chapter 1) at Infineum by Dr Steve Harris. Two control samples were used and the compositions are presented in Table 3-11. The results were graphed and are presented in Figure 3-33.

Components	Ref oil 1	Ref oil 2	Oleylhydroxamic acid solution
Dispersant	3.00%	3.00%	3.00%
FM1	0.15%	0.30%	0.15%
FM2	0.15%	0.00%	0.00%
Oleylhydroxamic	0.00%	0.00%	0.15%
Base oil	96.70%	96.70%	96.70%

Table 3-11: HFRR sample compositions. FM1 and FM2 are are known friction modifiers (chemistry was not provided).

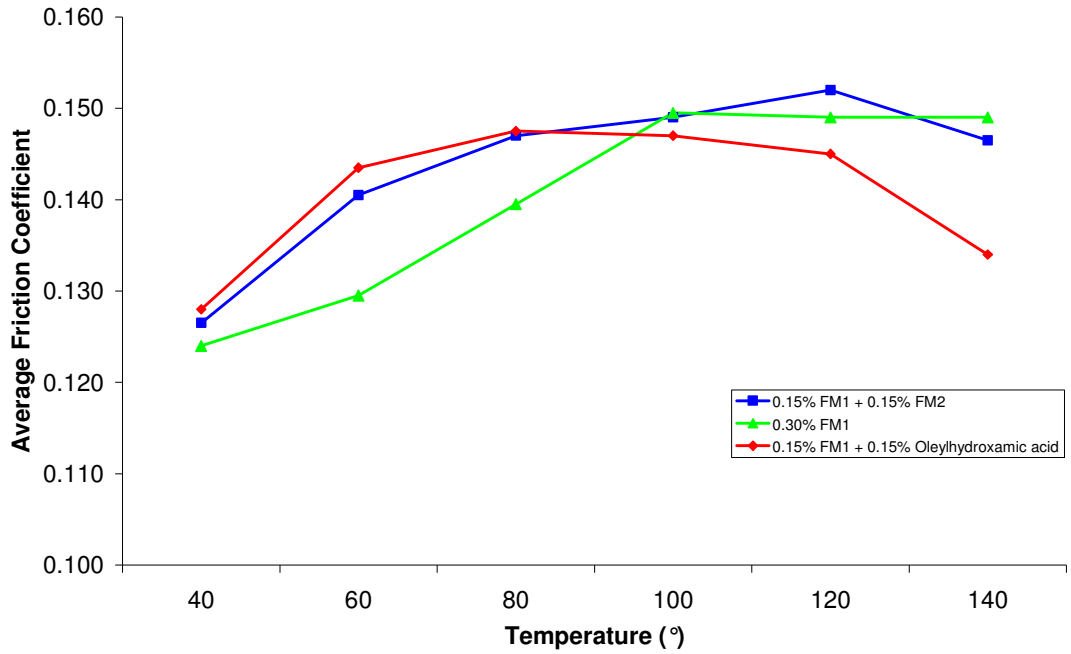

Figure 3-33: HFRR test results for oleylhydroxamic acid.

There is a slight improvement in the performance of the formulation containing oleylhydroxamic acid at the highest temperatures. One of the factors which may have influenced the effectiveness of oleylhydroxamic acid in reducing friction is its solubility. During preparations for tests it was noted that its solubility in base oil was low, so a co-surfactant marked as "dispersant" in Table 3-11 was used to aid dissolution. This was also added to reference oils. It is likely that in using a co-surfactant for dissolution the co-surfactant protects the hydrophilic polar functionality of the hydroxamate by hydrogen bonding to it producing hydrophobic dimers or micelles. Even with the addition of this agent only a small quantity of the hydroxamic acid appeared to dissolve. The marked increase of ~10% in performance in friction reduction at higher temperatures could be due to dissolution or breaking up hydrogen bonded dimers or micelles leading to film formation. The low quantity of ligand and the co-surfactant, used to aid dissolution, will both have reduced the potency of the hydroxamic acid as a friction modifier. The solubility of the compound was quite low in the base oil and the co-surfactant may be preventing deposition of sufficient quantities of hydroxamate onto the surface due to strong hydrogen bonding making it difficult to form a film except at high temperatures.

3.9. Conclusions

The use of X-ray crystal structures to elucidate the binding modes of ligands can be a very useful tool. In this chapter a crystal structure provided a starting point for the modelling of the binding mode of benzohydroxamic acids to iron oxy hydroxides. Using this crystal structure several surface models were derived and using energy minimisation molecular orientations and packing densities on the surface were studied. Several plausible models resulted and these were examined in the context of surface interactions and calculated energies. This allowed a final model to be determined

allowing a surface coverage to be calculated. The final model produced was very plausible and can explain the experimental observations presented at the outset of the chapter. Not only does the model show that hydroxamates can bind to iron oxide surfaces, it also predicts higher surface coverage than carboxylates, which is experimentally observed. The higher number of coordinate bonds to the surface predicts that the hydroxamate is expected to bind more strongly to the surface, also experimentally observed.

The model was used to make observations as to the effect of various changes to the molecule. The initial isotherms were obtained using benzohydroxamic acid, but the model derived by molecular modelling indicated that the phenyl ring was important to the binding strength and would only slightly affect surface coverage in comparison to methylhydroxamic acid. This observation was tested and ultimately confirmed using a competitive binding experiment.

The model showed that the role of the oximic oxygen atom and its ability to deprotonate were predicted to be central to the performance of the molecule as a surface ligand for iron oxide surfaces. This prediction was tested by measuring the isotherm of the OMe variant which showed no surface activity, confirming the hypothesis.
Finally the oximic nitrogen atom and its proton were expected not to be essential to binding and not to take part in strong hydrogen bonding and that only its bulk was important. To test this, an N-Me derivative was synthesised and its isotherm measured which confirmed its role as non-essential and indicated that the increased bulk reduced surface coverage.

Finally this project involved the study of hydroxamates as potential friction modifiers so a greasy derivative of benzohydroxamic acid, oleylhydroxamic acid, was synthesised and tested as a potential friction modifier on an HFRR. Despite undeniable strong surface activity in adsorption isotherm experiments, definitive results showing

enhancement of friction reducing character of base oils were not obtained from this testing although improvements in friction reduction over controls were noted. This may have been because of its solubility in the base oil or problems introduced by the use of co-surfactants used to aid dissolution.

Overall, the modelling in this chapter was very successful, providing a rationalisation of experimental observation and aiding in the screening of molecules for use in commercial applications.

3.10. References

1. R. J. Bergeron, J. Wiegand, J. S. McManis, W. R. Weimar and G. Huang, in *Advances in Experimental Medicine and Biology*, CRC, boca Raton, Editon edn., 2002, vol. 509, pp. 167-184.
2. K. J. Wallace, M. Gray, Z. Zhong, V. M. Lynch and E. V. Anslyn, *Dalton Trans.*, 2005, 2436-2441.
3. W. R. Harris, C. J. Carrano, S. R. Cooper, S. R. Sofen, A. E. Avdeef, J. V. McArdle and K. N. Raymond, *J. Am. Chem. Soc.*, 1979, **101**, 6097-6104.
4. M. Gaspar, R. Grazina, A. Bodor, E. Farkas and M. A. Santos, *Dalton Trans.*, 1999, 799-806.
5. C. J. Marmion, D. Griffith and K. B. Nolan, *Eur. J. Inorg. Chem.*, 2004, 3003-3016.
6. CytecIndustries, *Mining Chemicals Handbook*, Cytec Industries Inc., New Jersey, 2002.
7. I. M. R. Echevarría, *PhD Thesis*, 2007.
8. G. M. Sheldrick, Bruker-AXS, Madison, WIsconsin, USA, Editon edn., 2004.
9. G. M. Sheldrick, University of Gottingen, Germany and Bruker-AXS, Gottingen, Germany and Madison, Wisconsin, USA, Editon edn., 2001.
10. J. E. Patterson, I. R. Ollmann, B. F. Cravatt, D. L. Boger, C. H. Wong and R. A. Lerner, *J. Am. Chem. Soc.*, 1996, **118**, 5938-5945.
11. S. G. H. Harris, *PhD Thesis*, 1999.
12. H. Yang, L. Ren, R. T. Downs and G. Costin, *Acta. Cryst. E*, 2006, **62**, 250-252.
13. H. Christensen and A. N. Christensen, *Acta. Chem. Scand. Ser. A*, 1978, **32**, 87-88.
14. H. Fjellvag, F. Gronvold and S. S. B. C. Hauback, *J. Solid State Chem.*, 1996, **124**, 52-57.
15. G. Patrat, F. deBergevin, M. Pernet and J. C. Joubert, *Acta. Cryst* 1983, **B39**, 165-170.
16. S. C. Yu, J. S. Lee, S. F. Tung and C. L. Lan, *J. Geo. Soc. China*, 1999, **42**, 349-358.
17. A. K. Rappe, C. J. Casewit, K. S. Colwell, W. A. Goddard-III and W. M. Skiff, *J. Am. Chem. Soc*, 1992, **114**, 10024-10035.
18. Accelrys Inc., Accelrys Inc.,, San Diego, California, USA, Editon edn., 2000.
19. M. Frey, S. G. Harris, J. M. Holmes, D. A. Nation, S. Parsons, P. A. Tasker and R. E. Winpenny, *Chemistry - A European Journal*, 2000, **6**, 1407-1415.

Chapter 4

Crystallographic Studies of Phenolic Oxime Solvent Extraction Agents

Contents

4. Introduction

This chapter investigates the X-ray crystal structures of ligands which are intended to function as metal extractants in hydrometallurgical processes. A series of functionalised salicylaldoxime ligands synthesised by Dr Ross Forgan[1] were designed to function either as metal-*salt* extractants, transporting both a metal cation and its attendant anion (see sections 4.5.3 and 4.5.4), or as metal-only extractants, transporting metal cations (see sections 4.5.1 and 4.5.2). The effects of systematic substitution of these ligands at the 3 position, see Figure 4-1, is described in this chapter, together with the effect of axial interactions at the metal atom on the 'hole-size' in complexes.

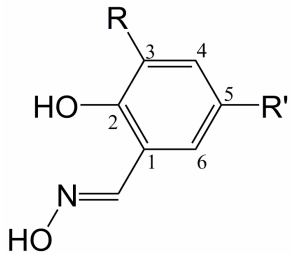

Figure 4-1: The salicylaldoxime ligand used as the basis for ligands used in complexes in this chapter.

4.1. Copper

As one of the first metals to be used, copper has played a central role in the advancement of the human race. Its availability in a metallic form on the surface of the earth meant it was readily available to be used for tools, weapons and other artefacts dating from as early as 10,000 years ago have been recovered.[2, 3] Around 4000 B.C. pyrometallurgical processes were discovered which enabled the production of copper from ores, such as $CuFeS_2$, chalcopyrite, and thus increased its availability. Copper has many properties which are useful technologically. It is

malleable, ductile, corrosion resistant, has high electrical conductivity and good thermal dissipation. Alloying copper with tin gives a hardier, more durable material, bronze, which, during the Bronze Age from 3000 - 500 B.C., allowed the production of more effective tools and weapons. Largely due to its malleability, early uses included weapons, tools, coinage, and ornaments and jewellery during various civilisations in human history such as the Babylonians,[4] ancient Egyptians,[5] Romans,[5] and the Song Dynasty of China.[6]

Figure 4-2: A selection of recovered copper and copper alloy artefacts. A: A late bronze age spearhead dating from the 12th century B.C.[7] B: A copper mirror with wooden handle from the Egyptian Middle Kingdom (circa. 2000-1500 B.C.).[5] C: Roman copper coinage from the reign of Caligula (circa 37-38 A.D.).[5] D: A decorated bronze mirror from the Song dynasty of China (circa. 926-1121 A.D.).[6]

Since the industrial revolution copper production has seen a marked increase.[8] In the modern world copper has found additional applications chiefly in the plumbing, electrical, and the electronics industries. The construction industry is responsible for 40% of all copper use, such that the average family home contains about 200 kg of copper.[9] Copper is also used as a heat sink material for many applications[10] and in fungicides,[11] catalysts,[12] and superconductors.[13] The ever expanding uses of copper

have seen demand outweigh supply in recent years. In 2007, 15 million tonnes of copper were produced worldwide whilst 17 million tonnes were consumed.[14] Consequently over the last year (2008) the price of copper peaked at approximately £5025 per tonne which is over five times more than its price 5 years ago at around £900 per tonne.[15] This trend is on average expected to continue as more high tech electronics are produced, homes built and new uses found. The high prices in recent times have even led to increased theft of copper with wiring from train signalling equipment having been stolen causing delays. Theft of copper from other infrastructure and construction sites is estimated to cost the economy £360 million a year.[16] As demand continues to grow, it is essential to increase the efficiency of copper extraction processes.

4.2. Pyrometallurgy

Metals such as copper generally exist in the Earth's crust in an oxidised form such as cuprite, mixed oxide/sulfide ("transition") ores or as sulfides e.g. chalcopyrite. The recovery from a thermodynamically stable ore involves four steps:[3] *concentration* of the metals of value; *separation* from other metals in the ore; *reduction* to the metallic form; and finally *refinement* to achieve high purity.[17] In a modern pyrometallurgy process, the concentration and separation steps are achieved via froth flotation of the ore. The crude ore is crushed and milled to produce fine powdered ore which is then wetted with water. Collectors or froth flotation agents are added and the mixture, called the 'pulp,' is fed into the first cell in a froth flotation battery. The collectors have polar head groups which bind to the polar ore particles and hydrophobic tail groups which impart hydrophobicity to the ore. The mixture is vigorously stirred and aerated causing the ore to float to the top of the cell in an oil based froth. The froth is run off from the top of the cell and collected whilst the remaining aqueous pulp is fed into the next cell along, where it is stirred and aerated further so that as much of the high value content of the ore mixture is removed from the pulp as possible. The remaining pulp contains silicaceous gangues which have no value and their disposal presents environmental problems.

For copper recovery the concentrated sulfide ore obtained by froth flotation is put through a two-stage high temperature smelting process at 1300 °C.[18] This involves heating of the concentrate with sand and air in a blast furnace producing Cu_2S as a liquid matte which is denser than the silicaceous iron slag, Fe_2SiO_4 generated from pyrite, FeS, or the iron component of ores such as chalcopyrite, $CuFeS_2$. Sulfur dioxide is also produced in the process which is vented from the top of the "flash furnace." The liquid Cu_2S matte is transferred to a "convection furnace" and then heated under controlled conditions to oxidise the sulfur to SO_2 as in:

$$Cu_2S + 2O_2 \rightarrow 2Cu + SO_2$$

The reduction of Cu^I to Cu^0 by dioxygen in the process is driven by the very thermodynamically favourable free energy of formation of SO_2.[19] The copper produced is impure, containing ~2% impurities such as gold and silver, and is known as blister copper. Refinement of the blister copper is achieved by electrolysis by casting it into electrodes which are used as the anodes in cells containing $CuSO_4$ as the electrolyte and aluminium cathodes onto which pure copper is deposited. The high value metal and other impurities from the anode fall to the bottom of the cell and this "anode slime" is collected for processing and recovery.[3]

Whilst pyrometallurgy is still the main process for copper extraction, in order to be profitable it has to be done on a very large scale requiring large centralised facilities[20] to which concentrates must be transported. Solid waste products, slags, are generated at locations remote from the mine sites. SO_2 is also produced during pyrometallurgy, most of which must be recovered as H_2SO_4 which may be sold as a commercial product. From an environmental perspective, recovery of base metals by pyrometallurgy is causing concern because it produces large quantities of materials of no commercial value and consumes large quantities of energy, in ore processing and transportation.

4.3. Hydrometallurgy

Hydrometallurgy can be more environmentally friendly than pyrometallurgy. In the case of copper it involves the use of aqueous chemistry to recover the metal from oxidic ores and is now responsible for ca. 25 % of the world's copper production.[21] For copper oxides the process involves acid *leaching* of metal ions into solution, *separation* of the desired metal from other metals, principally iron, by solvent extraction, *stripping* back into an aqueous phase and recovery of the copper from solution by *electrowinning*.[20, 22] A flowchart of this process is shown in Figure 4-3.

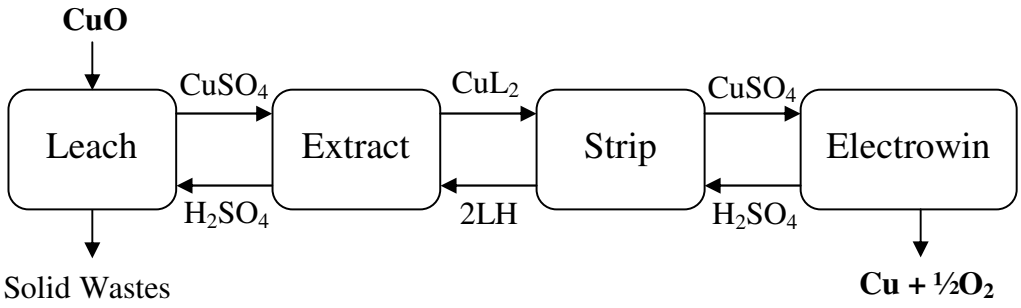

Leach: $CuO_{(s)} + H_2SO_4 \rightarrow CuSO_4 + H_2O$

Extract: $CuSO_4 + 2LH_{(org)} \rightarrow [CuL_2]_{(org)} + H_2SO_4$

Strip: $[CuL_2]_{(org)} + H_2SO_4 \rightarrow CuSO_4 + 2LH_{(org)}$

Electrowin: $CuSO_4 + H_2O \rightarrow Cu_{(s)} + ½O_2 + H_2SO_4$

Overall: $CuO_{(s)} \rightarrow Cu_{(s)} + ½O_2$

Figure 4-3: Recovery of copper from oxide ores using the heap leach / solvent extraction / electrowinning circuit.

Leaching is the simple process of dissolving the copper (and other metals) from the ore by treating it with sulfuric acid, H_2SO_4, forming $CuSO_4$ in aqueous solution. Extraction involves contacting with a kerosene solution of an acidic organic ligands, LH, which forms a charge-neutral kerosene-soluble complex, $[CuL_2]$, regenerating

H_2SO_4 which is recycled to the leaching step. The ligands which transfer the metal ions to the organic phase in such processes are designed to be selective, transporting only the desired metal across the phase boundary. Uptake or release of the metal ion by the ligand is a pH-controlled process and is referred to as a "pH swing" process. The complex $[CuL_2]$ in the organic phase is separated from the aqueous phase which contains the unwanted metals. The loaded organic phase is treated with aqueous H_2SO_4 which regenerates the ligand and produces $CuSO_4$ ("Strip" in Figure 4-3). The ligand is reused in the solvent extraction step and metallic copper is recovered from the aqueous $CuSO_4$ solution by electrolysis, collecting the copper metal at the cathode. The "Electrowinning" step (Figure 4-3) regenerates H_2SO_4 which is needed in the stripping step. One major advantage of this process is that the copper obtained is conductivity grade and requires no further refining as is the case in pyrometallurgical recovery.

The overall process has an excellent materials balance as all reagents are recycled and very few unwanted by-products are generated after leaching. The nature of hydrometallurgy allows it to be conducted on relatively small scale so low cost facilities can be placed close to the mine reducing transport costs whilst producing very few pollutants. Solid residues can also be disposed of in old mine workings.

4.3.1. Phenolic oximes extractants

Key considerations for choice of ligands used in solvent extraction processes are that the ligands should: be selective for a specific metal ion allowing *separation* and *refinement* of the chosen metal by extraction; show a high affinity for the metal ion, i.e. be strongly binding; load or deposit the metal under control, e.g. pH control; and form hydrophobic complexes to facilitate the extraction into organic media. Ligands commonly used in copper recovery are illustrated in Figure 4-4. These all have a large alkyl substituent para to the phenolic group to ensure that both the extractant and its copper(II) complexes have a high solubility in kerosene, and are very insoluble in water to ensure that the reagent is not lost from the system. The

presence of nonyl or dodecyl groups (usually mixed isomers) in the commercial reagents prevent crystallisation and make the preparation and characterisation of complexes difficult. Consequently in laboratory work in Edinburgh, and in this thesis, ligands have been used with a tertiary butyl group or a hydrogen atom in this site. All the ligands studied in this chapter are salicylaldehyde derivatives (related to the commercial reagent P50 in Figure 4-4 where R' = H. The aromatic ring numbering for salicylaldoxime is also shown in Figure 4-4. The influence of 3-substition on the strength and selectivity is of considerable interest (see below).

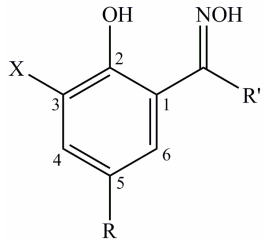

R	R'	X	Commercial Name
C_9H_{19}	H	H	P50
C_9H_{19}	$C_6H_5CH_2$	H	P17
C_9H_{19}	CH_3	H	LIX84
$C_{12}H_{25}$	C_6H_5	H	LIX64
C_9H_{19}	C_6H_5	H	HS-LIX 65N
C_9H_{19}	C_6H_5	Cl	LIX70
$C_{12}H_{25}$	H	H	LIX860

Figure 4-4: Structures of some phenolic oxime solvent extraction agents used commercially[22-26]

The extractants shown in Figure 4-4 bind to copper via the oximic nitrogen and deprotonated phenolic oxygen atoms. The complexes formed are 2:1 ligand to metal complexes in which the copper atom generally adopts square planar geometry.

In the free ligands there is strong intermolecular hydrogen bonding between the oxime hydrogen atom and the phenolic oxygen atom in non-polar solvents. Depending on the substitution of the phenyl ring this can lead to the formation of dimers or linear polymers as shown in Figure 4-5. The *pseudo* macrocyclic structure of the ligand dimer (bottom in Figure 4-5) is preserved in the copper(II) complexes, and the size of the cavity in the dimer is thought to be a good fit for Cu^{II} ions ensuring that this family of ligands bind strongly and selectively.

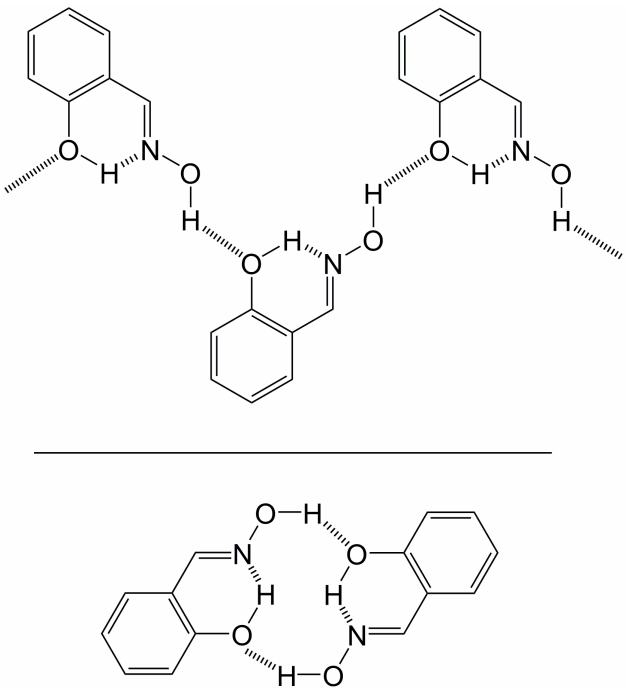

Figure 4-5: Linear hydrogen bonded polymers formed by salicylaldoxime ligands (top) and hydrogen bonded dimers (bottom).

One of the themes dealt with in this chapter is the effect of substitution of these ligands at the 3-position with electronegative groups, such as NO_2, which are intended to provide additional hydrogen bond acceptors to strengthen or "buttress" the hydrogen bonding between ligands. Alternatively substitution with bulky ligands would shield the oximic oxygen and thus perturb the existing hydrogen bonding pattern. The effects of 3-substitution on the dimerisation of salicylaldoximes have been investigated using PIXEL calculations based on coordinates taken from the X-ray crystal structures.[1, 27, 28] These calculations give a detailed breakdown of the intermolecular interaction energies. Strong correlations were observed between extraction strength, which is determined using pH loading curves shown in Figure 4-6, and cavity sizes.[29] Work in this chapter aimed to establish a similar link between complex cavity sizes in copper complexes and extractant strength. The situation is, however, more complicated than initially envisaged as there are electronic effects to consider as well as buttressing and additional intermolecular contacts in the solid state. These effects are discussed in sections 4.5.1 and 4.5.2.

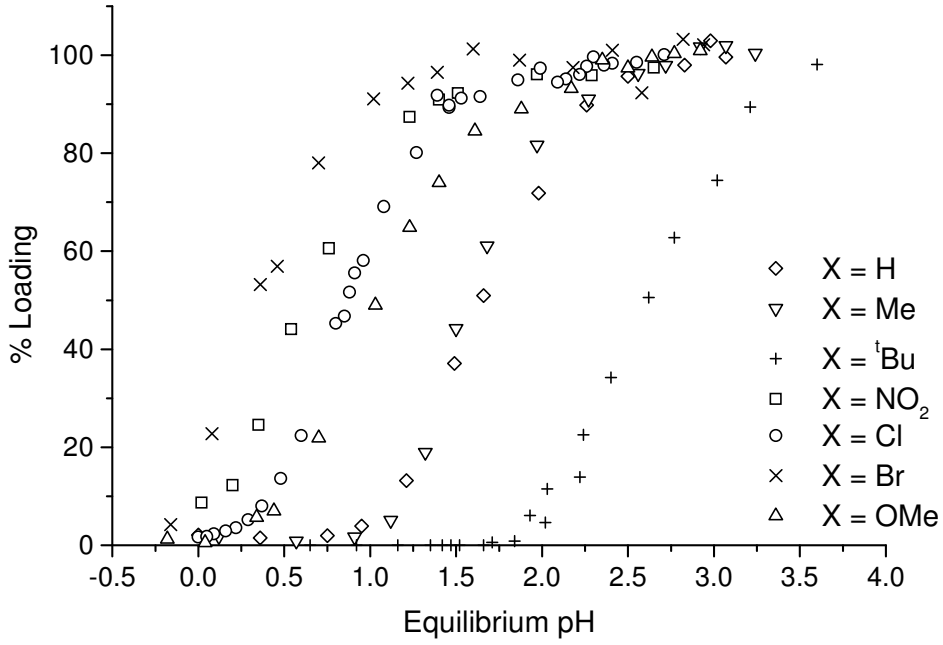

Figure 4-6: Copper loading curves for phenolic oxime ligands with X substitutions.

4.3.2. Metal-salt extractants

The excellent materials balances for the recovery of copper from oxidic ores (Figure 4-7) depend on the leaching process using sulfuric acid which is regenerated in the solvent extraction step.

Leach:	$CuO_{(s)} + H_2SO_4$	$\rightarrow CuSO_4 + H_2O$
Extract:	$CuSO_4 + 2LH_{(org)}$	$\rightarrow [CuL_2]_{(org)} + H_2SO_4$
Strip:	$[CuL_2]_{(org)} + H_2SO_4$	$\rightarrow CuSO_4 + 2LH_{(org)}$
Electrowin:	$CuSO_4 + H_2O$	$\rightarrow Cu_{(s)} + ½O_2 + H_2SO_4$
Overall:	$CuO_{(s)}$	$\rightarrow Cu_{(s)} + ½O_2$

Figure 4-7: Equations pertaining to hydrometallurgical recovery of copper from oxide ores

This cannot be applied to the more commonly occurring types of copper ores which are sulfides such as chalcopyrite $CuFeS_2$. Usually if a sulfidic ore is used in oxidative leaching, little or no sulfuric acid is consumed in leaching and recovery by a conventional pH swing reagent generates one mole of H_2SO_4 for every mole of copper extracted (see Figure 4-8). The acid produced must then be recovered or neutralised and the resulting salt recovered, all of which incur additional expense and reduce the economic viability of the process.[30, 31]

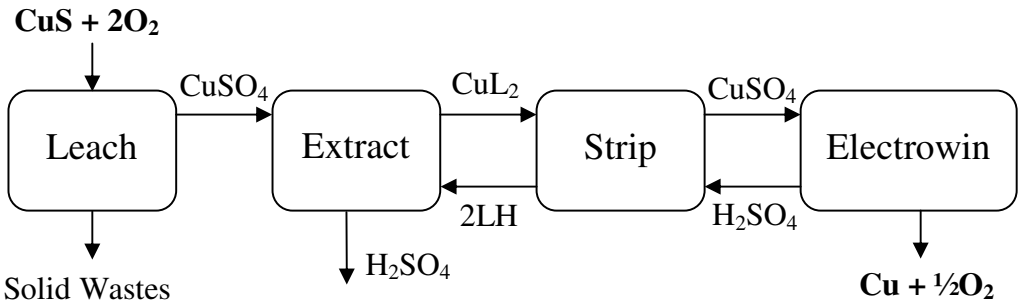

Leach: $CuS_{(s)} + 2O_2 \rightarrow CuSO_4$

Extract: $CuSO_4 + 2LH_{(org)} \rightarrow [CuL_2]_{(org)} + H_2SO_4$

Strip: $[CuL_2]_{(org)} + H_2SO_4 \rightarrow CuSO_4 + 2LH_{(org)}$

Electrowin: $CuSO_4 + H_2O \rightarrow Cu_{(s)} + ½O_2 + H_2SO_4$

Overall: $CuS_{(s)} + \frac{3}{2}O_{2(g)} + H_2O \rightarrow Cu_{(s)} + H_2SO_4$

Figure 4-8: The hydrometallurgy circuit and materials balance for recovery of copper from sulfidic ores using the conventional cation exchange extractants LH, showing build up of sulfuric acid in the front end of the circuit.

A large amount of development work has been undertaken recently to process sulfidic ores using hydrometallurgy. The three main approaches generate sulfate, chloride or ammoniacal process streams.[22] The first two of these are relevant to work described in this chapter because the pregnant leach solutions cannot be efficiently processed by the conventional phenolic oxime reagents and consequently research to develop copper *salt* reagents was undertaken at Edinburgh.

4.3.2.1. Oxidative leaching of sulfides to generate sulfate streams

A metal sulfide can be leached using an oxidative leaching process which produces the metal sulfate. This can be achieved by several methods. A common approach is to employ high pressure and temperature oxidative conditions during leaching of the ore with acid. One example of such a process is the Total Pressure Oxidation[32] method used at the Bagdad plant in Arizona.

$$CuFeS_2 + O_2 + 2H_2SO_4 \rightarrow CuSO_4 + FeSO_4 + 2H_2O + 2S$$

$$S + H_2O + \frac{3}{2}O_2 \rightarrow H_2SO_4$$

$$\text{Overall: } CuFeS_2 + O_2 \rightarrow CuSO_4 + FeSO_4$$

Figure 4-9: Oxidative leaching of sulfide ores using high pressure and high temperature.

Alternative methods such as bioleaching can be used for the leaching of copper-gold concentrates with high arsenic levels. In these processes microbes are used to catalytically oxidise sulfidic minerals to metal sulfates at temperatures of 65-80 °C such as in the BioCOP™ process developed by BHP Billiton[33] (Figure 4-10). This process generates a build-up of sulfuric acid although this cannot be recovered as it must be neutralised.[34]

$$CuFeS_2 + 4Fe^{3+} \rightarrow 5Fe^{2+} + Cu^{2+} + 2S$$

$$2Fe^{2+} + 2H^+ + ½O_2 \rightarrow 2Fe^{3+} + H_2O$$

$$2S + 3O_2 + 2H_2O \rightarrow 2H_2SO_4$$

$$\text{Overall: } CuFeS_2 + 4O_2 + 4H^+ \rightarrow Cu^{2+} + Fe^{2+} + 2H_2SO_4$$

Figure 4-10: Oxidation of sulfidic ores by thermophilic bacteria to produce a sulfate stream.

4.3.2.2. Oxidative chloride leaching of sulfides to generate chloride streams

A substantial amount of research has been invested in developing leaching process in chloride media.[35, 36] The CLEAR process[37] uses oxidative conditions with chloride salts such as $FeCl_3$ to solubilise copper from chalcopyrite, $CuFeS_2$. Using this process more than 95% of the copper in the chalcopyrite can be converted to $CuCl_2$ according to the process:

$$CuFeS_2 + 4FeCl_3 \rightarrow 5FeCl_2 + CuCl_2 + 2S$$

From this it is then possible to recover copper from solution at the cathode by electrolysis.

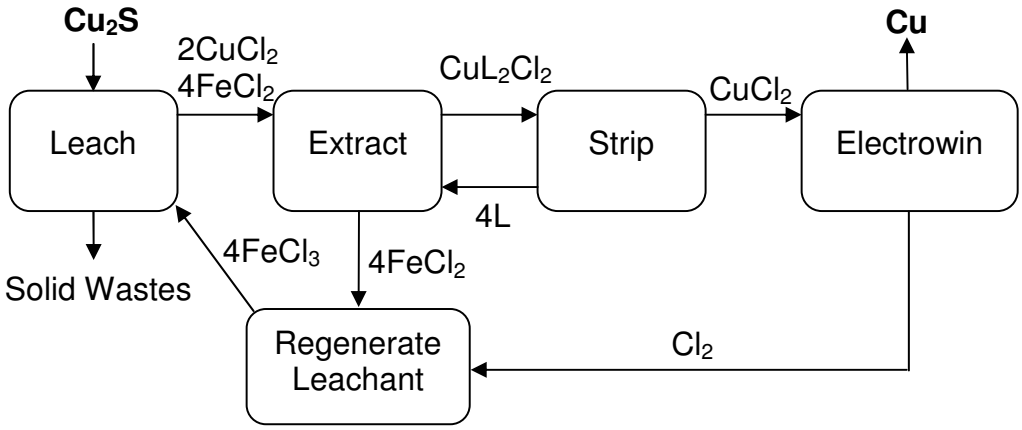

Leach:	$Cu_2S_{(s)} + 4FeCl_3$	$\rightarrow 2CuCl_2 + 4FeCl_2 + S_{(s)}$
Extract:	$2CuCl_2 + 4L_{(org)}$	$\rightarrow 2[CuL_2Cl_2]_{(org)}$
Strip:	$2[CuL_2Cl_2]_{(org)}$	$\rightarrow 2CuCl_2 + 4L_{(org)}$
Electrowin:	$2CuCl_2$	$\rightarrow 2Cu_{(s)} + 2Cl_{2(g)}$
Leach Regen:	$4FeCl_2 + 2Cl_{2(g)}$	$\rightarrow 4FeCl_3$
Overall:	$Cu_2S_{(s)}$	$\rightarrow 2Cu_{(s)} + S_{(s)}$

Figure 4-11: The CUPREX process for recovery of copper from sulfidic ore.[38]

The CUPREX process[38] provides another method for recovery of copper from chloride streams. The leach step is similar to the CLEAR process, liberating elemental sulfur from chalcocite (Cu_2S) by treatment with $FeCl_3$ generating $CuCl_2$. The $CuCl_2$ can then be transported in a hydrometallurgical circuit using a ligand, L, to generate $[CuL_2Cl_2]$ in the organic phase. Electrolysis of the stripped $CuCl_2$ generates chloride which is used to regenerate the leachant. All reagents internally recycled and a very good materials balance obtained (Figure 4-11).

4.3.2.3. Design of metal-salt extractants

As discussed previously, using the conventional phenolic oxime extractants to transport Cu^{2+} from these new leach streams presents problems. For high pressure sulfate leaching of sulfidic ores, the acid liberated in the extraction step exceeds that required in leaching and the build-up of this acid at the front end of the circuit is a problem. For chloride leaching the activity of protons in solutions of high chloride concentration is too great to allow the pH-dependent extraction equilibrium

$$CuCl_2 + 2LH_{(org)} \rightleftharpoons [CuL_2]_{(org)} + 2HCl$$

to be favourable. If metal sulfate or chloride were carried across the circuit to the strip step these problems would be overcome.

Two strategies have been employed in Edinburgh to transport metal *salts*:

- polytopic ligands have been designed which provide separated binding sites for the base metal cation and its attendant anion(s)
- monotopic ligands have been used which accommodate the metal cation with the attendant anion(s) in its inner coordination sphere

The first polytopic ligands developed at Edinburgh were ditopic. These provided a binding site for the metal dication and a site for an attendant sulfate and allow for transport of the metal sulfate across the phase boundary. A ligand which incorporates both a protonatable site and a deprotonatable site for anion and cation

binding respectively can adopt a zwitterionic form to allow for the stripping of the cation and anion under pH control (Figure 4-12).[39]

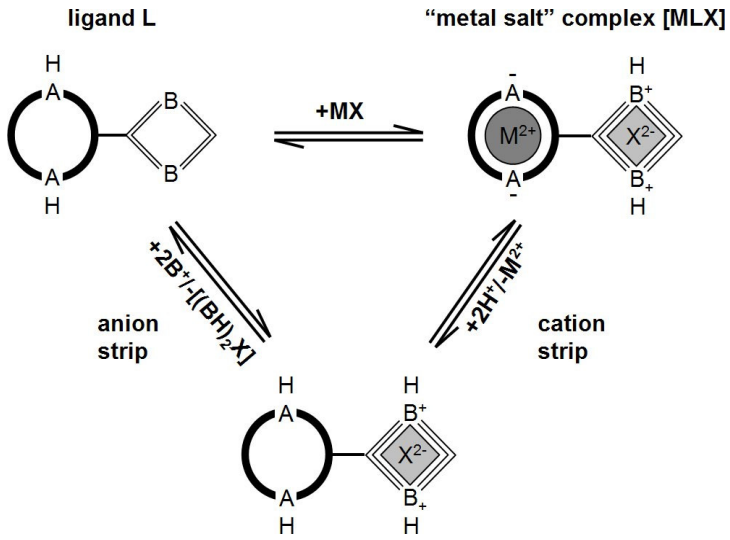

Figure 4-12: Metal *salt* extraction with ditopic ligands and sequential stripping of ions from the ligand.[1]

The advantages of this system are that the ions can be stripped individually under different conditions. The cation may be stripped by addition of H_2SO_4 regenerating the metal sulfate as in a conventional pH-swing system and the anion can be stripped by addition of an aqueous base, B, generating its sulfate salt which results in a materials balance shown by the equations in Figure 4-13.

Leach:	$MS_{(s)} + 2O_{2(g)}$	$\rightarrow MSO_4$
Extract:	$MSO_4 + L_{(org)}$	$\rightarrow [ML_2SO_4]_{(org)}$
Cation Strip:	$[ML_2SO_4]_{(org)} + H_2SO_4$	$\rightarrow MSO_4 + [LH_2]SO_{4(org)}$
Anion Strip:	$[LH_2]SO_{4(org)} + 2B$	$\rightarrow L_{(org)} + [BH]_2SO_4$
Electrowin:	$MSO_4 + H_2O$	$\rightarrow M_{(s)} + ½O_{2(g)} + H_2SO_4$

$$\text{Overall:} \quad MS_{(s)} + \frac{3}{2}O_{2(g)} + H_2O + 2B \rightarrow M_{(s)} + [BH]_2SO_2$$

Figure 4-13: Materials balance for metal recovery using a polytopic metal *salt* extractant.

The overall reaction process has a better materials balance provided the sulfate salt produced has a commercial value.[31]

4.4. Experimental

The complexes discussed in this chapter are listed in Table 4-1. They were synthesised and crystallised by Dr Ross Forgan. The parent ligands and the abbreviations used to describe them in the rest of this chapter are shown in Figure 4-14.

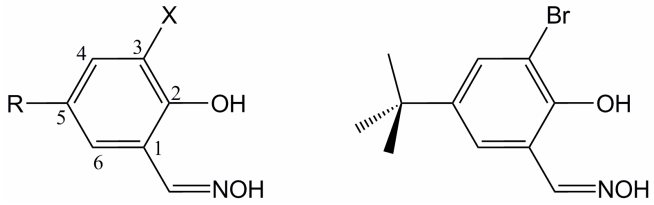

X	R	Name
H	^{t}Bu	5-^{t}Bu-salox
H	^{t}Pentyl	5-^{t}Pentyl-salox
Br	^{t}Bu	3-Br-5-^{t}Bu-salox
Me	^{t}Bu	3-Me-5-^{t}Bu-salox
O-Me	^{t}Bu	3-MeO-5-^{t}Bu-salox
NO_2	^{t}Bu	3-NO_2-5-^{t}Bu-salox
^{t}Bu	^{t}Bu	3-^{t}Bu-5-^{t}Bu-salox
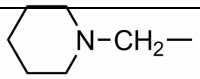	^{t}Bu	3-CH_2pip-5-^{t}Bu-salox

Figure 4-14: The ligand family studied in this chapter and in previous work[1] with a named example, 3-Br-5-^{t}Bu-saloxH (right)

X-ray crystal structure determination was then conducted according to the following basic procedure.

Diffraction data were collected on a 3-circle Bruker Smart Apex CCD diffractometer with graphite-monochromated Mo-Kα radiation (λ = 0.71073 Å) equipped with an

Oxford Cryosystems low temperature device operating at 150 K. The crystal was indexed using the Bruker Smart software[40] unless otherwise stated in Table 4-1. In some cases a sphere of data was collected. In all other cases a data collection strategy was refined, based on initial indexing, which aimed to collect complete data to a resolution of 53° in 2θ in as short a time as possible. An absorption correction was performed using a multi-scan method by applying the SADABS[41] program to the data. The data were merged according to the crystal system in SHELX[42]. The initial solution was determined by either by direct methods with the SHELXS[42] program or the Patterson method in the program DIRDIF.[43] All heavy atoms were refined anisotropically unless otherwise specified and most hydrogen atoms were placed geometrically and allowed to ride on their host atom. Hydrogen atoms on oxygen and nitrogen atoms were found in a Fourier difference map. Full matrix least squares refinement was carried out against F^2.

	[Cu(3-^{t}Bu-5-^{t}Bu-salox)$_2$]	[Ni(3-^{t}Bu-5-^{t}Bu-salox)$_2$]	[Cu(3-Br-5-^{t}Bu-salox)$_2$]	[Cu(5-^{t}Pentyl-salox)$_2$]
Sample code	PT0533	PT6025	PT7028	PT7029
Crystal Data				
Formula	$C_{30}H_{44}CuN_2O_4$	$C_{30}H_{44}N_2NiO_4$	$C_{22}H_{26}Br_2CuN_2O_4$	$C_{24}H_{32}CuN_2O_4$
M_r	560.21	555.38	605.81	476.06
Crystal System	monoclinic	monoclinic	triclinic	monoclinic
Space Group	$P2_1/c$	$P2_1/n$	$P\bar{1}$	$C2/c$
z	6	2	1	4
a /Å	31.7417(14)	11.7851(3)	5.8093(4)	24.7872(10)
b /Å	8.3449(4)	8.4396(2)	8.9279(6)	8.7381(3)
c /Å	16.3194(7)	15.1544(4)	12.0867(9)	10.9826(4)
α /°	90.00	90	71.499(5)	90
β /°	90.035(3)	106.9890(10)	82.942(5)	104.533(2)
γ /°	90.00	90	72.686(5)	90
V /Å^{-3}	4322.7(3)	1441.50(6)	567.26(7)	2302.64(15)
ρ_{calc} /g cm^{-3}	1.291	1.280	1.773	1.373
Shape/colour	brown plate	green block	green plate	brown block
Dimensions /mm	0.35x0.30x0.11	0.48x0.26x0.13	0.41x0.16x0.05	0.35x0.26x0.13
μ /mm^{-1}	0.724	0.709	4.516	0.981
Data Collection				
Instrument	Bruker Smart Apex CCD	Bruker Smart Apex CCD	Bruker Smart Apex CCD	Bruker Smart Apex CCD
λ /Å	0.71073	0.71073	0.71073	0.71073
Scan method	φ + ω	φ + ω	sphere (ω)	sphere (ω)
T_{min}/T_{max}	0.724 / 0.920	0.62 / 0.92	0.545,0.798	0.785, 0.880
θ_{min}, θ_{max} /°	0.64, 28.28	1.94, 29.98	1.78, 28.71	1.70, 28.82
T /K	150	150	150	150
Solution and refinement				
Solution method	direct	direct	direct	direct
Solution program	shelxs	shelxs	shelxs	shelxs
H placement	geometric	geometric	geometric	geometric
H refinement	riding	mixed	mixed	Mixed
Unique data ($F_o > 4\sigma(F_o)$)	10718 (5379)	4122 (3406)	2661 (2339)	2857 (2386)
R_{int}	0.0523	0.0378	0.0392	0.0304
Parameters	523	179	146	143
Restraints	0	0	1	1
Max shift	0.001	0.000	0.000	0.001
R_F	0.0400	0.0339	0.0342	0.0381
wR_2	0.1138	0.0875	0.0787	0.1045
Flack param.	-	-	-	-
Weighing Scheme	0.0472, 1.1756	0.0396, 0.06056	0.0320, 0.6070	0.0478, 3.7241
Extinction Param.	-	-	-	-
GoF	1.042	1.076	1.033	1.136
Residual density /e Å^{-3}	0.433, -0.669	0.451, -0.238	0.550, -0.409	0.939, -0.430

Table 4-1: Crystal data, data collection and solution and refinement details for the metal complexes discussed in chapter 4.

	[Cu(5-^{t}Bu-salox)$_2$]	[Cu(3-NO_2-5-^{t}Bu-salox)$_2$]	[Cu(3-Me-5-^{t}Bu-salox)$_2$]	[Cu(3-MeO-5-^{t}Bu-salox)$_2$]
Sample code	PT0532	PT6009	PT6012	PT7033
Crystal Data				
Formula	$C_{66}H_{84}Cu_3N_6O_{12}$	$C_{32}H_{36}CuN_6O_8$	$C_{24}H_{32}CuN_2O_4$	$C_{24}H_{32}CuN_2O_6$
M_r	1344.01	696.21	476.06	508.06
Crystal System	triclinic	triclinic	tetragonal	monoclinic
Space Group	$P\bar{1}$	$P\bar{1}$	$P4_2/n$	$P2_1/c$
z	1	2	8	4
a /Å	10.3884(5)	8.7844(4)	18.6883(2)	17.7657(9)
b /Å	10.3905(5)	13.1827(7)	18.6883	20.8218(11)
c /Å	18.9956(9)	14.3481(8)	13.3732(2)	6.5914(4)
α /°	77.787(3)	79.250(4)	90	90
β /°	83.298(3)	77.374(4)	90	96.641(3)
γ /°	60.492(2)	82.427(4)	90	90
V /Å^{-3}	1743.86(14)	1585.71(14)	4670.62(9)	2421.9(2)
ρ_{calc} /g cm^{-3}	1.280	1.458	1.354	1.393
Shape/colour	brown block	green block	green plate	brown needle
Dimensions /mm	0.31x0.23x0.20	0.60x0.22x0.21	1.06x0.24x0.08	0.21x0.16x0.13
μ /mm^{-1}	0.967	0.750	0.967	0.943
Data Collection				
Instrument	Bruker Smart Apex CCD	Bruker Smart Apex CCD	Bruker Smart Apex CCD	Bruker Smart Apex CCD
λ /Å	0.71073	0.71073	0.71073	0.71073
Scan method	φ + ω	ω	ω	sphere (ω)
T_{min}/T_{max}	0. 655 / 0. 820	0.43 / 0.86	0.38,0.92	0.759, 0.888
θ_{min}, θ_{max} /°	1.10, 30.57	1.98, 26.37	1.54, 28.67	1.51, 28.86
T /K	150	150	150	150
Solution and refinement				
Solution method	direct	patterson	direct	direct
Solution program	shelxs	dirdif	shelxs	shelxs
H placement	geometric	geometric	geometric	geometric
H refinement	riding	mixed	riding	mixed
Unique data ($F_o > 4\sigma(F_o)$)	10240 (6785)	6448 (4835)	2661 (2339)	5917 (5363)
R_{int}	0.0638	0.0639	0.0911	0.0527
Parameters	409	434	291	304
Restraints	0	0	0	2
Max shift	0.000	0.000	0.000	0.000
R_F	0.0569	0.0800	0.0511	0.0734
wR_2	0.1455	0.2093	0.1470	0.1537
Flack param.	-	-	-	-
Weighing Scheme	0.0907, 0.0000	0.0637, 5.7920	0.0381, 8.2524	0.0274, 7.4974
Extinction Param.	-	-	-	-
GoF	0.936	1.185	1.062	1.221
Residual density /e Å^{-3}	1.439, -1.272	0.947, -0.473	0.637, -0.981	0.827, -0.865

Table 4-1: Crystal data, data collection and solution and refinement details for the metal complexes discussed in chapter 4.

	[Cu(3-CH_2pip-5-^{t}Bu-salox)$_2$(NO_3)$_2$]	[Cu(3-CH_2pip-5-^{t}Bu-salox)$_2$(BF_4)$_2$]	[Cu_2(3-CH_2pip-5-^{t}Bu-salox)$_2$$Br_2$]
Sample code	RF0005	PT0541	PT6010
Crystal Data			
Formula	$C_{34}H_{52}CuN_6O_{10}$	$C_{34}H_{52}B_2CuF_8N_4O_4$	$C_{35.75}H_{53.75}Br_4Cu_2N_{5.75}O_4$
M_r	768.37	817.96	1074.82
Crystal System	monoclinic	triclinic	orthorhombic
Space Group	$P2_1/n$	$P\bar{1}$	$Pbcn$
z	2	2	4
a /Å	11.8945(6)	8.4253(3)	16.8492(5)
b /Å	11.1622(6)	10.7811(4)	24.7009(8)
c /Å	14.8414(7)	11.2498(4)	10.5521(3)
α /°	90	84.524(3)	90
β /°	112.682(3)	77.179(2)	90
γ /°	90	69.818(2)	90
V /Å^{-3}	1818.08(16)	935.01(6)	4391.7(2)
ρ_{calc} /g cm^{-3}	1.403	1.453	1.626
Shape/colour	green block	green block	brown block
Dimensions /mm	0.71x0.37x0.24	0.18x0.15x0.13	0.99x0.20x0.13
μ /mm^{-1}	0.665	0.667	4.649
Data Collection			
Instrument	Bruker Smart Apex CCD	Bruker Smart Apex CCD	Bruker Smart Apex CCD
λ /Å	0.71073	0.71073	0.71073
Scan method	φ + ω	φ + ω	ω
T_{min}/T_{max}	0. 67 / 0. 85	0.675 / 0.920	0.11,0.55
θ_{min}, θ_{max} /°	1.89, 30.50	2.01, 30.58	1.65, 27.48
T /K	150	150	150
Solution and refinement			
Solution method	direct	patterson	direct
Solution program	shelxs	dirdif	shelxs
H placement	geometric	geometric	geometric
H refinement	riding	mixed	mixed
Unique data ($F_o > 4\sigma(F_o)$)	5178 (4128)	5293 (4241)	5036 (3888)
R_{int}	0.0490	0.0376	0.0444
Parameters	232	252	232
Restraints	0	0	0
Max shift	0.000	0.001	0.001
R_F	0.0390	0.0554	0.0354
wR_2	0.1094	0.1560	0.0895
Flack param.	-	-	-
Weighing Scheme	0.0609, 0.2220	0.0931, 0.3490	0.0456, 1.2569
Extinction Param.	-	-	-
GoF	0.967	1.066	1.061
Residual density /e Å^{-3}	0.880, -0.420	1.380, -1.129	1.304, -0.873

Table 4-1: Crystal data, data collection and solution and refinement details for the metal complexes discussed in chapter 4.

	$[Co_2(3\text{-}NO_2\text{-}5\text{-}^tBu\text{-}salox)_4(DMSO)_2]$	[Ni(((4-benzylpiperazin-1-yl)(mercapto)methylamino)(4-tert-butylphenyl)methanol)$_2$]
Sample code	PT6009	PT6006
Crystal Data		
Formula	$C_{48}H_{64}Co_2N_8O_{18}S_2$	$C_{46}H_{56}N_6NiO_2S_2$
M_r	1223.05	847.80
Crystal System	triclinic	triclinic
Space Group	$P\bar{1}$	$P\bar{1}$
z	1	2
a /Å	8.6299(2)	11.4685(2)
b /Å	10.6694(3)	11.9007(3)
c /Å	16.7585(4)	17.1758(4)
α /°	83.7670(10)	93.4810(10)
β /°	89.2150(10)	99.6340(10)
γ /°	66.7330(10)	106.4050(10)
V /Å^{-3}	1408.46(6)	2202.56(8)
ρ_{calc} /g cm^{-3}	1.442	1.278
Shape/colour	orange block	purple block
Dimensions /mm	0.35x0.18x0.12	0.30x0.28x0.15
μ /mm^{-1}	0.740	0.579
Data Collection		
Instrument	Bruker Smart Apex CCD	Bruker Smart Apex CCD
λ /Å	0.71073	0.71073
Scan method	φ + ω	φ + ω
T_{min}/T_{max}	0.77 / 0.92	0.59 / 0.92
θ_{min}, θ_{max} /°	2.09, 30.53	1.80, 30.52
T /K	150	150
Solution and refinement		
Solution method	direct	patterson
Solution program	shelxs	dirdif
H placement	geometric	geometric
H refinement	riding	Riding
Unique data ($F_o > 4\sigma(F_o)$)	8509 (7481)	12164 (9120)
R_{int}	0.0399	0.0402
Parameters	352	514
Restraints	0	0
Max shift	0.000	0.001
R_F	0.0521	0.0609
wR_2	0.1142	0.1122
Flack param.	-	-
Weighing Scheme	0.0433, 0.9563	0.0609, 0.2658
Extinction Param.	-	-
GoF	1.154	1.038
Residual density /e Å^{-3}	0.717, -0.378	0.592, -0.292

Table 4-1: Crystal data, data collection and solution and refinement details for the metal complexes discussed in chapter 4.

4.5. Structural analyses

Previous work[1] has looked at some of the ligands shown in Figure 4-14 in the context of the 'hole size' found in the dimers of the free ligands formed by these structures and its relationship to their performance as solvent extraction agents (see Figure 4-6).[29, 44] The 'hole size' in the hydrogen-bonded dimers is defined as the average distance from the centroid to the phenolic oxygen and the oximic nitrogen atoms (see Figure 4-15).

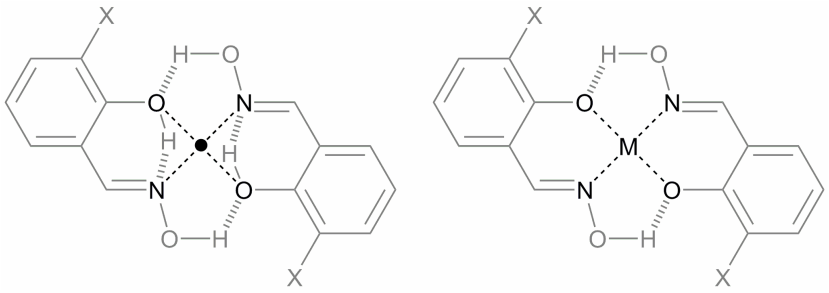

Figure 4-15: A salicylaldoxime ligand dimer (left) and complex (right). The cation cavity or 'hole size' is defined by the mean distance of the N and O donor atoms from their centroid (black dotted lines) which in the case of metal complexes frequently coincides with the metal atom site. Hydrogen bonds are shown in grey dashed lines.

The dimers are linked by two hydrogen bonds in which the donor is the oximic OH of one molecule and the acceptor is the phenolic oxygen of the other. Intraligand hydrogen bonds are also present between the phenolic oxygen and the oximic nitrogen atoms. The dimers are often slightly staggered so that the planes of the molecules are offset from one another. At the outset of the study into the hydrogen bonded dimers conducted by Ross Forgan,[1] two theories as to the dominant effect of 3-substitution on the efficacy of the ligands as copper extractants were proposed. The first was that the electronic effects, i.e. substitution with electron withdrawing or donating groups will affect the pK_a of the phenolic hydrogen atom making it either more or less acidic, affecting deprotonation thus dictating the performance of the ligand as a solvent extractant. Considering the effect of the phenolic hydrogen atom's pK_a raises the question of whether ligand acidity or conjugate basicity of the

phenolate oxygen atom is more important in determining the position of the extraction equilibrium. Previous work[29] has shown via calculated pK_a values that ligand acidity is likely to be more important than conjugate basicity but it is likely that other factors are involved. Reaction of such ligands with metals and their associated equilibrium constants, shown in Figure 4-16, indicate that there is a squared dependence of K_e on K_a, which suggests that the acidity is more important.

$$Cu^{2+} + 2LH \rightleftharpoons [CuL_2] + 2H^+ \qquad K_e = \frac{[CuL_2][H^+]^2}{[Cu^{2+}][LH]^2} \qquad (1)$$

$$Cu^{2+} + 2L^- \rightleftharpoons [CuL_2] \qquad \beta_2 = \frac{[CuL_2]}{[Cu^{2+}][L^-]^2} \qquad (2)$$

$$LH \rightleftharpoons L^- + H^+ \qquad K_a = \frac{[L^-][H^+]}{[LH]} \qquad (3)$$

$$K_e = \beta_2 K_a^2 \qquad (4)$$

Figure 4-16: Equilibrium equations representing the binding of a ligand, LH, to Cu^{II}. (1) shows the overall equilibrium for the reaction of LH with Cu^{2+} with a constant K_e. (2) shows the equilibrium for binding with deprotonated ligands, L^-, and the associated equilibrium constant β_2. (3) shows the equilibrium of ligand deprotonation defined by the acid dissociation constant K_a. (4) shows the result of rearranging (3) and substituting for $[H^+]$ in (1).[29]

The second theory was that dominant effect of a 3-subsituent, X, will arise from the influence on interligand hydrogen bonding. Hydrogen bond acceptor properties of X could buttress the hydrogen bond which will enhance the stability of the ligand dimer, and by extension the complexes, by drawing the two ligands closer together. This would also change the hole-size, tuning the selectivity for specific metal ions.

Drs Peter Wood and Ross Forgan studied extractant strength and crystal structures of free phenolic oxime ligands which formed hydrogen bonded dimers as a function of the 3-substituent, X. In their study it was found that the hydrogen bond acceptor strength of the 3-substituent correlated to extractant strength. A correlation was also

found between the cavity size measured as shown in Figure 4-15 and hydrogen bond acceptor strength so by extension extractant strength is also linked to cavity size.

The crystal structures of the complexes were expected to follow this same trend and the initial intent of part of the work reported in this chapter was to look at hole-sizes in Cu^{II} complexes and establish a correlation between the metal cation cavity size (Figure 4-15) and extractant strength. A series of crystals were grown of the Cu^{II} complexes by Dr Ross Forgan and their structures were determined (see below). Difficulties were encountered in growing crystals of some of the complexes. Some of the solvents used interacted with the complexes in the Cu^{II} axial positions perturbing equatorial bond lengths. Consequently in the analysis below discussion is split into sections on:

- *Metal-only complexes*. These are defined as complexes in which two salicylaldoximate ligands bind to a single metal ion, there are no other anions present and no significant axial contacts to the copper atoms. The effects of 3-position substitution and metal substitution will be discussed in section 4.5.1.
- *Axially perturbed metal-only complexes.* This class defines complexes which formed as above but where the copper atom has axial interactions. These are discussed in section 4.5.2.

In later sections other complexes formed in extractions are considered.

- *Metal salt complexes.* Complexes formed from ligands which include binding sites for attendant anions as well as the metal cation which are discussed in section 4.5.3.
- *Metal halide complexes.* Complexes in which a single ligand binds to MX_2. These are covered in section 4.5.4.

4.5.1. Metal-only complexes

4.5.1.1. Summary of structural features

Only a small number of structures were obtained in which the axial positions of the copper atom were not occupied. The non-axially perturbed metal-only complex structures discussed in this section are summarised in Figure 4-17.

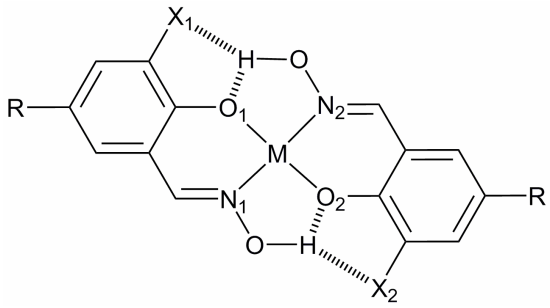

Abbreviated Name	Sample Code	Metal	R	X
[Ni(3-^{t}Bu-5-^{t}Bu-salox)$_2$]	PT6025	Ni	^{t}butyl	^{t}butyl
[Cu(3-^{t}Bu-5-^{t}Bu-salox)$_2$]	PT0533	Cu	^{t}butyl	^{t}butyl
[Cu(5-^{t}pentyl-salox)$_2$]	PT7029	Cu	^{t}pentyl	H
[Cu(3-Br-5-^{t}Bu-salox)$_2$]	PT7028	Cu	^{t}butyl	Br
[Cu(3-Me-5-^{t}Bu-salox)$_2$]	PT6012	Cu	^{t}butyl	Me
[Cu(3-MeO-5-^{t}Bu-salox)$_2$]	PT7033	Cu	^{t}butyl	MeO

Figure 4-17: The metal complexes studied in this chapter with subscripts showing atom labelling used in Table 4-2.

4.5.1.1.1. [Cu(5-^{t}Pentyl-salox)$_2$] - PT7029

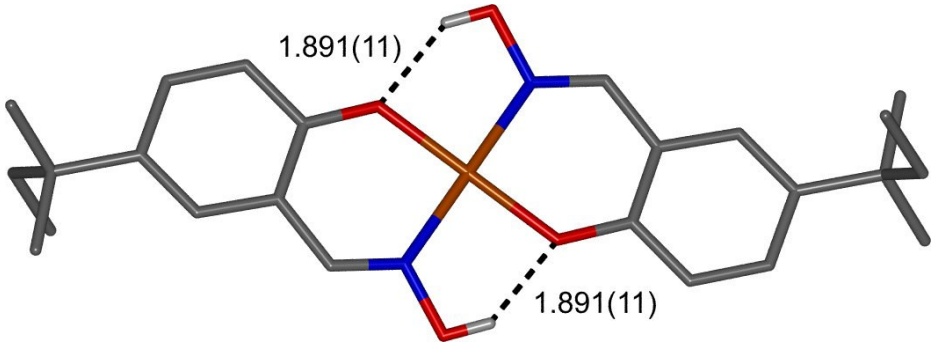

Figure 4-18: The molecular structure of [Cu(5-^{t}pentyl-salox)$_2$] in the solid state.

Cu(5-^{t}pentyl-salox)$_2$ crystallises in the monoclinic space group *C*2/*c*. The asymmetric unit contains half of a molecule in which the Cu atom sits on an inversion centre. This structure contains a tertiary-pentyl group rather than the tertiary butyl group used in other compounds. The groups in this position are used to impart solubility to the complex in the organic phase and have been shown not to be crucial to solvent extraction performance. Long, weak intermolecular CH…O hydrogen bonds between C21-H21 of one molecule and O2 of a neighbouring molecule with D-A and DH-A distances of 3.558 and 2.637 Å link molecules to form 1D ribbons in the *b* direction. No π-π stacking interactions exist as the tertiary butyl groups shield the aromatic ring. The complex is overall planar and chains stack in the *ac* direction. Intramolecular OH…O hydrogen bonding occurs in the complex which is directly related to the intermolecular hydrogen bonds formed in the dimeric ligand structures. The ligands form good OH…O hydrogen bonds with one another with D-A and DH-A distances of 2.591 and 1.891 Å which are tabulated alongside values for the other complexes in Table 4-2. The hole size and other relevant measurements are presented later alongside those of the other structures.

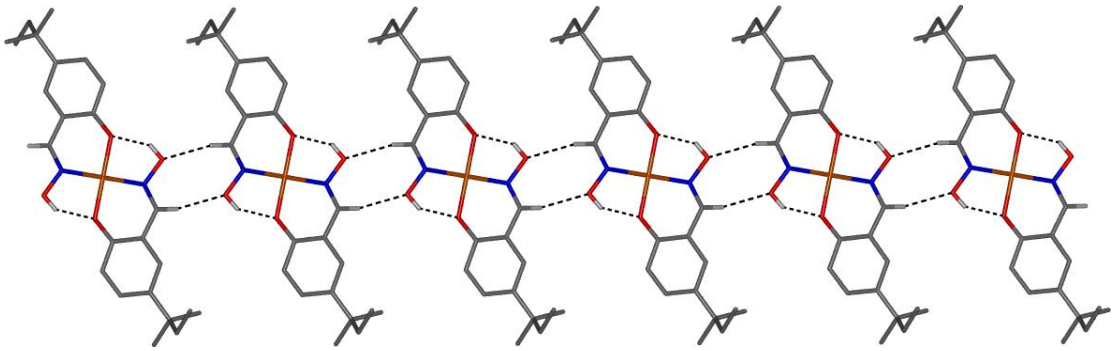

Figure 4-19: The crystal structure of [Cu(5-^{t}pentyl-salox)$_2$] showing ribbons in the *b* direction.

4.5.1.1.2. [Cu(3-^{t}Bu-5-^{t}Bu-salox)$_2$] – PT0533

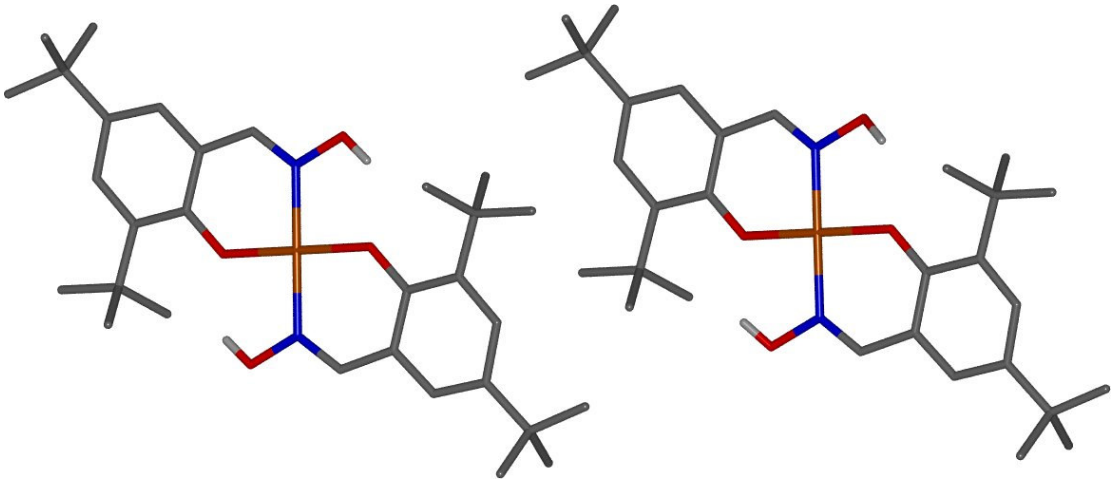

Figure 4-20: The crystal structure of [Cu(3-^{t}Bu-5-^{t}Bu-salox)$_2$]

The 3-^{t}Bu-5-^{t}Bu-salox copper complex crystalises in the monoclinic space group $P2_1/c$. There is one complete molecule and a half molecule whose copper sits on an inversion centre in the asymmetric unit. There are no intermolecular hydrogen bonds or π-π stacking interactions in the structure. Molecules are generally planar and the intramolecular hydrogen bonding in these was measured and presented alongside other relevant parameters in Table 4-2.

4.5.1.1.3. [Ni(3-^{t}Bu-5-^{t}Bu-salox)$_2$] – PT6025

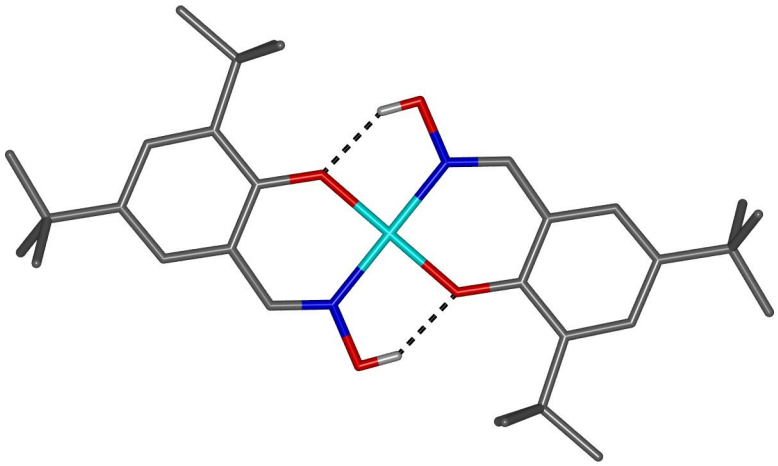

Figure 4-21: The molecular structure of [Ni(3-^{t}Bu-5-^{t}Bu-salox)$_2$] in the solid state.

The 3-^{t}Bu-5-^{t}Bu-salox nickel complex crystalises in the monoclinic space group $P2_1/n$. There is one half molecule in the asymmetric unit whose copper sits on an inversion centre. There are no intermolecular hydrogen bonds or π-π stacking interactions in the structure. Molecules are nearly planar and the intramolecular hydrogen bonding in these was measured and presented alongside other relevant parameters in Table 4-2.

4.5.1.1.4. [Cu(3-Br-5-^{t}Bu-salox)$_2$] – PT7028

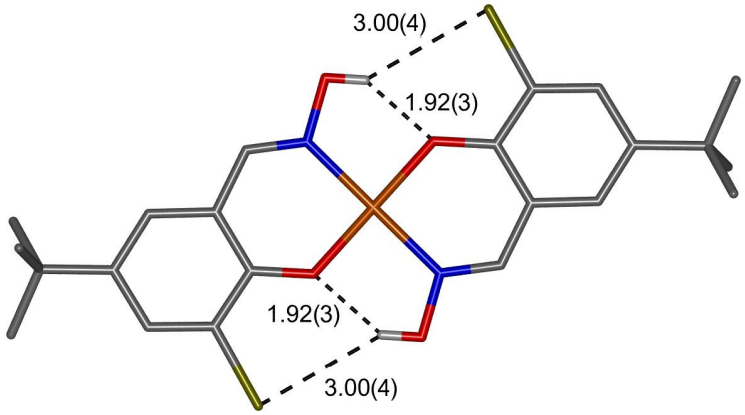

Figure 4-22: The molecular structure of [Cu(3-Br-5-^{t}Bu-salox)$_2$] in the solid state demonstrating hydrogen bond buttressing.

The complex of the 3-bromo-substituted ligand was solved in the triclinic space group $P\bar{1}$ with one molecule in the asymmetric unit. In these structures the oximic OH group forms bifurcated hydrogen bond to the bromide and the phenolic oxygen atom. These hydrogen bond lengths were measured and are presented in Table 4-2. The molecules in these structures are not completely planar as in the other complexes since there is a slight offset between the planes of each of the ligands (measured using the mean plane through the benzene rings) of about 0.3 Å.

4.5.1.1.5. [Cu(3-Me-5-^{t}Bu-salox)$_2$] – PT6012

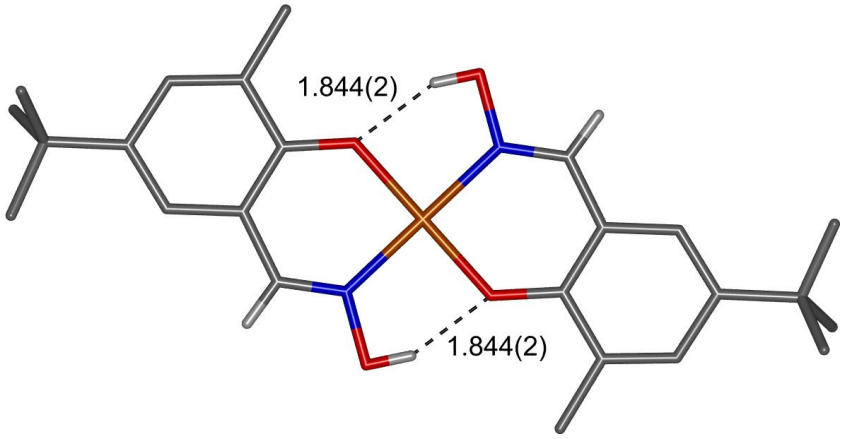

Figure 4-23: The molecular structure of [Cu(3-Me-5-^{t}Bu-salox)$_2$] in the solid state determined by X-ray crystallography.

The copper complex formed with 3-Me-5-^{t}Bu-salox crystallised in the tetragonal space group $P4_2/n$ with two half molecules in the asymmetric unit. The molecules stack up in the *c* direction with both copper atoms lying on the 4_2 axis with Cu…Cu distances of 3.345(1) and 3.341(1) Å. The tertiary butyl groups cause the neighbouring molecules to have a rotational offset between them so that they form helices as shown in Figure 4-24 and two of these are present in the unit cell. The offset prevents π-π stacking interactions from occurring and the bulk of the tertiary butyl groups prevents hydrogen bonding contacts to neighbouring helices.

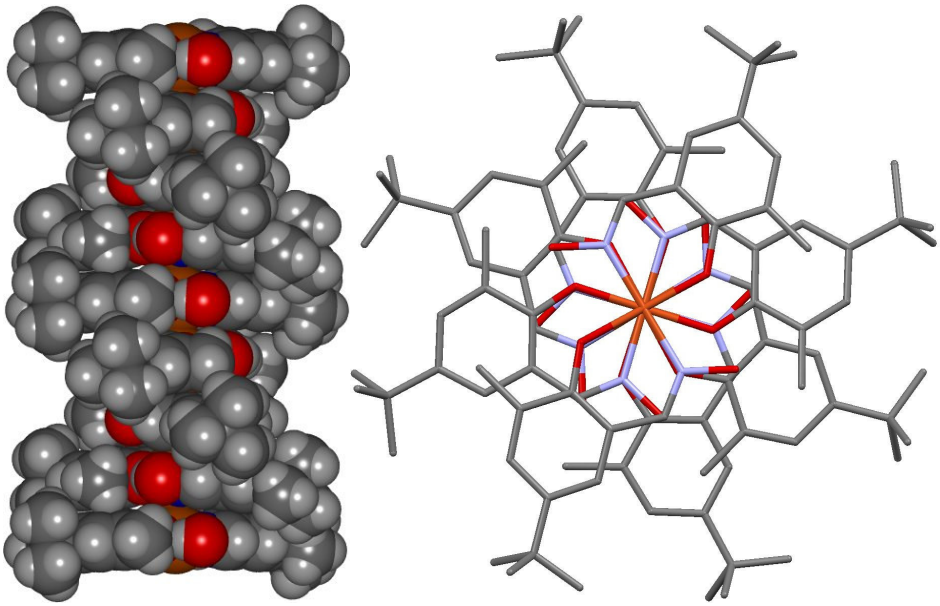

Figure 4-24: Helices formed along the *c* axis in the structure of [Cu(3-Me-5-^{t}Bu-salox)$_2$]. The view perpendicular to the *c* axis (left) and down the *c* axis (right).

4.5.1.1.6. [Cu(3-MeO-5-^{t}Bu-salox)$_2$] – PT7033

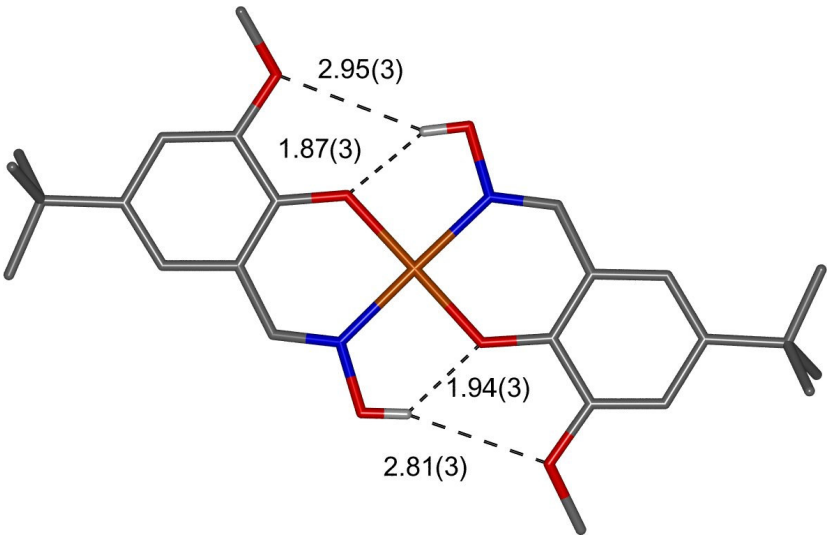

Figure 4-25: The molecular structure of [Cu(3-MeO-5-^{t}Bu-salox)$_2$] in the solid state determined by X-ray crystallography.

In the copper complex formed with 3-MeO-5-^{t}Bu-salox crystallised in the monoclinic space group $P2_1/c$. There is one molecule in the asymmetric unit and molecules stack up in the *c* direction with as shown in Figure 4-26. The Cu…Cu distance in the stack is 3.303(1) Å. There are two stacks in each unit cell and no intercomplex hydrogen bonds or π-π stacking interactions in the structure. The intramolecular hydrogen bonds shown in Figure 4-25 indicate that the MeO group forms weak hydrogen bonds with long H…A distances of 2.81(3) and 2.95(3) Å being considerably longer than those normally considered to form OH…O hydrogen bonds.[45]

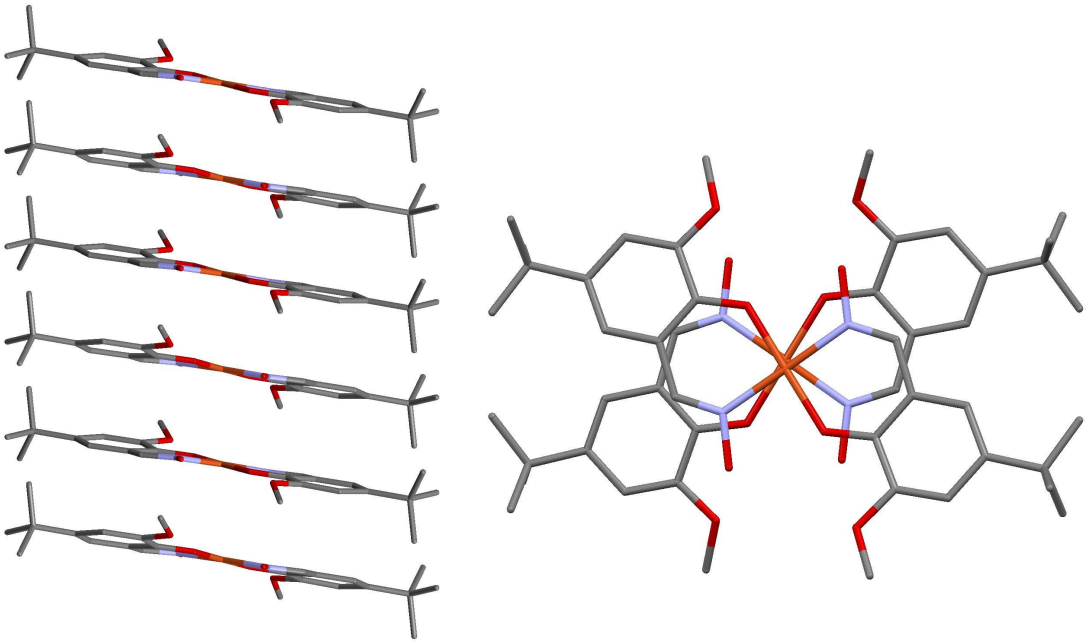

Figure 4-26: Stacking along the *c* axis in the structure of [Cu(3-MeO-5-^{t}Bu-salox)$_2$], viewed down the *a* axis (left) and *c* axis (right).

4.5.1.2. Analysis

Initially a comparison of the copper and nickel complexes was undertaken to investigate the effect of metal ion on the pseudo-macrocyclic ligand superstructure. The data in Table 4-2 show that the hole size is smaller for the nickel complex, 1.860(2) cf. 1.922(13) Å. This is expected as low-spin Ni(II) has a smaller covalent radius of 1.20 Å[46] than that of Cu at 1.32 Å[47]. The average M-O bond lengths are

also significantly different with Ni and Cu complexes having values of 1.850(1) and 1.909(8) Å whilst the average M-N bond lengths are 1.869(1) and 1.936(10) Å. The interligand hydrogen bonding in the nickel complex is also shorter than in the copper complex. It appears that the pseudo-macrocyclic structure is easily compressible and can adjust to match the complexed cation's requirements.

Metal	Ni	Cu						
X	^{t}Bu	H	^{t}Bu		Br	MeO	Me	
M-O_1 /Å	1.850(1)	1.896(2)	1.907(4)	1.909(4)	1.885(2)	1.869(3)	1.886(2)	1.875(3)
M-O_2 /Å	1.850(1)	1.896(2)	1.910(3)	1.909(4)	1.885(2)	1.869(3)	1.886(2)	1.875(3)
M-N_1 /Å	1.869(1)	1.942(2)	1.924(5)	1.941(5)	1.954(3)	1.950(3)	1.940(3)	1.932(3)
M-N_2 /Å	1.869(1)	1.942(2)	1.936(5)	1.941(5)	1.954(3)	1.950(3)	1.940(3)	1.932(3)
OH...O_1 /Å	1.80(2)	1.89(1)	1.988(4)	1.964(4)	1.92(3)	1.88(3)	1.844(2)	1.816(3)
OH...O_2 /Å	1.80(2)	1.89(1)	2.034(4)	1.964(4)	1.92(3)	1.88(3)	1.844(2)	1.816(3)
O…O_1 /Å	2.529(2)	2.591(2)	2.627(6)	2.624(7)	2.627(4)	2.621(4)	2.628(4)	2.604(4)
O…O_2 /Å	2.529(2)	2.591(2)	2.623(5)	2.624(7)	2.627(4)	2.621(4)	2.628(4)	2.604(4)
OH...X_1 /Å	-	-	-	-	3.00(4)	2.95(3)	-	-
OH...X_2 /Å	-	-	-	-	3.00(4)	2.95(3)	-	-
O…X_1 /Å	-	-	-	-	3.722(2)	3.713(4)	-	-
O…X_2 /Å	-	-	-	-	3.722(2)	3.713(4)	-	-
Hole Size /Å	1.860(2)	1.919(4)	1.919(9)	1.925(9)	1.919(5)	1.910(6)	1.913(5)	1.904(6)
			Mean = 1.922(13)				Mean = 1.909(8)	

Table 4-2: Selected bond lengths and contact distances in Å in the metal-only complexes of the 3-X substituted ligands shown in Figure 4-17.

Based on the work carried out on ligand dimers[1, 29] (see also section 4.5), it might be expected that the substituents which give small hole-sizes in the free ligand dimers, and which generally appear to increase the strength of the ligands as a copper extractant, would result in smaller cavities in the copper-only complexes. In the context of the limited series of complexes included in Table 4-2 (recall that only structures with no axial contacts in the solid-state are included) we might expect the complex [Cu(3-Br-5-^{t}Bu-salox)$_2$] to have a the smallest cavity defined by the $N_2O_2^{2-}$ donor set because this ligand is a particularly strong extractant (see Figure 4-6). Table 4-2 shows that for this subset of structures, this not true. The Br complex has a

hole size of 1.919(5) Å whilst at the other end of the extractant strength scale the two crystallographically independent ^{t}Bu complexes have hole sizes of 1.925(9) and 1.919(9) Å. These values and those for the other Cu complexes in Table 4-2 are not significantly different from one another and even if one disregards the e.s.d.s no obvious trend reveals itself. Thus looking at the H, Me and ^{t}Bu 3-substituted structures there is no correlation between bulk and hole size; the H and ^{t}Bu structures are at opposite ends of the bulk scale yet have the same hole size, and the Me structure giving smaller measurements although again this disregards the statistical significance of the errors.

This observation that hole sizes in the copper complexes are essentially unaffected by hydrogen bond buttressing has three implications. Firstly that the current method of measuring hole size may be inadequate to describe complex stability properly, secondly that hydrogen bond buttressing does not have any effect on the hole size at all, or thirdly that the electronic effects of substitution counter the hydrogen bond buttressing. In order to address this phenomenon, alternative methods for correlating the complex stability to extractant strength will be considered and the electronic effects of substitution will be examined more closely.

Using the hole-size method to determine the effect of X substitution is perhaps a little simplistic in that this method ignores three-dimensional inner coordination sphere geometry and concentrates solely on the bond lengths. The 'ligand closeness,' defined here as the distance between the centroids of the aromatic rings of the two ligands, is not a function of the bond lengths alone but also the planarity of the CuN_2O_2 unit and the angles formed at the copper atom. Fortunately, in all but two of the structures relevant to this section, the metal ion sits on an inversion centre and therefore the CuN_2O_2 is perfectly planar. In those structures in which one of the Cu atoms does not sit on an inversion centre deviations from the mean plane of the 5 atoms are all smaller than 0.001 Å and so planarity is assumed. This measurement therefore provides a simple way to describe the ligand interaction with greater consideration of ligand and metal ion geometry than the hole-size method. According to the hydrogen buttressing hypothesis, the 'ligand closeness' should

decrease from left to right in Table 4-3. If a tertiary butyl group is put in the 3-position, the ligands are further apart than in the 'H' structure. This is reflected by a smaller O-M-N angle, a shorter *intra*ligand N…O distance and a longer *inter*ligand N…O distance, while the M-O and M-N bond lengths do not change. Comparison of the 'H' and 'Br' structures shows statistically indistinguishable values and the same is true when comparing the Me and MeO structures. The tertiary butyl structure has a significant difference which is likely a consequence of the bulk of the group interfering with the other ligand.

3-Position (X)	^{t}Bu (mean values)	Me (mean values)	H	MeO	Br
'Ligand closeness' /Å	8.530(4)	8.418(2)	8.448(1)	8.420(1)	8.447(1)
O-M-N *intra*ligand /°	91.3(4)	92.1(2)	92.5(1)	92.2(1)	92.2(1)
O…N *intra*ligand /Å	2.749(13)	2.748(6)	2.772(2)	2.752(4)	2.766(5)
O…N *inter*ligand /Å	2.688(12)	2.650(6)	2.656(3)	2.641(4)	2.663(3)

Table 4-3: Parameters describing the geometry of Cu(salox)$_2$ complexes and 'ligand closeness.'

The hypothesis that strengthening the interactions *between* ligands will reduce the cavity size available for the copper appears, on this evidence to be incorrect. Computational research on the effects of pressure on crystal structures[48] has shown that covalent bond lengths change very little during compression studies with some examples of bonds lengthening[49, 50] and that soft interactions such as hydrogen bonds are more compressible. Whilst in this case we are looking at coordinate bonding, the implication of this in the current project is that in a situation where soft interactions are competing with harder interactions, it is likely that the soft hydrogen bonding interactions will change in length much more than the harder coordinate bonds. This is expected behaviour if one considers that hydrogen bonds by their very nature are known to be much weaker than coordinate bonds. In structures where X is electronegative such as the 3-bromo derivative, the buttressing of the hydrogen bonds increases the attraction between the ligands but neither the cavity size nor the OH…O hydrogen bond lengths significantly change. The 'ligand closeness' measurement given above does not show a significant change either. Table 4-4 is

arranged to show the ranking of ligands, defined by their X substituent, according to solvent extractant strength, cavity size and 'ligand closeness.' The data show that no correlations exist between extractant strength and these measures.

Criterion	weak extractant large hole far				strong extractant small hole close
Extractant strength	^{t}Bu	H	Me	MeO	Br
Hole size	^{t}Bu	H	Br	MeO	Me
Ligand closeness	^{t}Bu	H	Br	MeO	Me

Table 4-4: Ranking of ligands according to solvent extractant strength, hole-size and 'ligand closeness.'

If we consider the implications of X substitution on the individual interactions involved in holding the complex together, the reasons behind the negligible changes in the hole-size are a little clearer.

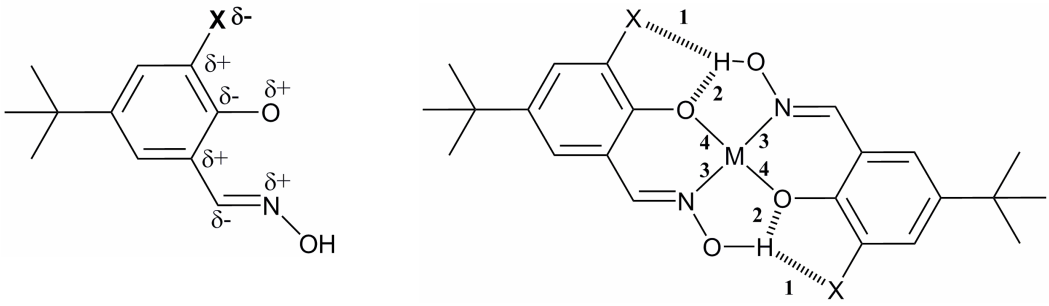

Figure 4-27: The effect of electronegative substitution on the donor atoms involved in coordinate bonding to metal ions is shown on the left. Key bonding and non-bonding interactions within the complex are numbered on the right.

The initial assumption was that the interactions marked **1** in Figure 4-27 would be strengthened if X were a good hydrogen bond acceptor and that this would effectively pull the ligands towards each other reducing the size of the metal ion cavity observed the copper complex. However, the electronic effect of X

substituents which are good hydrogen bond acceptors, e.g. bromine, will be expected to reduce the electronic charge density on phenolate oxygen atom and the imino nitrogen atom, making them less effective in bonding to the positively charged Cu^{II} ion. The OH…O hydrogen bond would also be adversely affected by a slight positive shift in the charge of the phenolic oxygen. This would mean that the interactions marked **2**, **3** and **4** in Figure 4-27 will all be weakened. Crudely, on this basis, the more electronegative the substituent, the *larger* the hole size is expected to be as three of four types of bond will be adversely affected and expected to lengthen. Such a prediction ignores the relative magnitude of the effects, but, since it is clear that the only type of bond which will benefit from the influence of a strongly electronegative X atom is the interligand hydrogen bond (**1** in Figure 4-27) and that this is clearly a very weak bond based on its length, it is unlikely that incorporation of electronegative X atoms will shrink the cavities in the copper complexes. A factor leading to the weak OH…Br bonds in [Cu(3-Br-5-^{t}Bu-salox)$_2$] is the geometric constraint placed by having the hydrogen bond acceptor in the 3-position. A spacer between the acceptor atom and the aromatic ring will decrease the contact distances. The NO_2 structure discussed in the next section fits this description. However, it is discussed in the next section as it was isolated as the bispyridine adduct [Cu(3-NO_2-5-^{t}Bu-salox)$_2$py$_2$] which has axial bonds to the copper such that the effect of the NO_2 group cannot be evaluated.

Fortunately a structure exists in the CSD which has no axial perturbation and includes a linking atom between the aromatic ring and the electronegative hydrogen bond acceptor. The structure, RIBYEG,[51] is shown in Figure 4-28. It has a dimethyl acetal substituent in the 3-position.

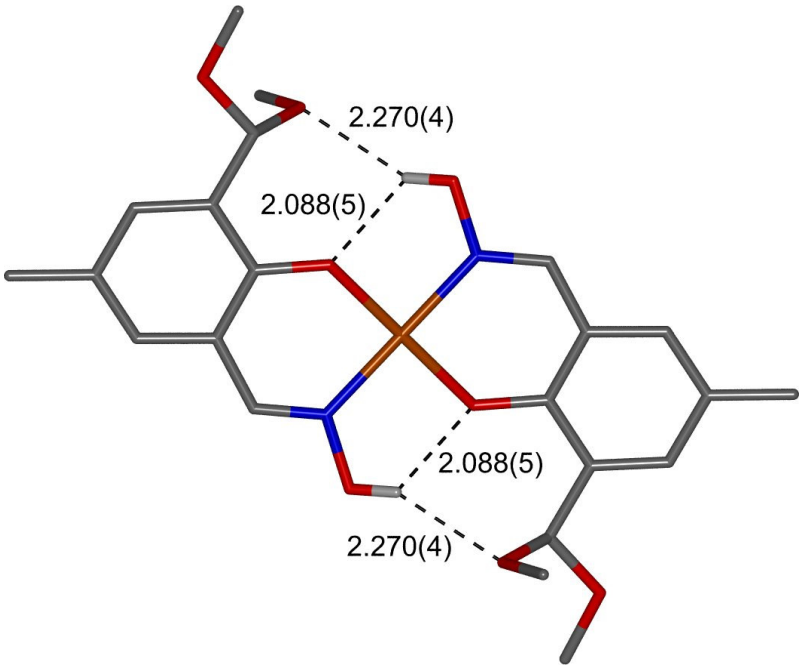

Figure 4-28: The crystal structure of RIBYEG,[51] a phenolic oxime copper complex retrieved from the CSD[52] with a dimethyl acetal substituent in the 3-position.

The electronic properties of the $(MeO)_2CH$ group will increase electron density on the ON^- donor set of the ligand. The 5-position is occupied by a methyl group which is somewhat different from the tertiary alkyl groups used in other structures but should have relatively small differences in electronic properties c.f. the ^{t}Bu groups. For [Cu(3-$((MeO)_2CH)$-5-Me-salox$)_2$] then the interactions marked **1**, **2**, **3**, and **4** in Figure 4-27 would all be beneficially affected in comparison to the X = H structure. This should mean that the hole-size and the ligand closeness measurements are smaller. The parameters for this compound are tabulated in Table 4-5.

Distance or angle	Value
Cu-O_1 /Å	1.864(3)
Cu-O_2 /Å	1.864(3)
Cu-N_1 /Å	1.946(4)
Cu-N_2 /Å	1.946(4)
OH…O_1 /Å	2.088(5)
OH…O_2 /Å	2.088(5)
O…O_1 /Å	2.652(5)
O…O_2 /Å	2.652(5)
OH…X_1 /Å	2.270(4)
OH…X_2 /Å	2.270(4)
O…X_1 /Å	3.033(5)
O…X_2 /Å	3.033(5)
Hole Size /Å	1.904(7)
'Ligand closeness' /Å	8.393(5)
O-M-N *intra*ligand /°	91.9(2)
O…N *intra*ligand /Å	2.738(5)
O…N *inter*ligand /Å	2.651(5)

Table 4-5: Geometric parameters for the structure of RIBYEG, [Cu(3-((MeO)$_2$CH)-5-Me-salox)$_2$].

The hole size, 1.904(7) Å, is the smallest for all structures but taking into account the e.s.d.s, the difference is not statistically significant. The Cu-O bond lengths are significantly shorter in this structure at 1.864(3) Å whilst the Cu-N bond lengths remain unchanged within experimental error. Unfortunately whilst this looks at face value like a potentially useful parameter, there is no trend which can be established according to Cu-O bond lengths for the whole set of structures.

4.5.1.3. Conclusions

It was initially thought that the 'pressure' applied to the copper and its inner coordination sphere by addition of hydrogen bonding between the salicylaldoxime ligands would be strong enough to alter the metal ion cavity size in copper complexes. Investigation found that a number of factors appear to influence the observed cavity sizes. It has also become apparent that simply measuring the hole-sizes as outlined in Figure 4-15 is insufficient in predicting the thermodynamic stability of complexes or solvent extraction strength of the ligand as, in contrast to the ligand dimers, measured hole sizes do not correlate to experimentally measured extractant strength. The structure of RIBYEG[51] implies that the hole size and ligand closeness may be altered by appropriate substitution but without extraction data for this complex, useful correlations between structure and extractant strength still cannot be made. Bulk also seems to have some effect on the ligand closeness as the tertiary butyl ligand had one of the largest in the series. The remaining structures showed no obvious trend with the H and Br structures being extremely similar despite the expectation that they would be very different.

4.5.2. Axially perturbed metal-only complexes

The previous section investigated the effects at play in the square-planar metal-only complexes with no axial interactions. In many cases, however, the copper atom which is normally square planar in solution has Jahn-Teller distorted octahedral geometry in the solid state with solvent molecules or neighbouring molecules coordinated to the axial copper sites. For the d^9 electronic configuration, square-planar transition metal geometry can be regarded as an extreme form of Jahn-Teller distortion.[53] The theorem can apply to any transition metal system in which there is degeneracy in the HOMO orbitals e.g. the e orbitals in a d^8 system like Ni^{2+} or a d^9 system like Cu^{2+}. The energy of the complex can be lowered if the degeneracy of the two orbitals is lost, for example in a high spin system the e_g

orbitals contain one unpaired electron each. Should the degeneracy be lost such that one orbital is lower in energy than the other, the electrons may pair up and occupy the lower energy orbital. The changes in energy depend on the ligand field stabilisation energy and therefore the ligands bound to the metal atom. This change in orbital energies can manifest as tetrahedral or square planar distortions, although the structures discussed in this section all exhibit essentially square geometry (in the xy plane) with very weak axial bonds along the z axis. As the nature of the ligands is important, the interdependence of the length of axial and equatorial bonds is difficult to predict given that there are two variables at play in this series of structures, the 3-substituent of the ligands and the axially bound ligand.

4.5.2.1. Summary of structures

In this work two structures were obtained in which axial interactions with the metal ion were present. In both structures the metal ion was copper and these are tabulated in Figure 4-29.

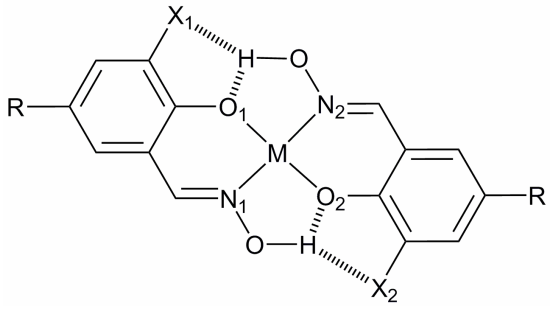

Abbreviated name	Sample code	R	X	Axial interaction
[Cu(5-^{t}Bu-salox)$_2$]	PT0532	^{t}butyl	H	neighbouring oximic O
[Cu(3-NO$_2$-5-^{t}Bu-salox)$_2$py$_2$]	PT6009	^{t}butyl	NO$_2$	pyridine

Figure 4-29: The metal complexes studied in this section with subscripts showing atom labelling used in Table 4-6.

4.5.2.1.1. [Cu(5-^{t}Bu-salox)$_2$] - PT0532

This structure crystallised in the triclinic space group $P\bar{1}$ with three half molecules in the asymmetric unit. Each molecule has axial interactions with the oximic oxygen atom of two of its neighbours forming a polymeric structure. These interactions link the molecules into triangular assemblies (left in Figure 4-30) which link up to form 2D sheets in the *ab* plane.

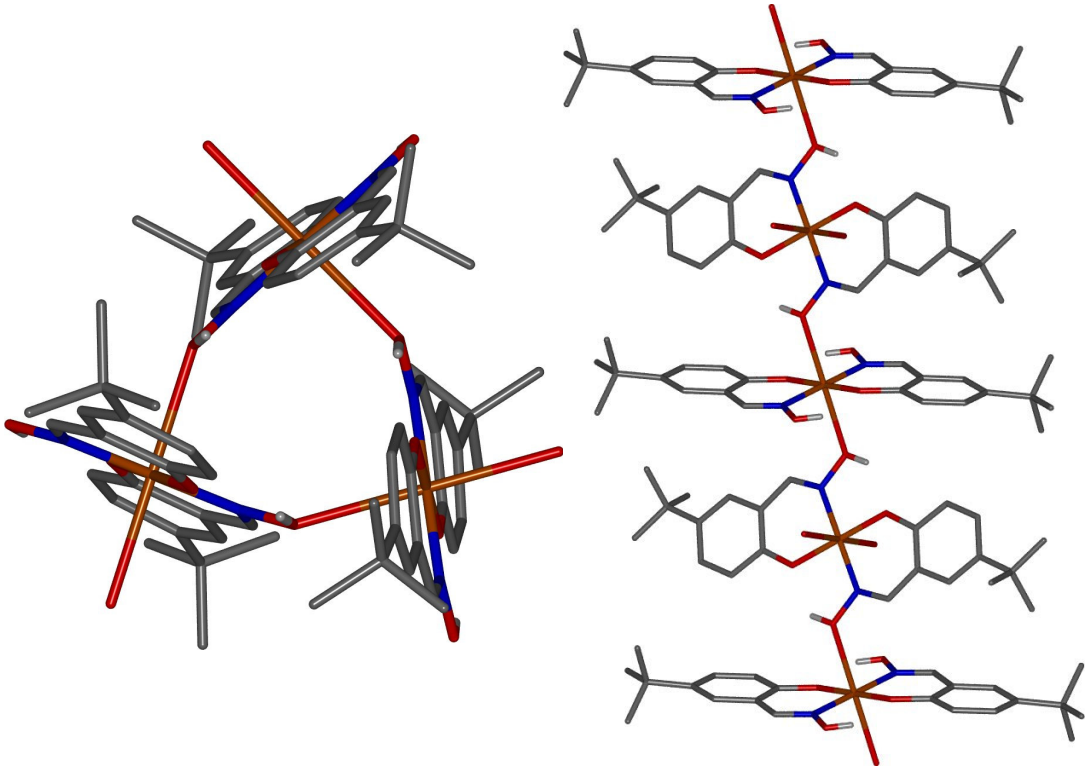

Figure 4-30: The structure of [Cu(5-^{t}Bu-salox)$_2$] showing the view down the *c* axis (left) and along the *a* axis (right).

4.5.2.1.2. [Cu(3-NO_2-5-^{t}Bu-salox)$_2$py$_2$] - PT6009

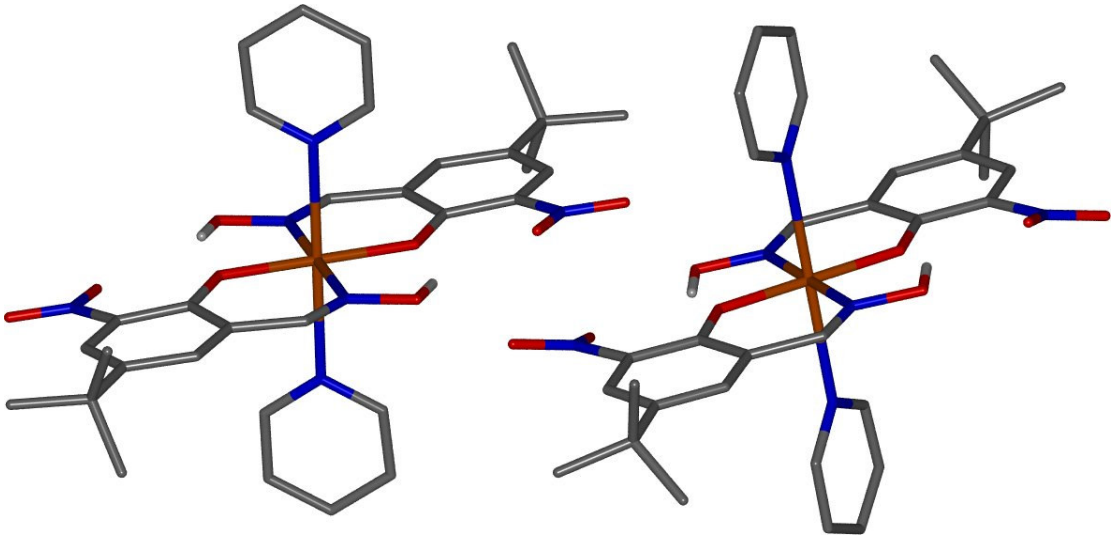

Figure 4-31: The two crystallographically independent molecules from the crystal structure of [Cu(3-NO_2-5-^{t}Bu-salox)$_2$py$_2$].

Axial positions are occupied by pyridine which was used as the recrystallising solvent. Intramolecular hydrogen bonds exist between the oximic oxygen atom and the nitro group with hydrogen bond H-A distances of 2.300(4) Å for one of the molecules and 2.310(4) Å for the other. There are no intermolecular hydrogen bonds and no π-π stacking interactions.

4.5.2.2. Analysis

The structure [Cu(5-^{t}Bu-salox)$_2$], PT0532, contains the copper complex formed with salicylaldoxime ligands in which X=H. This is similar to the structure [Cu(5-^{t}Bu-salox)$_2$], PT7029, the only difference in the ligand being tertiary butyl rather than tertiary pentyl which is not expected to have significant implications for the electronic structure. The introduction of axial interactions to the X=H structure would be expected to increase the hole-size by increasing the Cu-O and Cu-N bond lengths. The data in Table 4-6 shows that the Cu-O bond lengths have increased

slightly in length and that the Cu-N bond lengths have not. The overall hole size, however, does not appear to have changed, at least when considering errors.

Abbreviated Name	[Cu(5-^{t}Bu-salox)$_2$]			[Cu(3-NO_2-5-^{t}Bu-salox)$_2$py$_2$]	
Sample Code	PT0532			PT6009	
X	H			NO_2	
M-O_1 /Å	1.905(2)	1.900(2)	1.907(2)	1.926(4)	1.911(4)
M-O_2 /Å	1.905(2)	1.900(2)	1.907(2)	1.926(4)	1.911(4)
M-N_1 /Å	1.941(2)	1.945(2)	1.943(2)	1.956(5)	1.957(5)
M-N_2 /Å	1.941(2)	1.945(2)	1.943(2)	1.956(5)	1.957(5)
OH…O_1 /Å	1.920(1)	1.919(2)	1.915(2)	1.862(4)	1.846(4)
OH…O_2 /Å	1.920(1)	1.919(2)	1.915(2)	1.862(4)	1.846(4)
O…O_1 /Å	2.581(2)	2.583(5)	2.584(3)	2.658(6)	2.651(6)
O…O_2 /Å	2.581(2)	2.583(5)	2.584(3)	2.658(6)	2.651(6)
OH…X_1 /Å	-	-	-	2.300(4)	2.310(4)
OH…X_2 /Å	-	-	-	2.300(4)	2.310(4)
O…X_1 /Å	-	-	-	2.947(6)	2.919(6)
O…X_2 /Å	-	-	-	2.947(6)	2.919(6)
Hole Size /Å	1.923(4)	1.923(4)	1.917(4)	1.941(9)	1.934(9)
'Ligand closeness' /Å	8.424(1)	8.542(1)	8.459(1)	8.508(1)	8.489(1)
O-Mn-N *intra*ligand /°	92.3(1)	92.1(1)	91.8(9)	91.9(2)	91.5(2)
O…N *intra*ligand /Å	2.773(2)	2.769(3)	2.764(4)	2.791(5)	2.771(5)
O…N *inter*ligand /Å	2.665(3)	2.668(3)	2.681(3)	2.699(6)	2.700(7)
Axial bond /Å	2.588(3)	2.558(2)	2.591(3)	2.483(5)	2.560(4)

Table 4-6: Data for axially perturbed metal-only structures.

The NO_2 substituted unit, [Cu(3-NO_2-5-^{t}Bu-salox)$_2$], has bonds to two axial pyridine molecules. The pyridine is a stronger base than the oximic oxygen atoms which are axial donors in the solid state structure of [Cu(5-^{t}Bu-salox)$_2$]. This would imply stronger axial bonds which in turn would result in a larger hole size than in

[Cu(5-^{t}Bu-salox)$_2$]. The data in Table 4-6 show that this is indeed the case with the hole-size being slightly larger and the axial bonds significantly shorter for one of the molecules. The other molecule has a longer axial bond length which is reflected by a slightly smaller hole size. The role of the NO_2 group is, however, unclear, as was the case for X substitution in the previous section. Hydrogen bond buttressing by the NO_2 group is expected to reduce the hole size, but the electron withdrawing properties will weaken the Cu-O and Cu-N bonds. Addition of the axial pyridine groups will also weaken these bonds and thus increase the hole size. The latter two effects appear to dominate and result in overall increases in the hole size.

4.5.2.3. Conclusions

The axially perturbed metal-only complex series contains too few structures and too many variables to be able to draw any satisfying conclusions or identify any trends. Metal-only structures showed little in the way of useful trends for targeted ligand design based on variation of the 3-substituent. It appears that several factors affect the structure and that hydrogen bond buttressing or disruption is not the major factor influencing solid state structures. The addition of axial interactions serves only to further complicate matters by perturbing equatorial bonding. It does, however, appear that the axial perturbation is the dominant effect, provided a strong base is used to bond to the copper. In the next section, metal salt complexes are discussed in which the ligands are constant and the anion is located on the axial site. It was hoped that this would allow the effect of the axial perturbations on the hole size in the complexes to be analysed.

4.5.3. Metal salt complexes

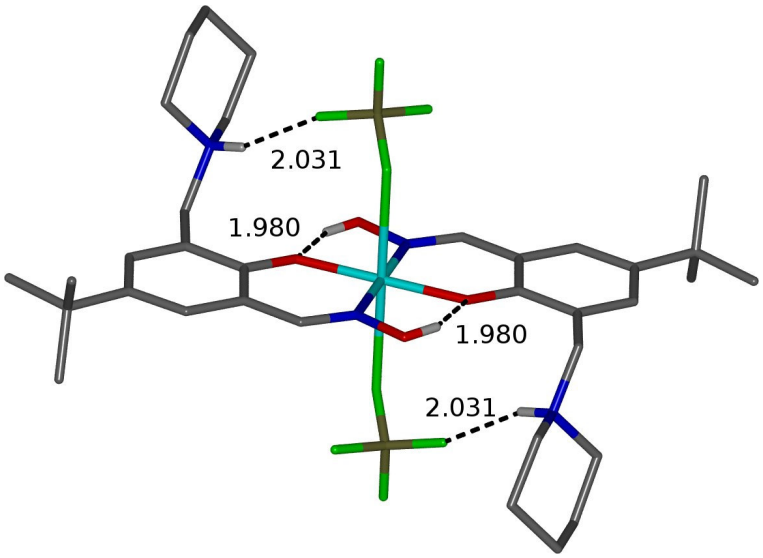

Figure 4-32: The molecular structure of [Cu(3-pipCH$_2$-5-^{t}Bu-salox)$_2$(BF$_4$)$_2$] in the solid sate showing intramolecular hydrogen bonds.

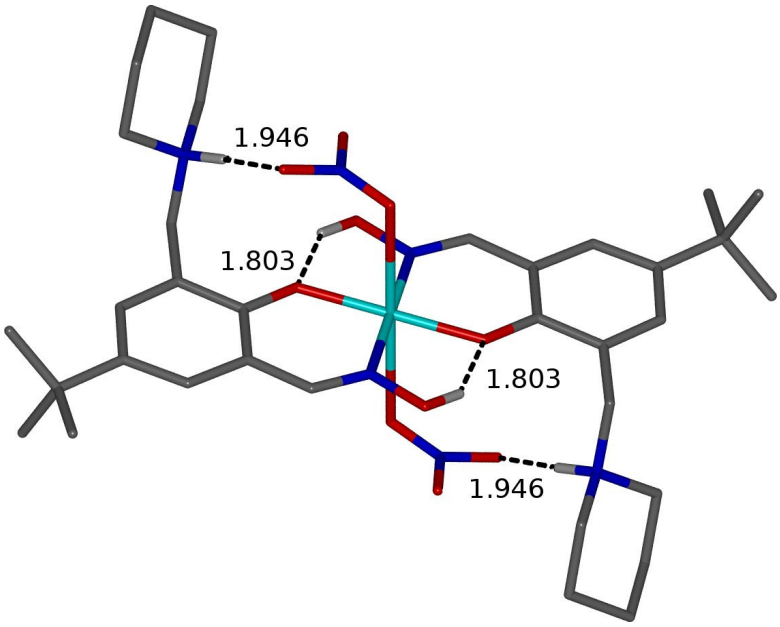

Figure 4-33: The molecular structure of [Cu(3-pipCH$_2$-5-^{t}Bu-salox)$_2$(NO$_3$)$_2$] in the solid state showing intramolecular hydrogen bonds.

In contrast to the structures discussed in the previous section, the two metal salt complexes discussed here are chemically identical except for the nature of the anion. In each case the anion is very weakly bonded to the copper atom and hydrogen bonded to the piperidinium NH. The data in Table 4-7 indicate that the axial interactions have led to small increases in the metal ion cavity radii over those observed (range: 1.904 – 1.925 and mean: 1.916 Å) for copper-only structures discussed in section 4.5.1 whilst not being as large as those for the axially perturbed copper-only complexes in section 4.5.2. The piperidinium NH…X hydrogen bond in the BF_4 structure is likely to be stronger than in the NO_3^- structure despite the slightly longer H…A distance due to fluorine acting as the acceptor. The BF_4 structure also has a shorter axial bond length than in the NO_3 structure. It is possible that the strength of the hydrogen bond and the axial bond length are linked.

Anion	BF_4^-	NO_3^-
Axial Cu-X distance /Å	2.638(2)	2.722(2)
Cu-O /Å	1.920(2)	1.912(1)
Cu-N /Å	1.943(2)	1.946(1)
NH-X hydrogen bond D…A /Å	2.780(3)	2.842(2)
H…A /Å	2.031(4)	1.946(2)
Cavity size /Å	1.931(4)	1.929(2)

Table 4-7: Selected structural parameters from tritopic metal salt complexes [Cu(3-pipCH$_2$-5-^{t}Bu-salox)$_2$(BF$_4$)$_2$] and [Cu(3- pipCH$_2$-5-^{t}Bu-salox)$_2$(NO$_3$)$_2$].

With only two structures in this sample set it is difficult to draw any conclusions as to the effect of anion substitution. Shorter axial bonds (2.638(2) c.f. 2.722(2) Å) in the BF_4^- structure lead to longer equatorial bonds overall with Cu-O bond lengths being longer (1.920(2) c.f. 1.912(1) Å) and no significant difference in Cu-N bonds (1.943(2) c.f. 1.946(1) Å) compared to the NO_3^- structure.

4.5.4. Metal halide complexes

Base metal chloride feeds for extractive metallurgy can now be generated very efficiently[35, 36] by the oxidative leaching processes described in section 4.3.2.2. Transport of a metal chloride salt across the phase boundary as in $MCl_2 + L_{(org)} \rightarrow [MLCl_2]_{(org)}$ is a desirable route to recovery of the base metal because it can lead to very good materials balance in the circuit (see section 4.3.2.2). Also the conventional pH-swing reagents which transport the metal as in $MCl_2 + 2LH_{(org)} \rightleftharpoons [ML_2]_{(org)} + 2HCl$ are inefficient in processing feeds with high chloride concentrations because these have very high proton activity.

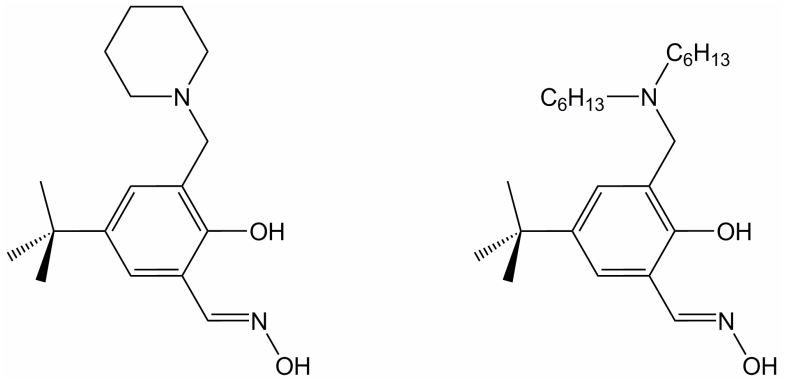

Figure 4-34: The ligands, 3-(pipCH_2)-5-^{t}Bu-salox and 3-(($(C_6H_{13})_2$NCH2)-5-^{t}Bu-salox which can be used as a metal *salt* extractants.

The salicylaldoxime metal *salt* extractants shown in Figure 4-34 were tested[1, 44] as extractants for base metal chlorides. It was expected that these would give tritopic assemblies, $[ML_2Cl_2]$, as shown in Figure 4-35a with the chloride anions hydrogen-bonded to the pendant alkylammonium groups. When the organic phases of these extraction experiments were analysed, loadings of greater than 100% based on formation of $[ML_2Cl_2]$ were observed, and under forcing conditions loadings of close to 200% were detected. This is consistent with the formation of a 1:1 ligand to metal chloride complex with the extracted species having the formula $[MLCl_2]$.

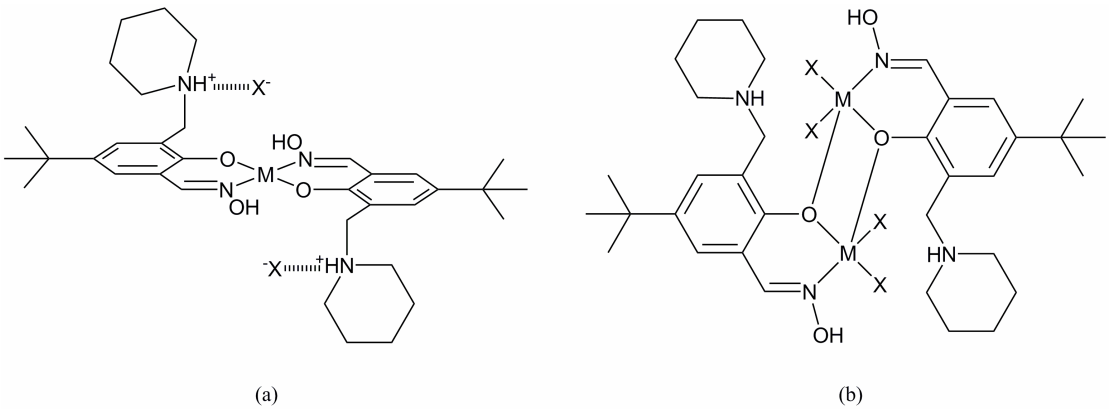

Figure 4-35: (a) The expected tritopic assembly for MX_2 loading by the salicylaldoxime metal *salt* extractants. (b) The arrangement observed in crystal structures of copper(II) and zinc(II) halide complexes with 3-(pip CH_2)-5-^{t}Bu-salox.

X-ray structure determinations[44, 54] of complexes of $CuCl_2$, $ZnCl_2$ and $CuBr_2$ confirm the formation of complexes with such stoichiometry. In the solid state these form dimers of the type shown in Figure 4-35b. An understanding of what favors the formation of these $[M_2L_2Cl_4]$ units is of great interest because the mass transport efficiency of metal chloride (1 mol per mol of ligand) is double that in the tritopic assembly (Figure 4-35a).

4.5.4.1. $[Cu_2Br_2(3\text{-}pipCH_2\text{-}5\text{-}^tBu\text{-}salox)_2]$ – PT6010

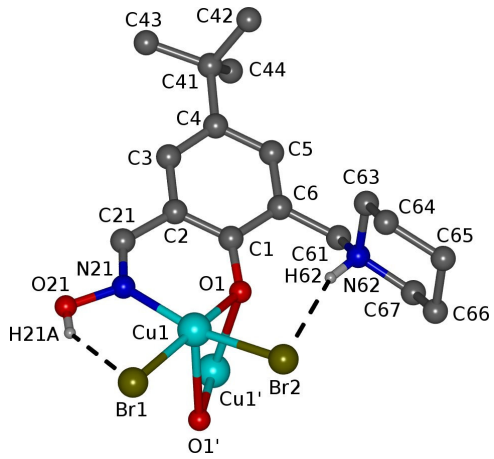

Figure 4-36: The asymmetric unit of $[Cu_2Br_2(3\text{-}pipCH_2\text{-}5\text{-}^tBu\text{-}salox)_2]$ with atom labelling relevant to Table 4-7 and symmetry equivalents of Cu1 and O1 shown.

The structure, shown in Figure 4-37, is isostructural with $[Cu_2Cl_2(3\text{-}pipCH_2\text{-}5\text{-}^tBu\text{-}salox)_2]$ and similar to $[Zn_2Cl_2(3\text{-}pipCH_2\text{-}5\text{-}^tBu\text{-}salox)_2]$ previously reported by Dr James Davidson[54] with connectivity as shown in Figure 4-35b. There was mild disorder in the position of the one of the bromine atoms which was treated as two components, the primary component having a site occupancy factor of 0.95. The NH group of the piperidinium group forms a hydrogen bond to one of the bromine ions at a DH…A distance of 2.84 Å. The oximic hydrogen atom also forms a hydrogen bond to the nearest bromine atom with a DH…A distance of 2.306 Å and there are no intermolecular hydrogen bonds as with the structures reported by James Davidson.[54]

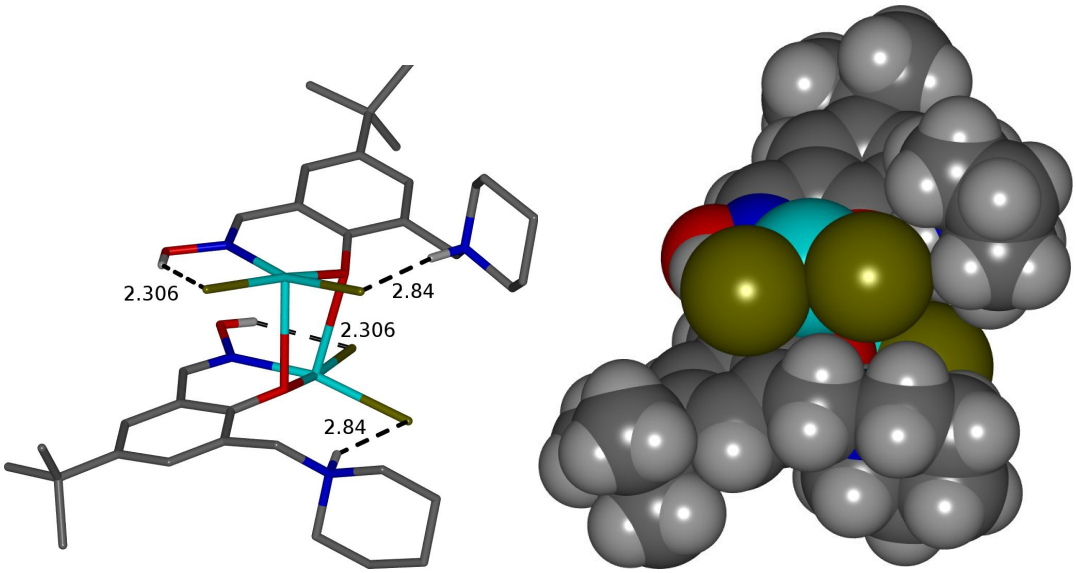

Figure 4-37: The molecular structure of $[Cu_2Br_2(3\text{-}pipCH_2\text{-}5\text{-}^tBu\text{-}salox)_2]$ in the solid state.

The $[MLX_2]$ units and the dimers $[M_2L_2X_4]$ are charge neutral because the complex is formed between the MCl_2 unit and a zwitterionic form of the ligand. Whilst the metal dication is surrounded by a trianionic NOX_2^{3-} donor set the complex is neutral because the pendant piperidine groups are protonated. In the solid state structures of all the copper(II) and zinc(II) halide complexes of the salicylaldoxime metal *salt* extractants the halide ions are present in the inner coordination sphere of the metal ion and the tritopic assemblies of the type shown in Figure 4-35a are not observed. The Cu-Cl, Cu-Br and Zn-Cl bond lengths (see Table 4-8) fall within the ranges (2.052 to 3.196 Å, 2.162 to 3.428 Å and 2.278 to 2.778 Å) found within the CSD.

A comparison of the various parameters in the structure of [Cu_2Br_2(3-pipCH_2-5-^{t}Bu-salox)$_2$] with those of the zinc chloride and copper chloride analogues is given in Table 4-8. Substitution of the copper atom with zinc gives longer bonds as the covalent radius is larger. The Zn structure is significantly distorted from square planar geometry and there is solvent in the unit cell. In the $CuCl_2$ and $CuBr_2$ structures a 2-fold rotation axis runs through the centre of the Cu_2O_2 unit and so only half of the molecule is present in the asymmetric unit. The change in metal ion geometry for the $ZnCl_2$ structure removes this symmetry element and so one complete molecule is in the asymmetric unit. It is therefore in a different space group, $P\bar{1}$, to the others which are in *Pbcn*. The ONX_2^{3-} donor sets are slightly distorted from planar in the copper complexes with angles of 5.4(1)° and 14.2(1)° between the Cu-Cl vectors and the plane defined by Cu-O1-N21 and 5.0(1)° and 13.5(1)° for their equivalents in the bromide structure. This gives the copper square pyramidal geometry in contrast with the zinc chloride structure which is best described as trigonal bipyramidal with O1'-Zn1-Cl1 and O1-Zn2-Cl1' forming the approximately linear axes around which the trigonal equatorial donor sets sit. In this structure the angles made by Zn-Cl vectors with the planes defined by the Zn-N-O atoms are 8.6(1)° and 53.5(1)° for one of the Zn atoms and 13.8(1)° and 56.5(1)° for the other. The equatorial angles are 112.2(1), 121.2(1), 123.3(1) and 114.5(1), 116.2(1), 126.4(1). As a result of this different geometry, the $ZnCl_2$ structure has significantly shorter M-O1' distances than the $CuCl_2$ structure which results in a shorter M1…M1' distance.

	$CuCl_2$	$ZnCl_2$		$CuBr_2$
Distance/Angle		Part A	Part B	
d(O21-H)	0.84	0.84	0.84	0.841(2)
d(H..X)	2.226	2.290	2.260	2.306(1)
<O-H…X	140.8	143.0	145.0	147.3(1)
d(O21…X)	2.925 (3)	3.003(3)	2.986(2)	3.047(2)
d(N62-H)	0.803	0.93	0.93	0.87(3)
d(H…O1)	2.05 (4)	2.510	2.430	2.17(3)
<N62-H...O1	147(4)	120.0	122.0	130(3)
d(N62…O1)	2.754(3)	3.079(3)	3.024(3)	2.803(3)
d(H…X)	2.901 (4)	2.480	2.560	2.84(3)
<N62-H...X	142 (3)	162.0	160.0	154(3)
d(N62…X)	3.560 (3)	3.379(2)	3.446(2)	3.642(3)
d(M1-O1)	1.933(2)	2.0775(17)	2.1085(17)	1.922(2)
d(M1-N21)	2.021(3)	2.121(2)	2.116(2)	2.013(3)
d(M1-X1)	2.2689(9)	2.2853(8)	2.2679(7)	2.403(1)
d(M1-X2)	2.2682(9)	2.3620(7)	2.3715(7)	2.415(1)
d(M1-O1')	2.570(2)	2.0213(18)	2.0310(18)	2.630(2)
<(O1-M1-N21)	87.27(10)	81.91(8)	82.69(8)	87.44(9)
<(O1-M1-X2)	91.12(7)	91.87(5)	90.85(5)	91.00(6)
<(O1-M1-X1)	173.84(8)	167.66(5)	163.99(5)	174.71(6)
<(N21-M1-X2)	165.69(9)	126.36(7)	123.28(7)	166.37(7)
<(N21-M1-X1)	89.76(8)	89.24(6)	89.20(6)	90.77(7)
<(X2-M1-X1)	93.08(3)	100.32(3)	105.12(3)	91.89(2)
<(O1-M1-O1')	81.68(8)	78.83(7)	77.90(7)	82.35(7)
<(O1'-M1-N21)	99.34(10)	116.21(9)	121.18(8)	99.98(7)
<(X1-M1-O1')	93.49(5)	114.54(6)	112.05(6)	93.06(4)
<(Cl2-M1-O1')	94.47(6)	97.61(5)	94.79(5)	93.23(5)
d(M1…M1')	3.3698 (9)	3.1620(5)		3.367(1)
<(M1-O1-M1')	95.86(8)	100.63(9)		82.35(7)
<(M1'-O1'-M1)	95.86(8)	99.91(10)		82.35(7)
<(C1-C6-C61-N62)	55.6 (4)	-70.3(3)	-66.5(3)	-57.5(3)
<(C6-C61-N62-H62)	-53 (3)	51.3	53.0	55(2)
<(C6-C61-N62-C63)	63.3 (3)	-67.4(3)	-65.8(3)	-62.7(3)
<(C6-C61-N62-C67)	-172.0 (3)	169.1(2)	171.0(2)	172.7(2)

Table 4-8: Selected distances, angles and torsions relating to the structures of metal halide complexes.

The $CuBr_2$ structure is very similar to the $CuCl_2$ structure. The metal ion geometry differs slightly with shorter Cu-O1 and Cu-N21 and longer Cu-X distances observed in the bromo structure. The longer Cu-X bond length is due to the larger ionic radius of the Br atom. The Cu-O1' bond lengths are longer in the bromo structure by

approximately 0.06 Å. The longer Cu-X and Cu-O' distances (ca. 2.41 and 2.63 Å c.f. 2.27 and 2.57 Å) in the bromo structure means that the electron density around the Cu atom is reduced which allows the N and O atoms to approach it more closely giving the shorter Cu-N and Cu-O bond lengths in the bromo structure. The Cu-O and Cu-N distances are much longer than those in the 2:1 ligand to copper complexes discussed in earlier sections (the mean values for the complexes in Table 4-8 are 1.983 and 2.051 Å compared to 1.890 and 1.941 Å for those in Table 4-2). This is also likely to be due to the crowding of negative charge around the Cu atom making these bond lengths larger.

The assembly to form dimers which present a largely hydrophobic exterior (see Figure 4-37) helps to explain why copper extraction into non-polar water-immiscible solvents is so efficient with these new reagents.[44] The polar functionalities and the attendant halide anions in the copper salt complexes are located in the centre of the assembly and are screened form the non polar solvent.

4.6. Conclusions

At the beginning of the work described in this chapter evidence had been obtained by other workers at Edinburgh that the structures of the ligand dimers in the solid state, particularly their observed 'hole-sizes' correlated well with the ligands' extractant strengths as copper-extractants. It was expected that a similar correlation would be found to link the radii of the donor set cavities in the copper complexes in the solid state with the ligands' strengths as copper-extractants. This was not found in practice because a number of other issues must be considered in relating hole sizes in *the complexes* with ligands' extractant strengths. It was found that the situation is complicated.

It had been assumed that the measurements of the hole sizes would correlate with the thermodynamic stability of the copper(II) complex. Even if this were true (see below) there is no reason why the thermodynamic stability of a copper complex

would correlate directly with the extractant strength of the complexed ligand because this also depends on the acidity of the ligands[29] and other solution-dependent phenomena which relate to solvation and re-organization of ligand substituents.

On reflection, it is also clear that variations in the hole sizes observed in the solid state forms of copper complexes will not necessarily reflect their relative thermodynamic stabilities. The original hypothesis fails to account for any effects of the 3-substituents beyond those of strengthening the hydrogen bonding between ligands within the complex, the so called "buttressing" effect. This will clearly dominate in determining the hole sizes in the *free ligands* and whilst it will make a favourable contribution to the stability of the copper *complexes*, it is only one of the factors involved in bonding in the inner and outer coordination spheres I the complexes. For the series of complexes analysed in this work, the electronic effects of ligand substitution in the 3-position seems also to play an important role.

In addition to the flaws in the hypothesis that hole sizes in the complexes would reflect the relative thermodynamic stabilities of the complexes and the "strength" of the ligands, there was a major practical difficulty in using solid state structures to probe the binding strengths of the oximate ligands. Some of the solid state structures were found to have significant interactions with axial ligands. These will have a significant effect on the charge densities at the copper centres and consequently will influence the equatorial copper to donor atom bond lengths and hole sizes defined by the oximate ligands.

The Cu-O bond lengths appear to be affected more than the Cu-N bond lengths with average Cu-O, Cu-N bond lengths of 1.890 and 1.941 Å for square planar complexes and 1.911 and 1.947 Å for those with axial interactions. Shorter axial bond lengths led to larger hole sizes which was expected, although the basicity of the axial group appears to be important too. The relationship between axial bond lengths and the hole size are explored in more depth in the next chapter using high pressure as a probe.

The ability to tune extractant strengths through ligand substitutions is of great practical importance. Whilst extractant strength has been shown to vary significantly with 3-substitution,[27, 29] the work reported in this chapter indicates that it is difficult to interpret full how these variations in strength arise. Groups which both buttress interligand hydrogen bonding and increase the acidity of the phenol groups are always stronger extractants but this does not lead to shorter Cu-O and Cu-N bond lengths and smaller ligand cavities.

Solid-state structure determination proved key to defining the origin of unexpectedly high efficiencies of transporting copper chloride by the metal *salt* extractants and has pointed the way to enhancing the solubilities of these new reagents.

4.7. References

1. R. Forgan, *PhD Thesis*, University of Edinburgh, 2008.
2. N. N. Greenwood and A. Earnshaw, *Chemistry of the Elements*, Butterworth-Heinmann, 1997.
3. in *Kirk-Othmer Encyclopedia of Chemical Technology*, eds. M. Grayson and D. Eckroth, Editon edn., 1978.
4. Berthelot, *Comptes Rendus Hebdomadaires des Seances de l'Academie des Sciences*, 1902, **134**, 142-146.
5. *Dartmouth Toxic Metal Research*, http://www.dartmouth.edu/~toxmetal/TXSHcu.shtml, Accessed 23/09/2008, 2008.
6. *Chinese Cultural Items*, http://djtravel.homestead.com/Souvenirs.html, Accessed 23/09/2008, 2008.
7. *The Metropolitan Museum of Art*, http://www.metmuseum.org/toah/hd/cyco/ho_74.51.5283.htm, Accessed 23/09/2008, 2008.
8. S. Hong, J. P. Candelone, C. C. Patterson and C. F. Boutron, *Science*, 1996, **272**, 246.
9. *Copper.org*, http://www.copper.org/education/c-facts/c-home.html, Accessed 23/09/2008, 2008.
10. T. Chu and M. Yamada, *Japanese Jounal of Applied Physics, Part 1*, 1999, **38**, 1153-1155.
11. F. Briganti, A. Scozzafava and C. T. Supuran, *European Journal of Medicinal Chemistry*, 1997, **32**, 901-910.
12. N. Borduas and D. A. Powell, *Journal of Organic Chemistry*, 2008, **73**, 7822-7825.
13. N. Kristoffel, P. Rubin and T. Ord, *Journal of Physics: Conference Series*, 2008, **108**.
14. P. J. Mackey, in *CIM Magazine*, Editon edn., 2007, vol. 2, p. 35.
15. *The London Metal Exchange*, http://www.lme.co.uk/copper_graphs.asp, Accessed 23/09/2008, 2008.
16. *ContractJournal.com*, http://www.contractjournal.com/Articles/2008/08/11/60760/copper-theft-causes-five-hour-train-delays.html, Accessed 23/09/2008, 2008.
17. D. J. G. Ives, *Principles of the Extraction of Metals*, Royal Institute of Chemistry, 1960.
18. T. W. Swaddle, ed., *Inorganic Chemistry: An industrial and environmental perpesctive*, 1996.
19. R. Sridhar, J. M. Toguri and S. Simeonov, *JOM*, 1997, **49**, 48-52.
20. F. Habashi, *Handbook of Extractive Metallurgy*, Wiley-VCH Verlag GmbH, 1997.
21. G. A. Kordosky, International Solvent Extraction Conference, Cape Town, South Africa, 2002.

22. P. A. Tasker, P. G. Plieger and L. C. West, *Comprehensive Coordination Chemistry II*, 2004, **9**, 759.
23. M. Yamada, J. M. Perera, F. Grieser and G. W. Stevens, *Analytical Sciences*, 1998, **14**, 225-229.
24. C. Hanson, M. A. Hughes and R. J. Whewell, *Journal of Applied Chemistry & Biotechnology*, 1978, **28**, 426-434.
25. C. Parija and P. V. R. Bhaskara Sarma, *Hydrometallurgy*, 2000, **54**, 195-204.
26. D. Doungdeethaveeratana and H. Y. Sohn, *Hydrometallurgy*, 1998, **49**, 229-254.
27. P. A. Wood, R. F. Forgan, A. R. Lennie, S. Parsons, E. Pidcock, P. A. Tasker and J. E. Warren, *CrystEngComm*, 2008, **10**, 239-251.
28. R. F. Forgan, P. A. Wood, J. Campbell, D. K. Henderson, F. E. McAllister, S. Parsons, E. Pidcock, R. M. Swart and P. A. Tasker, *Chemical Communications*, 2007, **46**, 4940-4942.
29. P. A. Wood, D. K. Henderson, F. E. McAllister, P. A. Tasker, F. J. White, J. Campbell and R. M. Swart, *Canadian Metallurgy Quarterly*, 2008, **47**, 293-300.
30. S. G. Galbraith, *PhD Thesis*, University of Edinburgh, 2005.
31. S. G. Galbraith and P. A. Tasker, *Supramolecular Chemistry*, 2005, **17**, 191-207.
32. J. O. Marsden, R. E. Brewer and N. Hazen, Proceedings of the International Symposium honoring Professor Ian M. Ritchie, 5th, Vancouver, BC, Canada, 2003.
33. J. D. Batty and G. V. Rorke, *Hydrometallurgy*, 2006, **83**, 83.
34. M. E. Clark, J. D. Batty, C. B. van Buuren, D. W. Dew and M. A. Eamon, *Hydrometallurgy*, 2006, **83**, 3.
35. D. Muir, in *Chloride Metallurgy 2002 - Volume II, 32nd Annual Hydrometallurgy Meeting of CIM*, CIM, Montreal, Canada, Editon edn., 2002.
36. G. Senanayake and D. M. Muir, Proceedings of the International Symposium honoring Professor Ian M. Ritchie, Vancouver, BC, Canada, 2003.
37. J. Liddicoat and D. Dreisinger, *Hydrometallurgy*, 2007, **89**, 323-331.
38. R. W. Gibson and N. M. Rice, in *Hydrometallurgy and Refining Nickel and Cobalt, 27th Annual Hydromettalurgy Meeting of CIM*, Sudbury, Canada, Editon edn., 1997.
39. P. A. Tasker and D. J. White, *Extraction of metal salts from aqueous solutions, WO2000-GB1251*, 2000.
40. Bruker-Nonius, Bruker-AXS, Madison, Wisconsin, USA, Editon edn., 2002.
41. G. M. Sheldrick, Bruker-AXS, Madison, WIsconsin, USA, Editon edn., 2004.
42. G. M. Sheldrick, University of Gottingen, Germany and Bruker-AXS, Gottingen, Germany and Madison, Wisconsin, USA, Editon edn., 2001.
43. P. T. Beurskens, G. Admiraal, G. Beurskens, W. P. Bosman, S. Garcia-Granda, R. O. Gould, J. M. M. Smits and C. Smykalla, Crystallography Laboratory, University of Nijmegen, Editon edn., 1999.
44. R. F. Forgan, J. E. Davidson, S. G. Galbraith, D. K. Henderson, S. Parsons, P. A. Tasker and F. J. White, *Chemical Communications*, 2008, **34**, 4049-4051.
45. T. Steiner, *Angewandte Chemie, International Edition*, 2002, **41**, 48-76.

46. L. Pauling, *The Nature of the Chemical Bond*, Third edn., Cornell University Press, Ithaca, 1960.
47. D. Harker, *Zeitschrift fuer Kristallographie, Kristallgeometrie, Kristallphysik, Kristallchemie*, 1936, **93**, 136-145.
48. H. V. Brand, *Journal of Physical Chemistry B*, 2005, **109**, 13668-13675.
49. A. Katrusiak, *Acta Crystallographica, Section B*, 1990, **46**, 246-256.
50. E. V. Boldyreva, *Journal of Molecular Structure*, 2003, **647**, 159-179.
51. E. V. Rybak-Akimova, D. H. Busch, P. K. Kahol, N. Pinto and N. W. Alcock, *Inorganic Chemistry*, 1997, **36**, 510.
52. F. H. Allen, *Acta Crystallographica, Section B*, 2002, **58**, 380-388.
53. D. F. Shriver and P. W. Atkins, *Inorganic Chemistry*, Third edn., Oxford University Press, 2001.
54. J. E. Davidson, *PhD Thesis*, University of Edinburgh, 2005.

Chapter 5

High Pressure Crystallographic Studies:

A Metal S*alt* Solvent Extraction Agent

Contents

5. Background

In this chapter a compression study of one of the metal salt complexes, [Cu(3-pipCH$_2$-5-^{t}Bu-salox)$_2$(NO$_3$)$_2$] (Figure 5-1), discussed in chapter 4 is presented. The previous chapter investigated the effect of chemical substitution of ligands on complexes related to those involved in extractive metallurgy processes. The effect of pressure on ligand dimers has previously been studied and this chapter seeks to advance this by examining its effect on the unit cell dimensions, molecular geometry (including the effect on metal-donor bonds) and crystal packing in a copper complex.

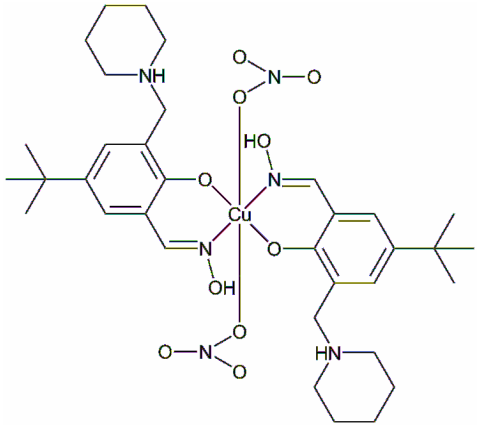

Figure 5-1: The metal salt complex, [Cu(3-pipCH$_2$-5-^{t}Bu-salox)$_2$(NO$_3$)$_2$], studied in this chapter.

5.1. High pressure X-ray diffraction

The application of pressure to systems can give rise to very interesting phenomena in a material such as inducing metallic behaviour in hydrogen,[1] or inducing superconductivity in silicon.[2, 3] Recently, the effect of pressure on organic compounds in the solid state has been investigated. Examples include the study of amino acids, such as glycine[4, 5] and L-serine,[5-8] and protein structures such as tetragonal lysozyme found in chicken egg white,[9] and cubic cowpea mosaic virus[10]. Such work has mostly been limited to single crystal diffraction below 10 GPa.

Nevertheless the results have been of interest for the light they shed on areas such as polymorphism and the factors which determine the course of phase transitions. High pressure structural research has the potential to be of value to the pharmaceutical industry[11, 12] given the phase of a chemical may affect properties such as solubility and the preparation of drugs often involves application of pressure which may induce phase transitions. Recently it has been shown that high pressure phases of maleic acid, malonamide and paracetamol can be recovered at ambient pressure.[13] Study of pressure-induced changes in molecular systems has enormous potential to aid understanding of structure-activity relationships and with recent developments in high pressure cell design coupled with the use of synchrotron radiation larger molecules can be studied. This technique has been used to enhance understanding of magneto-structural correlations in single molecule magnets.[14]

5.2. The Diamond Anvil Cell (DAC)

Pressure (P) is defined by the equation $P = F/a$, which indicates that the pressure applied varies inversely with the surface area (a) over which a force (F) is applied. The implication of this is that extremely high pressures can be applied to a sample with relatively low force if the sample chamber is small.

A diamond anvil cell uses this principle to apply pressures up to hundreds of thousands of atmospheres by applying load to two diamond anvils which are opposed above and below a drilled gasket to form a sample chamber. The form of the diamond anvil cells used in this thesis is based on the design of Merrill and Bassett[15] shown in Figure 5-2.

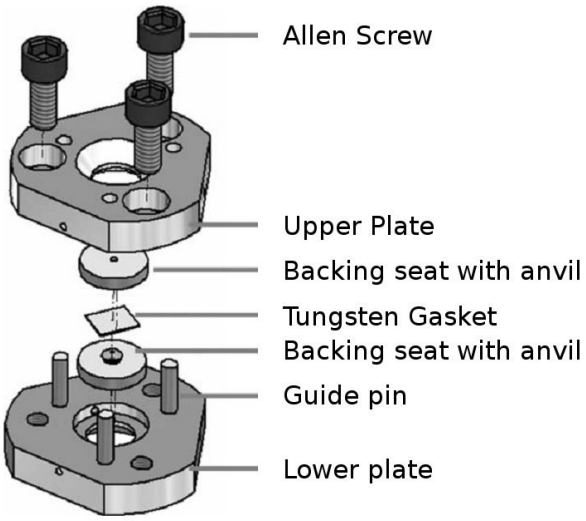

Figure 5-2: An exploded view of the Merill-Bassett diamond anvil cell[15] showing the steel plates comprising the cell body, backing disks with anvils and gasket. Pressure is applied using Allen screws.

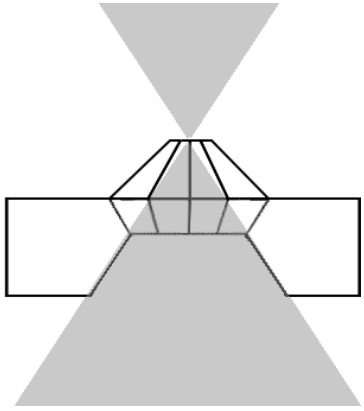

Figure 5-3: The passage of X-rays through a tungsten carbide cell. To provide sufficient support for the diamond, and to allow X-ray access to the sample, the backing disk specially cut.

In this design two modified Boehler-Almax cut gem-quality diamonds are used; the diamonds are cut with a flat face or *culet* of approximately 600 µm. Each diamond is set into a tungsten-carbide backing disk which provides support and is cut with an opening angle of 80° to allow access to the sample (see Figure 5-3).[18] These are set in a steel mount, and the cell is assembled with the culet faces of each diamond opposing each other across a hole (ca. 300 µm) drilled into a tungsten gasket. The inside edges of the hole and the culets of the top and bottom diamonds form a sample

chamber. Force is applied to the top and bottom faces of the cell, and pressure generated in the sample chamber, by screwing together the two halves of the cell together.

In order to ensure hydrostatic conditions in the sample cavity a sample is always mounted along with a pressure transmitting medium. These are usually liquids; examples include paraffin, isopropyl alcohol or mixtures of various solvents such as a 4:1 ethanol methanol mixture. The choice of medium used depends on the pressure range over which the medium retains its hydrostatic properties; for example 4:1 ethanol methanol remains hydrostatic up to 10 GPa, but becomes vitreous beyond this pressure. In addition, of course, the medium chosen must not react with or dissolve the material under investigation.

Pressure inside the cell is measured using ruby fluorescence. When excited with laser light, ruby (Cr-doped Al_2O_3) fluoresces producing an intense doublet at approximately 694 nm.[16] The wavelength at which the signal is observed lengthens with increasing pressure and the shift has been calibrated to the Decker equation of state for NaCl,[17] allowing the pressure inside the cell to be measured.

The size of the sample chamber places constraints on the size of crystal which can be used, and this means that diffraction data sets collected at high pressure tend to be weaker than those collected at ambient pressure (particularly as they are also collected at ambient temperature). In addition, incident and diffracted X-ray beams pass through the diamond anvils. Although carbon is light enough that absorption of the X-rays with $\lambda < 0.8$ Å is low enough that useful diffraction data can be collected, absorption remains a significant systematic error. Absorption errors can be reduced by using short wavelength X-rays. Finally, shading of reciprocal space by the body of the pressure cell means that high-pressure data sets suffer from low-completeness; this can also be minimised by using short wavelength radiation. The need for intense, short-wavelength X-rays makes synchrotron radiation a natural choice for high-pressure work.

5.3. Experimental

A crystalline sample of [Cu(3-pipCH_2-5-^{t}Bu-salox)$_2$(NO_3)$_2$] was supplied by Dr Ross Forgan. A single crystal measuring 0.03 by 0.07 by 0.10 mm was selected and placed inside a diamond anvil cell with a small chip of ruby as the pressure calibrant and a 4:1 methanol:ethanol solution as the hydrostatic medium. Data were then collected according to procedures established by Dawson *et al.*[19] on Station 9.8 at the Synchroton Radiation Source, Daresbury laboratory, using X-rays with $\lambda = 0.4863$ Å. These data were integrated using the program SAINT[20] with dynamic masks generated by ECLIPSE[21] used to treat detector regions shaded by the cell body and to remove intense rings caused by diffraction from the tungsten gasket. Absorption corrections were then applied using a two-stage process with the programs SHADE[22] and SADABS.[23] Data-sets were recorded at approximately 0.5 GPa intervals up to a final pressure of 3.8 GPa.

Refinements were carried out using the coordinates determined at low temperature and ambient pressure for initial atom positions. Minimisation was carried out against $|F|$ using all data.[24] As the data-sets exhibited low completeness, all bond distances and angles in the ligands were restrained to values observed in the ambient pressure structure. All non-hydrogen atoms were refined with anisotropic displacement parameters and in some cases thermal similarity restraints were used to improve poor ellipsoid shapes. At the lowest pressures high thermal motion is evident in the NO_3^- group which has been modelled using ADP's rather than two component disorder.

As pressure was applied to the crystal, data quality gradually deteriorated. At the highest pressure (3.8 GPa) data quality had reduced considerably and higher resolution data negatively impacted data integration and so fewer reflections were available for use in refinement. For the 3.8 GPa structure, symmetry was consistent with P*n*. However, in order to maintain a more reasonable data-to-parameter ratio, the model is in $P2_1/n$ with two-component disorder and isotropic displacement

parameters for non-centrosymmetrically related parts of the complex. The aromatic ring was refined as a rigid body with one set of ADP's to describe thermal motion.

Table 5-1 provides details of the crystal data and refinement data for all data-sets. Structural visualisations were produced using either Mercury CSD[25] or Diamond[26] and the void diagrams presented in section 5.4.2.3 were produced using the program Mercury CSD using a probe radius of 0.5 Å and a grid spacing of 0.4 Å.

Pressure (GPa)	**0**	**0.2**	**0.7**	**1.1**	**1.7**	**2.4**	**2.9**	**3.8**
Chemical formula	$C_{34}H_{52}CuN_6O_{10}$	$C_{34}H_{52}CuN_6O_{10}$	$C_{34}H_{52}CuN_6O_{10}$	$C_{34}H_{52}CuN_6O_{10}$	$C_{34}H_{52}CuN_6O_{10}$	$C_{34}H_{52}CuN_6O_{10}$	$C_{34}H_{52}CuN_6O_{10}$	$C_{34}H_{52}CuN_6O_{10}$
M_r	768.37	768.37	768.37	768.37	768.37	768.37	768.37	768.37
Cell setting, space group	Monoclinic, $P2_1/n$	Monoclinic, $P2_1/n$	Monoclinic, $P2_1/n$	Monoclinic, $P2_1/n$	Monoclinic, $P2_1/n$	Monoclinic, $P2_1/n$	Monoclinic, $P2_1/n$	Monoclinic, $P2_1/n$
a, b, c /Å	11.8945(6) 11.1622(6) 14.8414(7)	11.9606(8) 11.1907(14) 14.9881(17)	11.7266(5) 10.8689(9) 14.7780(10)	11.6515(5) 10.7495(10) 14.7023(10)	11.5740(5) 10.5940(9) 14.6089(9)	11.5114(5) 10.4608(9) 14.4885(11)	11.4925(7) 10.3860(12) 14.4601(14)	11.7388(9) 9.7360(16) 14.7231(18)
β /°	112.682 (3)	112.46 0(6)	112.656 (4)	112.796 (4)	113.014(4)	113.354(4)	113.469(5)	115.796(7)
V /Å^3	1818.1 (2)	1854.0 (3)	1738.18 (16)	1697.59 (18)	1648.71(17)	1601.8(2)	1583.2(2)	1515.0(3)
Z	2	2	2	2	2	2	2	2
D_x /Mg m^{-3}	1.403	1.375	1.468	1.503	1.548	1.593	1.612	1.684
Radiation	Mo $K\alpha$	Synchrotron	Synchrotron	Synchrotron	Synchrotron	Synchrotron	Synchrotron	Synchrotron
Wavelength, λ	0.71073 Å	0.4863 Å	0.4863 Å	0.4863 Å	0.4863 Å	0.4863 Å	0.4863 Å	0.4863 Å
No. of reflections for cell parameters	7043	1437	1506	1037	1145	963	887	814
θ range /°	2–31	2–15	2–16	2–15	2–15	2–14	2–15	2–13
μ /mm^{-1}	0.665	0.652	0.696	0.712	0.733	0.755	0.764	0.798
Temperature /K	150	293	293	293	293	293	293	293
Crystal colour, shape	Green block	Green block	Green block	Green block	Green block	Green block	Green block	Green block
Crystal size /mm	0.71 0.37 0.24	0.03 0.07 0.10	0.03 0.07 0.10	0.03 0.07 0.10	0.03 0.07 0.10	0.03 0.07 0.10	0.03 0.07 0.10	0.03 0.07 0.10

Table 5-1: Crystal data for high pressure data collections

Pressure (GPa)	**0**	**0.2**	**0.7**	**1.1**	**1.7**	**2.4**	**2.9**	**3.8**
Diffractometer	Bruker Smart Apex CCD	Daresbury 9.8	Daresbury 9.8	Daresbury 9.8	Daresbury 9.8	Daresbury 9.8	Daresbury 9.8	Daresbury 9.8
Data collection method	ω	ω	ω	ω	ω	ω	ω	ω
Absorption correction	Multi-scan	Multi-scan	Multi-scan	Multi-scan	Multi-scan	Multi-scan	Multi-scan	Multi-scan
T_{min}	0.67	0.96	0.68	0.67	0.71	0.55	0.76	0.85
T_{max}	0.85	0.98	0.98	0.98	0.98	0.98	0.98	0.98
Reflections measured, independent, I > 2.00σ(I)	28245 5192 4429	5812 1705 1045	5192 1506 1103	5154 1485 1095	4947 1426 1100	4924 1414 1040	4659 1360 996	3800 983 670
Completeness /%	100	64	60.0	60.6	59.7	60.9	59.6	64.6
R_{int}	0.0363	0.1083	0.1442	0.1447	0.1298	0.1374	0.1338	0.094
θmax	57.4	15.8	15.7	15.7	15.7	15.7	15.7	13.9
Refinement on	*F*	*F*	*F*	*F*	*F*	*F*	*F*	*F*
R[F > 2s(F)] wR(F) GoF	0.0409 0.1174 1.054	0.0773 0.0871 1.248	0.0662 0.0417 1.150	0.0682 0.714 1.173	0.0649 0.0722 0.997	0.0623 0.0644 1.168	0.0647 0.0685 1.114	0.0833 0.0444 1.822
No. of parameters	237	232	232	232	232	232	232	168
H-atom treatment	Mixed	Not refined	Not refined	Not refined	Not refined	Not refined	Not refined	Not refined
Maximum shift	<0.0005	<0.0001	<0.0001	<0.0001	<0.0001	<0.0001	<0.0001	0.002
Residual Density /e Å^{-3}	0.917 -0.413	0.43 -0.40	0.32 -0.32	0.40 -0.44	0.40 -0.58	0.38 -0.39	0.30 -0.31	0.36 -0.41

Table 5-1: Data collection and refinements details

5.4. Results

In total seven data-sets up to a final pressure of 3.8 GPa were obtained (see Table 5-1).

5.4.1. The effect of pressure on unit cell dimensions

Increasing pressure to 2.9 GPa caused the volume of the unit cell to decrease by 14.6%, 6.2% occurring within the first 0.7 GPa (see Figure 5-4). The biggest change in cell axes was observed in the *b* axis which decreased by 7.2 %. The *a* and *c* axes decreased by 3.9 and 3.5 %, respectively whilst the β angle increases by 0.9%. Between 2.9 and 3.8 GPa a single-crystal to single-crystal phase transition occurred. This is indicated by a sudden change in the cell dimensions, with *b* dropping sharply, and *a*, *c* and β increasing, leading to a sharper decrease in cell volume (see Figure 5-4 and Figure 5-5). The cell indices obtained for the 3.8 GPa data-set continue the trends observed prior to the transition with *a*, *b*, and *c* decreasing and β increasing as before. The final percentage changes in cell dimensions up to 3.8 GPa were 1.9, 13.0 and 1.8 % for *a*, *b* and *c* and 3.0 % for β. The volume changed by 18.3 % overall.

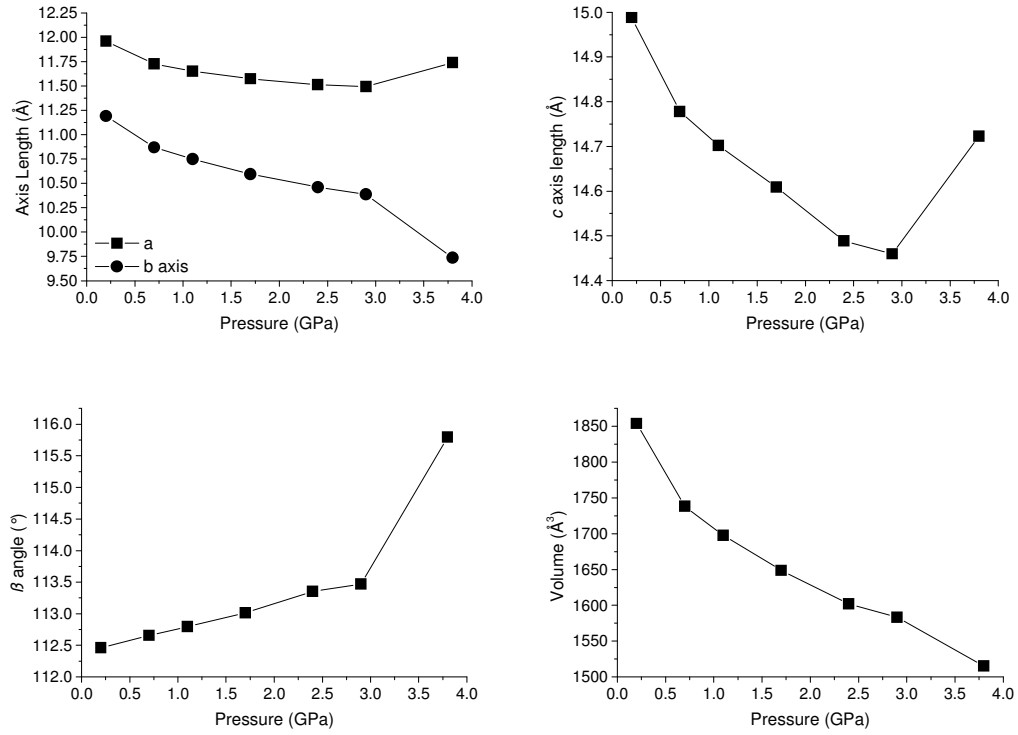

Figure 5-4: Graphs indicating the effect of pressure on unit cell parameters. *a* and *b* (top left), *c* (top right), *β* (bottom left) and volume (bottom right)

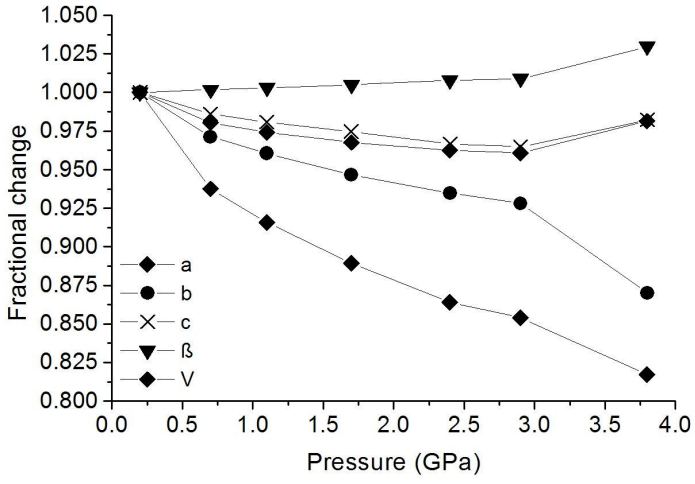

Figure 5-5: The effect of increasing pressure on the unit cell parameters *a*, *b*, *c* and *β* and the cell volume displayed as fractional change from the lowest pressure. A phase transition is apparent between 2.9 and 3.8 GPa.

5.4.2. The effect of pressure on molecular structure

[Cu(3-pipCH$_2$-5-^{t}Bu-salox)$_2$(NO$_3$)$_2$] crystallises in space group $P2_1/n$ at ambient pressure with the copper atom on an inversion centre. The molecular structure and atomic numbering scheme is shown in Figure 5-6.

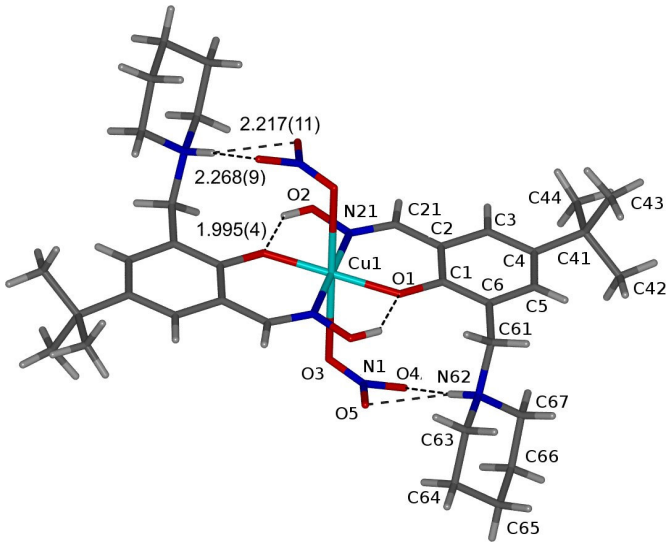

Figure 5-6: The molecular structure of [Cu(3-pipCH$_2$-5-^{t}Bu-salox)$_2$(NO$_3$)$_2$] at 0.2 GPa with atomic labels for the assymetric unit and intramolecular hydrogen bonds.

After the phase transition which occurs between 2.9 and 3.8 GPa, the inversion symmetry is broken. As pressure is increased towards 2.9 GPa, the cavity in which the NO_3^- group resides becomes smaller (see section 5.4.2.3). This is indicated by decreases in the inter and intramolecular NO_3^- contact distances which are discussed later in sections 5.4.2.2 and 5.4.2.3. The shape of the cavity and its reduction in size is the likely cause of the twisting of the NO_3^- group as O4 moves towards to the NH. The other NO_3^- group which has the shorter Cu-O distance is oriented perpendicular to the mean plane of the complex. This reorientation of the NO_3^- group frees up space between adjacent molecules in the stack allowing the piperidine ring to change conformations shown in Figures 5-7 and 5-8. This reduces the volume occupied by the ring in the interstitial area between molecules and allows molecules to approach one another much more closely.

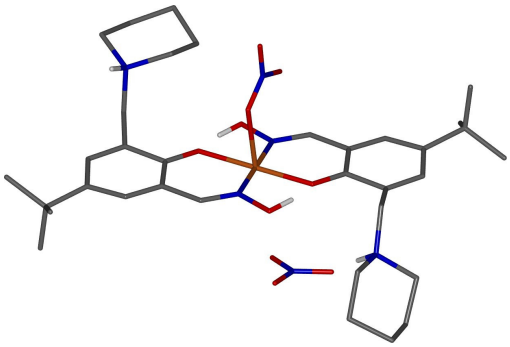

Figure 5-7: The structure of [Cu(3-pipCH$_2$-5-^{t}Bu-salox)$_2$(NO$_3$)$_2$] at 3.8 GPa showing one NO$_3^-$ approximately parallel and on approximately perpendicular to the mean plane through CuN$_2$O$_2$

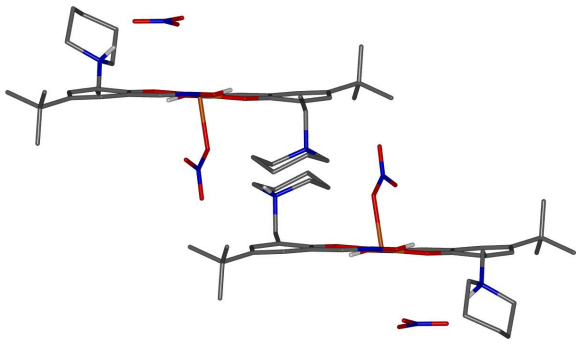

Figure 5-8: Stacking in the structure of [Cu(3-pipCH$_2$-5-^{t}Bu-salox)$_2$(NO$_3$)$_2$] at 3.8 GPa

5.4.2.1. Metal ion geometry

Of greatest interest is the effect of pressure on metal ion geometry. A number of previous studies have shown that the application of pressure to metal complex systems can alter the geometry and coordination of the metal ion. High-pressure studies conducted by Allan *et al*[27] show that the application of pressure can lead to an increase in the coordination number of the square-planar palladium complex, *cis*-[PdCl$_2$(1,4,7-trithiacyclononane)] from four to [4+2] coordinate at 4.4 GPa forming an intensely coloured chain polymer. A study of an organic-inorganic hybrid structure containing $SbCl_5^{2-}$ anions by Bujak and Angel[28] showed that bridges between the anions are formed so that a chain of corner-sharing octahedra is formed at ~3.1 GPa. By contrast, though a compression study of [Ru$_3$(CO)$_{12}$][29] revealed no

change in metal coordination, the Ru-Ru bond lengths decreased from 2.844(2) to 2.764(15) Å. Study of magnetic systems also shows a trend for decreasing Mn-Cl bond distances in $[(CH_3)_4N][MnCl_3]$ studied by Tancharakorn *et al.*[30]

The application of pressure to $[Cu(3\text{-}pipCH_2\text{-}5\text{-}^tBu\text{-}salox)_2(NO_3)_2]$ was expected to follow trends seen in some of these other systems where metal-ligand bonds can become shorter when pressure is increased in order to reduce the molecular volume. However, work conducted in collaboration with Lindoy and Clegg (University of Sydney),[31] has shown for a dinuclear copper complex containing 1-methylpiperazine a phase transition in which 6-coordinate copper atoms become 5-coordinate at only 0.2 GPa. Table 5-2 contains bond lengths pertaining to the inner coordination sphere of the copper atom in $[Cu(3\text{-}pipCH_2\text{-}5\text{-}^tBu\text{-}salox)_2(NO_3)_2]$ and Figure 5-9 shows these distances as a function of pressure. It is clear that the response of pressure by this system is unusual in exhibiting with a *lengthening* of the axial bonds and shortening of equatorial bonds with the most significant changes occurring between 0.2-0.7 GPa and between 2.9-3.8 GPa.

Pressure /Gpa	0.2	0.7	1.1	1.7	2.4	2.9	3.8
Cu-O1 /Å	1.926(6)	1.906(4)	1.905(5)	1.897(4)	1.874(4)	1.884(5)	1.929(6)
Cu-N22 /Å	1.922(7)	1.935(4)	1.933(5)	1.935(5)	1.918(5)	1.927(5)	1.901(5)
Cu-O3 /Å	2.647(9)	2.781(7)	2.784(7)	2.802(7)	2.789(7)	2.795(7)	3.234(8)
Cu-O31 /Å	2.647(9)	2.781(7)	2.784(7)	2.802(7)	2.789(7)	2.795(7)	2.259(11)

Table 5-2: Bond lengths in the inner coordination sphere of copper atoms. The atom labelled O31 is the symmetry equivalent of O3 until after the phase transition.

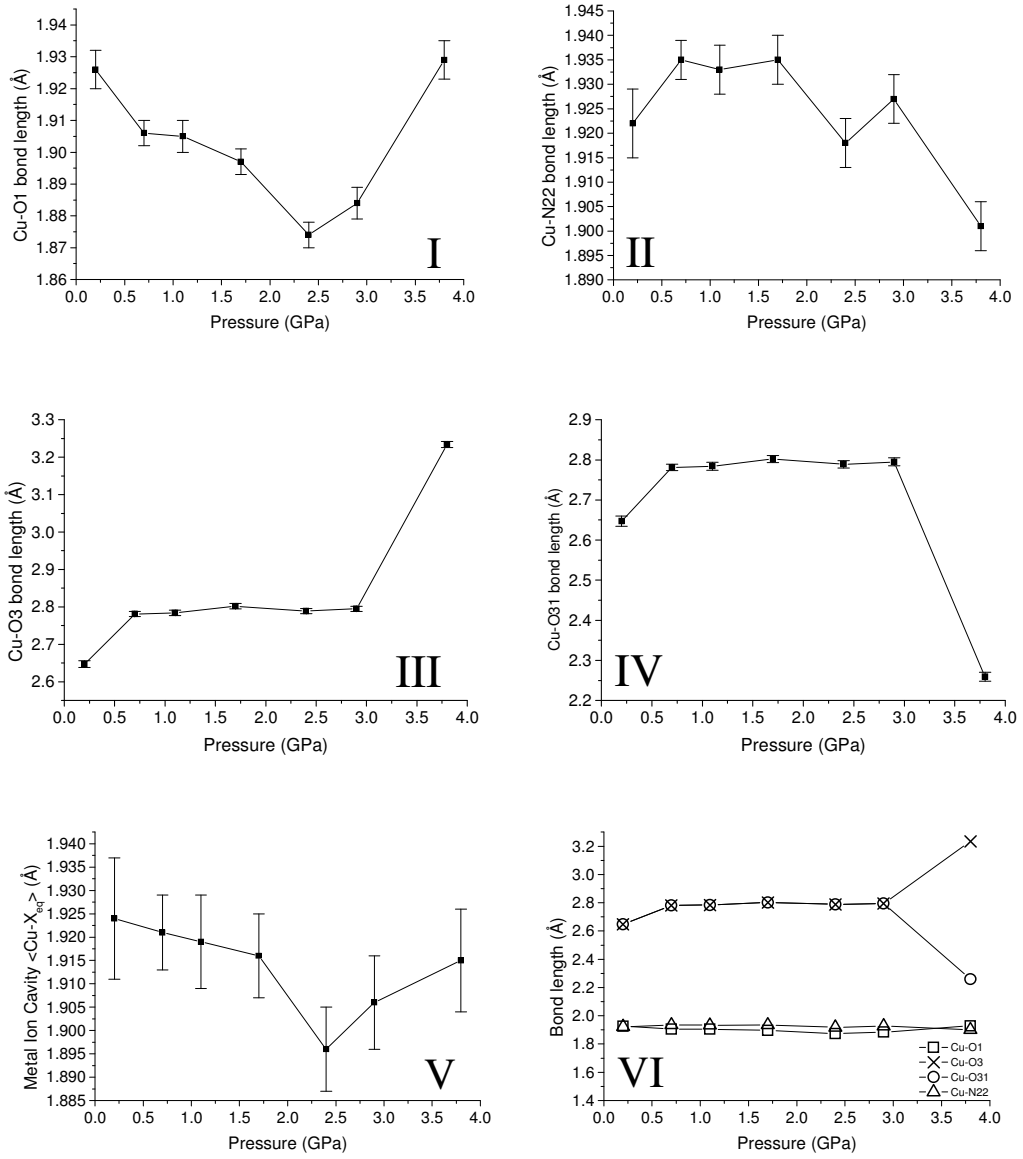

Figure 5-9: Graphs showing the trends in inner coordination sphere bond lengths of the copper atom as a function of pressure. The Cu-O1 bond length is shown in I (top left), Cu-N22 in II, the axial Cu-O3 bond in III, the axial Cu-O31 bond in IV, bottom left and the metal ion cavity (defined as the average of the Cu-X equatorial bonds) in V. Graphs I-IV are combined onto one set of axes in graph VI. Error bars indicate one standard deviation.

The phase transition which occurs between 2.9 and 3.8 GPa is accompanied by large changes in the axial interactions. The graphs presented above in Figure 5-9 show that overall the axial bond lengths have increased between 0.2 GPa and 2.9 GPa. Between 2.9 and 3.8 GPa symmetry is broken denoted by a marked increase in one

of the axial bond lengths, Cu1-O3, with a change from 2.795(7) to 3.234(8) Å whilst the other, Cu1-O31, decreases to 2.259(11) Å. The equatorial Cu1-O1 bond decreases from 1.926(6) to 1.884(5) Å towards 2.9 GPa before increasing to 1.929(6) after the phase transition. Changes between pressure for the Cu1-N22 bond length are not statistically significant although overall a decrease is suggested by the data. The errors associated with the cavity ion size indicate that changes are not statistically significant.

It is important to determine whether the Cu-O3 bond has truly broken or not when the pressure is increased to 3.8 GPa which would indicate a change in coordination number. The offset of the O3 atom from the 'ideal' axis, which is defined as the axis running through Cu1 perpendicular to the CuN_2O_2, plane along with the Cu-O3-N1 angle and the Cu-O3 bond length are tabulated in Table 5-3. As pressure increases the offset increases steadily until 2.9 GPa is reached at which point the offset almost doubles to 0.97 Å. This is accompanied by a significant reduction in the Cu-O3-N1 angle, and a big change in the length of the Cu-O3 bond.

Pressure /GPa	0.2	0.7	1.1	1.7	2.4	2.9	3.8
Cu-O3-N1 /°	110.4(8)	104.9(5)	104.9(5)	104.0(5)	105.5(5)	105.4(5)	93.8(6)
O3 offset /Å	0.36(1)	0.48(1)	0.50(1)	0.52(1)	0.54(1)	0.56(1)	0.97(1)
Cu-O3 /Å	2.647(9)	2.781(7)	2.784(7)	2.802(7)	2.789(7)	2.795(7)	3.234(8)

Table 5-3: The angle made by the Cu-O3 bond vector with the CuN_2O_2 plane at different pressures.

The breaking of the bond Cu-O3 would represent a change to square pyramidal geometry at the copper atom. Angles surrounding the copper ion are tabulated in Table 5-4 and the structure shown in Figure 5-10. Angles involving O3 are significantly different to the expected values of 90° or 180° found in a perfect octahedron whilst the other angles indicate show some distortion but indicate square based pyramidal geometry if O3 is considered not to bond to Cu1.

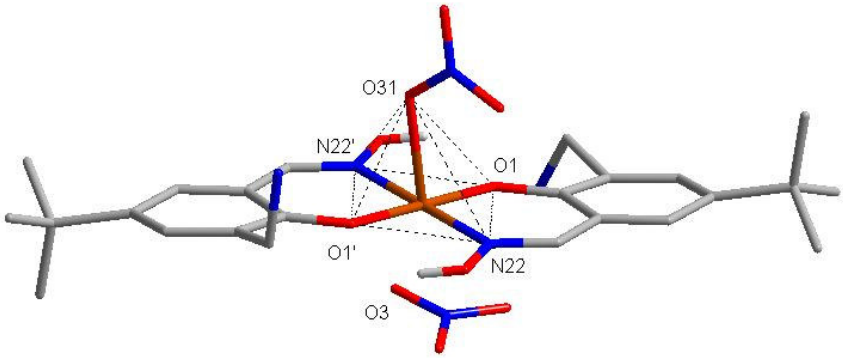

Figure 5-10: The structure of [Cu(3-pipCH$_2$-5-^{t}Bu-salox)$_2$(NO$_3$)$_2$] with the piperidine arms removed. The labelling used in Table 5-4is given and the square based pyramidal geometry highlighted.

Parameter	Angle /°
O1-Cu1-O31	100.9(3)
O1-Cu1-N22	93.4(3)
O1-Cu1-O1'	180
O1-Cu1-N22'	86.6(3)
O1-Cu1-O3	62.9(2)
N22-Cu1-O31	99.2(3)
N22-Cu1-O1'	86.6(3)
N22-Cu1-N22'	180
N22-Cu1-O3	120.8(3)
O1'-Cu1-O31	79.1(3)
O1'-Cu1-N22'	93.4(3)
O1'-Cu1-O3	117.1(2)
N22'-Cu1-O31	80.8(3)
N22'-Cu1-O3	59.2(3)
O31-Cu1-O3	136.4(3)

Table 5-4: Angles surrounding the copper atom in the 3.8 GPa structure.

For comparison, bond lengths in square pyramidal copper complexes were investigated using the CSD for comparison to those in this complex. The structures used were restricted to those in which eight 90° and two 180° angles were present in a square based pyramid arrangement, allowing deviations of up to 15°. The axially bound atom, i.e. at the apex of the pyramid, was restricted to be only oxygen and all equatorially bound atoms were allowed to be any element.

This produced a dataset in which equatorial bonds were distributed around a peak at ~1.97 Å with minimum and maximum values of ~1.85 and ~2.10 Å disregarding a small number of outliers. The axial bond lengths in this dataset lie between ~2.05 and 2.70 Å with a peak at ~2.30 Å. These are very similar to the bond lengths observed in the 3.8 GPa structure in which equatorial bond lengths are 1.901, 1.901, 1.929, 1.929 Å for the equatorial bonds and 2.259 Å for the axial bond.

5.4.2.2. Intramolecular hydrogen bonding

In the ambient pressure phase of [Cu(3-pipCH$_2$-5-^{t}Bu-salox)$_2$(NO$_3$)$_2$], the N62-H of the piperidine groups forms an intramolecular bifurcated hydrogen bond to O4 and O5 of the NO_3^- group with very similar distances of 2.24 and 2.25 Å (see Table 5-5). For structures determined by x-ray diffraction in the CSD, a peak is observed at ~2.03 Å for (non-normalised) all inter and intramolecular NH…O hydrogen bond lengths.

Pressure /GPa	0.2	0.7	1.1	1.7	2.4	2.9	3.8
NH…O4 /Å	2.241(11)	2.014(6)	1.939(6)	1.925(6)	1.914(6)	1.901(7)	1.711(9)
N…O4 /Å	3.105(14)	2.887(8)	2.844(8)	2.812(8)	2.799(8)	2.795(9)	2.608(13)
NH…O5 /Å	2.245(10)	2.366(6)	2.400(7)	2.412(6)	2.474(6)	2.462(7)	2.756(10)
N…O5 /Å	3.006(13)	3.094(8)	3.121(9)	3.126(8)	3.158(7)	3.156(9)	3.484(15)

Table 5-5: Intramolecular hydrogen bonding distances formed between the piperidine NH and the NO_3^- group.

As pressure is increased, one of the hydrogen bonds gradually becomes shorter with the NH…O4 distance decreasing to 1.90 Å at 2.9 GPa whilst the NH…O5 bond lengthens to 2.46 Å. This corresponds to the movement of the NO_3 group away from the copper, and thus the lengthening of the Cu-O3 bond, and slight rotation about the axis normal to the NO_3 plane. At 3.8 GPa the N62-H…O5 hydrogen bond length has increased to 2.76 Å whilst the N62-H…O4 has decreased further to 1.71 Å which is very short for NH…O hydrogen bonds (see above).

5.4.2.3. Packing analysis

For the lowest pressure (0.2 GPa) structure, large voids exist which are concentrated in the regions above and below the aromatic rings. Molecules stack on top of one another in the manner shown in Figure 5-11 with the NO_3^- group, which sits in the interstitial sites between complexes, in a cavity formed by the piperidine arms of adjacent molecules (see Figure 5-12). The shortest intermolecular distances involving the NO_3^- group are 2.48 Å to H672 and 3.14 Å to H422 of the adjacent molecule's piperidine and tertiary butyl groups respectively (see Figure 5-12). The oxygen atom, O3, which is bound to the copper atom has contacts with C63-H and C61-H of the piperidine ring of a neighbouring molecule with H…A distances of 2.39 and 2.52 Å.

Pressure /GPa	0.2	0.7	1.1	1.7	2.4	2.9	3.8
C61H…O4 /Å	2.560(9)	2.446(6)	2.398(6)	2.336(6)	2.330(5)	2.296(6)	2.408(8)
C61…O4 /Å	3.215(12)	3.045(8)	2.997(9)	2.932(8)	2.877(8)	2.856(9)	2.823(10)
C63H…O5 /Å	2.456(9)	2.413(6)	2.443(7)	2.471(6)	2.426(6)	2.397(7)	2.567(10)
C63…O5 /Å	3.283(14)	3.217(9)	3.225(10)	3.199(9)	3.189(9)	3.168(10)	3.132(15)

Table 5-6: Intermolecular CH...O and C...O contact distances.

Other intermolecular contacts exist between piperidine arms and the aromatic rings of the adjacent molecules near C3. The bulk of the tertiary butyl groups prevents π-π stacking from occurring. There are no significant *inter*molecular hydrogen bonds involving nitrogen or oxygen atoms which is largely due to the shielding of potential hydrogen bond donors by either intramolecular hydrogen bonds or steric effects.

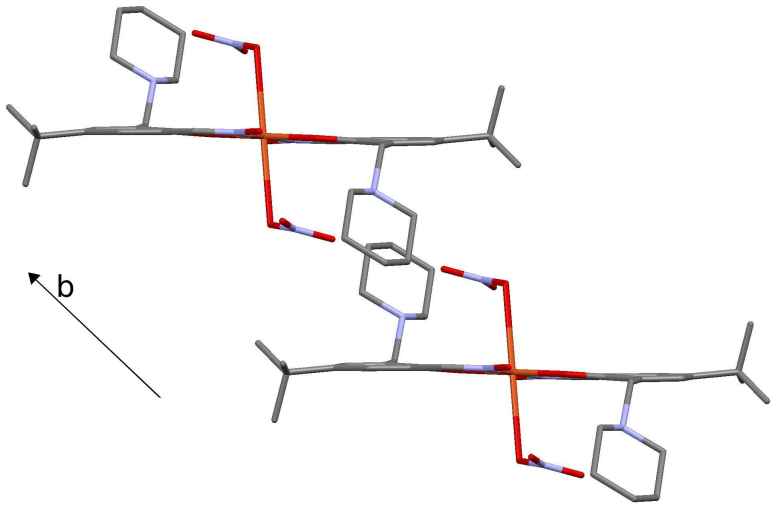

Figure 5-11: Stacking of adjacent molecules in the structure of [Cu(3-pipCH$_2$-5-^{t}Bu-salox)$_2$(NO$_3$)$_2$] at 0.2 GPa. The *b* axis lies along the vector indicated.

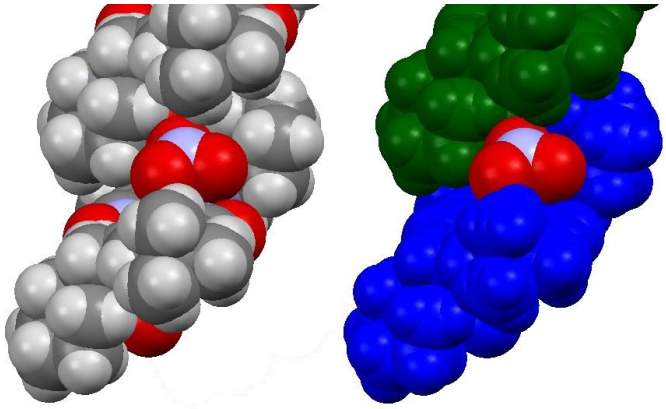

Figure 5-12: Space filling plot showing the NO_3^- group and its surrounding environment. Discrete molecules surrounding the NO_3^- group are shown in different colours on the right.

The application of pressure tends to cause voids between molecules to close up before significant conformational changes are observed. This is observed in this pressure series with a gradual decrease in the volume of voids as pressure is increased towards 2.9 GPa. The voids significantly reduce up to this point with a scattering of a few small voids remaining and the rate of change in unit cell volume decreasing (see Figures 5-14, 5-15 and 5-16).

On increasing pressure to 2.9 GPa, the molecules move steadily towards one another and the tertiary butyl group gradually rotates. After the phase transition a larger change is observed (see Table 5-7 and Figure 5-13).

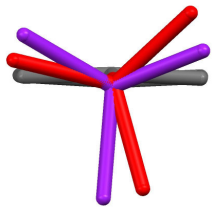

Figure 5-13: High pressure forces the tertiary butyl group to adopt a less eclipsed conformation at 3.8 GPa (purple) with the aromatic ring (grey) when compared to the lower pressure 0.2 GPa structure (red).

Pressure /GPa	0.2	0.7	1.1	1.7	2.4	2.9	3.8
C3-C4-C41-C44 /°	15.8(14)	17.3(9)	16.6(9)	20.8(9)	22.9(9)	23.1(9)	37.6(6)
Distance between planes /Å	7.212	6.911	6.809	6.704	6.569	6.440	5.704

Table 5-7: Torsion angles of ^{t}Bu groups relative to the aromatic ring and the distance between CuN_2O_2 planes within the stack (as shown in Figure 5-11) in [Cu(3-pipCH_2-5-^{t}Bu-salox)$_2$(NO_3)$_2$] for all pressures. A large jump is seen between 2.9 and 3.8 GPa

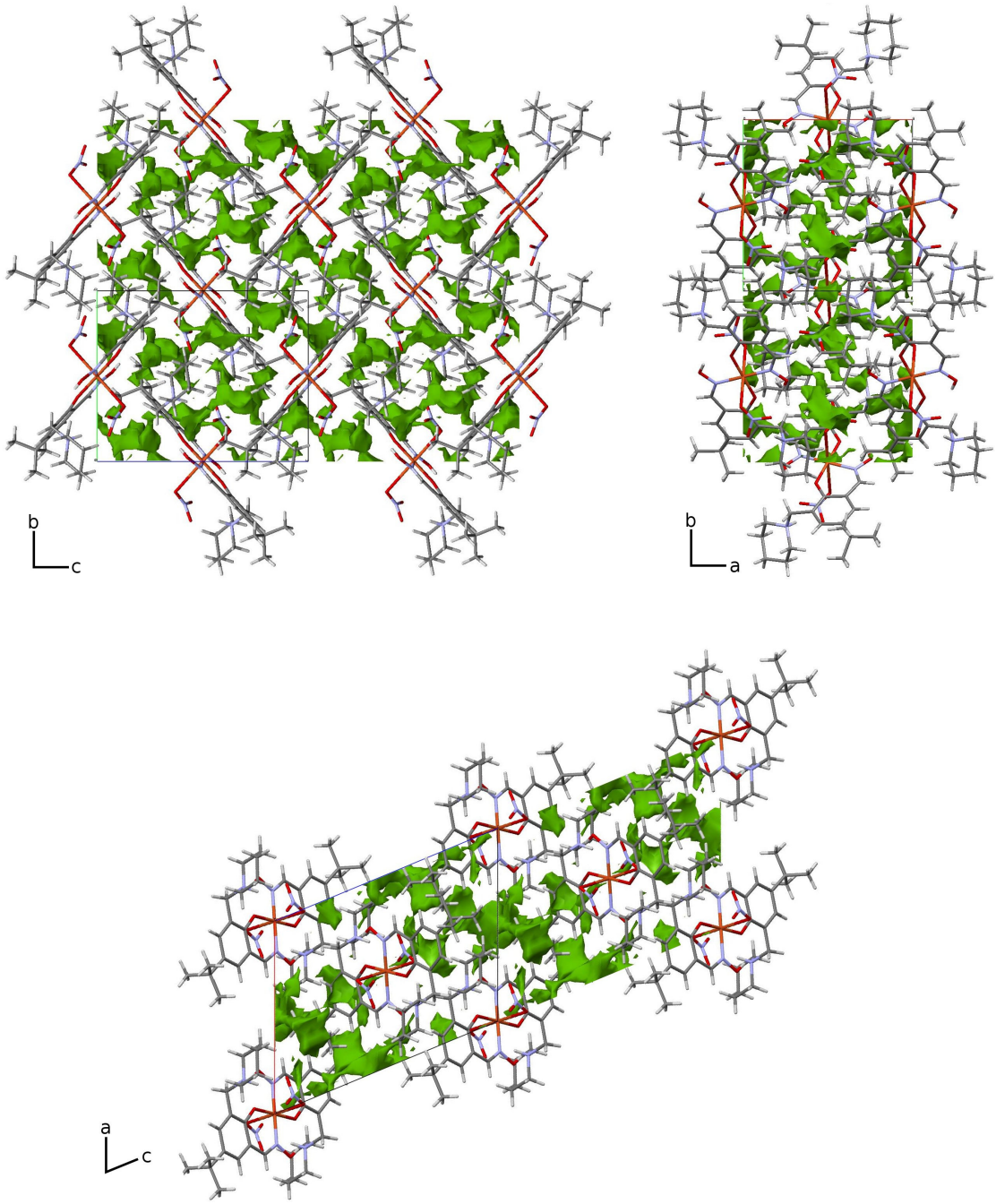

Figure 5-14: The crystal packing structure of [Cu(3-pipCH$_2$-5-^{t}Bu-salox)$_2$(NO$_3$)$_2$] at 0.2 GPa. Views are shown along the *c* axis (top left), *a* axis (top right) and *b* axis (bottom) with voids shown in green. Many large voids are visible filling the spaces between molecules, particularly around the NO$_3^-$ and piperidine groups.

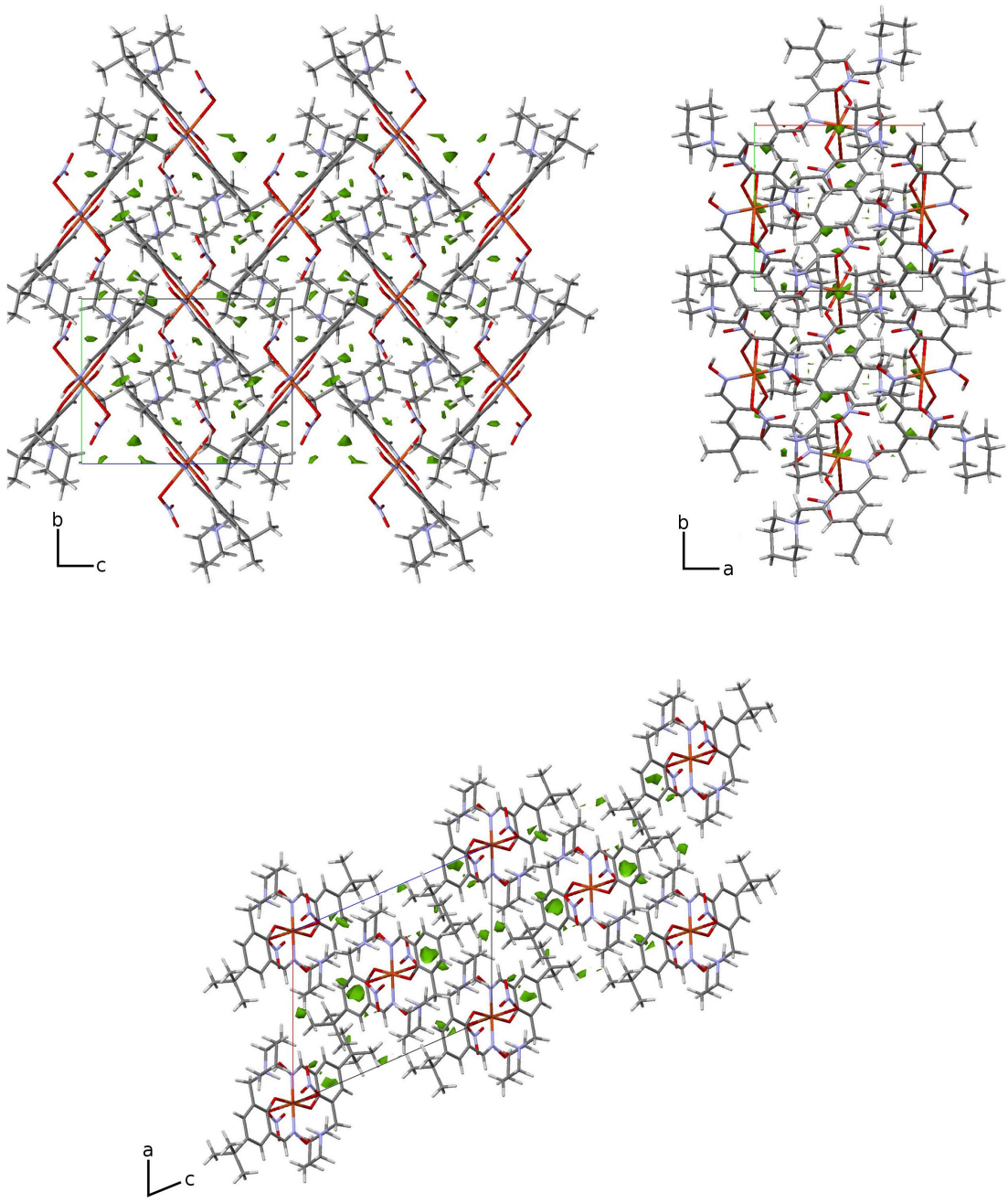

Figure 5-15: The crystal packing structure of [Cu(3-pipCH$_2$-5-^{t}Bu-salox)$_2$(NO$_3$)$_2$] at 2.9 GPa. Views are shown along the c axis (top left), a axis (top right) and b axis (bottom) with voids shown in green. Voids seen at low pressure have closed up with fewer smaller voids still present.

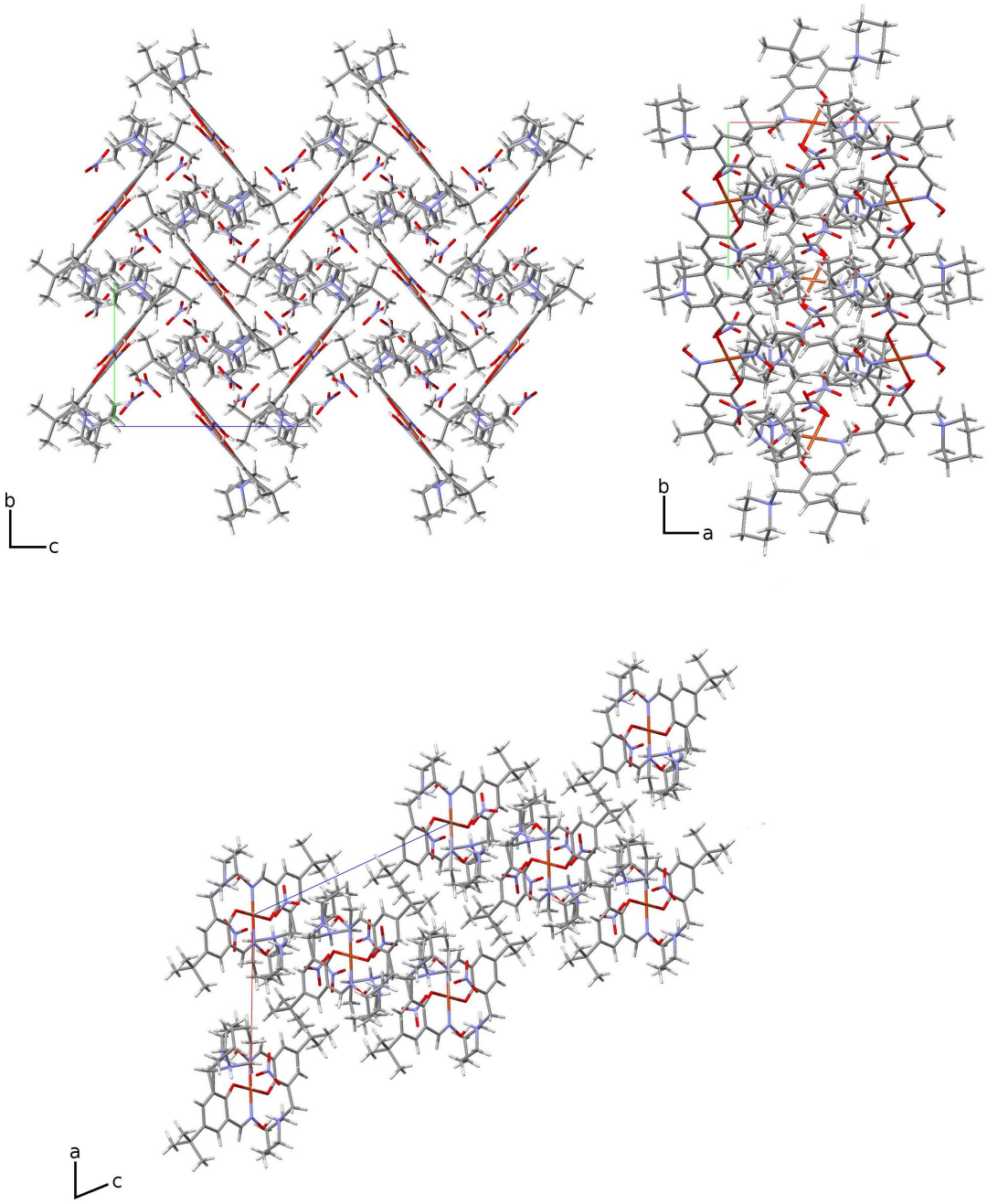

Figure 5-16: The crystal packing structure of [Cu(3-pipCH$_2$-5-^{t}Bu-salox)$_2$(NO$_3$)$_2$] at 3.8 GPa. Views are shown along the c axis (top left), a axis (top right) and b axis (bottom) with voids shown in green. At the highest pressure, voids accessible by a spherical probe with radius 0.5 Å have disappeared.

5.5. Conclusions

The application of pressure to a single crystal of the metal salt complex [Cu(3-pipCH$_2$-5-^{t}Bu-salox)$_2$(NO$_3$)$_2$] brings about a large reduction in unit cell volume. The biggest change in the unit cell lengths are in the *b* direction. Up to 2.9 GPa the decrease in cell volume is characterised by the closing up of voids which lie between molecules in the stacks in which complexes are aligned in the *b* direction. At 3.8 GPa a single-crystal to single-crystal phase transition occurs indicated by a sharp change in unit cell axes accompanied by a further decrease in volume. These changes indicated that a single-crystal to single-crystal phase transition has occurred.

Investigation of the structure showed that the axial bonds in the low pressure $P2_1/n$ phase I structure increased in length up to 2.9 GPa after which a phase transition occurred with the inversion symmetry being broken for the NO_3^- group and the piperidine groups. The change in the orientation of these groups allows them to occupy the space lying between adjacent molecules more efficiently, which allows closer packing. The coordination number of the copper atom appears to have changed from [4+2] to [5+1]. Similar changes in coordination were observed, albeit at considerably lower pressure, in the copper system studied in collaboration with Lindoy and Clegg.[31]

5.6. References

1. W. J. Nellis, *Reports on Progress in Physics*, 2006, **69**, 1479-1580.
2. T. H. Lin, W. Y. Dong, K. J. Dunn, C. N. J. Wagner and F. P. Bundy, *Physical Review B: Condensed Matter and Materials Physics*, 1986, **33**, 7820-7822.
3. T. V. Valyanskaya and G. N. Stepanov, *Solid State Communications*, 1993, **86**, 723-725.
4. A. Dawson, D. R. Allan, S. A. Belmonte, S. J. Clark, W. I. F. David, P. A. McGregor, S. Parsons, C. R. Pulham and L. Sawyer, *Crystal Growth & Design*, 2005, **5**, 1415-1427.
5. S. A. Moggach, S. Parsons and P. A. Wood, *Crystallography Reviews*, 2008, **14**, 143-184.
6. S. A. Moggach, D. R. Allan, C. A. Morrison, S. Parsons and L. Sawyer, *Acta Cryst*, 2005, **B61**, 56-68.
7. S. A. Moggach, W. G. Marshall and S. Parsons, *Acta Cryst*, 2006, **B62**, 815-825.
8. E. V. Boldyreva, H. Sowa, Y. V. Seyotkin, T. N. Drebushchak, H. Ahsbahs, V. Chernyshev and V. Dimitriev, *Chem. Phys. Lett.*, 2006, **429**, 474-478.
9. R. Fourme, R. Kahn, M. Mezouar, E. Girard, C. Hoerentrup, T. Prange and I. Ascone, *Journal of Synchrotron Radiation*, 2001, **8**, 1149-1156.
10. R. Fourme, I. Ascone, R. Kahn, M. Mezouar, P. Bouvier, E. Girard, T. Lin and J. E. Johnson, *Structure*, 2002, **10**, 1409-1414.
11. F. P. A. Fabbiani, D. R. Allan, W. I. F. David, A. J. Davidson, A. R. Lennie, S. Parsons, C. R. Pulham and J. E. Warren, *Crystal Growth & Design*, 2007, **7**, 1115-1124.
12. F. P. A. Fabbiani, D. R. Allan, A. Dawson, W. I. F. David, P. A. McGregor, I. D. H. Oswald, S. Parsons and C. R. Pulham, *Chem Comm*, 2003, **24**, 3004-3005.
13. I. D. H. Oswald, I. Chataigner, S. Elphick, F. P. A. Fabbiani, A. R. Lennie, J. Maddaluno, W. G. Marshall, T. J. Prior, C. R. Pulham and R. I. Smith, *CrystEngComm*, 2008, In press.
14. A. Prescimone, C. J. Milios, S. A. Moggach, J. E. Warren, A. R. Lennie, J. Sanchez-Benitez, K. V. Kamenev, R. Bircher, M. Murrie, S. Parsons and E. K. Brechin, *Angew. Chem. Int. Ed.*, 2008, **47**, 2828-2831.
15. L. Merrill and W. A. Bassett, *Rev. Sci. Instrum.*, 1974, **45**, 290-294.
16. G. J. Piermarini, S. Block, J. D. Barnett and R. A. Forman, *J. Appl. Phys.*, 1975, **46**, 2774-2780.
17. P. M. Bell, J. A. Xu and H. K. Mao, *Shock Waves in Condensed Matter*, Plenum Press, New York, USA, 1986.
18. S. A. Moggach, D. R. Allan, S. Parsons and J. E. Warren, *Journal of Applied Crystallography*, 2008, **41**, 249-251.
19. A. Dawson, D. R. Allan, S. Parsons and M. Ruf, *Journal of Applied Crystallography*, 2004, **37**, 410-416.
20. Bruker-Nonius, Bruker-AXS, Madison, Wisconsin, USA, Editon edn., 2006.

21. S. Parsons, The University of Edinburgh, Edinburgh, UK, Editon edn., 2004.
22. S. Parsons, The University of Edinburgh, Edinburgh, United Kingdom, Editon edn., 2004.
23. G. M. Sheldrick, Bruker-AXS, Madison, WIsconsin, USA, Editon edn., 2004.
24. P. W. Betteridge, J. R. Carruthers, R. I. Cooper, K. Prout and D. J. Watkin, *Journal of Applied Crystallography*, 2003, **36**, 1487.
25. C. F. Macrae, I. J. Bruno, J. A. Chisholm, P. R. Edgington, P. McCabe, E. Pidcock, L. Rodriguez-Monge, R. Taylor, J. van de Streek and P. A. Wood, *Journal of Applied Crystallography*, 2008, **41**, 466-470.
26. K. Brandenburg and H. Putz, Crystal Impact, Bonn, Germany, Editon edn., 2005.
27. D. R. Allan, A. J. Blake, D. Huang, T. J. Prior and M. Schroder, *Chem Comm*, 2006, **39**, 4081-4083.
28. M. Bujak and R. Angel, *Journal of Physical Chemistry B*, 2006, **110**, 10322-10331.
29. C. Slebodnick, J. Zhao, R. Angel, B. E. Hanson, Y. Song, Z. Liu and R. J. Hemley, *Inorganic Chemistry*, 2004, **43**, 5245-5252.
30. S. Tancharakorn, F. P. A. Fabbiani, D. R. Allan, K. V. Kamenev and N. Robertson, *J. Am. Chem. Soc.*, 2006, **128**, 9205-9211.
31. J. K. Clegg, *PhD Thesis*, University of Sydney, 2007.

Chapter 6

Conclusions

6. Conclusions

The work presented in this thesis sought to address two central themes,

- the development of molecular models to elucidate the structure of surface complexes of malonates and hydroxamates in order to understand and predict their surface activity and to guide the design of new friction modifiers, and
- the analysis of solid state structures determined by X-ray crystallography to understand the binding in copper(II) complexes related to those formed in solvent extraction processes used industrially and the effects of ligand substituents on complex formation, stability and solubility.

Methods established previously[1] were used in chapters 2 and 3 to produce models for the binding of surface active ligands to iron oxide surfaces. In chapter 2 modelling was employed to explain the enhancement in binding of 2-(4-chlorophenyl)malonic acid to goethite over 4-keto acids. There were no available polynuclear iron(III) malonate crystal structures which could be used as structural motifs for docking onto faces of crystalline faces of iron(III) oxyhydroxides. An alternative approach was used in which the CSD was interrogated to extract all polynuclear binding motifs for transition metal malonato complexes as no iron malonato structures relevant to surfaces were present. This produced a large number of types of motifs which had to be scrutinized closely to identify structures which could apply to surface binding. A combination of CSD data mined for closely related iron(III) carboxylato structures, modelling on iron oxide surfaces and chemical intuition was used to select plausible models which were able to explain the enhancement in binding activity.

In chapter 3 the availability of a dinuclear iron(III) hydroxamate crystal structure $[Fe_2(\mu_2\text{-bha})_2(bha)_2Br_2]$ guided modelling efforts to explain high surface activity for goethite by benzohydroxamic acid. This allowed a more targeted approach to be adopted than was possible for the modelling of malonic acids. The packing density and relative disposition of molecules on the surface were investigated producing several models. These models were distilled down to a single one which indicated

that the aromatic ring did not participate in π-π stacking and, as such, only its bulk was important to binding strength. The model also suggested that substitution at the oximic nitrogen and oxygen atoms would affect its surface binding properties. These predictions were confirmed by experiments in which competitive binding of benzohydroxamic acid and methyl hydroxamic acid with a positive control were measure and showed little difference. The substitution of the hydrogen on the nitrogen of the oxime group with a methyl group was expected to reduce the packing efficiency of molecules by decreasing the planarity of the molecules and increasing their bulk. This prediction was also confirmedby observation lower surface coverage in its adsorption isotherm. Replacement of the oximic OH group with OMe was expected to remove the ability act as a dinucleating surface ligand. This was confirmed by adsorption isotherm measurements.

Modelling in both cases was successful. Even in the absence of appropriate polynuclear crystal structures it proved possible to produce plausible models which achieved the aims of the project. It is, however, much more desirable to be able to use crystal structures to define motifs as this considerably reduces the effort required to produce useful models. The hydroxamate binding model was used successfully to predict how substitution of the ligand framework would affect binding to goethite.

Chapters 4 and 5 describe the determination and analysis of the structures of copper complexes relevant to commercial solvent extraction processes. A series of salicylaldoxime ligands in which the substituent in the 3-position varied had previously shown a correlation between extractant strength and intermolecular attraction, between ligands as defined by the 'hole-sizes' in solid state dimeric crystal structures and ligand dimerisation enthalpies calculated in the gas phase. The initial expectation of the work presented in chapter 4 was that the crystal structures of their copper(II) complexes could also be used to correlate structural features with extractant strength. It turned out that there were many additional factors at play for complexes in the solid state such as the electronic effect of substitution on bond strengths or perturbation of bond lengths by axial interactions. The structures of the copper halide complexes of salicylaldoximes containing pendant anion binding groups provided definitive evidence for their mode of operation in transporting one mole of copper salt per mole of extractant. The high transport efficiency has

important industrial implications and the structures have guided the efforts of other workers to improve various aspects of their function.

Chapter 5 describes the use of high pressure to investigate its effect on the inner coordination sphere geometry of Jahn-Teller distorted copper atoms in a salicylaldoxime copper(II) complex. Conventional wisdom indicates that longer axial bonds in metal complexes are more likely to shorten in response to pressure in order to achieve a smaller molecular volume which increases packing efficiency. In this study it was found that the axial bonds lengthened. This occurred in such a way that the axial ligand could detach and achieve an orientation parallel to the mean plane through the complex which was more conducive to efficient packing.

Structural methods, both theoretical and experimental, are powerful tools which provide valuable insights into the function of ligands and their interaction with the metal ion or metal oxide surfaces they are designed for. Information derived this way can and has been used to understand key features and guide efforts to improve effectiveness of such ligands in metal extraction and surface engineering.

References

1. S. G. H. Harris, University of Edinburgh, 1999.